TALLINN UNIVERSITY OF TECHNOLOGY
DOCTORAL THESIS
5/2019

Chemical Processes Involved in $Cu_2ZnSnSe_4$ Synthesis and SnS Recrystallization in a Molten Salt Medium

INGA LEINEMANN

TTÜ PRESS

TALLINN UNIVERSITY OF TECHNOLOGY
School of Engineering
Department of Materials and Environmental Technology
This dissertation was accepted for the defense of the degree 21/12/2018

Supervisor:	Dr. Mare Altosaar School of Engineering: Department of Materials and Environmental Technology, TalTech, Tallinn, Estonia
Cosupervisor:	Dipl.-Chem., Dr. Rer. Nat., Dr. Dieter Meissner School of Engineering: Department of Materials and Environmental Technology, TalTech, Tallinn, Estonia
Opponents:	Dr. Kaia Ernits *crystalsol OÜ*, Head of Powder Development, Tallinn, Estonia
	Dr. Jonathan Scragg Department of Engineering Sciences, Solid State Electronics, Uppsala University, Uppsala, Sweden

Defense of the thesis: 24/01/2019, Tallinn

Declaration:
I hereby declare that this doctoral thesis, my original investigation and achievements submitted for the doctoral degree at Tallinn University of Technology, has not been previously submitted for a doctoral or equivalent academic degree.

Inga Leinemann

Signature

European Union
European Regional
Development Fund

Investing
in your future

Copyright: Inga Leinemann, 2019
ISSN 2585-6898 (publication)
ISBN 978-9949-83-384-9 (publication)
ISSN 2585-6901 (PDF)
ISBN 978-9949-83-385-6 (PDF)

TALLINNA TEHNIKAÜLIKOOL
DOKTORITÖÖ
5/2019

Keemilised protsessid $Cu_2ZnSnSe_4$ sünteesil ja SnS rekristallisatsioonil sulade soolade keskkonnas

INGA LEINEMANN

TTÜ
KIRJASTUS

Contents

List of Publications 7

Author's Contributions to Publications 8

Introduction 9

Abbreviations 11

Terms 14

Symbols 17

1 Literature Review 20
1.1 Development of Solar Cells 20
1.2 Tin Sulfide Solar Cells 21
1.3 Kesterite Solar Cells 22
1.4 Chemical Pathway to CZTSe Formation 24
1.4.1 Epitaxial Approach 24
1.4.2 Combined Thermodynamic and Experimental Approach 25
1.5 Monograin Powder Technology 31
1.6 Stability of Flux Materials 33
1.6.1 Cadmium Iodide 33
1.6.2 Sodium Iodide 35
1.6.3 Potassium Iodide 37
1.6.4 Tin Chloride 37
1.7 Phase Diagrams 38
1.7.1 Na-Se and K-Se Phase Diagrams 38
1.7.2 Cu-Se Phase Diagram 40
1.7.3 Cu-I and Sn-I Systems 42
1.7.4 Sn-Se and Sn-S Phase Diagrams 44
1.7.5 Pseudobinary Phase Diagrams 46
1.8 Summary of the Literature Overview and the Aim of the Study 48

2 Experimental 51
2.1 Selection of Composition and Calculation of the Amount of Flux Material 52
2.2 Analysis of Flux Salts (KI, NaI and CdI_2) and DTA Calibration 54
2.3 Analysis of Binary Precursors (ZnSe, SnSe and CuSe) 55
2.4 Thermodynamic Calculations with the HSC6 Chemistry Software 55
2.5 Analysis of the By-Products 56
2.6 Determination of the Solubility of the Precursors and CZTSe in KI and CdI_2 57
2.7 Analysis of Mixtures 57
2.8 Doping Determination in CZTSe 58
2.9 Procedure for CZTSe and SnS Recrystallization 59
2.10 Characterization Methods 60
2.10.1 Differential Thermal Analysis (DTA) 60
2.10.2 Mass Spectrometry (MS) 61
2.10.3 Differential Scanning Calorimetry (DSC) 61
2.10.4 Inductively Coupled Plasma Mass Spectrometry (ICP-MS) 62
2.10.5 Raman Spectroscopy 62
2.10.6 X-ray Diffraction (XRD) 62
2.10.7 Energy-Dispersive X-ray Spectroscopy (EDX) 63

2.10.8 Scanning Electron Microscopy (SEM) ... 63
2.10.9 X-ray Photoelectron Spectroscopy (XPS) ... 63

3 Results and Discussion ... 64
3.1 Results of Flux Analyses ... 64
3.2 Results of Precursor Analyses ... 68
3.3 Analysis of Expected By-Products ... 69
3.4 Determined Solubility ... 70
3.5 Results of the Mixture Analyses ... 70
3.5.1 Flux-ZnSe ... 70
3.5.2 Flux-SnSe ... 75
3.5.3 Flux-CuSe ... 82
3.5.4 Flux-SnSe-CuSe ... 92
3.5.5 Flux-ZnSe-SnSe-CuSe ... 99
3.6 Determination of Doping ... 114
3.7 CZTSe and SnS Recrystallization ... 115
3.7.1 CZTSe Recrystallization in CdI_2 ... 115
3.7.2 SnS Recrystallization in CdI_2, $SnCl_2$, and KI ... 117

Conclusions ... 120

References ... 122

Acknowledgments ... 133

Abstract ... 134

Lühikokkuvõte ... 136

Appendix 1 ... 139

Appendix 2 ... 205

Appendix 3 ... 207

Curriculum vitae ... 211

Elulookirjeldus ... 214

List of Publications

List of the author's publications, on the basis of which this thesis has been prepared:

I **Leinemann, I**., Timmo, K., Grossberg, M., Kaljuvee, T., Tõnsuaadu, K., Traksmaa, R., Altosaar, M., Meissner, D. (2015). Reaction enthalpies of $Cu_2ZnSnSe_4$ synthesis in KI. *J Therm Anal Calorim, 119*(3), 1555-1564. doi: 10.1007/s10973-014-4339-5

II **Klavina, I.,** Kaljuvee, T., Timmo, K., Raudoja, J., Traksmaa, R., Altosaar, M., Meissner, D. (2011). Study of $Cu_2ZnSnSe_4$ monograin formation in molten KI starting from binary chalcogenides. *Thin Solid Films, 519*(21), 7399-7402. doi: 10.1016/j.tsf.2011.01.365

III **Leinemann, I.,** Zhang, W., Kaljuvee, T., Tõnsuaadu, K., Traksmaa, R., Raudoja, J., Grossberg, M., Altosaar, M., Meissner, D. (2014). $Cu_2ZnSnSe_4$ formation and reaction enthalpies in molten NaI starting from binary chalcogenides. *J Therm Anal Calorim, 118*(2), 1313-1321. doi: 10.1007/s10973-014-4102-y

IV **Leinemann, I.,** Nkwusi, G. C., Timmo, K., Danilson, M., Raudoja, J., Kaljuvee, T., Traksmaa, R., Altosaar, M., Meissner, D. (2018). Reaction pathway to $Cu_2ZnSnSe_4$ formation in CdI_2 Part 1: Chemical reactions and enthalpies in mixtures of CdI_2-ZnSe, CdI_2-SnSe, and CdI_2-CuSe. *J Therm Anal Calorim, 134*(1), 409-421. doi: 10.1007/s10973-018-7102-5

V **Leinemann, I.,** Pilvet, M., Kaljuvee, T., Traksmaa, R., Altosaar, M. (2018). Reaction pathway to $Cu_2ZnSnSe_4$ in CdI_2 Part 2: Chemical reactions and enthalpies in mixtures of CdI_2-CuSe-SnSe and CdI_2-CuSe-SnSe-ZnSe. *J Therm Anal Calorim, 134*(1), 433-441. doi: 10.1007/s10973-018-7415-4

VI Timmo, K., Kauk-Kuusik, M., Pilvet, M., Mikli, V., Kärber, E., Raadik, T., **Leinemann, I.,** Altosaar, M., Raudoja, J. (2015). Comparative study of SnS recrystallization in molten CdI_2, $SnCl_2$ and KI. *Phys. Status Solidi C, 13*(1), 8-12. doi: 10.1002/pssc.201510082.

Copies of these articles are included in Appendix 1.

Author’s Contributions to Publications

The contributions to the papers in this thesis are as follows:

I-V Sample preparation (including in a glove box), heating, quenching, sample washing, some of the XRD (X-ray diffraction) measurements and spectral fittings, majority of the Raman measurements and spectra plotting, MS (mass spectrometry) and DTA (differential thermal analysis) data plotting and analysis, all measurements with the NETZSCH STA 449 F3 Jupiter, majority of data interpretation, majority of simple SEM-EDX (scanning electron microscopy and energy dispersive X-ray) measurements and data analysis, all work with the database (software HSC6 Chemistry Ver. 6.0.), determination and calculations of solubility data, majority of writing the papers.

VI Sample preparation for DSC (differential scanning calorimetry), measurements with the NETZSCH STA 449 F3 Jupiter, writing of chapter 3.3 for an article.

Introduction

The present thesis is devoted to investigations of the synthesis-growth process of single crystal $Cu_2ZnSnSe_4$ (CZTSe) powder for use as a solar cell absorber material. The research in this thesis was inspired by the need to understand the factors determining CZTSe formation and growth in molten salts with a focus on controlling the process.

The development of sustainable energy production has intensified during recent decades. Photovoltaic (PV) solar cells, which directly convert inexhaustible sunlight into electricity, can be used both in small-scale device applications and as large-area panel systems. PV solar cells can be used as energy suppliers for households and for terrestrial and space applications. Therefore, solar cell production is developing as a growing industry with a decrease in production costs (Yua-Shan, 2013).

Under the conditions of the global energy crisis, the desire to achieve high-efficiency, low-cost solar cells has been the key motivation for photovoltaic researchers. The cost of the absorber layer in a solar module can be reduced by using cheaper materials and technologies. Thus far, three types of thin-film materials – amorphous silicon, cadmium telluride and copper-indium-gallium-selenide/sulfide – have become commercially available. The last group of materials has achieved the highest efficiency, but unfortunately, indium is a rare metal (Ito, 2015). Despite the fact that dye-sensitized, organic and quantum dot cells have shown good performance in terms of efficiency, there are considerable issues with instability (Chuan-Pei, Chun-Ting & Kuo-Chuan, 2017). These circumstances have led to the development of new types of solar absorber materials – $Cu_2ZnSnSe_4$ (CZTSe), Cu_2ZnSnS_4 (CZTS) and a solid solution of $Cu_2ZnSn(S,Se)_4$ (CZTSSe). These materials have a high optical absorption coefficient ($> 10^4$ cm^{-1}), and they consist of low-cost, earth-abundant elements; the expensive In and Ga are substituted by Cu and Sn (Ito, 2015). Record efficiency is an important parameter for solar cells, and the method used to calculate this parameter is provided in Appendix 2, Section A2.1. The pure CZTSe absorber material in solar cells has shown a record efficiency of 11,6 % (Lee *et al.,* 2015), and the efficiency of CZTSSe solar cells fabricated by IBM (*International Business Machines*) *via* the hydrazine-solution method is even higher, with a value of 12,6 %. However, hydrazine is highly toxic and explosive (Wang *et al.*, 2013). In South Korea at DGIST (Daegu Gyeongbuk Institute of Science and Technology), a CZTSSe solar cell produced *via* the sputtering method in 2017 showed an efficiency of 13,8 % on an $18{,}1\cdot10^{-2}$ m^2 device (Wallace, Mitzi & Walsh, 2017). The *crystalsol OÜ* company (Tallinn, Estonia) uses monograin powder growth technology for the synthesis of CZTSSe, which was developed and patented by researchers of TalTech. These powder grains are used as absorber crystals in monograin layer (MGL) solar cells in which every grain works as an individual solar cell. Thus far, the spin-off company *crystalsol OÜ* in cooperation with the Laboratory of Photovoltaic Materials of TalTech has reached 8,4 % of the certified efficiency for a CZTSSe MGL solar cell, as published by (Ito, 2015). The power conversion efficiency (PCE) of the material in this cell is approximately 10,8 % due to the specific construction of the MGL solar cell (crystalsol lab, 2015).

In the monograin powder synthesis-growth method, the chemical conversion of the precursors during the growth of powder grains proceeds in the molten phase of suitable inorganic salts (flux materials). However, the large number of components in the CZTSe semiconductor and the complicated phase diagram if the environment of the molten phase of fluxes is used are problems for the synthesis of a single-phase absorber material due to the high probability of forming secondary solid phases. The chemical pathway for CZTSe formation in molten salts (KI, NaI, and CdI_2) and the chemical interactions of the salts with precursor compounds for CZTSe synthesis have not yet been studied.

SnS is a cheap and abundant material with a low toxicity. Its characteristics, including its high absorption coefficient of 10^4-10^5 cm^{-1}, optical bandgap energy value of 1,3 eV and *p*-type conductivity, show its suitability as an absorber material in solar cells (Sinsermsuksakul, Hartman, Kim, Heo & Sun, 2013); however, for unknown reasons, the efficiency of SnS solar cells is far below the expected value, and research on this material will be beneficial.

The aims of the research described in this thesis were a) to study and describe the formation of CZTSe in molten salts from polycrystalline binary compounds (ZnSe, SnSe and CuSe) for use as starting materials, b) to study the chemical interactions between precursor compounds and flux salts used in the synthesis, c) to study the processes occurring in the recrystallization of polycrystalline SnS in different molten salts and d) to clarify the possibilities of chemical formation of low melting compounds that can cause sintering of solid particles and interfere with the monograin growth.

This work is novel because there was a gap in knowledge regarding the chemical formation of CZTSe and the recrystallization of SnS in different flux salts, which has now been filled. The thermodynamic data obtained can also be used in inorganic databases for other research purposes. Recommendations for the CZTSe molten salt synthesis-growth process can be provided (for the flux selection to minimize the risks of byproduct formation and sintering).

Before starting the experiments with mixtures, analyses of binary precursors and flux materials were performed. The methods used in this research were based on thermodynamic simulations by a database (software HSC6 Chemistry Ver. 6.0.) to reduce the number of experiments. Then, DTA or DSC was again performed to reduce the number of experiments and to detect where any changes in the mixtures occurred. Afterwards, the required number of samples were prepared *via* quenching at higher or lower temperatures as changes occurred in the DTA or DSC curves to then analyze the "*freeze-in*" phase composition or morphology *via* Raman, XRD, SEM and EDX.

This dissertation is divided into three chapters. Chapter 1 provides a literature overview and contains different subsections that focus on the theoretical background of the working principles and production possibilities of kesterite and SnS-based solar cells. Chapter 1 is especially focused on the monograin powder technology. The role and importance of flux materials, such as KI, NaI, $SnCl_2$ and CdI_2, in monograin powder technology are also highlighted. The phase diagrams of compatible binary, ternary and quaternary compounds and the expected byproducts described in literature are discussed. Chapter 1 summarizes the literature review and formulates the aims of these studies. The experimental details of CZTSe monograin powder synthesis and the characterization methods used are described in Chapter 2. The results and discussion of the studies are presented in the last chapter. The thesis is based on six published papers, and the results have been presented at different conferences.

Abbreviations

3N purity	Purity of 99,9 %
4N purity	Purity of 99,99 %
AA	Aerosol Assisted
ALD	Atomic Layer Deposition
AP	Atmosphere Pressure
Aq	Aqueous Solution
CBD	Chemical Bath Deposition
CCD	Charge-Coupled Device
Cd*	Cadmium Radical
CIGSe	$Cu(In,Ga)Se_2$
CISe	$CuInSe_2$
CPV	Concentrator Photovoltaic
CTSe	Cu_2SnSe_3
CVD	Chemical Vapor-Phase Deposition
CZT	Cu-Zn-Sn Metal Alloy
CZTS	Cu_2ZnSnS_4
CZTSe	$Cu_2ZnSnSe_4$
CZTSSe	$Cu_2ZnSn(S,Se)_4$
DC	Direct Current
DI	Deionized
DIGIST	Daegu Gyeongbuk Institute of Science and Technology
DSC	Differential Scanning Calorimetry
DTA	Differential Thermal Analysis
EAS	Energy-Aware Scheduling
ECR	Electron-Cyclotron Resonance
EDX	Energy-Dispersive X-ray Spectroscopy
g	Gas Phase
HF	Heat Flux
HVE	High Vacuum Evaporation
HW	Hot Wire
i-ZnO	Intrinsic ZnO
IBM	*International Business Machines*
ICDD	The International Centre for Diffraction Data
ICP-MS	Inductively Coupled Mass Spectrometry
JCPDS	Joint Committee on Powder Diffraction Standards
KS	Kesterite
l	Liquid Phase
L	Liquidous
L_1, L_2, L_3, L_4	Different Liquids

LP	Low Pressure
M	Metal
MGL	Monograin Layer
MOCVD	Metalorganic Chemical Vapor Deposition
MS	Mass Spectrometry
MW	Microwave
NREL	National Renewable Energy Laboratory
OV	Organic Vapor
PB	Plasma Beam
PCE	Power Conversion Efficiency
PE	Plasma-Enhanced
PLD	Pulsed Laser Deposition
PV	Photovoltaic
PVD	Physical Vapor-Phase Deposition
R&D	Research and Development
RF	Radio Frequency
RM	Reactive Magnetron
RT	Rapid Thermal
s	Solid Phase
SEM	Scanning Electron Microscopy
Solar Frontier K. K.	*Solar Frontier Kabushiki Kaisha*
ST	Stannite
TG	Thermogravimetric
T_{Inf}	Temperature of Inflection
VHF	Very High Frequency
WST	Wurtzite-Stannite
XPS	X-ray Photoelectron Spectroscopy
XRD	X-ray Diffraction
α-$Cu_{2-x}Se$	Low-temperature monoclinic Cu_2Se compound (Murray & Heyding, 1975)
α-CuI	Low-temperature Zinc-blende face-centered cubic CuI (Rapaport & Pistorius, 1968)
α-CuSe	Low-temperature CuSe compound with a hexagonal structure and the space group of *P6₃/mmc* (Berry as cited in Chakrabarti & Laughlin, 1981)
α-$Cu_{2-x}Se$	Monoclinic $Cu_{2-x}Se$ compound (Berry as cited in Chakrabarti & Laughlin, 1981)
α-S	Octasulfur
α-Sn	Sn with cubic structure
α-Sn_2S_3	Low-temperature Sn_2S_3 compound with an orthorhombic structure in the space group *Pnma* (Burton & Walsh, 2012)

α-SnS	Low-temperature SnS phase with *B16* structure in the *Pbnm* space group (Bletskan, 2005)
α-SnSe	Low-temperature SnSe compound with structural type *B16* in the space group *Pbnm* (Bletskan, 2005)
β-$Cu_{2-x}Se$	High-temperature $Cu_{2-x}Se$ compound with *cF12* structure in the space group *Fm3m* (Murray & Heyding, 1975)
β-Cu_2S	Hexagonal high-chalcocite Cu_2S compound with *hP6* structure in the space group $P6_3/mmc(c)$ (Chakrabarti and Laughlin, as cited in Zhang, 2013)
β-CuI	Intermediate-temperature hexagonal wurtzite CuI (Rapaport & Pistorius, 1968)
β-CuSe	Orthorhombic intermediate CuSe compound (Berry as cited in Chakrabarti & Laughlin, 1981)
β-Na	Na with *cI2* structure in the space group $Im\bar{3}m$
β-S	Polymorph sulfur
β-Sn	Sn with a malleable metal structure
β-Sn_2S_3	Intermediate-temperature Sn_2S_3 compound with a rocksalt structure in the space group $Fm\bar{3}m$ (Burton & Walsh, 2012)
β-SnS	High-temperature SnS phase with *B33* structure in the *Cmcm* space group (Bletskan, 2005)
β-SnSe	High-temperature SnSe compound with the structural type *B33* in the space group *Cmcm* (Bletskan, 2005)
β-$SnSe_2$	Polymorphous high-temperature $SnSe_2$
β_c	β-Cu_2Se
β_z	β-ZnSe
γ-CuI	High-temperature disordered zinc-blende face-centered cubic CuI (Rapaport & Pistorius, 1968)
γ-CuSe	High-temperature CuSe compound with a hexagonal structure in the space group $P6_3/mmc$ (Murray & Heyding, 1975)
γ-Se	Se with *hP3* structure in the space group $P3_121$ (Minaev, Timoshenkov & Kalugin, 2005)
γ-Sn_2S_3	High-temperature Sn_2S_3 compound with an orthorhombic structure in the space group *Cmcm* (Burton & Walsh, 2012)
γ-$SnSe_2$	The same as β-$SnSe_2$
δ-$Cu_2ZnSnSe_4$	Low-temperature polymorphous CZTSe phase (Dudchak & Piskach, 2003; Oleksejuk, Dudchak & Piskach, 2001)
δ-Sn_2S_3	High-temperature Sn_2S_3 compound with zinc-blende structure in the space group $Fm\bar{4}3m$ (Burton & Walsh, 2012)
δ'-$Cu_2ZnSnSe_4$	High-temperature polymorphous CZTSe phase (Dudchak & Piskach, 2003; Oleksejuk *et al.*, 2001)
ε-Cu_3Cd_{10}	Cu-Cd metal alloy with a composition of ~85 wt% Cd in the space group $P6_3/mmc$ (Okamoto & Okamoto, 2013)

Explanations of abbreviations used in this thesis are provided in the table.

Terms

Absorber	Material in a solar cell that is able to absorb energy of incident sunlight
Anhydrous	Dry (crystalline) substance that is free from water (water of crystallization)
Bandgap (energy gap)	Energy range (the energy difference between the top of the valence band and the bottom of the conduction band) in a semiconductor (or insulator) where no electron states can exist
First-principles calculations	Calculations that are based on the laws of quantum mechanics and use only the fundamental constants of physics as inputs to provide detailed insight into the origin of mechanical, electronic, optical and magnetic properties of materials and molecules
Triple point	The temperature and pressure at which all three phases (gas, liquid, and solid) exist in equilibrium
Melting point depression	Reduction in melting temperature of a solid due to impurities
Chemical Bath Deposition	Frequently used for the chemical solution deposition method, which is based on the formation of a low-solubility solid phase from a solution containing the precursor ions of the forming solid compound
Chemical equilibria	State in where reactants and products are present in concentrations that have no further tendency to change with time, and no change in the properties of the system is observed (Atkins, Paula & Keeler, 2018)
Conduction band	Energy band of orbitals where electrons can move freely
Congruent melting	Melting where the composition of the formed liquid is the same as the composition of the solid (Atkins *et al.*, 2018)
Critical melting point	End point of a solid-liquid phase equilibrium curve (Atkins *et al.*, 2018)
Cu Kα1 radiation	Copper irradiation with energy of 8,04 keV, which corresponds to an X-ray wavelength of 1,5406 Å ($1{,}5406 \cdot 10^{-10}$ m)
Czohralski process	Process for growing single crystals from the melt. A precisely oriented rod-mounted seed crystal is dipped into the molten phase and slowly pulled upwards with simultaneous rotation.
Dimer	Oligomer consisting of two monomers
Electrodeposition	Migration of ions (or colloidal particles suspended in liquid) due to an electric field and deposition onto an electrode (Lin & Chen, 2016).
Enthalpy	Thermodynamic quantity that is equal to the system's internal energy plus the product of its pressure and volume. The change in enthalpy is equal to the heat absorbed or released for processes at constant pressure.
Enthalpy of dissolution	Enthalpy calculated per dissolved part of a solid
Enthalpy of melting/solidification	Enthalpy calculated per molten or solidified substance

Enthalpy of mixture	Enthalpy calculated using the sum of all substances in the mixture
Enthalpy of phase change	Enthalpy calculated per substance taking place in the phase change
Enthalpy of reaction	Enthalpy calculated per formed products
Enthalpy of formation	Enthalpy calculated per formed product
Enthalpy of solution	Enthalpy calculated per sum of solute and solvent
Entropy	Degree of disorder or randomness in the system (Atkins *et al.*, 2018)
Epitaxy	Deposition of a crystalline overlayer on a crystalline substrate (Greve & Mahi, 2016)
Eutectic point	Temperature at which a particular eutectic mixture freezes or melts. An eutectic mixture is a mixture of two or more substances that melt at the lowest freezing point of any mixture of the components. The liquid melt has the same composition as the solid (Atkins *at al.*, 2018)
Eutectic reaction	Three-phase reaction in which, upon cooling, a liquid transforms into two solid phases simultaneously (Atkins *et al.*, 2018)
Gibbs energy	Thermodynamic potential (Atkins *et al.*, 2018)
Heat capacity	Heat added to (or removed from) an object, resulting in a temperature change (Atkins *et al.*, 2018)
Heteroepitaxy	Different compounds are fitted (Greve & Mahi, 2016)
Homoepitaxy	Use of the same compound as the underlayer (Greve & Mahi, 2016)
Hydrate	Crystalline compound in which water molecules are chemically bound to a compound
Incongruent melting	Melting of a substance where the solid phase decomposes into another substance
Invariant point	Invariant equilibria (P, T), where neither P nor T can be changed without changing the number of phases. All three physical phases (solid, liquid and gas) are in equilibrium
Liquidus	Curve on a temperature-composition phase diagram describing the equilibrium between solid and liquid phases, showing temperatures above which only the liquid phase can exist
Monomer	Molecule that can undergo a polymerization
Monotectic reaction	The reversible transition – three-phase invariant reaction in some binary system that occurs at cooling if, at a particular temperature, one liquid phase decomposes into a solid phase and a new liquid phase
p-*n* junction	Boundary or interface between two types of semiconductor materials: *p*-type and *n*-type
p-type conductivity	Electrical conductivity associated with positive charge carriers (holes) in a semiconductor material

Peritectic reaction	An isothermal reversible reaction in a binary phase diagram in which upon cooling, a solid phase reacts with the coexisting liquid phase to form another solid phase
Phase diagram	Graphical representation of the physical states of a substance under different conditions of temperature and pressure (Atkins *et al.*, 2018)
Photovoltaic materials	Semiconductors, which can form a *p-n* junction, which is the contact in a solar cell structure
Quantum dot	Semiconductor nanostructure, where a nanosized semiconductor particle (2-10 nm) confines the motion of conduction band electrons, valence band holes, or excitons (bound pairs of conduction band electrons and valence band holes) in all three spatial directions. Its optical and electronic properties differ from those of larger bulk crystals.
Screen printing	Film formation by ink transfer onto a substrate (Lin & Chen, 2016)
Semiconductor	Material that starts to conduct electricity after absorption of light
Sintering	Sticking of separate particles of a material *via* heat or pressure
Solar cells, (PV) cells or photoelectrical cells	Electronic devices that directly convert sunlight into electricity *via* the photovoltaic effect (Ito, 2015)
Sonochemistry	Method of using ultrasound irradiation to induce rapid chemical reactions (Feng, 2013)
Spin coating	A technique for applying thin films to substrates. A small amount of coating material is applied on the center of the substrate, which is either spun at a low speed or not spun at all (Lin & Chen, 2016)
Thin film	Material created *ab initio via* the random nucleation and growth processes of individually condensing or reacting atomic, ionic or molecular species on a substrate, which may encompass a considerable thickness range from a few nanometers to tens of micrometers (Ito, 2015)
Vacuum	Space devoid of matter. Gaseous pressure is much less than atmospheric pressure. Ultrahigh vacuum chambers, commonly used in chemistry, physics, and engineering, operate below one trillionth (10^{-12}) of atmospheric pressure (100 nPa) and can reach approximately 100 particles cm^{-3} (Atkins *et al.*, 2018)

Explanations of terms used in the thesis are provided in this table.

Symbols

Δm	Change in mass, kg
A	Unknown peak area, μVs
a, c	Lattice parameters
A_{max}	Largest measured unknown peak area, μVs
A_{min}	Smallest measured unknown peak area, μVs
C_p	Heat capacity at constant pressure (specific heat), J K^{-1}
C_v	Heat capacity at constant volume, J K^{-1}
D	Distance between atomic layers, nm
E_g	Energy gap, eV
FF	Fill factor, %
G	Gibbs energy, J
G_i	Gibbs energy of *i* species, J
H	Enthalpy, J
H_i	Enthalpy of *i* species, J
I	Number of reactants or products
J_{SC}	Short circuit current density, A m^{-2}
K	Calibration constant, μV W^{-1} or μV $(Js^{-1})^{-1}$
M	Mass, kg
M	Molar mass, kg mol^{-1}
N	Amount of chemical substance, mol
N	Number of atoms
N_A	Avogadro's constant, $6{,}0 \cdot 10^{23}$ mol^{-1}
N_i	Amount of chemical substance *i*, mol
N_{tot}	Amount of total chemical substances, mol
P	Constant pressure, Pa
P_0	Standard pressure at 273,15 K, $101{,}3 \cdot 10^3$ Pa
p_{H2O}	Partial pressure of H_2O, Pa
P_i	Incident power of a solar cell, W
p_{Se2}	Partial pressure of Se_2, Pa
Q_s	Heat flow of a sample, W
Q	Heat flow, J
R	Molar gas constant, 8,3 J mol^{-1}
r	Ratio
r_{doping}	Doping level
R_D	Resistance of a thermoelectric disc, K W^{-1}
S	Entropy, J K^{-1}
$S(T)$	Seebeck's coefficient of material, V K^{-1}
S_f	Area of peak, produced by flux, μVs
T	Temperature, K

T_b	Boiling temperature, K
T_{bCdI2}	Boiling temperature of CdI_2, K
T_{bI2}	Boiling temperature of I_2, K
T_{bS}	Boiling temperature of S, K
T_{bSe}	Boiling temperature of Se, K
T_{bSnI2}	Boiling temperature of SnI_2, K
T_{bSnI4}	Boiling temperature of SnI_4, K
T_m	Melting temperature, K
T_{mCdI2}	Melting temperature of CdI_2, K
T_{mCuI}	Melting temperature of CuI, K
$T_{melting\ flux}$	Melting temperature of flux, K
T_{mI2}	Melting temperature of I_2, K
T_{mS}	Melting temperature of S, K
T_{mSe}	Melting temperature of Se, K
T_{mSn2S3}	Melting temperature of Sn_2S_3, K
T_{mSnI2}	Melting temperature of SnI_2, K
T_{mSnI4}	Melting temperature of SnI_4, K
V	Volume, m^3
v_i	Stoichiometric coefficient of species *i* in the reaction
V_L	Volume of the liquid phase, m^3
V_{OC}	Open circuit voltage, V
V_S	Volume of the solid phase, m^3
X, Y	Reactants
x, y, z, w	Stoichiometric coefficients of corresponding reactants or products
x^*, y^*, z^*, w^*	Sum of stoichiometric coefficients of corresponding reactants or products
Z, W	Products
$\Delta_d H^0$	Heat (enthalpy) of standard dissociation for a substance at 298,15 K, J
ΔG	Gibbs free energy, J
$\Delta G_{I2(g)}$	Gibbs free energy, if the reactant is I_2 gas, J
$\Delta G_{I2(s)}$	Gibbs free energy, if the reactant is solid I_2, J
ΔG_r	Gibbs free energy of reaction, J
ΔG_W	Gibbs free energy of products W, J
ΔG_X	Gibbs free energy of reactants X, J
ΔG_Y	Gibbs free energy of reactants Y, J
ΔG_Z	Gibbs free energy of products Z, J
ΔH	Change in enthalpy, J
ΔH_f	Heat (enthalpy) of formation, J
$\Delta H_{f298,15K}$	Heat (enthalpy) of standard formation for a substance at 298,15K, J
ΔH_r	Enthalpy of reaction, J

ΔH_{tr}	Enthalpy of the transformation of a substance, J
ΔH_W	Change in enthalpy of products W, J
ΔH_X	Change in enthalpy of reactants X, J
ΔH_Y	Change in enthalpy of reactants Y, J
ΔH_Z	Change in enthalpy of products Z, J
ΔS	Change in entropy, J K^{-1}
$\Delta_{sub}H^{o}$	Heat of standard sublimation for a substance at 298,15 K, J
ΔT	Gradient of temperature, K
ΔV	Gradient of voltage, V
η	Efficiency of a solar cell, %
θ	Certain incident angles in XRD, degree
λ	Wavelength of the incident X-ray beam, nm
ρ	Density, kg m^{-3}
χ	Integral in XRD

Explanations of symbols used in the thesis are provided in the table.

1 Literature Review

In this chapter, an overview of the theoretical background is provided. The working principle of SnS and kesterite solar cells and their possible production *via* monograin technology are explained. Additionally, the importance of the stability of flux materials, such as KI, NaI, $SnCl_2$, CdI_2, will be described.

The available phase diagrams of binary ternary and quaternary compounds and expected by-products will be discussed.

1.1 Development of Solar Cells

An ideal absorber material for an efficient terrestrial solar cell should be a direct ~1,5 eV band gap semiconductor. It has to have a high solar optical absorption ~10^5 cm^{-1}. Since there are no suitable elemental semiconductor materials available with a direct band gap near 1,5 eV, multielemental compounds are primarily used (Ito, 2015).

Since the 1960s, solar cells have been the main power source for most Earth-orbiting satellites (Fraas, 2014). Overall, solar cells are divided into first-, second- and third-generation solar cells (Askari, Mirzaei & Mirhabibi, 2015). The Shockley-Queisser limits for conversion efficiencies for single junction solar cells are 33,7 % using nonconcentrated light and 86,8 % when using concentrated light (Rühle, 2016). The maximum efficiencies of indoor photovoltaic devices that were calculated from the detailed balance model reached 72,98 % (Freunek, Freunek & Reindl, 2013).

The commercially dominant cells are first-generation wafer-based cells. A slice of single-crystalline material, synthesized *via* the Czochralski process, is used. This is expensive technology (Zheng *et al.*, 2016). In 2014, a record conversion efficiency (27,6 %) was achieved by *Panasonic* using a monocrystalline heterostructure silicon solar cell (NREL, 2018). Multi-junction GaAs solar cells are made of multiple thin films that are epitaxially grown on top of each other on a wafer *via* metal-organic chemical-vapor deposition (Okada *et al.*, 2015). The highest achieved efficiency (46,0 %) of any solar cell with the 4-junction cell of GaInP/GaAs//GaInAsP/GaInAs using concentrator photovoltaic (CPV) technology was achieved by the research team at Fraunhofer Institute for Solar Energy Systems (ISE, 2014). However, using nonconcentrated light, a value of 38,8 % was reached for a 5-multijunction AlGaInP/GaInP/AlGaInAs/GaInAs/Ge solar cell grown on GaAs and InP wafers by Boeing Spectrolab, as reported by researchers in 2013 (Chiu *et al.*, 2015).

Second-generation solar cells are based on thin films that usually have grain boundaries in them. This is a disadvantage for their application in solar cells (Aguiar, Patel, Aoki, Wozny & Al-Jassim, 2016). A high concentration of grain boundaries acts as internal interfaces (Ito, 2015). For these, amorphous Si (α-Si) cells have been used, with a record power conversion efficiency (PCE) value of 14,0 %, as have CdTe cells (22,1 %) (NREL, 2018). CdTe has a direct bandgap of 1,5 eV and an absorption coefficient of 10^5 cm^{-1}; however, the Cd toxicity, recycling of modules and rare abundance of Te, which contribute to the costs of modules, are disadvantages (Ito, 2015). The facts mentioned above led to copper indium (gallium) diselenide (CIGSe) solar cell development. Solid solutions containing Ga (CIGSe) have increased band gap values for CISe-type absorber materials. The manufacturing costs are not low since expensive and rare metals (In, Ga) are used (Sun *et al.*, 2017). Hedström *et al.* (as cited in Sun *et al.*, 2017) found that sodium incorporation is necessary for optimal performance to increase *p*-type conductivity. The record efficiency of 23,3 % for a CIGS thin-film solar cell produced *via* coevaporation was achieved by the National Renewable Energy Laboratory (NREL, 2015) using a concentrator. A non-concentrator efficiency of 22,9 % was achieved by Solar Frontier K. K. (Solar Frontier K. K., 2017).

Third-generation solar cells are still in the research or development phase. Here, a few instable materials are used, which are manufactured *via* cheap and simple solvents or *via* vapor deposition techniques. Some are perovskite absorbers, such as methylammonium lead trihalide or formamidinum lead trihalide, with band gaps of 1,5-2,3 eV, depending on the halogen content (Supreeth & Shreya, 2016; Eperon, 2015), and a record efficiency of 22,7 % has been achieved (NREL, 2018). Others include ruthenium metalorganic compounds for dye-sensitized solar cells, as used by O'Regan and Grätzel (as cited in Chuan-Pei *et al.,* 2017), who achieved a record efficiency of 11,9 % (NREL, 2018). Nelson (as cited in Ostraverkhova, 2013) also developed organic semiconductors, such as polyphenylene vinylene, copper phthalocyanine, carbon fullerenes and fullerene derivatives with band gaps above 2,0 eV. An efficiency of 11,5 % was achieved according to their report (NREL, 2018). Beiley and McGehee (as cited in Ahmed *et al.*, 2015) used quantum dot solar cells by employing low band gap semiconductor nanoparticle crystallites (such as CdS, CdSe, Sb_2S_3, and PbS) as light absorbers with a tuned band gap by changing the particle size. Thus far, the highest efficiency achieved has been 10,6 % (NREL, 2018). Additionally, from polycrystalline Zn_3P_2 (similar to InP), a solar cell was developed with a 6,0 % efficiency by Bhushan and Catalano (as cited in Ito, 2015). However, the research was stopped after Kimball, Müller, Lewis, and Atwater (as cited in Ito, 2015) reported that the conduction band edge of the compound is located at 1,38 eV above the valence band edge but the electron transition is of an indirect nature. Kesterites are also included in third-generation solar cells and are mostly free of toxic elements. They are suitable as absorber materials for solar cells due to their high absorption coefficient (more than 10^4 cm^{-1}); however, more work is needed for their commercialization. Kesterites can be derived from CIGS by substituting In and Ga with Zn and Sn (Ito, 2015). Looking for simpler components, the research trend has moved to binary compounds, such as SnS, due to its suitable characteristics for PV applications. These solar cells will be described in more detailed in Sections 1.2-1.3.

1.2 Tin Sulfide Solar Cells

The most popular synthesis method for SnS is chemical bath deposition (CBD) because of the low costs (Sreedevi & Reddy, 2013). Theoretical calculations confirm a conversion efficiency of up to 25,0 % (Raadik, 2015); however, the world record is currently only 4,5 % (Sinsermsuksakul *et al.*, 2014). One reason could be that different additional phases, such as SnS_2 and Sn_2S_3, are present (Sinsermsuksakul *et al.*, 2013), and the growth of SnS for a solar cell absorber must be very carefully controlled. Deviations in temperature, time or vapor pressure cause changes in the resulting composition. Different SnS band gap values of 1,1-1,87 eV at room temperature have been reported in the literature (Raadik, 2015; Sinsermsuksakul *et al.*, 2014). The SnS crystal structure is an orthorhombic structure in the space group *Pbnm*, where six sulfur atoms surround each tin atom with three short Sn-S bonds within the layer and three long bonds connecting two SnS layers. Other possible structures of SnS are hexagonal and cubic and are less stable at room temperature (Bashkirov, Gremenok & Ivanov, 2011).

In recent years, the chemical bath deposition of SnS thin films from solutions with different concentrations of tin and sulfur have been reported (Safonova *et al.*, 2014), and the thermal annealing (Safonova *et al.*, 2015; Safonova, 2016) was investigated. However, Revathi *et al.* (2015) investigated SnS films deposited by high-vacuum evaporation (HVE). Burton *et al.* (2013) showed that the coexistence of Sn(II) and Sn(IV) oxidation states limits the performance of SnS in photovoltaic devices due to the valence band alignment of the respective phases and the "*asymmetry*" in the underlying point defect behavior. Furthermore, the results suggest that Sn_2S_3, in addition to SnS, is a candidate material for low-cost thin-film solar cells.

1.3 Kesterite Solar Cells

Solar cells based on CZTS, CZTSe and their solid solution, CZTSSe, are often called kesterite solar cells since these compounds are minerals of the kesterite form found in nature. Schorr *et al.* (as cited in Ito, 2015) used neutron powder diffraction to confirm that the most stable crystal structure for these compounds is kesterite. Recent studies (Nateprov, Kravtsov, Gurieva & Schorr, 2013) of single crystals of CZTSe showed that for the model in the space group *I*-42*m*, the copper and zinc atoms alternate in the *d* Wickoff position of the space group and statistically occupy this position with equal probability. This model has the main features of the kesterite structure but belongs to the *I*-42*m* space group, unlike the conventional kesterite structure in the *I*-4 space group. The lattice parameters of tetragonal kesterite CZTSe (Figure 1.1) are a = 0,5688 Å (10^{-10} m) and c = 11,347 Å (10^{-10} m).

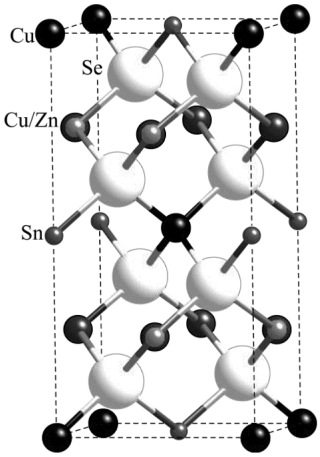

Figure 1.1 Kesterite structure of CZTSe, adapted from Nateprov et al. (2013)

The calculated formation enthalpy of kesterite-type CZTSe is more negative than those of the stannite- and wurtz-stannite-type. However, for $Cu_2CdSnSe_4$, the enthalpy is more negative for the stannite structure. The enthalpy of formation determined by first-principles calculations from binaries (Cu_2Se, $SnSe_2$ and ZnSe) at -273 °C (0 K) for kesterite $Cu_2ZnSnSe_4$ is -84,1 kJ mol^{-1}, as shown in Figure 1.2 (a), and that for stannite $Cu_2CdSnSe_4$ is -82,3 kJ mol^{-1}, as shown in Figure 1.2 (b) (Nakamura, Maeda & Wada, 2011). However, these data should be considered with care, since any reaction at absolute zero (-273 °C or 0 K) cannot proceed due to the definition of absolute zero temperature at which no atom movement is expected. Additionally, this same group of authors published other work (Maeda, Nakamura & Wada, 2011) in which the calculated enthalpies of formation for elements at -273 °C (0 K) by this same method of binary and ternary compounds are -141,5 kJ mol^{-1} (ZnSe), -106,6 kJ mol^{-1} ($SnSe_2$), and -169,9 kJ mol^{-1} (Cu_2SnSe_3), which all disagree with the value of -228,6 kJ mol^{-1} for the mixture of Cu_2Se, ZnSe, and $SnSe_2$ shown in Figure 1.2 (a) and the thermodynamic equation (1.5), as will be discussed below.

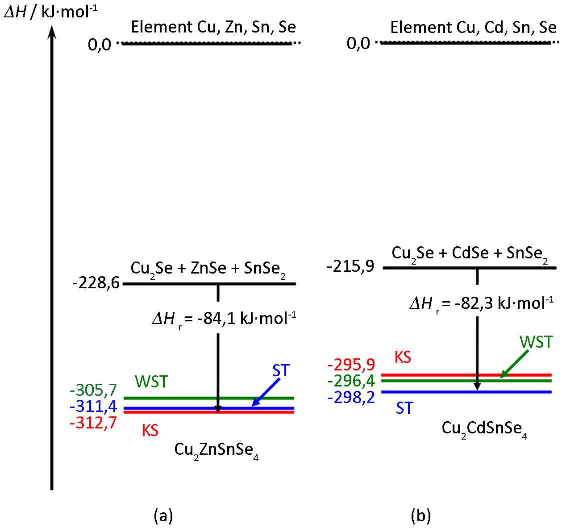

Figure 1.2 Enthalpies of formation for kesterite, stannite and wurtzite-stannite CZTSe and CCdTSe, adapted from Nakamura et al. (2011)

There are slight differences in the literature values of the band gap for the CZTS and CZTSe compounds due to the different calculations and experimental growth methods applied. Currently, solar cells use absorbers with an optimal direct band gap of 1,5 eV for CZTS or 1,0 eV for CZTSe or a linearly and continuously tunable band gap from 1,0 eV to 1,5 eV for the alloy CZTSSe (Liu *et al.*, 2018). The band gap of the $Cu_2CdSnSe_4$ compound determined by Matsushita *et al.* (as cited in Nakamura *et al.*, 2011) was reported to be 0,96 eV. The reported record efficiencies achieved *via* vacuum evaporation methods were 9,3 % for CZTS (Liu *et al.*, 2017), 11,6 % for CZTSe (Lee *et al.*, 2015) and 13,8 % for CZTSSe (Wallace *et al.*, 2017). Another first-principles calculation was performed (Xiancong, Jinhong, Yuming & Xiaoquan, 2013), which reported that the Gibbs energy of CZTS is lower than that of CZTSe at approximately -3000,0 kJ mol^{-1} at the same temperature and pressure.

Kesterites can be prepared by a variety of vacuum and nonvacuum techniques, similar to CIGS. Two well-known vacuum methods exist: chemical (CVD) and physical (PVD) vapor-phase deposition. The source material is evaporated (coevaporation), and vapor particles travel directly to the target object (substrate), where they condense to a solid state. The produced volatile byproducts can be removed by gas flow through a reaction chamber. Vapor-phase deposition can be classified as AP, LP, AA, PE, MW, ALD, RT, ECR, HW, VHF, OV, MO, RM, PB, DC, or PLD (see list of abbreviations). For thin-film depositions on substrates, different solution-based methods can also be used: screen printing, spin coating, spray deposition, electrodeposition, and CBD. In these methods, films are deposited on substrates immersed in dilute solutions containing metal and nonmetal ions. However, the achieved composition is not uniform (Lin & Chen, 2016).

1.4 Chemical Pathway to CZTSe Formation

The chemical pathway to CZTSe formation strongly depends on the deposition conditions. In the literature, there are some proposed chemical methods involving vacuum techniques and CBD. In principle, there are two ways to describe the chemical pathway of CZTSe formation: the thermodynamic or epitaxial approach. The thermodynamic approach explains the formations due to the more negative ΔG principle, whereas the epitaxial approach considers the crystallographic structures that are most suitable for epitaxy.

Thus, there could be two possibilities for producing CZTSe: the reduction of Cu(II) to Cu(I) and oxidation of Sn(II) to Sn(IV). This is the so-called reduction-oxidation reaction (which has a more negative Gibbs free energy (ΔG) for formation of a quaternary compound) or combination (synthesis) reaction, when the epitaxy approach is considered. These possibilities will be considered below.

1.4.1 Epitaxial Approach

Epitaxy is the deposition of a crystalline overlayer on a crystalline substrate. The deposited material forms a crystalline overlayer that should have one well-defined orientation with respect to the crystal structure of the substrate. If the same compound is used as the underlayer, the process is called homoepitaxy, but if different compounds are used, it is called heteroepitaxy. Minerology defines epitaxy as the overgrowth of one mineral on another in an orderly way since the crystal directions of the two minerals are aligned (the same planes in the lattices between two compounds have similar spacing between the atoms). The epitaxial relationship can be deduced by the geometry (Greve & Mahi, 2016).

Predictions of CZTS and CZTSe formation were first performed using a crystallographic model (epitaxial) in (Hergert & Hock, 2007). An epitaxial relation exists between crystal faces that are expected to form, which initiates solid-state reactions. The predicted reactions were found to proceed remarkably fast compared with other solid-state reactions. SnS or SnSe allows epitaxy with CuS, Cu_2S or CuSe and Cu_2Se. However, the most promising compounds regarding epitaxy are $SnS(e)_2$. Then, ternary sulfides such as Cu_4SnS_4, Cu_2SnS_3, $Cu_4Sn_7S_{16}$, and $Cu_4Sn_{15}S_{32}$ (less likely are Cu_3SnS_4 and Cu_4SnS_6) were expected to develop, whereas for ternary selenides, only Cu_2SnSe_3 (CTSe) was discussed. The authors stated that the most favorable reactions are expected between the cation conductive phases of β-$Cu_2S(e)$ or β-$Cu_{2-x}S(e)$, while ZnS(e) and $SnS(e)_2$ form quaternary compounds. The phases of Sn_2S_3, low-temperature SnS(e), and Cu_4SnS_4 appeared to be impossible as educts. Only in the case of [Zn] deficiency can a ternary compound, most likely $Cu_2SnS(e)_3$, form. No other ternary compounds were found to be possible. The $Cu_2SnS(e)_3$ compound can react with the ZnSe *via* an epitaxially initiated reaction in a separate reaction step. Furthermore, the chalcogen should be provided in excess, and $SnS(e)_2$ with layered crystal structures forms. $Cu_2ZnSnS(e)_4$ can be formed by epitaxially assisted direct reactions either in one step from three binary chalcogenide educt compounds or in two successive reactions with

$Cu_2SnS(e)_3$ as the intermediate product. According to the authors, these are competing processes. However, there is some disagreement regarding the formation according to the thermodynamic predictions since the formation from binaries should have a more negative ΔG.

1.4.2 Combined Thermodynamic and Experimental Approach

A database (software HSC6 Chemistry Ver. 6.0.) was used in this study. With this database, it is possible to calculate chemical equilibria between pure substances and, to some extent, nonideal solutions. For these calculations only, enthalpy (H), entropy (S) and heat capacity (C_p) data for all prevailing compounds or pure substances are needed. In many cases, these calculation results may simulate real chemical reactions and processes at a sufficient accuracy for practice. However, this method does not take into account all the necessary factors, such as rates of reactions and heat and mass transfer issues. The heat capacity, C_p, at constant pressure (specific heat) can be calculated from equation (1.1).

$$C_p = \left(\frac{dH}{dT}\right)_P, \tag{1.1}$$

where C_p – heat capacity, J K^{-1},
H – enthalpy, J,
T – temperature, K,
P – constant pressure, Pa.

Equation (1.1) allows the calculation of enthalpy as:

$$H(T) = H_{f298,15} + \int_{298,15}^{T} C_P dT + \sum H_{tr}, \tag{1.2}$$

where $H_{f298,15}$ – enthalpy of formation at 298,15 K (0 °C), J K^{-1},
H_{tr} – enthalpy of transformation of the substance, J K^{-1},
C_p – heat capacity, J K^{-1},
T – temperature, K.

A comparison of the mutual stability of substances must be performed using the Gibbs energy defined by equation (1.3).

$$G = H - TS, \tag{1.3}$$

where G – Gibbs energy, J,
H – enthalpy, J,
T – temperature, K,
S – temperature, J K^{-1},

The thermodynamic enthalpy and Gibbs energy functions for a chemical reaction (1.4) are calculated as the difference between the products and reactants using equations (1.5) and (1.6).

$$x\,X + y\,Y + \ldots = z\,Z + w\,W + \ldots \tag{1.4}$$

where *x, y, z,* and *w* – the stoichiometric coefficients of the corresponding reactant or product,
X, Y – reactants,
Z, W – products.

$$\Delta H_r = \sum v_i H_i(Products) - \sum v_i H_i(Reactants) = (z^* H_Z + w^* H_W + \cdots) - (x^* H_X + y^* H_Y + \cdots) \quad (1.5)$$

where ΔH_r – enthalpy of reaction, J,
H_i – sum of enthalpy, J,
i – number of reactants or products,
v_i – stoichiometric coefficient of species i in the reactions,
x^*, y^*, z^*, and w^* – sum of stoichiometric coefficients of the corresponding reactant or product,
H_X – enthalpy of reactants X, J,
H_Y – enthalpy of reactants Y, J,
H_Z – enthalpy of products Z, J,
H_W – enthalpy of products W, J.

$$\Delta G_r = \sum v_i G_i(Products) - \sum v_i G_i(Reactants) = (z^* G_Z + w^* G_W + \cdots) - (x^* G_X + w^* G_W + \cdots) \quad (1.6)$$

where ΔG_r – Gibbs energy of reaction, J,
G_i – sum of the Gibbs energy, J,
i – number of reactants or products,
v_i – stoichiometric coefficient of species i in the reactions,
x^*, y^*, z^*, w^* – sum of stoichiometric coefficients of the corresponding reactant or product,
G_X – Gibbs energy of reactants X, J,
G_Y – Gibbs energy of reactants Y, J,
G_Z – Gibbs energy of products Z, J,
G_W – Gibbs energy of products W, J.

The other way to express ΔG is *via* equation (1.7) as described by (Atkins *et al.*):

$$\Delta G_r = \Delta H_r + T\Delta S, \quad (1.7)$$

where ΔH_f – heat of reaction, J,
T – temperature of the reaction, K,
ΔS – change in entropy, J K^{-1}.

Additionally, it is important that ΔG at the melting temperature of the substance is zero. Then, according to equation (1.3), the melting directly depends on the change in entropy, ΔS. The approximation that $\Delta G \approx \Delta H$ can be used for solid- and liquid-phase reactions since for solid-state reactions the change in entropy is on the order of 10^{-3} kJ mol^{-1} and can be neglected. However, with the expression of ΔG or ΔH in kJ mol^{-1}, we should be careful since there is no common way in which compounds should be calculated. In this thesis, in the "*Terms*" section, these terms such as the enthalpy of solution, enthalpy of dissolution, enthalpy of reaction, enthalpy of formation, enthalpy of phase change, enthalpy of mixture and enthalpy of melting (solidification) have been defined.

Primarily, in experiments, there is the assumption that the situation can be "*frozen*" by rapid cooling. The CZTSe reaction pathway has not been investigated as much as that of CZTS. According to experimental studies, the reaction pathways differ likely due to the different synthesis methods applied, different compositions used and different heating regimes chosen. In principle, CZTSe can be synthesized from metal powders, binaries or a ternary (CTSe) reacting with ZnSe. In the master's thesis of Zhang (2013), it was shown that there are many complications for synthesizing pure CZTSe from metal powders as starting materials because of impurities (mainly oxides) on the metal surface, which interfere with the monograin growth. Additionally, the synthesis from a ternary CTSe compound has a disadvantage because of the two-stage process, and CTSe requires purification before the reaction with ZnSe is performed since its synthesis does not lead to a 100,0 % yield of CTSe (Park *et al.*, 2014). There is no report that CZTS or CZTSe could be directly formed from elements, despite the fact that this thermodynamic reaction would be the most negative. The reason for this could be the reason discussed above in which the elements are not as suitable for epitaxy as binary compounds, and mostly, the formation of a binary compound is detected.

For the first time, CZTS formation was experimentally studied by Schurr *et al.* (2009) *via in situ* XRD experiments during crystallization of CZTS thin films from electrochemically codeposited metal films. Two types of precursor ratios in the work were used: copper-rich and copper-poor. Therefore, two different reaction paths depending on the metal ratios in the as-deposited films were observed. In copper-rich metal films, Cu_3Sn and CuZn were found after electrodeposition. In copper-poor or near-stoichiometric precursors, an additional phase, such as Cu_6Sn_5, was detected. Cu_6Sn_5 at 177-297 °C (450-570 K) reacts with S, forming the compounds SnS_2, $Cu_{2-x}S$ and Cu_3Sn. In the copper-rich environment, $Cu_{2-x}S$ forms at 347 °C (620 K) from the elements. In both cases, at 387 °C (660 K), the reactions of Cu_3Sn with S lead to the compounds SnS_2 and $Cu_{2-x}S$. At 507 °C (780 K) in the copper-poor environment and at 517 °C (810 K), the metal alloy of CuZn reacted with S, forming $Cu_{2-x}S$ and ZnS. In the copper-poor case, SnS_2, $Cu_{2-x}S$, and S at 507 °C (780 K) immediately formed Cu_4SnS_6. Cu_4SnS_6 melted at 517 °C (810 K), resulting in SnS_2, $Cu_{2-x}S$, and S and leading to Cu_2SnS_3 formation. For the copper-rich case, Cu_2SnS_3 formed from SnS_2 and $Cu_{2-x}S$ at 547 °C (820 K). CZTS crystallization occurred *via* the solid-state reaction of Cu_2SnS_3 and ZnS at 573 °C (846 K), and the formation was incomplete because other compounds, including $Cu_{2-x}S$, ZnS and Cu_2SnS_3, were found in addition to the main compound even during cooling. The reason for this is partial sulfur loss because of the high vapor pressure of sulfur, despite all experimental efforts to encapsulate the sample. Additionally, they observed that formation of CuO and SnO_2 may cause Sn and Cu off-stoichiometry in the sample. The melt phase may be advantageous for crystallizing the kesterite, leading to enhanced grain growth in the presence of a liquid phase, which starts from molten S formation. Scragg (2010) observed the difference in which a ZnS phase forms first from Cu_5Zn_8 at 350 °C (623 K), and the formation occurs according to reaction (1.8), involving liquid Sn. With high heating rates, this reaction is shifted to 500-550 °C (773-823 K). The CTS(e) reaction to CZTS(e) occurs very quickly.

$$Cu_2S(e)\,(s) + Sn\,(l) + [ZnS(e)\,(s)] + 2\text{ mol } S(e)\,(g) \rightarrow Cu_2SnS(e)_3,\ [Cu_2ZnSnS(e)_4] \qquad (1.8)$$

For the first time, CZTSe formation was experimentally studied by Wibowo, Jung, Al-Faruqi, Amal and Kim (2010). They used elemental Cu, Zn, Sn and Se powders to crystallize the CZTSe compound *via* a solid-state reaction. At 100 °C (373 K), the CZTSe exothermically formed α-CuSe from Cu and Se, while at 175 °C (448 K), the reaction of α-CuSe and Se led to $CuSe_2$. At 220 °C (493 K), it formed Cu_5Zn_8, and at 275 °C (548 K), SnSe formed from the corresponding elements. At approximately 300-320 °C (573-593 K), all binaries formed, and reactions (1.9-1.10) occurred:

$$CuSe_2\ (l) \rightarrow \gamma\text{-}CuSe\ (s) + Se\ (l) \tag{1.9}$$

$$Cu_5Zn_8\ (s) + 13\ Se\ (l) \rightarrow 5\ \gamma\text{-}CuSe\ (s) + 8\ ZnSe\ (s) \tag{1.10}$$

γ-CuSe phase transformation to β-Cu_2Se and liquid Se was not observed in their DTA, and they assumed that all β-Cu_2Se was consumed during Cu_2SnSe_3 (CTSe) formation at 380 °C (653 K). Additionally, reaction (1.11) occurred:

$$\gamma\text{-}CuSe\ (s) \rightarrow \beta\text{-}Cu_2Se\ (s) + Se\ (l) + SnSe\ (s) \rightarrow Cu_2SnSe_3\ (s) \tag{1.11}$$

According to XRD, CTSe and CZTSe were detected as early as 300 °C (573 K); however, at 400 °C (673 K), the dominant phase was CZTSe. They stated that the formation occurs *via* reaction (1.12), including the intermediate step of the CTSe formation reaction (1.11):

$$Cu_2SnSe_3\ (s) + ZnSe\ (s) \rightarrow Cu_2ZnSnSe_4\ (s) \tag{1.12}$$

Additionally, it was found that Se vaporization from the sample began at 300 °C (573 K) under closed experimental conditions, probably because of the colder zone of the reactor. Se loss is considerable above 600 °C (873 K), and a synthesis temperature above this is not recommended.

The most recent discovery by Hernandez-Martinez *et al.* (2018) using the rapid thermal (RT) process showed that CZTSe formation depends on Se availability the in system. A low Se content leads to direct formation from binaries, whereas a high Se content leads to formation from Cu_2SnSe_3 and ZnSe.

In Benaicha, Hamla and Derbal (2016) a Cu-Zn-Sn (CZT) alloy was electrochemically deposited onto substrates from a citrate electrolyte, followed by a thin layer of Se on the top that was annealed under vacuum. XRD measurements indicated that when annealed under vacuum at 350 °C (623 K), CZT + Se precursors were transformed into CZTSe. It was proposed that Cu_2Se, $SnSe_2$ and ZnSe form first, and then reaction (1.13) occurs, followed by reaction (1.12).

$$Cu_2Se\ (s) + SnSe_2\ (s) \rightarrow Cu_2SnSe_3\ (s) \tag{1.13}$$

In Son *et al.* (2015), a high-pressure Se vapor was used for Cu, SnS, and ZnS, which was found to be the optimal procedure in Son *et al.* (2014) for selenization to produce high-efficiency solar cells of CZTSSe. The pathway was observed until 330 °C (603 K), and the binaries from their elements formed, while Cu_2SnSe_3 formed from the CuSe reaction with SnSe. Additionally, at 430 °C (703 K), CZTSSe formed from the reaction of

CTSe with ZnS. Yang *et al.* (2014) employed thioglycolic acid and ethanolamine to dissolve elemental Cu, Zn, Sn, and Se powders to produce CZTSe at 540 °C (813 K). Kevin, Malik, Malik and O'Brien (2015) deposited pure CZTSe at 350 °C (623 K) from molecular organic precursors *via* AACVD. Fella *et al.* (2013) formed CZTSe during selenization of solution-deposited metal precursors. In this process, at 190-320 °C (463-593 K), copper selenides formed, whereas at 280 °C (553 K), CZTSe, CTSe and ZnSe formed. CTSe and CZTSe were present together until 370 °C (643 K), and above 420 °C (693 K), CZTSe was dominant. In another article (Kaune, Hartnauer, Syrowatka & Scheer, 2014), two-stage coevaporation at 510 °C (783 K) was first used to deposit a $Cu_{2-x}Se$-ZnSe layer and then to integrate Sn into the film to transform into CZTSe *via* reaction (1.8), according to Scragg (2010). Mao *et al.* (2015) selenized metal oxides at 550 °C (823 K). The facilitated selenization kinetics to form CZTSe were attributed to the oxidation state change of Cu(II) to Cu(I) and Sn(II) to Sn(IV) and the formation of ZnSe from ZnO. In another publication (Yoo *et al.*, 2013), the following processes were observed during a sputtered Cu-Zn-Sn layer reaction with evaporated Se and annealing at 550 °C (823 K): molten Sn reacted with Se and formed SnSe, and SnSe further reacted with gaseous SnSe if the pressure was sufficient. If the pressure was too low, the $SnSe_2$ in the vacuum chamber decomposed to SnSe and gaseous Se. The metal alloys were found to form similarly as in Scragg (2010). The hypothetical sequential reactions (1.14) for CZTSe formation were proposed as shown in (1.14):

$$Cu_xSn_ySe_{1+z}\ (s) + Sn_{(1-y)}Se_{(2-z)}\ (s) + ZnSe\ (s) \rightarrow Cu_2SnSe_3\ (s) + ZnSe\ (s) \rightarrow CZTSe\ (s) \qquad (1.14)$$

Using sonochemical synthesis from elemental precursors, another study (Feng, 2013) was not able to obtain single-phase CZTSe. They found that at 300 °C (573 K), CuSe, $CuSe_2$ form; however, Zn and Sn do not react with Se, despite the fact that they have a negative ΔG for the binary formation reaction to proceed. In contrast to other works at 400 °C (673 K), in addition to CTSe and CZTSe compounds, Cu_2SnSe_4 formed, and some unreacted Zn was present. Afterwards, Cu_2SnSe_4 decomposed into CTSe and $SnSe_2$ at temperatures below 500 °C (773 K), and the final CZTSe formation took place from CTSe and ZnSe, as in reaction (1.12). The authors stated that at 700 °C (973 K) CZTSe decomposed to CTSe, ZnSe and Cu_2Se.

In monograin growth studies, Kaarna (2014) showed that the synthesis condition of 700 °C (973 K) for 30 h was already sufficient for crystal growth, resulting in a tetragonal shape and sharp-edged monograins. The chemical and phase composition of the product did not change considerably upon changing the growth temperature and time. The sieving analysis revealed that the median particle size of the produced powder crystals increased with increasing synthesis temperature and duration. The particle growth process was found to occur *via* two parallel mechanisms simultaneously: single-crystal growth and sintering.

However, Scragg *et al.* (Scragg, Ericson, Kubart, Edoff & Platzer-Björkman, 2011) and (Scragg, Dale, Colombara & Peter, 2012) first recognized that CZTSe or CZTS formation or decomposition occurs due to the oxidation of SnS(e) and the reduction CuS(e) or oxidation of SnS(e) and reduction of elemental S(e). They studied the Se, Zn and Sn losses from CZTS(e) and found that Zn evaporates *via* elemental liquid Zn, and Sn and Se evaporate *via* gaseous SnS(e) and gaseous S(e) formation. Below some specific pressure, Sn(IV) is unstable and is reduced to Sn(II), and this is the driving force for CZTS(e) decomposition. SnS_2 is reduced to SnS or Sn_2S_3, and $SnSe_2$ is reduced to

SnSe during the decomposition. Piacente, Foglia and Scardal (as cited in Ito, 2015) published the vaporization process of SnS_2. This compound tends to decompose to Sn_2S_3 and S gas and further decomposes to SnS gas. However, these processes are impossible at room temperature and do not proceed until 800 °C (1073 K) under standard conditions, as determined by thermodynamic simulations using the database (software HSC6 Chemistry Ver. 6.0.) (see the Chapter 3).

Clearly, in a vacuum environment, there are no gaseous molecules near the surface (since they are systematically removed). The pressure is too low in the vacuum chamber where synthesis occurs, and some inert atmosphere pressure is required. Scragg *et al.* reported the decomposition at 550 °C (823 K) on the surface of the bulk *via* the two steps shown in equations (1.15-1.16):

$$Cu_2ZnSnS(e)_4\,(s) \rightarrow Cu_2S(e)\,(s) + ZnS(e)\,(s) + SnS(e)\,(s) + 0{,}5\ S(e)_2\,(g) \quad (1.15)$$

$$SnS(e)\,(s) \rightarrow SnS(e)\,(g) \quad (1.16)$$

To decompose $SnS(e)_2$ into solid or gaseous SnS(e) and S(e), ΔG is strongly positive, as found in the database (software HSC6 Chemistry Ver. 6.0.), and it is not thermodynamically supported under standard conditions. As described by Scragg *et al.* (2012), we anneal in vacuum or under flow of an inert gas, and we continually remove any vapor-phase products from the atmosphere. This means that equilibrium cannot be reached, and the decomposition reaction will proceed continually in the forward direction, only stopping when the all material decomposes. However, this is not valid for reactions in a closed ampoule since the vapor is not removed. However, if we provide a supply of gaseous products of the decomposition reaction at a suitable concentration (partial pressure), then the decomposition will proceed in reverse direction and will be inhibited. The authors observed loss of the Se gas and SnSe gas phases a) during annealing and b) during the CZTSe reaction with Mo. Supported Se loss also occurred from CZTSe *via* vacancies, since it is easier to remove Se from CZTSe so that decomposition can proceed. In Gibbs (2015), different decomposition products were proposed. They found that CZTS films that were annealed at 580 °C (853 K) led to decomposition into CTSe and ZnSe.

Based on the partial pressure of S, Scragg *et al.* (2011) calculated that the reverse decomposition reaction (1.15) is CZTS formation with an enthalpy of formation of $-22{,}0 \pm 6{,}0$ kJ mol^{-1} at 550 °C (823 K). Nkwusi, Leinemann and Altosaar (2016) found that CZTS synthesis during CdI_2 melting in a closed ampoule at 385 °C (658 K) leads to a formation enthalpy of $-8{,}0 \pm 2{,}0$ kJ mol^{-1} from a mixture of Cu_2S, SnS, ZnS, and S. Another study (Jackson & Walsh, 2014) reported that CZTS is thermodynamically stable with respect to its component elements and their major binary phases (binaries) under a modest partial pressure of sulfur and temperatures below 827 °C (1100 K). Under near-vacuum conditions with a sulfur partial pressure below 1,0 Pa, decomposition into binaries, including solid SnS, becomes favorable with a strong temperature-dependent stability window. Using the thermodynamic potentials of CZTS and its elemental and binary components based on energetic and vibrational data computed *via* density functional theory, they calculated the formation enthalpy of CZTS. At 25 °C (298,15 K), the formation enthalpy of CZTS from its elements is -369,1 kJ mol^{-1} and from binaries (Cu_2S, SnS_2 and ZnS) is -44,0 kJ mol^{-1}.

Another study (Yin, Tang, Sun, Shen & Gong, 2014) described the phase formation mechanism of a non- and near-stoichiometric CZTSSe film to determine the secondary phase formation mechanisms. According to Fairbrother *et al.* (2014), in Zn-rich (CZTSe) films, ZnSe was the main secondary phase in the films, and SnSe was at the back contact side of absorber. The electrodeposition method previously used (Guo, 2014) caused a problem due to the higher concentration of oxygen in the electrodeposited absorber, which was thought to be the main cause of the lower performance of the electrodeposited CZTS or CZTSe solar cells with respect to a solar cell fabricated by evaporation. In a different study (Lin, Lai & Hsu, 2017), it was found that excessive Na doping has an adverse effect on device efficiency. Increasing the Na content leads to an increase in the quantity of secondary-phase $SnSe_2$. An increase in secondary-phase $SnSe_2$ can shift the current pathway from CZTSe grain boundaries to $SnSe_2$ grains. Secondary-phase $SnSe_2$ acts as a channel for the current flow, which results in a high leakage of current.

1.5 Monograin Powder Technology

The problems caused by grain boundaries in thin films are avoided in MGL technology. The main challenge in the synthesis of a multicomponent compound is to produce a single-phase product with a uniform composition. In the monograin powder synthesis process, the molten phase of a suitable inorganic salt (flux) aids in the even distribution of the initial components, mediating fast diffusion of the elements from particle to particle.

A basic patent on the molten salt synthesis-growth of complex semiconductor powders was filed by researchers at TalTech: E. Mellikov, M. Altosaar and D. Meissner (as cited in Ito, 2015). This TalTech group began to create and commercialize modules of powder-based CZTSSe MGL solar cells in 2008 and has continued this work in collaboration with the TalTech spin-off company, *crystalsol OÜ*. The MGL solar cell has a superstrate structure of graphite/MGL/CdS/ZnO/glass (Figure 1.3). The monograin is a single-crystalline powder particle consisting of one single crystal or several single-crystalline blocks that are grown into a compact grain. The MGL is a layer of defined size grains (for example, ~45 μm) embedded into an organic resin. The upper part of the grains remains uncovered. CdS is deposited on top of the MGL by CBD, followed by RF sputtering of *i*-ZnO and conductive ZnO:Al layers. Grid contacts are evaporated on top of the ZnO window layer, and the structure is glued onto a transparent substrate. The bottom side is polished to remove the polymer from the powder crystals and to expose monograins before applying graphite contacts. Powder technologies are the cheapest technologies for producing materials, and the isothermal recrystallization of initial powders in different molten fluxes appears to be a relatively simple, inexpensive and convenient method to produce powder materials with an improved crystal structure and reduced concentration of inherent defects, as reported by Altosaar *et al.* (as cited in Ito, 2015).

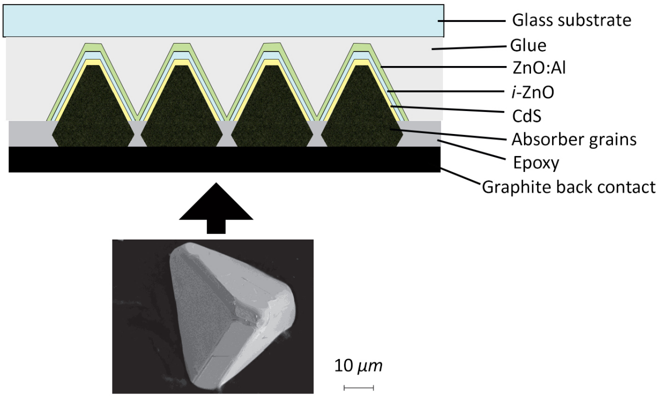

Figure 1.3 Structure of an MGL solar cell. An idea adapted from Danilson (2016); Samieipour, Kouhiisfahani, Galajev and Meissner (2015)

As reported by Mellikov *et al.* (as cited in Ito, 2015), single crystals that form single-crystalline powders grow at temperatures above the melting point of the used salt but lower than the melting point of the synthesized compound. Synthesis in molten salts can lower the reaction temperature and increase the homogeneity of the synthesized crystals to control the particle size and shape. Additionally, the liquid flux environment enhances the rate of solid-state reactions. If we compare the growth of monograin powder crystals with the growth process of single crystals from solutions, then the main difference is the nucleation. During single-crystal growth, the nucleation stage involves complete dissolution of the precursors in the molten salt. Boistelle and Astier (as cited in Ito, 2015) found that the nuclei of the products are formed in the supersaturated liquid phase. Then, during the monograin powder growth, the initial solid particles of low-solubility precursors react with each other in the molten salt media, and the formed solid particles of the product compound begin to recrystallize and grow *via* Ostwald ripening. Mellikov *et al.* (as cited in Ito, 2015) showed that the presence of the liquid phase of the used flux salt in an amount that fulfills all the empty space between the solid particles is required for the growth of monograin powder crystals. Otherwise, sintering of particles occurs. The process is controlled by the temperature, type and amount of salt. The volume of the used molten salt must exceed the volume of voids between precursor particles at the synthesis-growth temperature. Then, there is a sufficient amount of liquid phase to repel both the solid precursor particles and the formed powder particles to avoid sintering of the formed particles (see Figure 1.4). The amounts of precursors for CZTSSe and the flux salt have ratios of the forming volumes of solid phase V_S to liquid phase V_L within the range of 0,6-1,0. When selecting the flux material, the following requirements should be considered:

- the melting point of the flux salt should be lower than the melting point of the target product compound ($Cu_2ZnSnSe_4$ or SnS);
- the flux salt should be easily removable from solid $Cu_2ZnSnSe_4$ or SnS by dissolution in water or in some other solvent;
- the flux material should allow control over the composition of the target product compound ($Cu_2ZnSnSe_4$ or SnS).

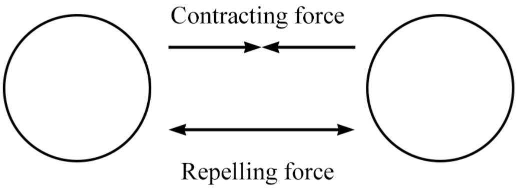

Figure 1.4 Growth of single crystals from particles

The reduction in melting temperature using mixtures of salts has been previously described (Paluch, 2016). The monograin powder growth is performed at relatively high temperatures in a molten salt; therefore, the semiconductor compound crystals are doped with the constituent elements (K, Na and I) if the salts used are KI and NaI at the level of their solubility at the synthesis temperature in the synthesized absorber material. The other problem is that at high temperatures, some of the precursors and synthesized kesterite dissolve in the flux material, and upon cooling, some of them precipitate on the surface of the monograins. It has been found (Timmo *et al.*, 2007) that by growing $CuInSe_2$ (CISe) monograin powder in KI at 627 °C (900 K), the solubilities of potassium and iodine in $CuInSe_2$, as determined by the ICP-MS analysis, were $9{,}4 \cdot 10^{-2}$ wt%, and $8{,}6 \cdot 10^{-3}$ wt%, respectively. Cu-poor and Zn-rich CZTSSe is a prerequisite for high-efficiency solar cells, as previously found (Sahayaraj *et al.*, 2016). The composition of the used materials is usually characterized by the concentration ratios of $Cu/(Zn + Sn) = 0{,}9$, $Zn/Sn = 1$ and $Se/metals = 1$, as experimentally investigated by Muska *et al.* (as cited in Ito, 2015).

1.6 Stability of Flux Materials

The stability of experimentally used flux materials, including cadmium iodide (CdI_2), sodium iodide (NaI), potassium iodide (KI) and tin chloride ($SnCl_2$), will be described in this chapter. The metal-halide structure from molecular clusters to the liquid state structure has been previously described (Tosi, 2015).

1.6.1 Cadmium Iodide

According to the database (software HSC6 Chemistry Ver. 6.0.), CdI_2 melts at 387 °C (660 K), has a boiling point of 742 °C (1015 K) and has a solubility in water of 847,0 g per liter at 20 °C (293 K). As previously described (Kolay, Mishra, Das & Dharwadkar, 2011) using derivative thermogravimetry, the mass loss of CdI_2 during heating from room temperature to 800 °C (1073 K) under Ar flow begins at the melting point and continues until the boiling point is reached. The enthalpy of vaporization was measured to be 110,9 kJ mol^{-1}, and the standard enthalpy of sublimation at 25 °C (298,15 K) is $148{,}5 \pm 7{,}6$ kJ mol^{-1} (Mishra *et al.*, 1997). The vapor pressure of liquid CdI_2 determined by DTG in the temperature range of 467-497 °C (740-770 K) is thus $28{,}5\text{-}57{,}5 \cdot 10^{-4}$ Pa, which is lower than the theoretically calculated value (Skudlarski, Dudek & Kapa 1987).

Additionally, CdI_2 has been found to be light sensitive, and its photodissociation has been studied (Kawasaki, Lee & Bersohn, 1979). These authors found that CdI_2 first dissociates into CdI^+ and I and then into Cd and 2I. However, Kasatani, Mori, Kawasaki and Hiroyasu (1987) used lasers and explained that the process for the decay of CdI is a radical-radical disproportionation reaction (1.17) or an abstraction reaction by the iodine atom generated, as shown in reaction (1.18):

$CdI\ (g) + CdI\ (g) \rightarrow CdI_2\ (g) + Cd\ (g)$ (1.17)

$CdI\ (g) + I\ (g) \rightarrow Cd\ (g) + I_2\ (g)$ (1.18)

Additionally, they suggested that the direct dissociation occurs due to the linear structure of CdI_2, as shown in reaction (1.19):

$ICdI\ (g) \rightarrow Cd\ (g) + I_2\ (g)$ (1.19)

Kasatani *et al.* (1987) suggested that Cd atoms are directly formed in the one-photon primary process. The decay mode of Cd atoms is considered to occur *via* reaction (1.20) because CdI radical formation requires a large heat of reaction and CdI_2 dimers are unstable. The formation mechanism (reaction 1.21) of $Cd*$ at 308 nm or 337,1 nm is largely believed to be three-photon absorption in CdI_2, since CdI signals in experiments have not been found:

$Cd\ (g) + CdI_2\ (g) \rightarrow (CdI)_2\ (g)$ (1.20)

$CdI_2\ (g) + 3\ h\nu \rightarrow Cd*\ (g)\ (n \geq 5) + 2\ I\ (g)$ (1.21)

Kuncewicz-Kupczyk, Kapała, Roszak and Miller (1998) studied the structure (Figure 1.5) and vaporization of CdI_2 (s) between 261 °C (534 K) and 340 °C (613 K) *via* Knudsen effusion mass spectrometry using electrons at 60 eV. Experimentally, the Cd_2I_4 dimer for a short time was found in concentrations that were three orders of magnitude smaller than that of the monomer itself, and CdI_2 vaporized similarly. The enthalpy of standard sublimation ($\Delta_{sub}H^o$) at 25 °C (298,15 K) for equation (1.22) was determined to be 222,5 ± 6,2 kJ mol^{-1}, and the enthalpy of standard dissociation ($\Delta_d H^o$) at 25 °C (298,15 K) for equation (1.23) was determined to be 70,7 ± 7,0 kJ mol^{-1}.

$2\ CdI_2\ (s) \leftrightarrow Cd_2I_4\ (g)$ (1.22)

$Cd_2I_4\ (g) \leftrightarrow 2\ CdI_2\ (g)$ (1.23)

The standard enthalpy of formation ($\Delta H_{f298,15K}$) at 25 °C (298,15 K) of Cd_2I_4 (g) was determined to be -188,1 ± 6,3 kJ mol^{-1}, according to the third law thermodynamics. The intensities of the CdI_2^+ and $Cd_2I_3^+$ ions over the CdI_2(s) were observed by mass spectrometry. Additionally, some ions, including Cd^+, CdI^+ and I^+, were detected. The structural and symmetrical calculations by Donald, Hargittai and Hoffmann (2008) agreed that the Cd_2I_4 dimer could be formed.

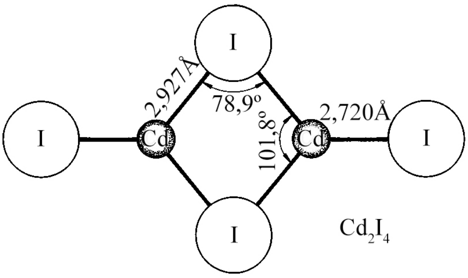

Figure 1.5 Structure of the Cd_2I_4 dimer, adapted from Kuncewicz-Kupczyk et al. (1998)

When processing the flux material at room temperature in air, reactions with substances in the air should be considered. Computations using the database (software HSC6 Chemistry Ver. 6.0.) found the ΔG values for the reactions below to be negative. CdI_2 does not directly react with H_2O vapor; therefore, $Cd(OH)_2$ formation is not possible. However, $Cd(OH)_2$ is produced if CdO forms. The ΔG = -56,4 kJ mol^{-1} for the reaction (1.24) at room temperature (23 °C or 296 K), and CdO can react with the moisture in air *via* reaction (1.25). Since ΔG = -15,8 kJ mol^{-1}, the reaction proceeds in the reverse direction at temperatures above 128 °C (401 K):

$$2\ CdI_2\ (s) + O_2\ (g) \rightarrow 2\ CdO\ (s) + 2\ I_2\ (s, g) \tag{1.24}$$

$$CdO\ (s) + H_2O\ (g) \leftrightarrow Cd(OH)_2\ (s) \tag{1.25}$$

CdO does not react with NO_2 (ΔG is positive) but can react with SO_2 and CO_2. However, it should be emphasized that the equilibrium concentrations of SO_2 and CO_2 in air are rather low.

1.6.2 Sodium Iodide

NaI melts at 661 °C (934 K) and has an excellent solubility in water (1842,0 g per liter) at 25 °C (298 K) as described in the database (software HSC6 Chemistry Ver. 6.0.). Compared with CdI_2, NaI does not form oxides, and reactions with other gases do not proceed.

Primarily, the behavior of NaI under heating in vacuum has been studied using baric methods and spectrometry. Sofronov *et al.* (2005) connected the water release with decomposition of the hydroxyl groups that are present and are bound to impurities. Several hydrated crystal compounds have been found, including $NaI{\cdot}5H_2O$ (existing below -31,5 °C or -241,5 K), $NaI{\cdot}2H_2O$, existing at -13,5 °C (259,5 K) to 68 °C (341 K) with an invariant transition point to NaI at 68 °C (341 K) and 78,4 % of NaI (Sofronov *et al.*, 2005) at 68,2 °C (341,2 K) and p_{H2O} = 6,32 kPa, according to Digemans (as cited in Sofronov *et al.*, 2005), and a metastable form, $NaI{\cdot}xH_2O$, which shows an invariant transition at 60 °C (333 K) and 74,5 % NaI. Elsken and Zander (as cited in Sofronov *et al.*, 2005) suggested that the metastable form is present within the 30-40 °C (303-313 K) range at x = 0,5 mol. Grinyov (as cited in Sofronov *et al.*, 2005) showed that water molecules evaporate at 150 °C (423 K) and 300-350 °C (573-623 K). However, for the pressure-temperature dependence, dehydration was assigned at 127-347 °C (400-620 K) according to Goriletsky (as cited in Sofronov *et al.*, 2005), whereas in another study (Sofronov *et al.*, 2005), the 180-450 °C (453-723 K) temperature range was considered.

Other research (Grinyov *et al.*, 2004) showed that the sodium iodide crystal hydrates decomposed at 180-280 °C (453-553 K) (1.26-1.27):

$NaOH \cdot n\ H_2O\ (s) \rightarrow NaOH\ (s) + n\ H_2O\ (g)$ (1.26)

This reaction is followed by the decomposition of OH^- groups:

$2\ NaOH\ (s) \rightarrow Na_2O\ (s) + H_2O\ (g)$ (1.27)

Grinyov *et al.* (2004) found that dehydration is possible at room temperature and that it occurs according to reaction (1.28):

$NaI \cdot 2\ H_2O\ (s) \rightarrow NaI\ (s) + 2\ H_2O\ (g)$ (1.28)

As described by Smirnov (as cited in Grinyov *et al.*, 2004), the dehydration of $NaI{\cdot}2H_2O$ should be performed at 68-70 °C (341-343 K) in vacuum due to the sodium iodide interactions with oxygen-containing air components. In another study (Russell, 1986), the vapor-phase of NaI was discussed, and the authors proposed that at 795 °C (1068 K), the saturated NaI vapor consists of approximately 50,0 % monomers and 50,0 % dimers; however, the unsaturated absorption spectrum showed that the dimers dissociate to monomers at 948 °C (1221 K) and that the dimers are present at 20,0 %. In study (Voloshko *et al.*, 2004), drying of NaI with microwaves in vacuum was studied, and the authors concluded that microwave energy reduces the costs and provides a higher dehydration efficiency because the material is uniformly heated according to volume at 60-80 °C (333-353 K). As suggested by Grinyov *et al.* (2004), to prevent the accumulation of Na_2CO_3 in the material, NaI should be dehydrated and heated above 40 °C (313 K) or at 1,3 Pa at 20-30 °C (293-303 K) to accelerate the process by microwave agitation.

Sofronov, Kudin, Voloshko, Kudin and Shishkin (2009) analyzed in more detail the origin of the thermal desorption peaks of the gases in NaI above 180 °C (453 K). According to Goriletsky, it is known that NaI hydrolyzes even at room temperature (as cited in Sofronov *et al.*, 2009), and upon an increase in temperature, the hydrolysis increases. The hydrate decomposes at 65,0-6,5 Pa at 20 °C (293 K). The decomposition of the hydrate to anhydrous NaI reaches completion even at room temperature. The dehydration of the hydrate occurs in the temperature range of 20-200 °C (293-473 K). Water desorption is accompanied by the release of a small amount of CO_2. The dehydration is complete above 220 °C (493 K). The observed water release above 200 °C (473 K) is due to the impurities formed during dehydration of the hydrate hydroxyl groups. Sodium iodide dehydrate is nonreactive with oxygen; in contrast, during heating in O_2 + CO_2 at 30-60 °C (303-333 K), it produces sodium carbonate as the product. NaI itself is relatively nonreactive with O_2, CO_2, and H_2O separately; however, it is highly reactive with a mixture of any of two of them. The crystalline hydrate is more reactive with O_2 and CO_2 than anhydrous NaI (1.29-1.30):

$NaI \cdot 2\ H_2O\ (s) + 0{,}5\ CO_2\ (g) \leftrightarrow 0{,}5\ Na_2CO_3\ (s) + HI\ (g) + 1{,}5\ H_2O\ (g)$ (1.29)

$NaI \cdot 2\ H_2O(s) + 0{,}25\ O_2\ (g) \leftrightarrow NaOH\ (s) + 0{,}5\ I_2\ (g) + 1{,}5\ H_2O\ (g)$ (1.30)

As mentioned by Sofronov *et al.* (2009), reaction (1.31) does not occur at temperatures below 200 °C (473 K).

$NaI \cdot 2\ H_2O\ (g) + 0{,}5\ CO_2\ (g) + 0{,}25\ O_2\ (g) \leftrightarrow 0{,}5\ Na_2CO_3\ (s) + 0{,}5\ I_2\ (g) + 2\ H_2O\ (g)$ (1.31)

During heating, sodium carbonate reacts with water vapor according to reaction (1.32), which is more possible at temperatures above 600 °C (873 K):

$Na_2CO_3\ (s) + H_2O\ (g) \rightarrow NaOH\ (s) + NaHCO_3\ (s)$ (1.32)

1.6.3 Potassium Iodide

The information in the database (software HSC6 Chemistry Ver. 6.0.) shows that the KI melting temperature is 681 °C (954 K), and its solubility in water at 20 °C (293 K) is 1400,0 g per liter. It is expected to be rather stable in dry air, since there are no reports on the formation of KI crystal hydrates in the literature. Additionally, K_2O cannot be formed under these conditions. Based on the literature survey, KI is rather stable in dry air. However, exposure to light and moisture can accelerate the decomposition of potassium iodide. The instability of KI in air (1.33) is caused by the slow oxidation reaction of the salt in the presence of CO_2 to potassium carbonate and elemental iodine:

$4\ KI\ (s) + 2\ CO_2\ (g) + O_2\ (g) \rightarrow 2\ K_2CO_3\ (s) + 2\ I_2\ (g)$ (1.33)

In principle, reaction (1.33) in degassed sealed vacuum ampoules cannot proceed. The thermodynamic Gibbs free energy calculations show negative ΔG values in the temperature range of 0 °C (273 K), where $\Delta\ G$ = -12,0 kJ, to 56 °C (329 K), where it is almost equal to 0,0 kJ mol^{-1}, and the reaction can therefore proceed during storage of KI or during the sample preparation process.

KI can contain adsorbed iodine because KI is produced industrially by treating KOH with iodine. Iodine can be adsorbed on the surface of the KI crystals (Kaiho, 2014).

1.6.4 Tin Chloride

$SnCl_2$ is able to form a stable dehydrate; however, aqueous solutions of $SnCl_2$ tend to undergo hydrolysis, particularly if heated. Tin(II) chloride can dissolve in H_2O, and solutions of $SnCl_2$ are also unstable towards oxidation by air (1.34-1.35):

$SnCl_2\ (aq) + H_2O\ (l) \leftrightarrow Sn(OH)Cl\ (s) + HCl\ (aq)$ (1.34)

$6\ SnCl_2\ (aq) + O_2\ (g) + 2H_2O\ (l) \rightarrow 2\ SnCl_4\ (aq) + 4\ Sn(OH)Cl\ (s)$ (1.35)

The solubility of $SnCl_2$ in H_2O at 0 °C (273 K) is 839,0 g per liter. $SnCl_2$ melts at 37,7 °C or 310,7 K (hydrate) and at 247 °C or 520 K (anhydrous). At T_b = 623 °C (896 K), $SnCl_2$ decomposes during evaporation. $SnCl_2$ does not directly react with O_2 at room temperature or with other gases that are present in air. This information was obtained from the database (software HSC6 Chemistry Ver. 6.0.).

As shown in the phase diagram for the Sn-Cl system (Figure 1.6), $SnCl_2$ melts at 232 °C (505 K), and two molten phases of $SnCl_2$ and $SnCl_4$ exist in equilibrium at temperatures above 246 °C (519 K).

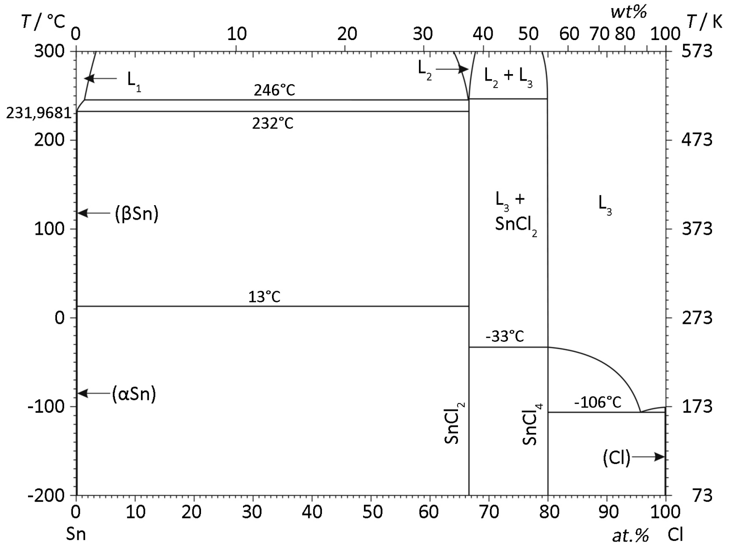

Figure 1.6 Sn-Cl phase diagram, adapted from Okamoto (2013)

1.7 Phase Diagrams

Phase diagrams provide an overview of the equilibrium conditions in which the existing solid, liquid and gaseous phases are thermodynamically stable at a certain temperature. The term "*phase*" can refer to elements with different modifications, and transitions occur upon heating or cooling. In phase diagrams, relations between atoms are described in atomic percent (at.%). Additionally, terms such as mole percent (mol%) or weight percent (wt%) are used. The mathematical expressions are provided in Appendix 2, Sections A2.2; A2.3; A2.4.

The **Cd-S, Cd-I, K-I and Zn-I** phase diagrams are not presented here due to their simplicity. CdS melts at 1750 °C (2023 K), while its boiling (sublimation) occurs at 980 °C (1253 K). The meltings of CdI_2 and KI are described above. The melting of ZnI_2 is at 446 °C (719 K) according to the database (software HSC6 Chemistry Ver. 6.0.). The **Na-I** phase diagram shows a partially miscible system. At concentrations of 50,0 % I, above 660,1 °C (933,1 K), Na and I are completely miscible. From 660,1 °C (933,1 K), NaI is precipitated (Massalski & Okamoto, 1990). **Sn-Cl** was described in Item 1.6.4.

CdSe is known to exist in wurtzite (hexagonal), sphalerite (cubic) and rock-salt (cubic) phases. The sphalerite CdSe structure is unstable and transforms upon moderate heating at approximately 130 °C (403 K), and at 700 °C (973 K), the transformation is complete within a day. The rock-salt structure is detected at high pressure (Sharma & Chang, 1996). CdSe melts at 1268 °C (1541 K), as provided in the database (software HSC6 Chemistry Ver. 6.0.). The **Zn-Se** system at 50,0 at.% Se has a melting point of ZnSe of 1526 °C (1799 K), as presented in the database (software HSC6 Chemistry Ver. 6.0.).

1.7.1 Na-Se and K-Se Phase Diagrams

The **Na-Se** system is shown in Figure 1.7 (a). Solid Na is present below 97,8 °C (370,8 K). The melting point of Na_2Se is above 875 °C (1148 K). Moving to the Se-rich side, a peritectic reaction with Na_2Se_2 occurs 495 °C (768 K). Further cooling leads to a peritectic reaction with Na_2Se_3 at 313 °C (586 K), Na_2Se_4 at 290 °C (563 K) and Na_2Se_6 at

258 °C (531 K). The L_2 (molten Se) monotectic reaction occurs with L_1 + Na_2Se_6 at 255 °C (528 K), and it is not clear if this compound exists instead of the Na_2Se_5 form. Pure solid Se exists below 221 °C (494 K), according to data from Sangster and Pelton (1997). The thermal decomposition is more likely to occur with an increase in Se content. As summarized by Sangster and Pelton, the standard enthalpy of formation of Na_2Se is reported to be in the range of -377,0 to -341,4 kJ mol^{-1}, and for Na_2Se_2, it is -388,0 $\pm$ 40,0 kJ mol^{-1}.

Table 1.1 Equilibriums in the K-Se system, according to Sangster and Pelton (1997)

Reaction	**Composition of the respective phases / at.% Se**			***T* / °C (K)**	**Reaction type**
$L \leftrightarrow$ K		0,0		63,71 (336,71 K)	Melting
$L \leftrightarrow$ (K) + K_2Se	0,0	0,0	33,3	63,7 (336,7 K)	Eutectic
$L \leftrightarrow K_2Se$		33,3		900 $\pm$ 200 (1173 $\pm$ 200 K)	Congruent
$L \leftrightarrow$ (K_2Se) + K_2Se_2	48,0	37,5	50,0	430 $\pm$ 50 (703 $\pm$ 50 K)	Eutectic
$L \leftrightarrow K_2Se_2$		50,0		460 $\pm$ 20 (733 $\pm$ 20 K)	Congruent
$L \leftrightarrow K_2Se_2 + K_2Se_3$	56,0	50,0	60,0	360 $\pm$ 10 (633 $\pm$ 10 K)	Eutectic
$L \leftrightarrow K_2Se_3$		60,0		375 $\pm$ 5 (648 $\pm$ 5 K)	Congruent
$L + K_2Se_3 \leftrightarrow K_2Se_4$	69,0	60,0	66,7	206 $\pm$ 5 (479 $\pm$ 5 K)	Peritectic
$L \leftrightarrow K_2Se_4$ + (γ-Se)	78,0	66,7	100,0	160 $\pm$ 2 (433 $\pm$ 2 K)	Eutectic
$L_2 \leftrightarrow$ (γ-Se) + L_1	99,8	100,0	87,5	220,5 (493,5 K)	Monotectic
$L \leftrightarrow L_1 + L_2$		92,0		310 $\pm$ 2 (583 $\pm$ 2 K)	Critical
$L \leftrightarrow \gamma$-Se		100,0		221 (494 $\pm$ 2)	Melting

The **K-Se** system exhibits equilibria as summarized in Table 1.1 and shown in Figure 1.7 (b), as adapted from Sangster and Pelton (1997). It is assumed that K_2Se_5 melts incongruently and possibly decomposes in a peritectoid reaction below 160 °C (433 K). The K_2Se_6 compound was found to be unstable (Sangster & Pelton, 1997).

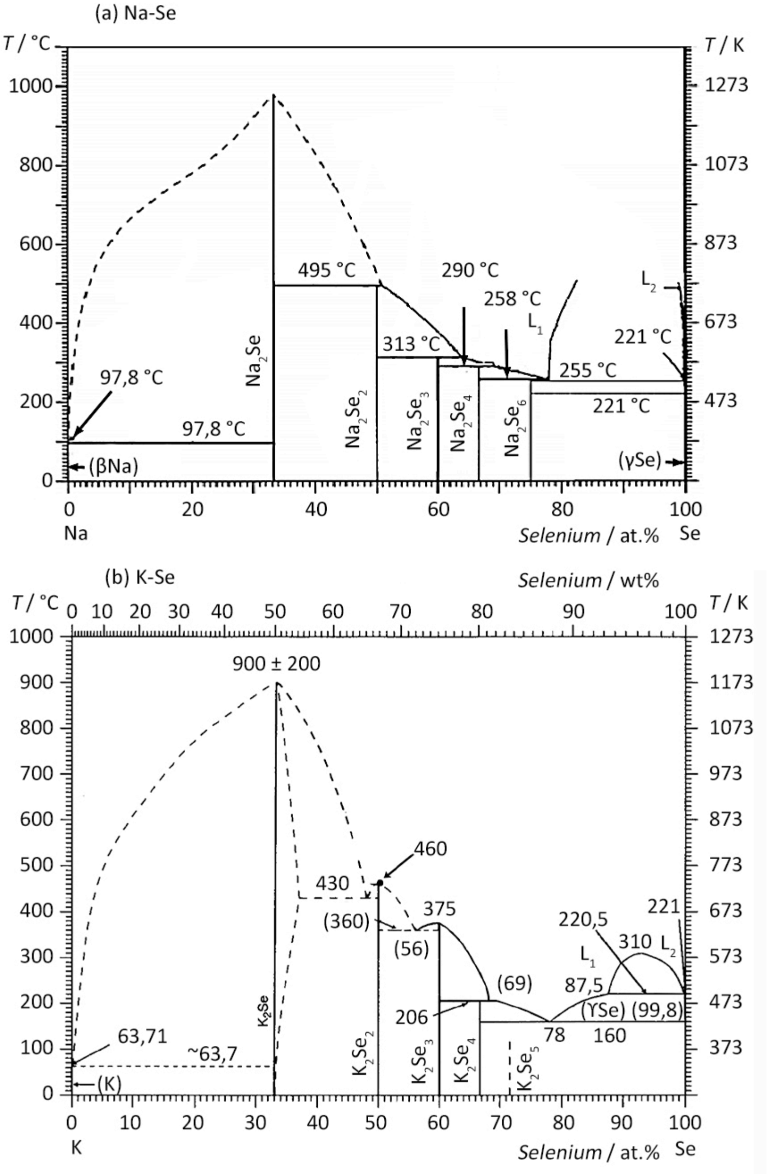

Figure 1.7 Phase diagrams of the Na-Se (a) and K-Se (b) systems, adapted from Sangster and Pelton (1997)

1.7.2 Cu-Se Phase Diagram

The Cu-Se system is shown in Figure 1.8. If CZTSe synthesis proceeds using CuSe at temperatures up to 800 °C (1073 K), there are three copper compounds that play a role: $Cu_{2-x}Se$ (berzelianite), CuSe (klockmannite) and $CuSe_2$. This system was investigated *via* DTA and XRD in Murray and Heyding (1975). The phase diagram was also previously reported in Chakrabarti and Laughlin (1981) and then improved in Glazov, Pashinkin and Fedorov (2000). The following discussion is based on those three articles. The enthalpy values of some phase transitions and reactions are provided in Table 1.2.

Monoclinic α-Cu_2Se is stable up to 123 ± 15 °C (396 ± 15 K). Then, it transforms to the face-centered cubic high-temperature modification of β-$Cu_{2-x}Se$ ($0 \leq x \leq 0,3$) with the space group of *F-43m* for β-Cu_2Se, which has an immobile zinc blende-type structure that exists as a solid up to 1130 °C (1403 K) and melts congruently. $Cu_{2-x}Se$ extends from Cu_2Se to $Cu_{1.75}Se$. At 123 °C (396 K), the peritectoid of β-$Cu_{2-x}Se$, α-$Cu_{2-x}Se$ and (Cu) is present. The tetragonal stoichiometric compound in the space group *P42₁m*, called umangite, Cu_3Se_2, is stable up to 112 °C (385 K). In the temperature range of 112-120 °C (385-393 K), it forms β-$Cu_{2-x}Se$ + β-CuSe (extremely slowly); however, at higher temperatures over 120 °C (393 K), β-$Cu_{2-x}Se$ + γ-CuSe is present. At 523 °C (796 K), there is a monotectic point where solid β-$Cu_{2-x}Se$ coexists with two liquids. According to Boettcher *et al.* (as cited in Chakrabarti & Laughlin, 1981), the metastable phase, $Cu_{1.9}Se$, is present in thin films at 20-320 °C (293-593 K). Murray and Heyding (1975) found that Cu_2Se slowly oxidizes in air to form Cu_2O and $Cu_{1.8}Se$, while the $Cu_{2-x}Se$ phase is less susceptible to oxidation.

The hexagonal stoichiometric compound α-CuSe (*$P6_3/mmc$*) is stable up to 51 °C (324 K); then, it transforms the orthorhombic modification of β-CuSe, which is stable up to 120 °C (393 K). It further transforms to the hexagonal high-temperature modification, γ-CuSe (*$P6_3/mmc$*), which is stable up to 377 °C (650 K), where the peritectic reaction starts and solid β-$Cu_{2-x}Se$ with liquid Se are formed. It decomposes into β-$Cu_{2-x}Se$ and a Se-rich melt.

The marcasite-type orthorhombic stoichiometric compound, $CuSe_2$ (*Pnnm*), is stable up to 332 °C (605 K) upon which a peritectic reaction occurs to form γ-CuSe and Se, and it melting congruently.

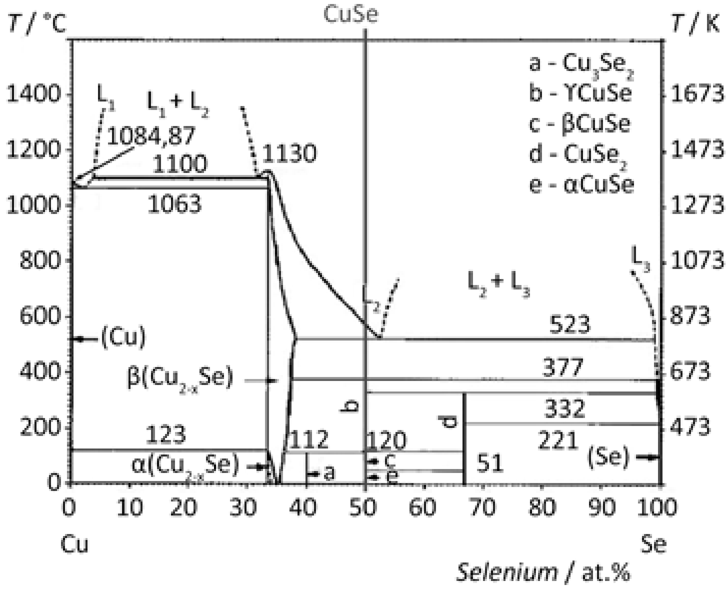

Figure 1.8 Phase diagram of Cu-Se, adapted from Chakrabarti and Laughlin (1981)

Table 1.2 Enthalpy values of some phase transitions and reactions in the Cu-Se system

Reaction	***T* / °C (K)**	***ΔH* / kJ mol^{-1}**	**Reference**
α-Cu_2Se ↔ β-Cu_2Se	123 ± 15 (396 ± 15 K)	4,9 6,4 ± 2,0 6,5 ± 0,1 6,8 20,5 ± 4,0	Kelley (as cited in Glazov *et al.*, 2000) (Murray & Heyding, 1974) Blachnik and Gunia (as cited in Glazov *et al.*, 2000) Kubaschewski and Nölting (as cited in Murray & Heyding, 1974) Heyding (as cited in Glazov *et al.*, 2000)
Cu_3Se_2 ↔ β-Cu_2Se + β-CuSe	112 (385 K)	10,0 ± 5,0	(Murray & Heyding, 1975)
α-CuSe ↔ β-CuSe	51 (324 K)	0,8 0,9 ± 0,0	(Murray & Heyding, 1975) Heyding (as cited in Glazov *et al.*, 2000)
2CuSe ↔ β-Cu_2Se + Se (Perictectic)	377 (650 K)	11,8 ± 0,0	Bernardini (as cited in Glazov *et al.*, 2000)
$CuSe_2$ ↔ CuSe + Se	332 (605 K)	9,6 ± 4,0 10,9 12,1 ± 2,9	(Murray & Heyding, 1975) Bernardini (as cited in Glazov *et al.*, 2000) Heyding (as cited in Glazov *et al.*, 2000)

1.7.3 Cu-I and Sn-I Systems

In the **Cu-I** system at 50,0 at.% Cu and 50,0 at.% I, according to Table 1.3, low-temperature α-CuI (zinc-blende face-centered cubic) transforms to β-CuI (hexagonal wurtzite) at temperatures of 367,9-380 °C (640,9-653 K) with different values of enthalpies between 2,6 and 8,2 kJ mol^{-1} and further to γ-CuI (face-centered cubic disordered zinc blende) in the temperature range of 397 to 420 °C (670-693 K) with an enthalpy value of 0,8-3,2 kJ mol^{-1}, depending on the literature source. The phase transitions are reversible. At pressures up to 2 kbar, the α to β transition increases to 374 °C (647 K), whereas the β to γ transition decreases to 403 °C (676 K). The triple point at those temperatures at approximately 2,0 kbar has been determined (Rapaport & Pistorius, 1968).

According to prior Wojakowska (1989) investigations of the SnI_2-CuI system, solid solutions of SnI_2 in the α, β, and γ CuI phases were formed, leading to CuI phase transition depressions for γ to β of 1 °C (K) and for β to α of more than 20 °C (K). The eutectic point parameters at 32,7 mol% CuI are 270,4 ± 0,1 °C (543,4 ± 0,1 K), and the invariant points at 64,0 mol% CuI are 385,3 ± 0,5 °C (658,3 ± 0,5 K) and 61,5 mol% CuI 366,6 ± 0,2 °C (639,6 ± 0,2 K), corresponding to the equilibria γ + liquid transformation and to the β and β + liquid transformation to α. From the eutectic temperature to the melting point of CuI, no intermediates have been found in this system.

For the **Sn-I** system, the transitions were not found in the literature, except for the melting and boiling points for SnI_4 (cubic) at 143 °C (416 K) and 364,4 °C (637,4 K), respectively; and for SnI_2, they are 320 °C (593 K) and 714 °C (987 K), respectively. SnI_2 can be easily oxidized to SnI_4 by I_2, according to simulations using the database (software HSC6 Chemistry Ver. 6.0.).

Table 1.3 Temperature and enthalpy values of the transitions for CuI

Transition	***T* / °C (K)**	***ΔH* / kJ mol^{-1}**	**Reference**
α-CuI $\leftrightarrow$ β-CuI	367,9 (640,9 K)	-	(Wojakowska, 1989)
	369 (642 K)	7,1	Miyake, Hoshino and Takenaka (as cited in Ferrate, Mrazek & Brown, 1930)
	370 (643 K)	3,1	(Ferrate *et al.*, 1930)
	370,5 ± 1 (643,5 ± 1 K)	2,6	(Rapaport & Pistorius, 1968)
	371 (644 K)	4,9	Ghosh and Nag (as cited in Ferrate *et al.*, 1930)
	375 (648 K)	2,6	Le-Van-My, Perinet and Bianco (as cited in Ferrate *et al.*, 1930)
	380 (653K)	8,2	Carré *et al.* (as cited in Ferrate *et al.*, 1930)
β-CuI $\leftrightarrow$ γ-CuI	397 (670 K)	0,8	Ghosh and Nag (as cited in Ferrate *et al.*, 1930)
	406 (679 K)	2,7	(Ferrate *et al.*, 1930)
	406,4 (679,4 K)	-	(Wojakowska, 1989)
	407 (680 K)	3,2	Miyake *et al.* (as cited in Ferrate *et al.*, 1930)
	408 (681 K)	2,8	(Rapaport & Pistorius, 1968)
	420 (693 K)	2,6	Carré *et al.* (as cited in Ferrate *et al.*, 1930)
CuI melting	588 (861 K)	-	Kauffman and Pinnell (as cited in Rapaport and Pistorius, 1968)
	600 (873 K)	-	Le-Van-My *et al.* (as cited in Rapaport & Pistorius, 1968)
	592,2 ± 0,2 (865,2 ± 0,2)	-	(Wojakowska, 1989)
	591 (864 K)	-	(Rapaport & Pistorius, 1968)
	600 (873 K)	4,0	Le-Van-My *et al.* (as cited in Ferrate *et al.*, 1930)
	605 (878 K)	8,3	Carré *et al.* (as cited in Ferrate *et al.*, 1930)
	606 (879 K)	7,9	(software HSC6 Chemistry Ver. 6.0.)

1.7.4 Sn-Se and Sn-S Phase Diagrams

In the **Sn-Se** system (Figure 1.9), there are SnSe and $SnSe_2$ compounds. The melting point of SnSe is at 860 °C (1133 K) according to the database (software HSC6 Chemistry Ver. 6.0.) or at 880 °C (1153 K) with 32,6 ± 3,7 kJ mol^{-1}, as reported by Karahanova, Pashinkin and Novoselova (as cited in Bletskan, 2005). It has been reported to be 873,7 °C (1146,7 K) in another report (Sharma & Chang, 1986) in Figure 1.9. A second-order transition from the low-temperature phase of the α-SnSe phase to the high-temperature phase of the β-SnSe phase occurs at 534 °C or 807 K (Bletskan, 2005) or as determined previously (Sharma & Chang, 1986) at 520,2 °C (793,2 K) with 1,6 kJ mol^{-1}. The sublimation and evaporation occur incongruently because after sublimation, metallic Sn remains, and the vapor consists of Se and $SnSe_2$ molecules above the solid SnSe. The vapor is enriched with Se. $SnSe_2$ melts congruently at 646,6 °C (919,6 K), as reported previously (Sharma & Chang, 1986). The eutectic mixture of SnSe and $SnSe_2$ melts at 625 °C (898 K) at 61,0 at.% Se (Bletskan, 2005), whereas another report (Sharma & Chang, 1986) was in agreement at 628 °C (901 K). Two eutectic points very close to pure Se and Sn (1 °C (K) below their melting points) have been determined (Sharma & Chang, 1986).

According to Bletskan (2005), there are two main processes in the **Sn-S** system (Figure 1.10) below 800 °C (1073 K). The eutectic reaction (1.36) varies at 740 °C (1013 K), 705 °C (978 K) in report by Bletskan (2005) or 738 °C (1011 K), as determined by Sharma and Chang (1986). Bletskan (2005) reported that the eutectic reaction (1.37) occurs at 745 °C (1018 K), but Sharma and Chang determined reaction (1.37) at 760 °C (1033 K):

$$L_2 \leftrightarrow \beta\text{-SnS (s)} + \gamma\text{-Sn}_2\text{S}_3\text{ (s)} \qquad (1.36)$$

$$L_2 + \beta\text{-SnS}_2\text{ (s)} \leftrightarrow \delta\text{-Sn}_2\text{S}_3\text{ (s)} \qquad (1.37)$$

Intermediate phases, including SnS, Sn_2S_3, and SnS_2, exist in the Sn-S system. SnS and SnS_2 melt congruently at 880 °C (1153 K) and 865 °C (1138 K), respectively; however, Sn_2S_3 peritectically forms a liquid + Sn_2S_3 at 841 °C (1114 K). Additionally, the existence of Sn_3S_4 has been previously considered by Sharma and Chang (1986). See Figure 1.10 (a) and (b).

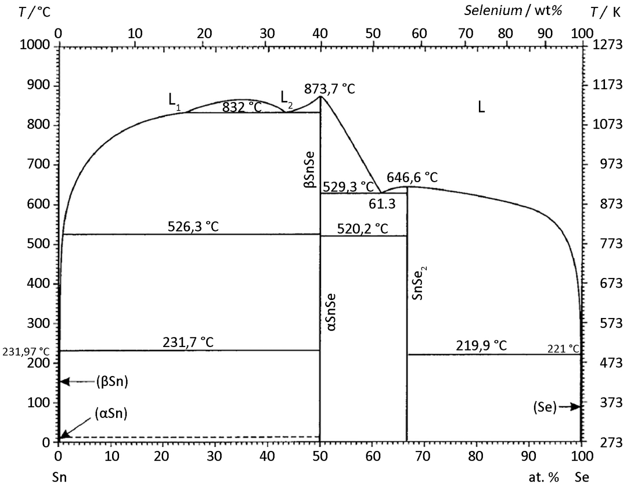

Figure 1.9 Phase diagram of Sn-Se, adapted from Sharma and Chang (1986)

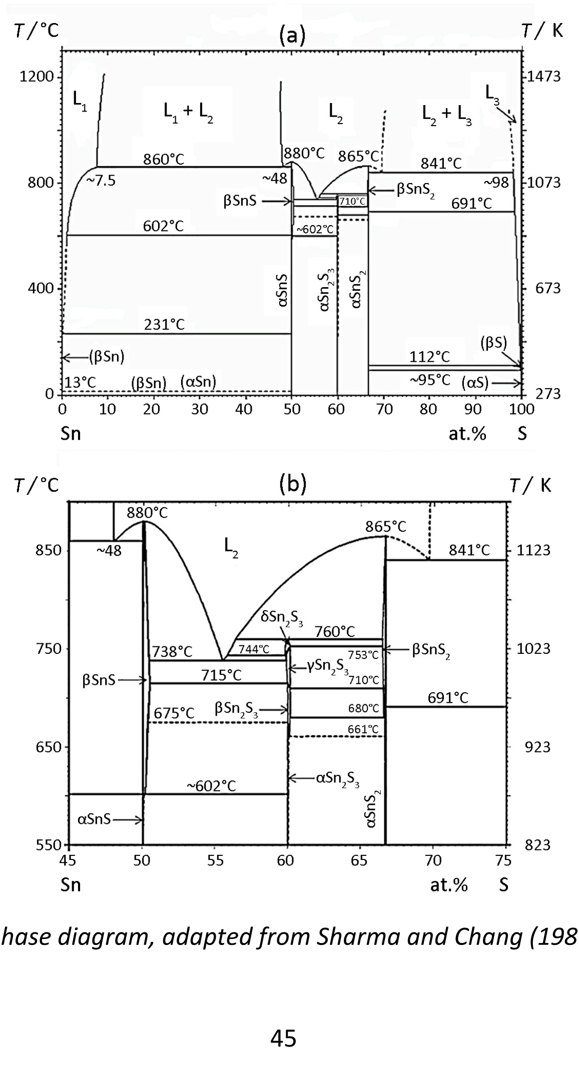

Figure 1.10 Sn-S phase diagram, adapted from Sharma and Chang (1986)

1.7.5 Pseudobinary Phase Diagrams

The **$SnSe_2$-Cu_2Se** pseudobinary phase diagram is shown in Figure 1.11. Cu_2SnSe_3 melts congruently at 690 °C (963 K), as reported in Parasyuk, Olekseyuk and Marchuk (1999), or at 695 °C (968 K) as reported in Dudchak and Piskach (2003). The eutectic coordinates are 17,0 mol% Cu_2Se at 604 °C (877 K) and 73,0 mol% Cu_2Se at 670 °C (943 K), as determined in one paper (Parasyuk *et al.*, 1999), or 16,0 mol% Cu_2Se at 580 °C (853 K) and 78,0 mol% Cu_2Se at 710 °C or 983 K (Oleksejuk *et al.*, 2001), and 20,0 mol% Cu_2Se and 76,0 mol% Cu_2Se (Matsushita & Katsuni, 2005). Oleksejuk *et al.*, 2001 determined that the solubilities of $SnSe_2$ and Cu_2Se were less than 3,0 mol% and 10,0 mol% in Cu_2SnSe_3, respectively. Cu_2SnSe_3 crystallizes into the cubic structure of $F\bar{4}3m$ (Matsushita & Katsuni, 2005).

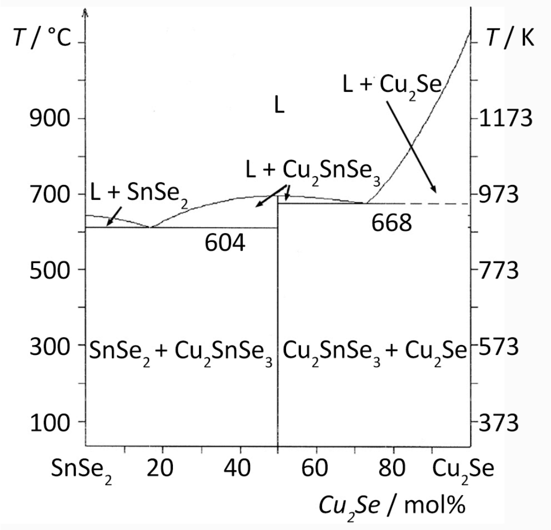

Figure 1.11 Phase diagram of the pseudobinary $SnSe_2$-Cu_2Se system, adapted from Matsushita and Katsuni (2005)

In other pseudobinary systems, such as the **$SnSe_2$-ZnSe** system, the eutectic point is at 642 °C (915 K) at 16,0 mol% ZnSe and has been reported by Dudchak and Piskach (2003); however, in the **Cu_2Se-ZnSe** system, no processes were found up to 800 °C (1073 K) for the temperatures used in this thesis (Oleksejuk *et al.*, 2001). The variables of **Cu_2SnSe_3-$SnSe_2$** and **Cu_2SnSe_3-Cu_2Se** systems are already covered in Figure 1.12. The average melting (Ito, 2015) point of CZTSe was previously determined to be 801 °C (1074 K). The melting point determination *via* DTA showed the endothermic effects at 805 °C (1078 K) for CZTSe and at 780 °C (1053 K) for compound, such as $Cu_2CdSnSe_4$ (Matsushita & Katsuni, 2005). In **Cu_2SnSe_3-ZnSe**, CZTSe formation begins at the peritectic point at 788 °C (1061 K) 14,0 mol% ZnSe, reaction (1.38):

$$L + \beta\text{-ZnSe (s)} \leftrightarrow Cu_2ZnSnSe_4\text{ (s)} \qquad (1.38)$$

$$\delta\text{-}Cu_2ZnSnSe_4\text{ (s)} \leftrightarrow \delta'\text{-}Cu_2ZnSnSe_4\text{ (s)} \qquad (1.39)$$

The temperature for the polymorphous CZTSe phase transformation from the low-temperature phase to the high-temperature phase, according to reaction (1.39), is at 616-619 °C (889-892 K). The eutectic process in **Cu_2SnSe_3-ZnSe** at 694 °C (967 K) and in ZnSe at 2,5 mol% was described by reaction (1.40) in Dudchak and Piskach (2003) and Oleksejuk *et al.* (2001):

$$L \leftrightarrow Cu_2SnSe_3\,(s) + \delta\text{-}Cu_2ZnSnSe_4\,(s) \qquad (1.40)$$

The variables of systems such as $Cu_2ZnSnSe_4$-(50,0 mol% Cu_2Se + 50,0 mol% ZnSe), $Cu_2ZnSnSe_4$-(50,0 mol% Cu_2Se + 50,0 mol% $SnSe_2$), $Cu_2ZnSnSe_4$-(50,0 mol% $SnSe_2$ + 50,0 mol% ZnSe), $Cu_2ZnSnSe_4$-ZnSe, $Cu_2ZnSnSe_4$-$SnSe_2$, and $Cu_2ZnSnSe_4$-Cu_2Se, can be reduced to constructing **$SnSe_2$-$Cu_2ZnSnSe_4$-(50,0 mol% ZnSe + 50,0 mol% $SnSe_2$)** in Figure 1.12 and **Cu_2Se-$Cu_2ZnSnSe_4$-(50,0 mol% Cu_2Se + 50,0 mol% ZnSe)** in Figure 1.13, according to Dudchak and Piskach (2003) and Oleksejuk *et al.* (2001). More detailed explanation on the processes is provided in Table 1.4.

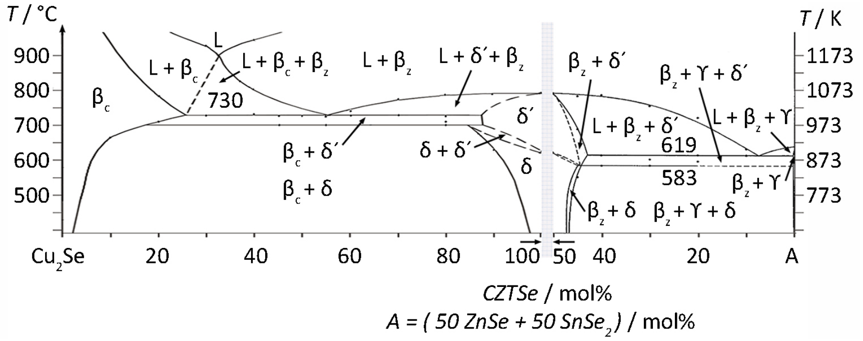

Figure 1.12 Phase diagram of $SnSe_2$-$Cu_2ZnSnSe_4$-(50,0 mol% ZnSe + 50,0 mol% $SnSe_2$), adapted from Dudchak and Piskach (2003) and Oleksejuk et al. (2001). L (liquid), β_C (β-Cu_2Se), β_z (β-ZnSe), γ (γ-$SnSe_2$), δ (δ-$Cu_2ZnSnSe_4$), δ' (δ-$Cu_2ZnSnSe_4$)

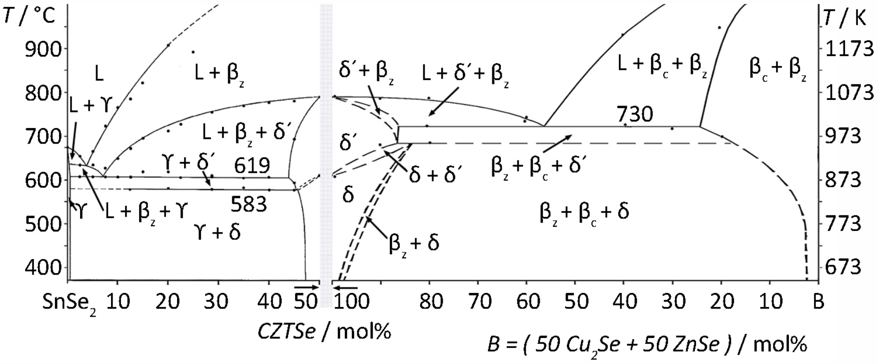

Figure 1.13 Phase diagram of Cu_2Se-$Cu_2ZnSnSe_4$-(50,0 mol% Cu_2Se + 50,0 mol% ZnSe), adapted from Dudchak and Piskach (2003) and Oleksejuk et al. (2001). L (liquid), β_C (β-Cu_2Se), β_z (β-ZnSe), γ (γ-$SnSe_2$), δ (δ-$Cu_2ZnSnSe_4$), δ' (δ'-$Cu_2ZnSnSe_4$)

Table 1.4 Processes, according to Figures 1.14-1.15 from Dudchak and Piskach (2003) and Oleksejuk et al. (2001)

System	Process	*T* / °C (K)
$Cu_2ZnSnSe_4$-Cu_2Se	Completed secondary crystallizations of binary peritectics: $L + \beta\text{-ZnSe} \leftrightarrow \beta\text{-Cu}_2\text{Se}$ $L + \beta\text{-ZnSe} \leftrightarrow \delta'\text{-Cu}_2\text{ZnSnSe}_4$	730 (1003 K)
	Peritectic reaction: $\delta\text{-Cu}_2\text{ZnSnSe}_4 \leftrightarrow \delta'\text{-Cu}_2\text{ZnSnSe}_4 + \beta\text{-Cu}_2\text{Se}$	677 (950 K)
$Cu_2ZnSnSe_4$-(50,0 mol% Cu_2Se; 50,0 mol% ZnSe)	Solidus for nonvariant peritectic. Completed secondary crystallizations of the binaries: $L + \beta\text{-ZnSe} \leftrightarrow \beta\text{-Cu}_2\text{Se}$ $L + \beta\text{-ZnSe} \leftrightarrow \delta\text{-Cu}_2\text{ZnSnSe}_4$	730 (1003 K)
$Cu_2ZnSnSe_4$-$SnSe_2$	Completed secondary crystallizations of: $L \leftrightarrow \gamma\text{-SnSe}_2 + \beta\text{-ZnSe}$ $L + \beta\text{-ZnSe} \leftrightarrow \delta\text{-Cu}_2\text{ZnSnSe}_4$	619 (892 K)
	$\delta\text{-Cu}_2\text{ZnSnSe}_4 \leftrightarrow \delta'\text{-Cu}_2\text{ZnSnSe}_4$ in range < 3,0 mol% $SnSe_2$	583 (856 K)
$Cu_2ZnSnSe_4$-(50,0 mol% ZnSe, 50,0 mol% $SnSe_2$)	Alloy crystallization is complete	619 (892 K)
	$\delta\text{-Cu}_2\text{ZnSnSe}_4 \leftrightarrow \delta'\text{-Cu}_2\text{ZnSnSe}_4$	583 (856 K)

1.8 Summary of the Literature Overview and the Aim of the Study

This thorough review of the literature produced the following findings:

- The motivation to achieve high-efficiency, low-cost solar cells has led to intensive research on new solar cell absorber materials composed of nontoxic, earth-abundant and low-cost components. $Cu_2ZnSnSe_4$ and SnS semiconductor compounds have suitable properties, such as E_g values of 0,95-1,06 and 1,3 eV, respectively, *p*-type conductivity and high absorption coefficients of > 10^4 cm^{-1}. The theoretically calculated and experimentally achieved power conversion efficiencies of solar cells based on CZTSe and SnS are promising.
- The cost of a solar module can be reduced not only with cheaper materials but also by using cheaper technologies. CZTSe technology has been developed from CIGS technology using mainly vacuum production methods. However, the recently developed nonvacuum methods are also efficient. The solar cell efficiency achieved with a tuned band gap CZTSSe material is 13,8 %. Monograin powder technology allows the production of absorber materials in single-crystalline powder form and the use of a monograin layer structure for solar cells in which each individual grain works as a single-crystalline solar cell. The problems met with vacuum technologies, such as grain boundary problems, inhomogeneity of components in thin-film layers, and the volatility of some metal components when vacuum production methods are used, can be avoided with the use of monograin synthesis-growth technology.

- Synthesis and growth *via* monograin powder technology proceed in an environment of molten flux salts. The chemical pathway to the formation of CZTSe compound and the chemical interactions between the used flux salts (CdI_2, NaI, and KI) and precursor compounds (CuSe, ZnSe, and SnSe) have not been studied. It is known that the presence of a liquid phase between solid particles must assure the requirements for monograin growth. The liquid phase should allow repelling forces to arise between solid particles; otherwise, sintering of particles occurs. The chemical processes occurring in mixtures of precursor compounds and flux salts results in low-melting byproducts that could cause sintering of particles, which this is often recognized in real synthesis-growth processes, and these are currently not understood.
- With an increasing number of components in a semiconductor compound, the phase diagrams of these materials become quite complicated, and the synthesis of single-phase absorber materials in the environment of a molten phase of inorganic salts (fluxes) is difficult due to the high probability of forming secondary phases. The chemical pathway for CZTSe compound formation in molten CdI_2 and the chemical interactions of CdI_2 salt with precursors for CZTSe synthesis have not yet been studied.

Therefore, the formation conditions for CZTSe and SnS absorber materials should be established because most reports have been focused on the production of devices, rather than on achieving an understanding of the chemical processes during the material synthesis. Therefore, **the aims of this thesis** were as follows:

To study and describe

a) the formation of CZTSe in monograin powder form from polycrystalline binary compounds (CuSe, ZnSe and SnSe) used as starting materials;

b) the chemical interactions occurring between precursor compounds and flux salts used during synthesis;

c) the processes occurring during the recrystallization of polycrystalline SnS in different molten salts and

d) the possibilities of chemical formation of low-melting compounds that can cause sintering of solid particles and interfere with monograin growth.

To reach the aims, **the following goals of this thesis** were set:

1.1. To investigate the (in)stability of flux salts (KI, NaI, $SnCl_2$ and CdI_2) by MS, TG, DTA, Raman and XRD analysis methods;

1.2. To analyze the purity and homogeneity of the used binary precursor compounds *via* DTA, Raman, XRD, EDX and SEM; to clarify the reasons for different byproduct formation.

1.3. To use different analysis methods, DTA and DSC, to determine the temperatures and thermal effects of the processes occurring in different mixtures; Raman, XRD, SEM and EDS were used to obtain information on the chemical changes in the mixtures. For this reason, a suitable calibration method for enthalpy evaluation *via* DTA and DSC should be developed for testing the thermal behavior in liquid-solid mixtures;

1.4. To evaluate the probability of possible chemical reactions, thermodynamic calculations of Gibbs free energy (ΔG) (using software HSC6 Chemistry Ver. 6.0.) of the different reactions between flux salts (CdI_2, NaI, and KI), the initial binary compounds (CuSe, ZnSe and SnSe) and the expected new compounds were performed and plotted. Additionally, the *ΔG* values for reactions between SnS and flux salts (CdI_2, $SnCl_2$, KI) are presented;

1.5. To determine the solubility of CuSe, ZnSe, SnSe, and CZTSe in fluxes and to determine the solubility of flux salt components (K, Na and I) in CZTSe;

1.6. In the case of using CdI_2 as a flux salt, to study the chemical behavior of CdI_2 and determine the incorporation mechanism of Cd into $Cu_2ZnSnSe_4$ crystals, resulting in the $Cu_2Zn_{1-x}Cd_xSnSe_4$ solid solution as the product of the synthesis-growth process.

2 Experimental

A diagram of the experimental procedures and sample preparation is shown in Figure 2.1. Basically, the methodology includes nine steps. The characterization methods and apparatus will be described separately in Section 2.10. The following methods and apparatus were used: DTA, MS, DSC, ICP-MS, Raman spectroscopy, XRD, EDX, SEM, and XPS.

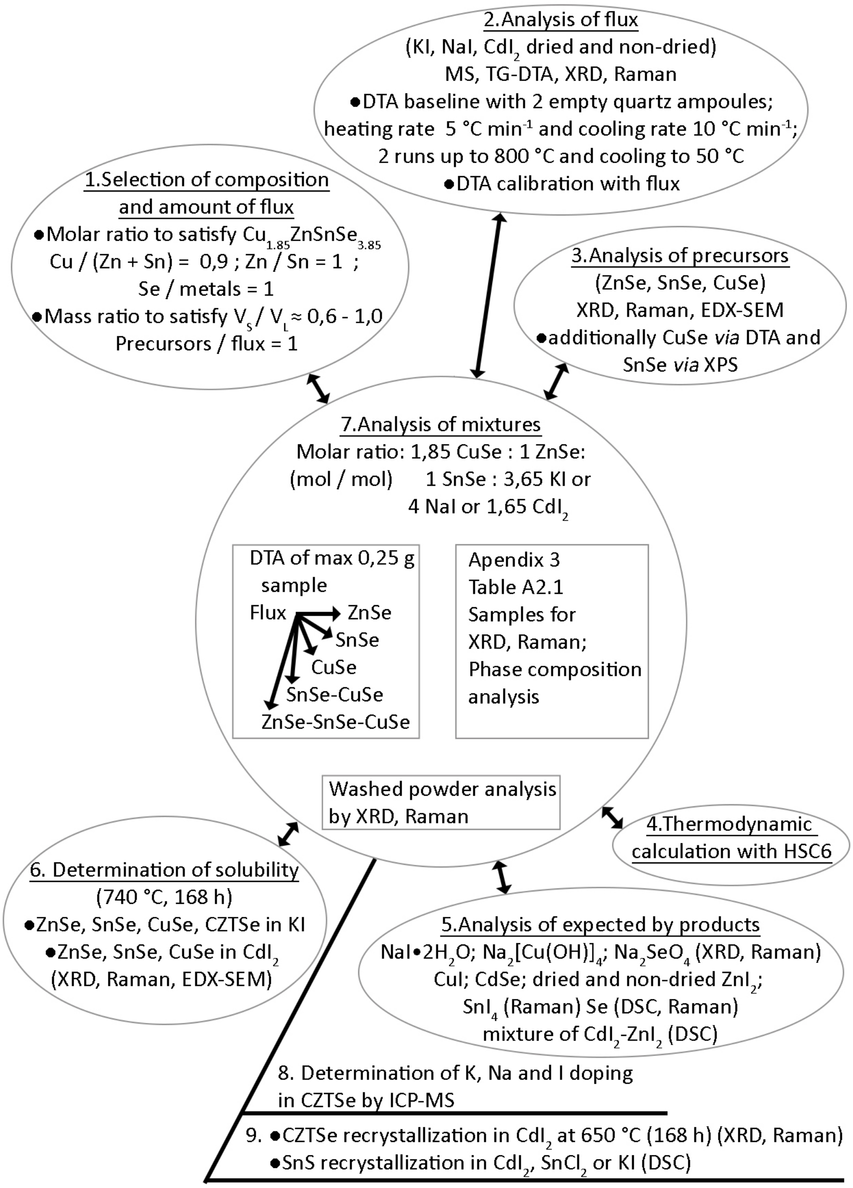

2.Analysis of flux
(KI, NaI, CdI_2 dried and non-dried)
MS, TG-DTA, XRD, Raman
●DTA baseline with 2 empty quartz ampoules; heating rate 5 °C min^{-1} and cooling rate 10 °C min^{-1}; 2 runs up to 800 °C and cooling to 50 °C
●DTA calibration with flux
1.Selection of composition and amount of flux
●Molar ratio to satisfy $Cu_{1.85}ZnSnSe_{3.85}$
Cu / (Zn + Sn) = 0,9 ; Zn / Sn = 1 ;
Se / metals = 1
●Mass ratio to satisfy $V_S / V_L \approx 0,6 - 1,0$
Precursors / flux = 1
3.Analysis of precursors
(ZnSe, SnSe, CuSe)
XRD, Raman, EDX-SEM
●additionally CuSe *via* DTA and SnSe *via* XPS
7.Analysis of mixtures
Molar ratio: 1,85 CuSe : 1 ZnSe:
(mol / mol) 1 SnSe : 3,65 KI or
4 NaI or 1,65 CdI_2
DTA of max 0,25 g sample
Flux
ZnSe
SnSe
CuSe
SnSe-CuSe
ZnSe-SnSe-CuSe
Apendix 3
Table A2.1
Samples for XRD, Raman;
Phase composition analysis
Washed powder analysis by XRD, Raman
4.Thermodynamic calculation with HSC6
6. Determination of solubility
(740 °C, 168 h)
●ZnSe, SnSe, CuSe, CZTSe in KI
●ZnSe, SnSe, CuSe in CdI_2
(XRD, Raman, EDX-SEM)
5.Analysis of expected by products
$NaI \cdot 2H_2O$; $Na_2[Cu(OH)]_4$; Na_2SeO_4 (XRD, Raman)
CuI; CdSe; dried and non-dried ZnI_2;
SnI_4 (Raman) Se (DSC, Raman)
mixture of CdI_2-ZnI_2 (DSC)
8. Determination of K, Na and I doping in CZTSe by ICP-MS
9. ●CZTSe recrystallization in CdI_2 at 650 °C (168 h) (XRD, Raman)
●SnS recrystallization in CdI_2, $SnCl_2$ or KI (DSC)

Figure 2.1 Diagram of the experimental procedure

The first step included the selection of the composition and amount of the flux material. Second, flux analyses by MS, TG-DTA, XRD, and Raman spectroscopy were performed to investigate the instability of the fluxes, as described in the literature review. Then, the baseline for DTA was set, and it was calibrated using the flux materials (KI, NaI and CdI_2). Additionally, in the third step, the purity of the self-synthesized or commercially acquired binary compounds (ZnSe, SnSe and CuSe) *via* XRD, Raman and EDX-SEM were studied. Additionally, CuSe *via* DTA and SnSe *via* XPS were investigated. Fourth, the thermodynamic calculations were performed, and graphs (using software HSC6 Chemistry Ver. 6.0.) were created to minimize the experimental work. The created graphs led to step five. Some of the self-synthesized and commercially purchased expected byproducts were analyzed to record DSC scans and Raman spectra to use as references in further studies. Additionally, in step six, the solubilities of the binary precursors and CZTSe in KI and CdI_2 were investigated. The seventh step involved the mixture preparation process. The fluxes (KI, NaI and CdI_2) were separately mixed with the binary compounds (ZnSe, SnSe and CuSe), and this process was also followed for ternary (CTSe) formation and for quaternary (CZTSe) formation. The molar ratios used were 1,85 mole of CuSe : 1 mole of ZnSe : 1 mole of SnSe : 3,65 mole of KI or 4 mole of NaI or 1,65 mole of CdI_2, to synthesize compound $Cu_{1,85}ZnSnSe_{3,85}$ and sufficient flux material, as described in Section 2.1. DTA was performed using sealed closed ampoules. According to DTA effects, samples at slightly higher temperatures for XRD and Raman analyses that were quenched as so-called "*frozen in*" phases were prepared for the determination of phase composition. The same samples were then washed with water in an ultrasonic bath. More detailed explanation is provided in Section 2.6. The arrows on both sides mean either procedure can be performed first. Step eight included potassium and iodide doping determination *via* ICP-MS for CZTSe synthesized in KI. Finally, step nine was the recrystallization of CZTSe in CdI_2 and SnS as a semiconductor material in CdI_2, $SnCl_2$ or KI.

2.1 Selection of Composition and Calculation of the Amount of Flux Material

The composition of precursor material mixtures was taken into consideration to produce a quaternary compound with a final composition of $Cu_{1,85}ZnSnSe_{3,85}$, which can be characterized by molar ratios of Cu/(Zn + Sn) = 0,9; Zn/Sn = 1 and Se/metals = 1 (Muska *et al.*, as cited in Ito, 2015) to result in a Zn-rich composition. The mass ratio of the binary precursor compounds (CuSe, SnSe and ZnSe) and the flux material (CdI_2 or NaI or KI) was kept at 1 : 1 because the volume of liquid phase should be larger than the volume of solid phase. Then, the ratio of the forming volumes of the solid phase, V_S, to the liquid phase, V_L, should be, according to Mellikov *et al.* (as cited in Ito, 2015), within the range of 0,6-1,0. Because CuSe decomposes to Cu_2Se by releasing Se *via* reaction (2.1) at temperatures above 377 °C or 650 K (Chakrabarti & Laughlin, 1981), for a composition of $Cu_{1,85}ZnSnSe_{3,85}$, the density of Cu_2Se was used to calculate the solid-phase volume while also considering reaction (2.1). The densities used for the calculations are summarized in Table 2.1.

$$1{,}85\ \mathrm{CuSe\ (s)} \leftrightarrow 0{,}925\ \mathrm{Cu_2Se\ (s)} + 0{,}925\ \mathrm{Se\ (l)} \qquad (2.1)$$

Then, at temperatures above 377 °C (650 K), when the melting of the flux material is possible, reaction (2.2) will be expected:

$$0{,}925\ Cu_2Se\ (s) + 0{,}925\ Se\ (l) + 1\ ZnSe\ (s) + 1\ SnSe\ (s) \leftrightarrow Cu_{1{,}85}ZnSnSe_{3{,}85}\ (s, l) \qquad (2.2)$$

According to the equation in (Atkins *et al.*, 2018), the number of moles in reaction (2.2) and equation (2.3) can be calculated. The mass of Cu_2Se is $190{,}6 \cdot 10^{-3}$ kg, the mass of ZnSe is $144{,}4 \cdot 10^{-3}$ kg, and that of SnSe is $197{,}7 \cdot 10^{-3}$ kg.

$$m = n \times M, \qquad (2.3)$$

where m – mass of the compound, kg,
n – moles of the compound, mol,
M – molar mass of the compound, kg mol^{-1}.

The volume of the solid phases can be calculated by using equation (2.4). The densities are provided in Table 2.1. The volume of Cu_2Se is $28{,}0 \cdot 10^{-6}$ m^3, that of ZnSe is $25{,}3 \cdot 10^{-6}$ m^3, and that of SnSe is $31{,}9 \cdot 10^{-6}$ m^3. Then, the total volume of the solid phases is $85{,}2 \cdot 10^{-6}$ m^3.

$$V = \frac{m}{\rho}, \qquad (2.4)$$

where V – volume, m^3,
m – mass, kg,
ρ – density, kg m^{-3}.

Table 2.1 Physical data of the compounds used for sample preparation

Compound and phase	**ρ / 10^{-3} kg m^{-6}**	**M / 10^{-3} kg mol^{-1}**	**Reference**
Cu_2Se (solid)	6,8	206,1	(software HSC6 Chemistry Ver. 6.0.)
ZnSe (solid)	5,7	144,4	
SnSe (solid)	6,2	197,7	
SnS (solid)	5,2	150,8	
Se (liquid)	4,0	79,0	(Linde, 2004)
CdI_2 (liquid)	4,4	366,2	
NaI (liquid)	2,5	149,9	
KI (liquid)	2,7	166,0	
$SnCl_2$ (liquid)	3,4	189,6	

If the mass ratio is 1 : 1, then the mass of the flux material is equal to the sum of the binary masses and it is $606{,}1 \cdot 10^{-3}$ kg. The calculated mass of formed Se from equations (2.2-2.3) is $73{,}1 \cdot 10^{-3}$ kg. The calculated volumes of the fluxes, according to equation (2.4), are $137{,}8 \cdot 10^{-6}$ m^3 for CdI_2, $242{,}4 \cdot 10^{-6}$ m^3 for NaI, and $224{,}5 \cdot 10^{-6}$ m^3 for KI. However, Se participates in liquid phase formation, and from equation (2.4), the expressed volume is $18{,}3 \cdot 10^{-6}$ m^3. The ratio (r) can be calculated using equation (2.5) according to Mellikov *et al.* (as cited in Ito, 2015), and in the case of CdI_2, it is 0,6; for

NaI, it is 0,3; and for KI, it is 0,4. In the case of SnS, according to Table 2.1 and equations (2.4-2.5):

a) $12{,}3\cdot10^{-5}$ kg ($3{,}6\cdot10^{-8}$ m^3) of $SnCl_2$ and $12{,}3\cdot10^{-5}$ kg ($2{,}4\cdot10^{-8}$ m^3) of SnS gave a ratio of 0,7;

b) $12{,}5\cdot10^{-5}$ kg ($4{,}6\cdot10^{-8}$ m^3) of KI and $12{,}5\cdot10^{-3}$ ($2{,}4\cdot10^{-8}$ m^3) of SnS gave a ratio of 0,5;

c) $12{,}5\cdot10^{-5}$ kg ($2{,}8\cdot10^{-8}$ m^3) of CdI_2 and $12{,}5\cdot10^{-5}$ kg ($2{,}4\cdot10^{-8}$ m^3) of SnS gave a ratio of 0,9.

$$r = \frac{V_S}{V_L}\ , \tag{2.5}$$

where r – ratio,

V_S – volume of solid phases, m^3,

V_L – volume of liquid phases, m^3.

2.2 Analysis of Flux Salts (KI, NaI and CdI_2) and DTA Calibration

The flux materials used for sample preparation were KI and NaI from *MERCK* (pro analysis with a purity of 99,5 %) and CdI_2 from *Fluka* with a purity of 99,0 %. The NaI was analyzed by a Bruker XRD set-up, whereas KI and CdI_2 were analyzed by a Rigaku XRD set-up. Raman spectra of nondried fluxes were recorded to determine the instability of the fluxes. The dehydration process was applied to KI and NaI. They were dehydrated in vacuum at 70 °C (343 K) for 2 h; then, the temperature was increased to 370 °C (643 K), and they were dehydrated for 4 h. After drying, the ampoules were filled with N_2 and sealed by Dr. J. Raudoja. The impact of drying was investigated with examination of the dried and nondried flux materials using MS and TG-DTA curves, which recorded from room temperature to 400 °C (673 K) for 10,3 mg of NaI and 97,1 mg of CdI_2 and to 500 °C (773 K) for $579{,}8\cdot10^{-1}$ mg KI at a heating rate of 5 °C (K) min^{-1}.

The baseline for DTA was recorded using 2 empty quartz ampoules as crucibles with experimental conditions that included heating/cooling rates of 5 °C (K) and 10 °C (K) min^{-1} up to 800 °C (1073 K) followed by cooling to 300 °C (573 K) or 50 °C (323 K) for 2 runs.

To estimate the enthalpy values, DTA calibration was needed. Calibration with the available standards for the DTA setup in the vacuum ampoules failed because the results were not reproducible and did not correlate with the available standards, probably due to the chemically active behavior of the ampoule material with the standard materials. The purified (dried) flux material was used as the standard for the calibration. Additionally, the properties of the purified flux materials are nearest to those of the sample because it contains 50,0 wt% flux material. The melting point of the flux material was within the same temperature region where most of the thermal effects were detected in the investigated samples. The values of the heat of fusion that were used were as follows: 20,7 kJ mol^{-1} (for CdI_2), 23,7 kJ mol^{-1} (for NaI) and 24,0 kJ mol^{-1} (for KI) (from software HSC6 Chemistry Ver. 6.0.). These values can be expressed according to reaction (2.3) as 56,5 J g^{-1} (for CdI_2), 158,1 J g^{-1} (for NaI) and 144,6 J g^{-1} (for KI). The peak positions at the top of the peaks and the peak areas in the DTA curves were determined and used for analyses. The DTA setup allowed estimation of the enthalpy values with errors of 10,0 %; however, the systematic errors from experiments were smaller. The calibrations were performed in evacuated quartz ampoules to obtain a transformation constant for closed system to be able use the data from the open system provided in the literature. The quartz ampoules were designed with a cylindrical base (Figure 2.2) and fitted to a thermocouple to increase the contact with the thermocouple for precise measurements for the enthalpy evaluation. For DTA, 125,0 mg of flux material was analyzed. To weigh the materials, a Mettler Toledo Xp5003S balance with a precision of $0{,}1\cdot10^{-7}$ kg was used.

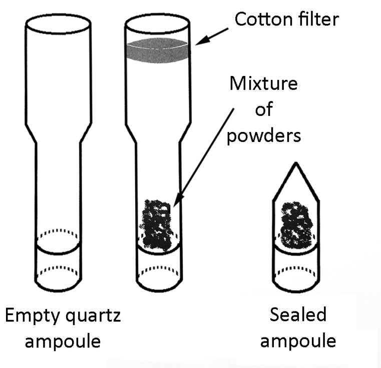

Figure 2.2 Design of the DTA ampoule

2.3 Analysis of Binary Precursors (ZnSe, SnSe and CuSe)

The CuSe and SnSe precursors were self-synthesized from metal shots (purity of 99,8 %) and Se shots (4N purity from the *Aldrich* company) by heating in vacuum quartz ampoules at 650 °C (923 K) and 700 °C (973 K), respectively, for 35 h. The polycrystalline ZnSe (grown using the chemical vapor deposition process) was purchased from *Crystaltechno Ltd*. The precursor compounds were analyzed by XRD, Raman spectroscopy and EDX-SEM. XPS measurements were performed by Dr. M. Danilson on SnSe to investigate the oxygen bonds on its surface. The phase transformations of 55,2 mg of CuSe (synthesized with an atomic ratio of Cu-Se equal to 1 : 0,9936) in a degassed sealed quartz ampoule were investigated with a DTA setup.

2.4 Thermodynamic Calculations with the HSC6 Chemistry Software

To eliminate part of the experimental work, calculations using a thermodynamic database (software HSC6 Chemistry Ver. 6.0.) were performed. Additionally, the expected byproducts could be observed from the created graphs and from the estimated ΔG values for the reactions. The applied temperature step for the calculations was 1 °C (K). It was possible to simulate flux-ZnSe, flux-SnSe, and flux-CuSe mixtures and some binary byproduct systems. SnS_2 was also investigated to show the stability of CZTSe compared with that of CZTS. The thermodynamic calculations will be discussed together with the experimental results for the mixtures.

2.5 Analysis of the By-Products

NaI was left to hydrolyze in air for 1 week, and *via* XRD analysis, the formation of $NaI \cdot 2H_2O$ was confirmed. Then, the Raman reference spectra of $NaI \cdot 2H_2O$ + NaI were recorded several times. Since the Raman data of the compounds $Na_2[Cu(OH)]_4$ and Na_2SeO_4 could not be found in the literature, they were self-synthesized. The $Na_2[Cu(OH)]_4$ compound was synthesized as described by Brauer (1963), and Na_2SeO_4 *via* stoichiometric oxidation of SeO_2 with H_2O_2 upon mixing with NaOH in a glove box under nitrogen atmosphere. The synthesized crystals were confirmed by XRD, and the reference Raman spectra were recorded.

CuI was self-synthesized according to room temperature reaction (2.6), which was found in the database (software HSC6 Chemistry Ver. 6.0.):

$$2\ CuSO_4\ (aq) + 4\ NaI\ (aq) \rightarrow 2\ CuI\ (s) + I_2\ (s) + 2\ Na_2SO_4\ (aq) \tag{2.6}$$

Then, $15{,}9 \cdot 10^{-4}$ kg of $CuSO_4$ and $29{,}9 \cdot 10^{-4}$ kg of dehydrated NaI were diluted with distilled water. The solution became brown, and white deposits were observed on the bottom of the flask. The brown water was poured off, and pure distilled water was added again 5 times until the solution became white, increasing the CuI formation. The solution was left to dry and crystallize at room temperature for 24 h. XRD confirmed the CuI phase, whereas EDX showed that some I_2 was present. The reference Raman spectra of α-, β-, and γ- modifications of CuI were experimentally measured. The quenching of CuI was performed after heating for 4 h at temperatures of 400 °C (673 K), 500 °C (773 K) and 700 °C (973 K) to ensure that the phase transformation of CuI from low-temperature to the high-temperature phase occurred.

According to the calculations performed using the database (software HSC6 Chemistry Ver. 6.0.), Se, ZnI_2, the CdI_2-ZnI_2 mixture, CdSe and SnI_4 could be formed in these experiments. To clarify the behavior of elemental Se in closed vacuum ampoules, the thermal heating curve of 40,0 mg of commercial Se (described above in Section 2.3) from room temperature to 600 °C (873 K) in DSC mode was studied. Then, 10,0 % error bars were used for all DSC measurements. The heating rate was 5 °C (K) min^{-1}, and the baseline was recorded with 2 empty quartz ampoules as an analogy for the needed experiments. The DSC setup was calibrated with available standard metals (In, Sn, Bi, Zn, Al, and Au) in closed ampoules. The Raman analysis of Se was performed. Commercial ZnI_2 (*Alfa Aesar*, with a purity of 98,0 %) was dried by vacuum heating and investigated using Raman spectroscopy (dried and nondried) to obtain the reference spectra. In nondried ZnI_2, the presence of $ZnCO_3$ was assumed. To understand the formation and melting of the CdI_2-ZnI_2 mixture, a DSC scan (under the same experimental conditions as for Se) for the CdI_2-ZnI_2 mixture with a molar ratio of 1 : 1 was performed. A mixture of 50,0 mg CdI_2 and 40,0 mg ZnI_2 was prepared in a glove box in an inert gas atmosphere and sealed in a quartz ampoule. The onset point and top peak temperatures will be discussed in the DSC results.

Commercial CdSe (extra high purity from *Crystaltechno Ltd*, synthesized *via* chemical vapor deposition) and SnI_4 (self-synthesized by the iodine transport method) were analyzed *via* Raman spectroscopy.

2.6 Determination of the Solubility of the Precursors and CZTSe in KI and CdI_2

The solubility was studied *via* the mass loss method. Solubility data for KI were provided by Dr. Kristi Timmo; however, for CdI_2, it was measured by myself. Single crystals of ZnSe, CuSe and SnSe were heated in separate ampoules in an excess amount of KI or CdI_2 for 1 week (168 h) at 740 °C (1013 K). After heating and opening the ampoules, the flux was removed by washing with DI (deionized) water. The solid part that stayed undissolved in the molten flux was collected on a 30 μm filter and weighted. The dissolved part in the molten flux formed colloidal particles in water that passed through the filter. The formed solid phases were separated from the soluble part of the flux material by washing several times (7-10) with DI water using an ultrasonic bath for agitation. The mass difference between the initial and final weight of the crystals was determined to be the dissolved part of the compound. Single crystals of $25{,}2\cdot10^{-4}$ mol of ZnSe in $154{,}2\cdot10^{-4}$ mol KI (molar ratio of 1 : 6,1), $35{,}3\cdot10^{-4}$ mol of CuSe in $191{,}0\cdot10^{-4}$ mol KI (molar ratio of 1 : 5,4), and $25{,}3\cdot10^{-4}$ mol of SnSe in $195{,}8\cdot10^{-4}$ mol KI (molar ratio of 1 : 7,7) were used for the solubility experiments. The mass loss method was also used to determine the solubility of CZTSe in KI. Thus, $4{,}0\cdot10^{-2}$ mol of CZTSe (molar mass for $Cu_{1,85}ZnSnSe_{3,85}$ used in the calculations was 605,7 g mol^{-1}) was dissolved in $35{,}3\cdot10^{-4}$ mol of KI (molar ratio of 1 : 8,8).

Ultra-highpurity single-crystal pieces of CuSe, SnSe, and ZnSe were heated to 740 °C (1013 K) for 168 h in CdI_2. The following amounts of the compounds were used: $39{,}3\cdot10^{-4}$ mol of single-crystal ZnSe in $94{,}3\cdot10^{-4}$ mol of CdI_2 (molar ratio of 1 : 2,4); $11{,}6\cdot10^{-4}$ mol of single-crystal SnSe in $37{,}6\cdot10^{-4}$ mol of CdI_2 (molar ratio of 1 : 3,2); and $36{,}3\cdot10^{-4}$ mol of single-crystal CuSe in $85{,}1\cdot10^{-4}$ mol of CdI_2 (molar ratio of 1 : 2,3). After separation of the soluble phases, the morphologies and exact compositions of the insoluble phases were investigated *via* SEM and EDX analyses. The fraction dissolved in water was dried by evaporation and then analyzed by SEM-EDX. Additionally, for the washed sample of CdI_2-ZnSe, XRD using the Rigaku setup and Raman analyses were performed. However, it was impossible to determine the solubility in CdI_2 because of the increase in the mass of the samples during chemical interaction; however, experimental knowledge based on the results was used for explanations of reactions in the flux-precursor mixtures.

The solubilities of precursors in NaI were not determined since the behavior is likely similar as in KI.

2.7 Analysis of Mixtures

Due to the small dimensions of the ampoules used for DTA (the design of the ampoule can be found in Figure 2.2) and possible emission of gases, for safety reasons, it was decided not to insert more than $2{,}5\cdot10^{-4}$ kg of sample of the flux-ZnSe-SnSe-CuSe mixture in an ampoule for the DTA experiments. Therefore, smaller amounts of flux-binary mixtures were used. The sample combinations were determined based on molar proportions to be 1,85 mole of CuSe : 1 mole of ZnSe : 1 mole of SnSe : 3,65 mole of KI or 4 mole of NaI or 1,65 mole of CdI_2. The mass and number of moles of the compounds used in the mixtures are provided in Table 2.2. To provide a homogeneous distribution of components, 10 times more was used for making the mixtures. The powder samples were ground in a planetary ball mill; then, the mixtures were degassed at 270 °C (543 K) (at 100 °C (373 K) in case of CdI_2) for approximately 2 h and sealed into quartz ampoules. All preparation work with the samples containing NaI was performed in a glove box in a N_2 atmosphere.

Table 2.2 Concentrations of precursors and flux materials used for DTA experiments

Compound	**m / 10^{-3} kg**	**n / mol**
ZnSe	$297{,}9 \cdot 10^{-4}$	$206{,}4 \cdot 10^{-6}$
SnSe	$40{,}8 \cdot 10^{-3}$	$206{,}4 \cdot 10^{-6}$
CuSe	$54{,}4 \cdot 10^{-3}$	$381{,}7 \cdot 10^{-6}$
KI	$125{,}0 \cdot 10^{-3}$	$753{,}3 \cdot 10^{-6}$
NaI	$125{,}0 \cdot 10^{-3}$	$833{,}9 \cdot 10^{-6}$
CdI_2	$125{,}0 \cdot 10^{-3}$	$341{,}3 \cdot 10^{-6}$

Because of the thermal effects found in the DTA curves, samples of identical mixtures were prepared for Raman and XRD studies with a mass of approximately 2,0 g total split among the needed samples according to the DTA curves. The samples were kept for prolonged periods (1 h or more) at slightly higher temperatures than the thermal effects observed in the DTA curves and then quenched in water. One hour is enough reaction time to observe the formed phases in the DTA curve, where the heating rate is 5 °C (K) min^{-1}. However, not all samples produced differences in their phases in comparison with the previous sample. In that case, the thermal effect was attributed to some phase changes or other physical processes. Only the samples in which different phases from the previous one were found will be discussed. The discussed samples are summarized in Appendix 3 (Table A2.1). The Rigaku XRD instrument was used for CdI_2-ZnSe samples heated to 740 °C (1013 K), for CdI_2-CuSe heated to 400 °C (673 K) and 740 °C (1013 K), and for CdI_2-ZnSe-SnSe-CuSe heated to 370 °C (643 K), 400 °C (673 K), 590 °C (863 K) and 740 °C (1013 K), whereas for other XRD investigations, the Bruker XRD instrument was used. Mixtures of KI-ZnSe, NaI-ZnSe and NaI-SnSe are not presented in Appendix 3, Table A2.1 since no new compounds in these mixtures were found.

After Raman and XRD analyses of the nonwashed samples, for the flux-ZnSe-SnSe-CuSe sample mixtures, the formed solid phases in the samples were separated from the soluble flux material by washing with DI water several times (7-10) using an ultrasonic bath for agitation until the washing water became transparent. The separation of flux material and other water-soluble phases provided clearer Raman spectra and XRD patterns of phases, which were nonsoluble in water (byproducts and CZTSe). Additionally, the surface morphology and elemental composition of the samples were investigated by SEM-EDX. The binary and ternary mixtures will not always be discussed in the context of the washed samples, since the binaries often formed in water-soluble phases and because, often, there were no differences observed for the ternary samples compared with those that were not washed.

2.8 Doping Determination in CZTSe

The concentrations of dissolved potassium and iodine in CZTSe were determined by the ICP-MS method. The doping level is important for solar cell performance. At low concentrations, doping is recommendable; however, at high concentrations, it will disturb the current flow.

2.9 Procedure for CZTSe and SnS Recrystallization

For the recrystallization investigations, a DSC setup was used. The baselines were experimentally recorded according to the experimental conditions using 2 empty quartz ampoules. Two heating/cooling cycles were recorded from room temperature to 900 °C (1173 K) (for CZTSe recrystallization in CdI_2) and to 800 °C (1073 K) (for SnS recrystallization). A heating rate of 5 degrees was used; then, isothermal heating segments with holding for 5 min at 800 °C (1073 K) and cooling to 55 °C (328 K) at a cooling rate of 10 °C (K) min^{-1} were applied. This was followed by an additional quasi-isothermal slow cooling at the rate of 0,15 °C (K) in segments of 55-45 °C (328-318 K). A set of standard metals (In, Sn, Bi, Zn, Al, and Au) in closed ampoules was used for calibration as described above. Experimental data from the salt fluxes (KI, CdI_2, and $SnCl_2$) were additionally used for calibration constant modulation. The maximum temperatures will be discussed.

The CZTSe (synthesized in KI) used had a composition of $Cu_{1,69}Zn_{1,07}SnSe_{3,62}$, as determined by EDX. To investigate the recrystallization of CZTSe in CdI_2, DSC curves for 30,0 mg of CZTSe and a mixture of 27,0 mg of CZTSe with 64,0 mg CdI_2 (with a molar ratio of 1 : 5) in the temperature range of room temperature to 900 °C (1173 K) were recorded. Additionally, XRD and Raman measurements were performed on a washed sample that was annealed at 650 °C (923 K) for 168 h.

SnS was self-synthesized from 3N purity Sn shots and elemental S in evacuated quartz ampoules. The precursors used for synthesis were slowly heated to 700 °C (973 K) for 500 h, annealed for 42 h and cooled to room temperature. The synthesized polycrystalline SnS was ground in an agate mortar before use in the powder recrystallization and growth process. Before investigations, SnS was analyzed by DTA in a temperature range from room temperature to 800 °C (1073 K) at a heating rate of 5 °C (K) min^{-1} *via* DCS and after *via* SEM-EDX. KI, CdI_2 (as described above) and anhydrous $SnCl_2$ (*Alfa Aesar*, purity 99,0 %) were used as the flux materials. Before use in the mixtures, the flux materials were analyzed separately by DSC. KI was dehydrated up to 270 °C (543 K). A separate flux of 72,0 mg ($3{,}8 \cdot 10^{-4}$ mol) of $SnCl_2$ in a N_2 atmosphere (glow-box) was inserted into a quartz ampoule and degassed for 3 h at 150 °C (423 K) to purify from any $SnCl_4$ because its boiling point is at 114 °C (387 K) (according to the database, software HSC6 Chemistry Ver. 6.0.); any $SnCl_2 \cdot 2H_2O$ decomposed since reaction (2.7) occurs at 130-135 °C (403-408 K):

$$SnCl_2 \cdot 2\,H_2O\,(l) \rightarrow SnCl_2\,(s) + 2\,H_2O\,(g) \qquad (2.7)$$

For comparison, the pure KI, CdI_2 and $SnCl_2$ melting and solidification effects were also determined. In total, three ampoules of flux-SnS were prepared: $SnCl_2$-SnS, KI-SnS, CdI_2-SnS. The following amounts in the samples were used: 123,0 mg ($6{,}5 \cdot 10^{-4}$ mol) of $SnCl_2$ and 123,0 mg ($8{,}2 \cdot 10^{-4}$ mol) of SnS in a molar ratio of 1 : 1,3; 125,0 mg ($75{,}3 \cdot 10^{-5}$ mol) of KI and 125,0 mg ($8{,}3 \cdot 10^{-4}$ mol) of SnS in a molar ratio of 1 : 1,1; 125,0 mg ($3{,}4 \cdot 10^{-4}$ mol) of CdI_2 and 125,0 mg ($8{,}3 \cdot 10^{-4}$ mol) of SnS in a molar ratio of 1 : 2,4. The mixtures were inserted into quartz ampoules, degassed under dynamic vacuum at 270 °C (543 K) for 2 h and sealed. The volume ratios of solid SnS and liquid flux materials were described in Section 2.1. The densities are provided in Table 2.1.

2.10 Characterization Methods

This section is divided into items in which each characterization method is described. In total, nine different methods and setups were used.

2.10.1 Differential Thermal Analysis (DTA)

DTA is used to record temperature differences between a sample and reference at experimental heating or cooling rates. This difference is measured with a thermocouple as voltage in μV. A thermocouple is an electrical device consisting of two dissimilar electrical conductors. These conductors form electrical junctions at different temperatures. A thermocouple produces a temperature-dependent voltage as a result of the thermoelectric effect, and this voltage can be interpreted to measure temperature. Under open-circuit conditions, the gradient of voltage (ΔV) is directly proportional to the gradient of temperature (ΔT), as shown by equation (2.8):

$$\Delta T = \frac{\Delta V}{-S(T)}, \tag{2.8}$$

where $S(T)$ is the temperature-dependent material property used in the thermocouple to induce the thermoelectric voltage, called Seebeck's coefficient, when simple characteristic functions of thermocouples exists, μV K^{-1},

ΔV – gradient of voltage, V, and
ΔT – gradient of temperature, K.

Then, the differential heat flow to the sample and reference is measured by the area of the thermocouple, according to Ohm's Law (2.9):

$$Q_S = \frac{\Delta T}{R}, \tag{2.9}$$

where Q_S – heat flow of the sample, W,
ΔT – temperature difference between the sample and reference, °C or K, and
R_D – resistance of the thermoelectric disk, K W^{-1}.

Exothermic or endothermic changes in the sample provide data on the physical and chemical changes (phase transitions, crystallization, melting, *etc.*) (Wagner, 2017). For both DTA and heat-flux DSC, the primary measuring signal during a measurement is the temperature difference between a sample and reference in μV (thermal voltage). This temperature difference can be converted to a heat-flux difference in mW or mJs^{-1} by means of an appropriate calibration. Conversion of μV to mW or mJs^{-1} can be achieved using a calibration constant (K) in μV·(mW)$^{-1}$ or μV·(mJs^{-1})$^{-1}$ (2.10):

$$K = \frac{S}{H}\frac{1}{m}, \tag{2.10}$$

where K – calibration constant, μV·(mW)$^{-1}$ or μV·(mJs^{-1})$^{-1}$,
H – heat of fusion of flux, used for calibration, J·g^{-1},
m – mass of the flux, $12{,}5 \cdot 10^{-2}$ g,
S – area of the peak, produced by flux, μVs,
A – any unknown peak area, μVs.

The heat flow, Q, can be calculated according to 2.11:

$$Q = \frac{A}{K}, \tag{2.11}$$

where Q – heat flow, J,
A – any unknown peak area, μVs,
K – calibration constant, $\mu V\cdot(mW)^{-1}$ or $\mu V\cdot(mJs^{-1})^{-1}$.

Since a DTA construction enables heat transfer by a purge gas and irradiation, quantitative measurements over 200 °C (473 K) can also be performed at a high accuracy when the construction of the DSC enables heat transfer *via* conduction and contact with the thermocouple. For the DTA measurements, closed ampoules were better fitted (Figure 2.2) since there were problems in designing a completely flat surface for the bottom of the ampoule to fit it into the DSC thermocouple and inserting into a crucible will cause losses from the heat-transfer process. Quantitative measurements with DTA were as good as those with DSC if a careful calibration was performed; therefore, calibration must be performed under conditions that are as close as possible to those of the experiment. DTA setups (Thermogravimetric Analyzer Labsys 1600, Setaram Instrumentation, Caluire, France) were used.

The accuracy in percent can be calculated according to (2.12):

$$\% = \frac{A_{max} - A_{min}}{A_{min}} \times 100\,\%, \tag{2.12}$$

where A_{max} – largest measured unknown peak area, μVs,
A_{min} – smallest measured unknown peak area, μVs.

2.10.2 Mass Spectrometry (MS)

A thermoanalyzer connected to a mass spectrometer (MS) OMNI^{Star} (producer Pfeiffer Vacuum, Germany) provides the opportunity to analyze the emitted gases from the sample during heating and the mass loss by TG read outs of the TG curves (Gross, 2017), which was used for NaI and CdI_2. For KI analysis, the NETZSCH QMS 403 *Aeolos* instrument was used.

2.10.3 Differential Scanning Calorimetry (DSC)

The DSC working principle is similar to that for DTA. The term DSC is used to describe an instrument that measures energy directly and allows precise measurements of heat capacity (Woods & Chavez, 2018). There are two types of DSC: Heat-flux (HF) DSC and power-compensating (true) DSC. Power-compensating DSC has two heaters. The differential signal is then the power difference required to keep the temperatures of the sample and reference identical during the defined temperature ramp. The signal is then in watts per unit of sample mass. In heat flux DSC, the difference from DTA is that in addition to using a connecting metal strip, the entire surface of the "*plate*" where the crucible can be placed can work as the detector. The heat flux DSC of the NETZSCH STA 449 F3 (Germany) setup was used for this study.

2.10.4 Inductively Coupled Plasma Mass Spectrometry (ICP-MS)

In ICP-MS, atoms are ionized into ions using a high-energy plasma. An electric and magnetic field separates the ions. The mass-to-charge ratio of the charged particles is measured. As the same mass-to-charge ratio can be focused with different speeds at the same point, ions with different mass-to-charge ratios focused on different points can be recorded as a mass spectrum. From the mass spectrum, the mass loss can be determined. Once the accurate mass of the ions is detected, the composition of ions can be presented (Thomas, 2013). The ICP-MS analyses were performed at the *AS Tallinna Vesi* company.

2.10.5 Raman Spectroscopy

Raman spectroscopy can be used for compositional and crystal structure investigations of prepared samples. Basically, the inelastic scattering of light by the medium leads to a change in the frequency of the incident light. The information provided by Raman spectroscopy based on the depth of the sample depends on the absorption coefficient of the material and on the chosen laser wavelength (Larkin, 2018). Using an objective (type Olympus), it is possible to vary the spot size from 10 times to 100 times, and the light intensity on the sample can be changed by 6 neutral filters. Room temperature Raman spectra were recorded using a Horiba's LabRam HR800 high-resolution spectrometer (France) equipped with a multichannel CCD (charge-coupled device) detection system in backscattering configuration. Micro-Raman measurements were performed using 532 nm incident laser light that was focused on a 1 μm spot of the studied sample. To obtain correct results, at least 5 Raman spectra were taken from different spots on every sample. Raman shifts used for the interpretation are provided in Appendix 3, Table A2.2.

2.10.6 X-ray Diffraction (XRD)

XRD is used to acquire crystalline structural and compositional information of a sample. X-ray beams are focused on the sample surface, and a detector collects the diffracted X-rays. Due to the short wavelength of X-rays, it is possible to see a diffraction pattern that arises from X-rays that are diffracted at atom planes in the lattice. The spacing between the layers will determine the reflection angle (2 θ) of the beam. XRD is a method used for material structure analysis to detect the space distribution of a material's internal atoms by utilizing the X-ray diffraction of the crystal. The diffraction follows Bragg's law (2.13):

$$\chi\lambda = 2\,d\sin\theta \tag{2.13}$$

where χ – integer,

λ – wavelength of the incident X-ray beam, nm,

d – distance between atomic layers, nm,

θ – certain incidence angles, degree.

The wavelength can be measured by knowing the X-ray diffraction angle, and the distance between atomic layers can be calculated. According to the X-ray diffraction intensity and comparison with a reference, quantitative analysis can be performed (Lee, 2016). XRD measurements were performed using a Bruker D5005 AXS diffractometer (Bragg-Brentano geometry) with Cu Kα1 radiation for λ = 1,5406 Å (10^{-10} m) at 40 kV, 40 mA and a graphite monochromator (Karlsruhe, Germany) with the ICDD

PDF-4+2016 database or using a Rigaku PDXL Ultima IV apparatus with a D/teX Ultra line detector with the JCDPS-2009 databases for phase detection. The ICDD and JCDPS file numbers are named on the figures and are provided in Appendix 3, Table A2.3.

2.10.7 Energy-Dispersive X-ray Spectroscopy (EDX)

EDX is an analytical technique that provides elemental compositions. Each element has a unique atomic structure and scatters the X-rays in a unique way. The emissions are a result of interactions with a high-energy beam of electron, protons or X-rays. The beam is focused on the sample. A ground-state electron in the atoms of the sample is excited and ejected, leaving an electron hole in its place. Another electron with a higher energy fills the hole and releases the energy difference in the form of X-rays (Goldstein, 2018). The number and energy of the X-rays emitted from the samples were measured *via* Röntec EDX XFlash energy-dispersive spectrometers equipped with a 3001 detector and Hitachi 1000.

2.10.8 Scanning Electron Microscopy (SEM)

In SEM, a very closely focused electron beam scans across the surface, and a detector detects secondary electrons that are scattered out of the material. The detector counts the electrons emitted from a specific point. Counting allows the formation of an image of the scanned area. The incident electrons have very short wavelengths, allowing a resolution of 5 nm. The scattered secondary electrons are collected by an appropriate detector, where they are transformed into a light signal and further into electric signals by a photomultiplier tube and amplifier to control the electron beam intensity on the screen, showing the surface structure of the sample (Goldstein, 2018). Zeiss HR SEM ULTRA 55 and Hitachi 1000 microscopes were used for these investigations.

2.10.9 X-ray Photoelectron Spectroscopy (XPS)

XPS is a surface sensitive method. The elemental composition in parts per thousand, chemical state and electronic state are measured. The measurements are performed from the top to a 10 nm depth in high vacuum conditions ($P \sim 10^{-8}$) (Sardela, 2014). In this work, SnSe was bombarded with an Ar ion beam in the analysis chamber of the XPS in a Kratos Analytical AXIS ULTRA DLD spectrometer fitted with a monochromatic Al Kα X-rays source and an achromatic Mg Kα/Al Kα dual anode X-ray source. XPS analysis was performed at depths of 0, 1 and 2 nm. SnSe was bombarded with an Ar ion beam in the analysis chamber of the XPS system at an etching speed of 4 nm min^{-1}.

3 Results and Discussion

In this chapter, the results of the analyses of the flux materials, binary precursors, expected byproducts and flux-binary precursor mixtures are discussed. The data for the determined solubilities and doping and recrystallization processes will also be discussed. These results are published in **Papers I-VI**. The results were gathered and are presented based on the idea of reducing the synthesis temperature and are described in decreasing sequence starting from the flux with the highest melting temperature (KI) to (NaI) and ending with the flux with the lowest melting temperature (CdI_2).

3.1 Results of Flux Analyses

In this study, in some cases, iodine was needed to explain the formation of some intermediate compounds, as determined experimentally. One possibility for having free I_2 in the studied systems is due to the instability of the flux iodides. Data on the stabilities of KI, NaI and CdI_2, as published in the literature, are provided in Section 1.6.

The stability issue of KI was discussed in **Papers I and II** and in another report (Leinemann *et al.*, 2011). It was mentioned in **Paper I** that the release of I_2 from KI can originate from its production process from I_2 and KOH, where I_2 can adsorb on the KI surface (theoretically) or be formed in reaction (1.33) as described in Item 1.6.3. The probability of reaction (1.33) is rather low in closed ampoules, whereas it is possible during the storage of KI and during the sample preparation process when the ampoules are opened for XRD and Raman analysis. For reaction (1.33), the ΔG at room temperature (23 °C or 296 K) is -7,6 kJ. However, nondried KI does not show any changes in the TG curve (not presented). Additionally, XRD confirmed that the material does not include any detectable concentrations of impurities. The Raman peaks, published in (Leinemann *et al.*, 2011), were at 90, 95, 102, and 106 cm^{-1}, and the Table A2.2 (Appendix 3) summarizes the values compared with those found in another study (Krishnamurthu & Krishnan, 1965) in which the Raman peaks were at different positions.

The dehydration of NaI was studied and was published in **Paper III** and in Leinemann *et al.* (2011). The TG curves of nondried and dried NaI are different (see Figure 3.1 (a)). In the TG curve of nondried initial NaI, there is a mass loss starting at the on-set point of 35 °C (308 K) with a maximum peak at 51 °C (324 K) until the off-set point at 69 °C (342 K). Analyses by MS confirmed that this mass loss is caused by H_2O loss. This phenomenon implies the presence of sodium iodide crystal hydrate. According to Sofronov *et al.* (2009), $NaI\cdot 2H_2O$ exists in the temperature range of -13,5 to 68 °C (259,5 to 341 K) and decomposes by melting to release H_2O molecules. The calculated mass loss according to the peak area is $20,6\cdot 10^{-2}$ mg, which can be expressed as 2,0 % (according to equation A2.4 in Appendix 2). The XRD spectrum of the investigated nondried NaI mostly consists of $NaI\cdot 2H_2O$ peaks. In addition to cubic NaI (*Fm-3m* (225) a = 6,47 Å or 10^{-10} m), triclinic $NaI\cdot 2H_2O$ (*P-1(2)* a = 7,146 and b = 7,169, c = 6,029 Å or 10^{-10} m) was detected. Corresponding Raman peaks of NaI + $NaI\cdot 2H_2O$ were found experimentally at 82, 90, 95, 99, 107, 115, 122, 135, 138, 150, 187, 194, 222, 230, 244, 323, 353 and 419 cm^{-1} and are published in **Paper III**. Raman peaks for dried NaI were at 95, 107, 122, 160, 167, 187, as published in Leinemann *et al.* (2011); however, compared to the results in Krishnamurthu and Krishnan (1965), the positions are different (Appendix 3, Table A2.2). Dried NaI did not release H_2O molecules during TG analyses, Figure 3.1. (a), and this is evidence that the applied dehydration process was suitable. According to another study (Sofronov *et al.*, 2009), $NaI{\cdot}2H_2O$ reacts with carbon dioxide and not only with oxygen in the gas phase during heating. They proposed that heating of $NaI{\cdot}2H_2O$ in a mixture of carbon dioxide and oxygen should lead to the formation of sodium carbonate; however, no sodium carbonate in this study in NaI was found, probably due to low concentration of CO_2 in air.

CdI_2 was discussed in **Paper IV**, whereas the first studies were reported in Klavina *et al.* (2010). During TG analyses, CdI_2 (Figure 3.1 (b)) already lost some mass at the experimental starting temperature (29 °C or 302 K) until the end of the experiment at 309 °C (582 K). The loss of mass was measured to be $20{,}6{\cdot}10^{-2}$ mg and expressed as 0,2 % of the initial mass. However, no H_2O emission was detected by MS. Then, considerations similar to NaI were performed. First, if the salt (flux) is processed at room temperature in air, its reactions with the gaseous substances present in air (O_2, H_2O, NO_2, SO_2, CO_2) should be considered. Computations performed using the database (software HSC6 Chemistry Ver. 6.0.) revealed that the ΔG value of reaction (3.1) was negative: ΔG was -56,4 kJ mol^{-1} at 23 °C (296 K), as shown in Figure 3.2. CdI_2 does not directly react with water vapor, and the direct formation of $Cd(OH)_2$ is not possible (*i.e.*, the ΔG value is positive). However, $Cd(OH)_2$ can be produced by reaction (3.2) from CdO, which is formed in reaction (3.1). The ΔG at room temperature for reaction (3.2) is -15,8 kJ mol^{-1} (software HSC6 Chemistry Ver. 6.0.). CdO does not react with NO_2 (the ΔG value is positive); however, it can react with SO_2 and CO_2 (software HSC6 Chemistry Ver. 6.0.). Of note, the concentrations of SO_2 and CO_2 in air are relatively low.

$$2\ CdI_2\ (s) + O_2\ (g) \rightarrow 2\ CdO\ (s) + 2\ I_2\ (s) \qquad (3.1)$$

$$CdO\ (s) + H_2O\ (g) \leftrightarrow Cd(OH)_2\ (s) \qquad (3.2)$$

This consideration has not been discussed in the literature, and the focus has been only on instability caused by photodissociation. Room temperature XRD investigations of CdI_2 did not show the presence of any CdO, I_2 or $Cd(OH)_2$; thus, reactions (3.1 and 3.2) did not likely occur. The experimentally measured Raman spectra of CdI_2 showed characteristic peak as in Montero and Kiefer (1973) at 111 cm^{-1} (Appendix 3, Table A2.2). Additionally, the detected wide band at 320 cm^{-1} corresponds to the triple position of this same characteristic peak. Since $Cd(OH)_2$ decomposes at 128 °C (401 K), according to the database (software HSC6 Chemistry Ver. 6.0.) and as shown in Figure 3.2, the emission of H_2O should be detected in the TG-MS measurements of CdI_2 (see Figure 3.1 (b)). Second, since no H_2O was found *via* MS, the low rate of mass loss at nearly room temperature suggests that iodine may be released. I_2 may condense before reaching the mass spectrometer and may therefore not be detected. There are two possible explanations for the presence of I_2 in CdI_2. First, I_2 as a reagent is used for CdI_2 production, or second, I_2 could form due to the photodecomposition of CdI_2. The photodissociation is described in Item 1.6.1. However, the melting effects of Cd and/or I_2 were not found in the DTA curves. Most likely, I_2 sublimates very quickly during sample degassing, and photodecomposition does not release elemental Cd.

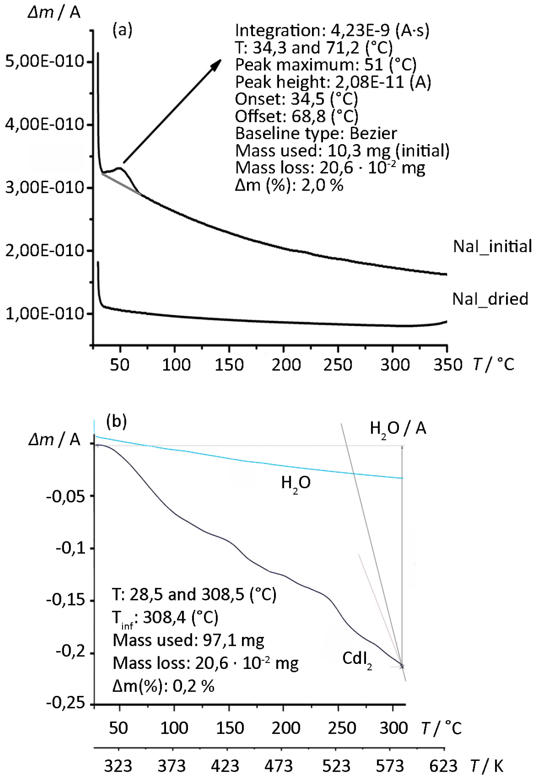

Figure 3.1 MS and TG analyses of NaI (a) and CdI_2 (b); heating rate of 5 ℃ min^{-1}

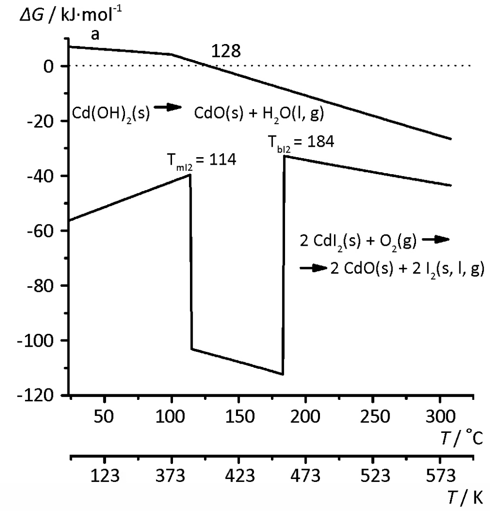

Figure 3.2 Instability of CdI_2 in air, adapted from the database (software HSC6 Chemistry Ver. 6.0.)

The melting of the flux materials, as shown in Figure 3.3, is endothermic for KI, NaI and CdI_2 at 685 °C (958 K), 660 °C (933 K) and 385 °C (658 K), respectively, but during cooling, exothermic solidification occurs at 660 °C (933 K), 639 °C (912 K) and 366 °C (639 K). It was experimentally determined from two heating/cooling runs that 125,0 mg of KI, 125,0 mg of NaI and 125,0 mg of CdI_2 gave average signals of 7107, 7996, and 3000 μV. Then, according to equation 2.10, the calibration constant for KI was 393,0 μV $(\mathrm{mJs}^{-1})^{-1}$, for NaI, it was 404,9 μV $(\mathrm{mJs}^{-1})^{-1}$ and for CdI_2, it was 424,4 μV $(\mathrm{mJs}^{-1})^{-1}$. From the calibration constants, the deviation (calculated from equation 2.12) was determined to be 8,0 %; however, a 10,0 % error is applied due to the DTA precision. Then, the heats according to equation (2.11) are 18,1 ± 1,8 J for KI, 19,8 ± 2,0 J for NaI and 7,1 ± 0,7 J for CdI_2. These values for each flux mixture were used for enthalpy expressions for the processes in the flux-binary mixtures. The CdI_2 boiling point at 742 °C (1015 K) (software HSC6 Chemistry Ver. 6.0.) was not observed in the DTA curve, probably due to the slightly high pressure in the closed ampoules.

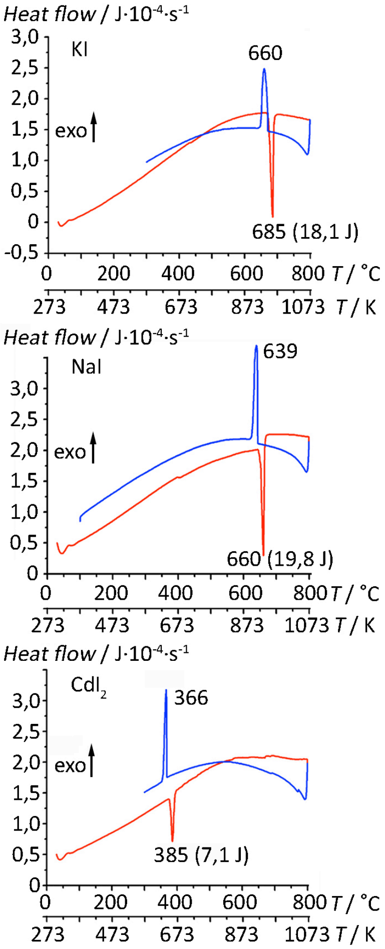

Figure 3.3 DTA curves of 125,0 mg dried flux materials. The red line corresponds to heating at a rate of 5 ℃ min^{-1}; blue – cooling at 10 ℃ min^{-1}

3.2 Results of Precursor Analyses

The **ZnSe** Raman spectra included peaks that are characteristic to the single-crystalline ZnSe at 202 cm^{-1} and 252 cm^{-1} (Klavina *et al.*, 2010) and an additional peak at 140 cm^{-1}, which is likely due to the presence of some elemental Se. Selenium was not found in the ZnSe precursor during XRD analysis, possibly due to its amorphous phase. Se could have remained on the ZnSe crystallites after the synthesis using gas-phase Se (**Paper IV**)The **SnSe** precursor exhibited the characteristic peaks provided in Chandrasekhar, Humphreys, Zwick and Cardona (1997) (Appendix 3, Table A2.2) and contained some $SnSe_2$, as detected by its characteristic Raman peak at 182 cm^{-1}. In Smith, Meek and Liang (1977), the $SnSe_2$ Raman peak was detected at 184,5 cm^{-1}, whereas higher values were reported in Lucovsky, Mikkelsen, Liang, White, and Martin (1976) (see Appendix 3, Table 2.2). However, XRD showed only the SnSe phase. Upon further experimental analysis, if $SnSe_2$ is detected in a mixture by using XRD, it means that its concentration is above that in the precursor, and it is assumed to have formed during a reaction. **Paper IV** showed that, according to XPS, SnO_2 existed on the surface of SnSe. The ΔG for SnO_2 formation from Sn (s) and O_2 (g) is more negative than for SnO at room temperature (23 °C or 296 K). These comparative values are -520,4 kJ and -504,2 kJ. Reaction (3.3) is very negative at room temperature (-536,5 kJ), according to data from the database (software HSC6 Chemistry Ver. 6.0.):

$$2\ SnO\ (s) + O_2\ (g) \rightarrow 2\ SnO_2\ (s) \qquad (3.3)$$

The Raman spectra of the **CuSe** precursor included the characteristic peak of $Cu_{2-x}Se$ at 263 cm^{-1} (**Paper I and IV**), as also observed in Ishii, Shibata and Nozaki (1993), and additional Raman peaks at 94, 186-194, and 307-326 cm^{-1}. The XRD pattern indicates that $Cu_{0.87}Se$, Cu_3Se_2, and Cu_3Sn phases were also present in the CuSe precursor (**Paper IV**). However, there may be different values for the enthalpies for the copper selenide phase transition since a deviation was found in the composition of the CuSe precursor. The presence of Cu_3Sn in the XRD pattern suggests that the initial Cu used for the synthesis of CuSe contained some Sn as an impurity. The DTA curves of the CuSe precursor were presented in **Paper IV**. A weak signal at 51 °C (324 K) was found in the heating curve, which could correspond to a phase change of α-CuSe to β-CuSe, and the change from the β- to γ-phase was found at 133 °C (406 K). During heating, a peritectic reaction (3.4) occurred at 383 °C (656 K). In Glazov *et al.* (2000) and Chakrabarti and Laughlin (1981), this reaction was found to occur at 377 °C (650 K). However, the data for reaction (3.4) in the database (software HSC6 Chemistry Ver. 6.0.) are different; during the formation reaction of β-$Cu_{2-x}Se$ (if x = 0) from γ-CuSe, ΔG becomes negative at 398 °C (671 K). The used amount of $551{,}8 \cdot 10^{-1}$ mg ($3{,}9 \cdot 10^{-4}$ mol) of CuSe gave a signal of 8,2 ± 0,8 J (see in **Paper IV)**, yielding an enthalpy for reaction (3.4) of 21,1 ± 2,1 kJ mol^{-1}. This value is above that reported in the literature for the process at 377 °C or 650 K (11,8 kJ mol^{-1}) according to Bernardini (as cited in Glazov *et al.*, 2000) but lower than that found in the database (software HSC6 Chemistry Ver. 6.0.) calculations at 383 °C or 656 K (30,4 kJ mol^{-1}). The signal for the second heating of 10,3 ± 1,0 J corresponds to an enthalpy value of 26,4 ± 2,6 kJ mol^{-1}, which is very close to the database value (software HSC6 Chemistry Ver. 6.0.). In a closed ampoule, liquid Se formation is expected.

$(2\text{-}x)\ \gamma\text{-CuSe (s)} \leftrightarrow \beta\text{-Cu}_{2\text{-}x}\text{Se (s)} + (1\text{-}x)\ \text{Se (l)}$ (3.4)

Paper IV reported the monotectic point at 523 °C (796 K), where solid β-$Cu_{2-x}Se$ exists together with two liquids. The incongruent melting of γ-CuSe at 535 °C or 808 K was also previously described in Glazov *et al.* (2000) and Chakrabarti and Laughlin (1981). It exhibited thermal effects in the first and second heating curves as total signals of 4,3 ± 0,4 J and 5,2 ± 0,5 J, respectively, which can be expressed as enthalpy values of 11,0 ± 1,1 and 13,3 ± 1,3 kJ mol^{-1}. The exothermic effect with values of -17,7 ± 1,8 J at 685 °C (958 K) in the first heating curve and -18,2 ± 1,8 J at 691 °C (964 K) in the second heating curve is represented as the dissolution of the two phases, such as $Cu_{2-x}Se$ and γ-CuSe. During the cooling cycles, reversible processes were observed with similar heat values (17,5 ± 1,8 and 17,2 ± 1,7 J). At 488 °C or 761 K (-7,0 ± 0,7 J) and at 357 °C or 630 K (-9,3 ± 0,9 J) in the first cooling curve and at 556 °C or 829 K (-0,8 ± 0,1 J) and at 508 °C or 781 K (-5,0 ± 0,5 J) in the second cooling curve, there is a cross between the $L_3 = L_3 + L_2$ mixtures of liquids in the phase diagram of Cu-Se in Figure 1.8 (Glazov *et al.*, 2000) and (Chakrabarti & Laughlin, 1981).

3.3 Analysis of Expected By-Products

CuI exhibited Raman peaks at 93, 122, 139 cm^{-1} (**Paper III**); however, in Mamedov, *et al.* (1999), only the peak at 122 cm^{-1} was observed. Additionally, **SnI_4** showed Raman peaks at 147, 207, and 215 cm^{-1} (**Paper IV**). The positions of the most intense Raman peaks differ only slightly from those published in Stammreich, Forneris and Tavares (1956) (149 and 216 cm^{-1}).

The **$NaI{\cdot}2H_2O$ + NaI** Raman spectra compared to dried NaI are described in the section on the flux analysis results. The XRD measurements of synthesized **$Na_2[Cu(OH)]_4$** also showed some Na_2CO_3 and CuO, and Raman peaks were at 219, 311, 438, and 443 cm^{-1} (Appendix 3, Table A2.2). The XRD confirmed the synthesized compound of Na_2SeO_4 with Raman peaks at 120, 338, 362, 424, 454, and 477 cm^{-1} (Appendix 3, Table A2.2 and **Paper III**).

Elemental Se exhibited weak Raman peaks at 92-93, 120 and 140 cm^{-1} are characteristic of glassy Se (Yannopoulos & Andrikopoulos, 2004), and at 233 and 237 cm^{-1} (in **Paper III** at 240 cm^{-1}), which are attributed to tetragonal Se, and at 253 cm^{-1} for disordered Se; similar values have been reported Poborchii, Kolobov, and Tanaka (1998), and these are published in **Paper IV** and are shown in Appendix 3, Table A2.2. The DSC heating curve in **Paper IV** of 40,0 mg Se in a degassed and sealed ampoule showed a DSC peak at 130-137 °C (403-410 K). This thermal effect was attributed to the phase transition of rhombohedral Se_6 rings into the trigonal spiral chains of Se_n, as in Minaev *et al.* (2005). The determined heat of this phase transition corresponded to an enthalpy value of -3,8 ± 0,4 kJ mol^{-1}. As reported in **Paper IV**, the melting of Se was detected at 221 °C (494 K), and Se evaporated after melting in the vacuum ampoule to the coldest part of the ampoule (to the top). Additionally, as reported in Wibowo *et al.* (2010) that Se evaporates at temperatures above 300 °C (573 K). The evaporation process continued until 476 °C (749 K) (7,5 ± 0,8 J or 14,5 ± 1,5 kJ mol^{-1}). The **CdSe** Raman spectra showed peaks at 168, 201, and 320 cm^{-1} in addition to the characteristic peaks at 198 and 207,5 cm^{-1} as in Teredesai, Leonard, Govindarja, Sood and Rao (2002) and as shown in Appendix 3, Table A2.2. The values of the peaks are published in **Paper IV**. In early studies (Klavina *et al.*, 2010), the CdSe Raman peak was found at 209 cm^{-1}

(Appendix 3, Table A2.2) and for the $Zn_xCd_{1-x}Se$ compound, peaks were at 95-97, 207, 238-242, and 476-477 cm^{-1}.

Dried ZnI_2 exhibited Raman peaks at 70, 77, 119, 127, and 188 cm^{-1}, while **nondried ZnI_2** had additional peaks at 62, 88, 141, 153, 161, and 178 cm^{-1}, probably due to the $ZnCO_3$ compound in the nondried ZnI_2. The **CdI_2-ZnI_2 mixture** (molar ratio 1 : 1) began to melt at 358 °C (631 K). A heat value of 1,8 ± 0,2 J (for the mixtures of 50,0 mg CdI_2 and 40,0 mg ZnI_2) corresponds to the melting enthalpy of the formed eutectic mixture (6,9 ± 0,7 kJ mol^{-1}). This was published in **Paper IV**.

3.4 Determined Solubility

The solubilities of the binary chalcogenides in KI were studied and reported in **Papers I** and **II**: $8,6 \pm 1,0 \cdot 10^{-2}$ mol% (in **Paper I**) of ZnSe; $27,0 \pm 4,0 \cdot 10^{-2}$ mol% of SnSe; $360,0 \pm 40,0 \cdot 10^{-2}$ mol% of CuSe. The solubility of $Cu_2ZnSnSe_4$ in KI was $61,0 \cdot 10^{-2}$ mol% (**Paper I**). The equation for the mol% calculations is provided in Appendix 2, Section A2.3.

3.5 Results of the Mixture Analyses

In this chapter, the results of the analyzed mixtures of flux-ZnSe, flux-SnSe, flux-CuSe, flux-SnSe-CuSe, and flux-ZnSe-SnSe-CuSe, where flux is KI, NaI or CdI_2, will be provided.

3.5.1 Flux-ZnSe

In **Paper II,** the **KI-ZnSe** mixture was not clearly understood, and it was discussed more in **Paper I**. During the heating cycle of KI-ZnSe (Figure 3.4), there was no endothermic signal observed for the melting process of 125,0 mg of KI because the exothermic signal at 683 °C (956 K) masks it. If we take into account the melting heat of KI, then the real value of the exothermic process is -11,4 J -18,1 J = -29,5 ± 3,0 J. It is well known that fused salts are typically highly dissociated into their ionic species (Blomgren & Artsdalen, 1960). It is also known that the I^- ion has a strong complexing ability with Zn to form a ZnI_4^{2-} complex (Wakita, Johansson, Sandström, Goggin & Ohtaki, 1991). In this case, if there are no other binaries present, there is much flux available. This exothermic process could affect the ZnSe dissolution in liquid KI and the formation of K_2ZnI_4 in the general reaction of (3.5), where A is Zn^{2+} and B is K^+:

$$ASe\ (s) + 4\ BI\ (l) \leftrightarrow B_2AI_4\ (s) + B_2Se\ \ (s) \qquad (3.5)$$

A similar process for ZnS dissolution and the following formation of ZnS nanosheets from NaI melt has been previously proposed (Li, 2013). However, the formation of K_2ZnI_4 and K_2Se was not confirmed by the XRD patterns of the samples quenched according to DTA effects. This could be explained by the ZnI_4^{2-} complex formation and the existence only in the liquid Kl, and its decomposition is a reversible process by cooling. The endothermic peak at 655 °C (928 K) with a determined effect of 5,4 ± 0,5 J during the cooling cycle completely compensates for the heat of KI solidification (18,1 ± 1,8 J), and it corresponds to 23,5 ± 2,4 J of the reversible process. If there was $19,0 \cdot 10^{-5}$ mol ZnSe in the ampoule, then this is the limiting factor, and this same amount (according to reaction (3.5)) K_2ZnI_4 will be produced. The complex formation enthalpy during the first heating was calculated to be from -29,5 J to -157,0 ± 15,7 kJ mol^{-1} per formed complex of K_2ZnI_4 since the area under the DTA curve is directly proportional to the heat transferred in the reaction. The difference in the enthalpy values of the direct and reversible processes (-6,0 ± 0,6 J) are probably caused by dissolved ZnSe in molten KI. ZnSe remains as a finely dispersed solid in frozen KI. To break the bonds of the solute (ZnSe) and solvent (KI), the consumed energy is endothermic, and this process occurs during melting. The formation of new bonds during the solvation is an exothermic process, and this occurs right after melting. The dissolution will be exothermic, if the released energy from the bond formation is larger than the energy needed to break the bonds of the solute and solvent (Atkins *et al.*, 2018). Thus, the heat difference between the endothermic peak during cooling and the exothermic peak during the heating cycle of -6,0 J can be attributed to the enthalpy of physical solvation of ZnSe in KI (enthalpy of solution). Since solvation is a process in which the solvent and solute take part, the effect per mixture of 125,0 mg ($75{,}3\cdot10^{-5}$ mol) KI solvent and dissolved ZnSe (see Section 3.4) was calculated. Proportionally, $6{,}5\cdot10^{-5}$ mol ZnSe dissolves in $75{,}3\cdot10^{-5}$ mol of KI. In this case, the enthalpy of dissolution of ZnSe in KI is 6,9 ± 0,7 kJ mol^{-1}. The other possibility is that if reaction (3.5) does not proceed, then the exothermic peak at -29,5 J (-37,0 ± 3,7 kJ mol^{-1}) could be attributed to the enthalpy of solution formation and the dissolution being a physical process. The enthalpy of solution was calculated per sum of $6{,}5\cdot10^{-5}$ mol ZnSe and $75{,}3\cdot10^{-5}$ mol KI.

The process is similar in the **NaI-ZnSe** system (**Paper III**). In the heating curve, the endothermic peaks of melting at 659 °C or 932 K (1,8 ± 0,2 J) are partly masked by the unobserved exothermic process that occurs during the melting of the mixture since the melting of pure NaI of an equal amount gave a signal of 19,8 ± 2,0 J. This unseen exothermic effect is then (-19,8 J +1,8 J) = -18,0 ± 1,8 J. The formation of a complex between liquid NaI and ZnSe can be proposed similar to reaction (3.5), where B is Na^+ and A is Zn^{2+}. Since the sample was prepared *via* the required molar ratio for reaction (3.5) of 1 : 4 for ZnSe : NaI (see Table 2.2 in Section 2.7), the enthalpy for it was determined to be -87,2 ± 8,7 kJ mol^{-1}. This was calculated as described above. The exothermic peak in the cooling curve in the vicinity of the melting and solidification points of pure NaI at 639 °C (912 K) was recorded at -1,8 J; then, the thermal effects of the reversible process is the same as for heating at (-1,8 J +19,8 J) = 18,0 ± 1,8 J. The sample mixtures investigated *via* DTA after annealing did not show formation of any new phases. Based on this phenomenon, complex formation occurs only in the liquid phase and is a reversible process. If we consider that dissolution was physical, then the -18,0 ± 1,8 J value corresponds to the difference in solvation energy needed to break the bonds and to form new bonds in the liquid phase (physical dissolution). Since the solubility of ZnSe in NaI has not been determined, the value of the heat effect cannot be expressed in kJ mol^{-1}.

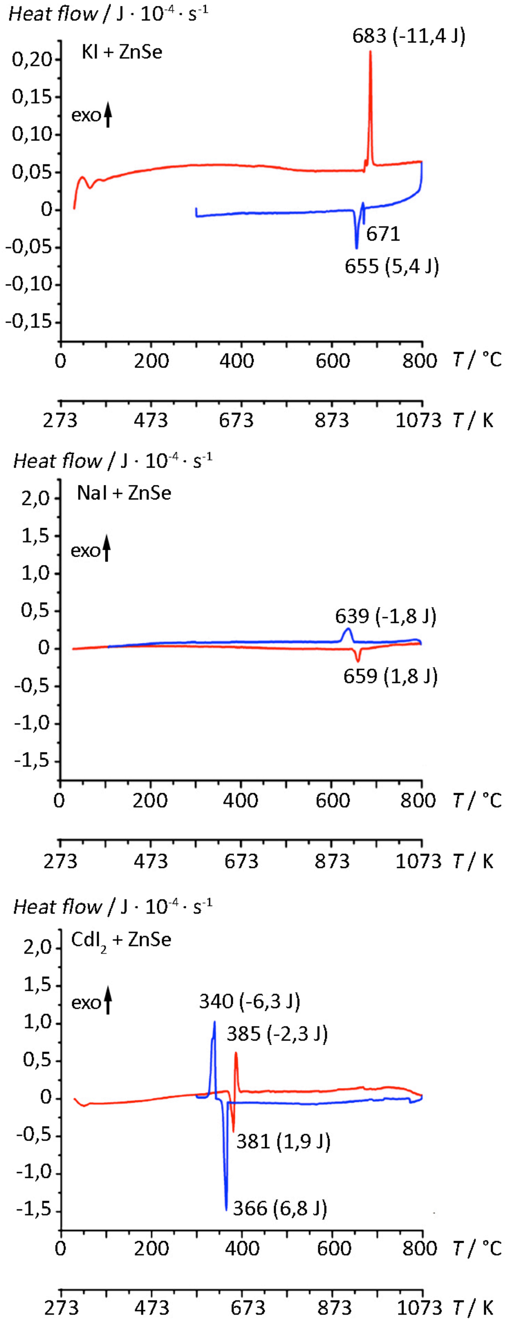

Figure 3.4 DTA curves of the flux-ZnSe mixtures of 125,0 mg of flux material and 29,8 mg of ZnSe (heating at 5 ℃ min^{-1} in red; cooling at 10 ℃ min^{-1} in blue)

However, a deeper understanding of the complex formation during dissolution was provided in the studies of the **CdI_2-ZnSe** mixture in **Paper IV**. The melting temperature of CdI_2 in the mixture with ZnSe is four degrees lower (at 381 °C or 654 K in Figure 3.4) than shown in Figure 3.3. This implies that ZnSe dissolves in molten CdI_2.

The endothermic melting effect in the CdI_2-ZnSe mixture (1,9 ± 0,2 J) may be partially masked by the exothermic effect of some simultaneous process, as the melting of the same amount of CdI_2 was accompanied by a signal of 7,1 ± 0,7 J (Figure 3.3). The compensated part of the CdI_2 melting should be 7,1 J -1,9 J = 5,2 ± 0,5 J. The exothermic effect in the heating (red) curve at 385 °C (658 K) can then be calculated to be (-2,3) J + (-5,2) J = -7,5 ± 0,8 J. To understand this exothermic effect, the XRD pattern of the single-crystalline sample, which was used for dissolution investigations, that was annealed at 740 °C (1013 K) was analyzed. XRD analysis confirmed that relatively high amounts of $Zn_{1-x}Cd_xSe$ and a small amount of CdSe formed, as shown in Figure 3.5 (a). A solid solution, such as ZnS-CdS, was previously described (Li, 2013; Nkwusi, 2017; Nkwusi et al. 2016; Nkwusi, Leinemann & Altosaar, 2016; Nkwusi et al., 2014). Visually, the color of the external surface of this sample was inhomogeneous, exhibiting contrasts ranging from black to red and even orange. EDX analysis revealed that the orange area consisted of 31,2 at.% Zn, 48,9 at.% Se and 17,5 a.t% Cd, suggesting the presence of a $Zn_{1-x}Cd_xSe$ phase, as also determined by XRD. The black area surrounding the orange part consisted of 51,4 at.% Cd, 29,7 at.% Se and 18,9 at.% I. However, the ΔG value of the straight exchange reaction between ZnSe and CdI_2 to form CdSe and ZnI_2 is positive. Most likely, after the formation of liquid CdI_2, some ZnSe dissolved in liquid CdI_2. $Zn_{1-x}Cd_xSe$ then formed in the molten phase. The precipitation from the molten phase was confirmed by the formation of leaf- and flower-like CdSe crystals, as shown in Figure 3.6 (a) and (b). Therefore, the formed compounds should be $Zn_{1-x}Cd_xSe$ and $Zn_xCd_{1-x}I_2$. The dried precipitate from the washing water was analyzed; it consisted of 12,3 at.% Zn, 12,8 at.% Cd and 74,9 at.% I, reflecting a ZnI_2-CdI_2 mixture. The formation of $Zn_{1-x}Cd_xSe$ in the mixture of liquid CdI_2 with ZnSe can now be explained after studying the properties of the liquid phase of CdI_2. It is well known that many salts in their molten phase are ionic liquids, but CdI_2 is not. The melt of MX_2 (M = Zn, Cd, Hg and X = Cl, Br, I) has an extremely low ionic conductivity (Gaune-Escard, 2002). Furthermore, MX_2 salts retain their solid-phase structure even in the liquid phase in which small metal M^{2+} ions occupy tetrahedrally coordinated sites in a closely packed anion structure with strong intermediate-range ordering (Donald, Hargittai & Hoffmann, 2008; Özen, Akdeniz, Ruberto, Pastore & Tosi, 2014).

Additionally, measurements of the scattering of thermal neutrons in natural samples of molten $ZnCl_2$, $ZnBr_2$ and ZnI_2 confirmed the above given structural model of $[ZnI_4]^{2-}$ with strong intermediate-range ordering (Triolo & Narten, 1981; Allen & Howe, 1991). According to Chikanov (2006), CdI_2-ZnI_2 mixtures form a continuous row of solid solutions. Therefore, it is proposed in this study that ZnSe dissolves in liquid CdI_2 and that the bonds of solid ZnSe will be broken, and dissolved Zn^{2+} can be displaced by Cd^{2+} ions in the closely packed anion structure, as indicated in reactions (3.6-3.11). In this work, it was found that the enthalpy of summary reaction (3.11) is -18,8 ± 1,9 kJ mol^{-1}, as calculated per the reagents. In summary, the observed exothermic effect in the DTA heating curve can be attributed to the chemical dissolution of ZnSe in molten CdI_2, resulting in the formation of $Zn_{1-x}Cd_xSe$ and $Zn_xCd_{1-x}I_2$. As was observed from the DTA curve of the CdI_2-ZnI_2 mixture in **Paper IV**, the presence of ZnI_2 in CdI_2 strongly reduces the melting temperature. During cooling, the precipitation of the $Zn_{1-x}Cd_xSe$ solid solution from the melt occurs at 366 °C (639 K), and the $Zn_{1-x}Cd_xI_2$ liquid solution freezes at 340 °C (613 K). Since the CdI_2 solidification should be -7,1 J (Figure 3.3), the effect in the cooling (blue) curve at 340 °C (613 K) is masked by -7,1 J - (- 6,3 J) = - 0,8 J, and the endothermic effect of cooling at 366 °C (639 K) is 6,8 J + 0,8 J = 7,6 ± 0,8 J, which is the same as the exothermic effect of heating (-7,5 ± 0,8 J). An analogous phenomenon in the second DTA cycle was found.

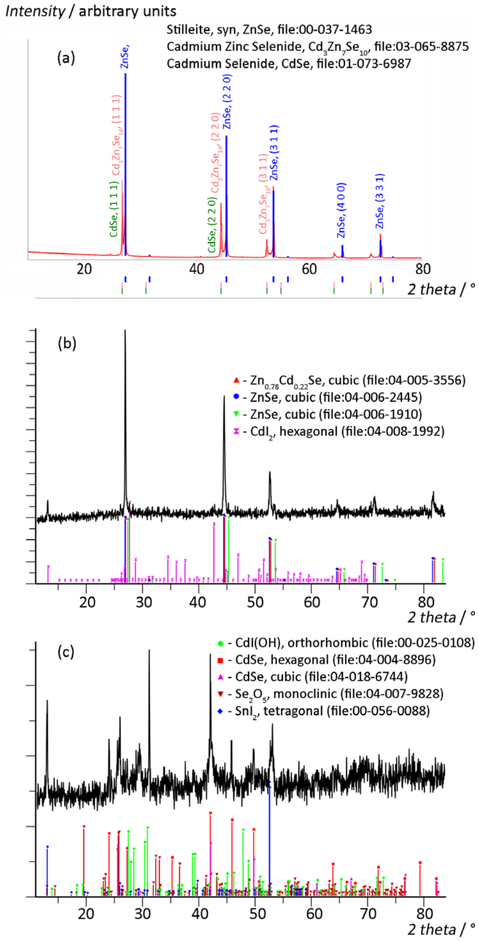

Figure 3.5. XRD pattern of: (a) the CdI$_2$-ZnSe sample (heated to 740 ℃ or 1013 K for 168 h and washed); opened DTA samples of (b) CdI$_2$-ZnSe and (c) CdI$_2$-SnSe. For phase detection, the files from database ICDD-PDF-4+2016 were used

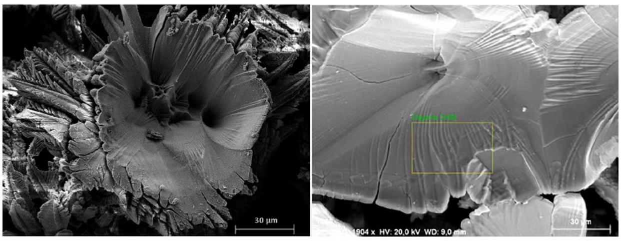

(a) (b)

Figure 3.6 SEM images of the CdI$_2$-ZnSe sample heated to 740 ℃ (1013 K) for 168 h and washed

Upon opening the ampoule used for DTA and performing XRD analysis, as shown in Figure 3.5 (b), in this study was found that in addition to the $Zn_{1-x}Cd_xSe$ ($Zn_{0.78}Cd_{0.22}Se$) phase, precipitation of ZnSe and CdI_2 was also found (but no separate CdSe). These differences compared with the sample that had been annealed to 740 °C (1013 K) may be ascribed to different cooling regimes and different contact areas of the liquid-solid phases. In the case of single-crystal ZnSe, the solid-liquid contact area (which is equal to the surface area of the crystal) is much smaller compared with the surface of the ZnSe powder that was used for the DTA sample. The dissolution process can be described by the following reactions (3.6-3.11):

Melting of CdI_2: $2\ CdI_2\ (l) \rightarrow [CdI_4]^{2-}\ (l) + Cd^{2+}\ (l)$ (3.6)

ZnSe dissolution in CdI_2: $ZnSe\ (s) \rightarrow Zn^{2+}\ (l) + Se^{2-}\ (l)$ (3.7)

$Zn^{2+}\ (l) + [CdI_4]^{2-}\ (l) \rightarrow [ZnI_4]^{2-}\ (l) + Cd^{2+}\ (l)$ (3.8)

Solidification: $Se^{2-}\ (l) + (x)\ Cd^{2+}\ (l) + (1-x)\ Zn^{2+}\ (l) \rightarrow Zn_{1-x}Cd_xSe\ (s)$ (3.9)

$(x)\ [ZnI_4]^{2-}\ (l) + (x)\ Zn^{2+}\ (l) + (1-x)\ [CdI_4]^{2-}\ (l) + (1-x)\ Cd^{2+}\ (l) \rightarrow 2\ Zn_xCd_{1-x}I_2\ (s)$ (3.10)

$ZnSe\ (s) + CdI_2\ (l) \rightarrow Zn_{1-x}Cd_xSe\ (s) + Zn_xCd_{1-x}I_2\ (s, l)$ (3.11)

3.5.2 Flux-SnSe

The **KI-SnSe** mixture was studied and reported in **Papers I and II**. In this mixture, KSn_2I_5 and elemental Se formed, as confirmed by the XRD pattern of the sample heated to 420 °C (693 K) for 13 h and quenched (Figure 3.7). The compounds formed at a much lower temperature than the thermal effect of KI melting; additionally, no melting of Se was observed in the DTA curve (Figure 3.8). A KSn_2I_5 formation reaction may occur between solid SnSe and gaseous I_2 as an oxidant. It is a complex chemical process that requires the availability of free iodine. The possible release of iodine was discussed in Item 1.6.3, where the release of free iodine was not found to occur practically in the dried flux analysis results.

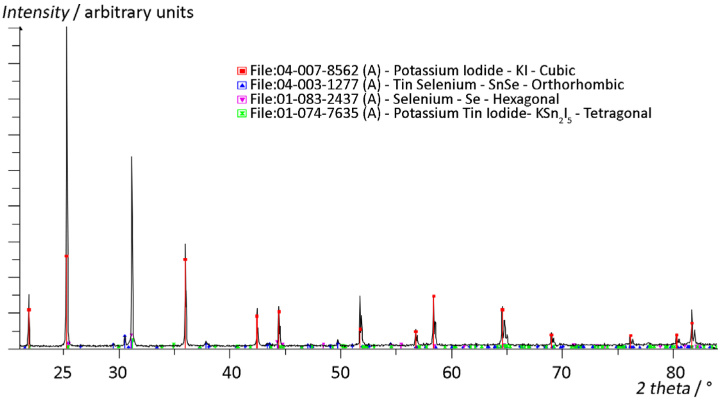

Figure 3.7 XRD pattern of the KI-SnSe mixture heated to 420 ℃ or 693 K (13 h) and quenched; the files from database ICDD-PDF-4+2016 were used.

Reaction (3.12) could occur if the SnSe precursor contained some overstoichiometric Se; however, Se was not experimentally detected in the precursor. As with DSC, the Se investigations showed that Se evaporation after melting continuously occurs. If there is some gaseous KI in the closed ampoule at 420 °C (693 K), then a negative *ΔG* is likely as calculated for the gas phase reaction (3.12) (**Paper II**). See Figure 3.9. The *ΔG* increases slightly and is close to 0,0 kJ mol^{-1} at 652 °C (925 K), as simulated using the database (software HSC6 Chemistry Ver. 6.0.):

$2\ KI\ (g) + Se\ (g) \leftrightarrow K_2Se\ (s) + I_2\ (g)$ (3.12)

Additionally, the saturated vapor pressure of Se is approximately 5 mm Hg at 400 °C (673 K), according to Gerasimow, Krestovnikov and Gorbov (as cited in Ito, 2015), and the vapor pressure of KI is 0,31 mm Hg at 25 °C or 298 K (1 mm Hg at 745 °C or 1018 K), while the vapor pressure of SnSe is approximately $3\cdot10^{-6}$ mm Hg at 400 °C (673 K), as determined by Gerasimow, Krestovnikov and Gorbov (as cited in Ito, 2015). The released I_2 could in turn react with SnSe (see in Figure 3.9), as determined from the software HSC6 Chemistry Ver. 6.0. Since no DTA effects were observed in the temperature range from room temperature to 420 °C (693 K), KSn_2I_5 and Se likely formed at room temperature during sample preparation for XRD. In reality, reactions, such as (3.13) and (3.14), occur at room temperature. The values are -56,7 kJ mol^{-1} for reaction (3.13) and -119,8 kJ mol^{-1} for reaction (3.14) if the reactant is solid I_2 or -76,4 kJ mol^{-1} for reaction (3.13) and -159,0 kJmol^{-1} for reaction (3.14) if the reactant is gaseous I_2. In a long experiment, unreacted SnSe was found, which it means that the limiting factor is the concentration of one of the reactants; here, this can only be free I_2. In **Paper IV**, it was shown that after melting, Se slightly vaporizes in a closed ampoule. A low vapor pressure may prevent the formation of $SnSe_2$ in larger amounts (larger than the amount already in the SnSe precursor as overstoichiometric Se). Since no $SnSe_2$ was experimentally found *via* XRD, the variables in which $SnSe_2$ participates, similar as in reactions (3.13-3.14), will be excluded. Moreover, the *ΔG* values for reactions with $SnSe_2$ were less negative compared to reactions (3.13-3.14), which means that those reactions are less probable.

$SnSe\ (s) + I_2\ (s, g) \leftrightarrow SnI_2\ (s, l, g) + Se\ (s, l, g)$ (3.13)

$SnSe\ (s) + 2\ I_2\ (s, g) \leftrightarrow SnI_4\ (s, l, g) + Se\ (s, l, g)$ (3.14)

According to Figure 3.9, reaction (3.14) has a more negative *ΔG*, and SnI_4 is more likely to form than SnI_2, which was found as a part of KSn_2I_5 (KI-$2SnI_2$). Instead of SnI_4, SnI_2 is formed, likely due to the deficiency of I_2 in reaction (3.13). The intermediate steps of KSn_2I_5 formation should be investigated in more detail; however, this was not the focus of this study. Since K_2Se, SnI_4 and SnI_2 as products were not found in the XRD patterns, it is likely that the reaction with released iodine directly proceeds *via* the proposed reaction (3.15):

$2\ SnSe\ (s) + KI\ (s, l) + 2\ I_2\ (g) \rightarrow KSn_2I_5\ (s, l) + 2\ Se\ (g)$ (3.15)

Reaction (3.15) could not be simulated (software HSC6 Chemistry Ver. 6.0.). It is also possible that Se sublimated in the closed ampoule, since Se melting was not observed in the DTA curve.

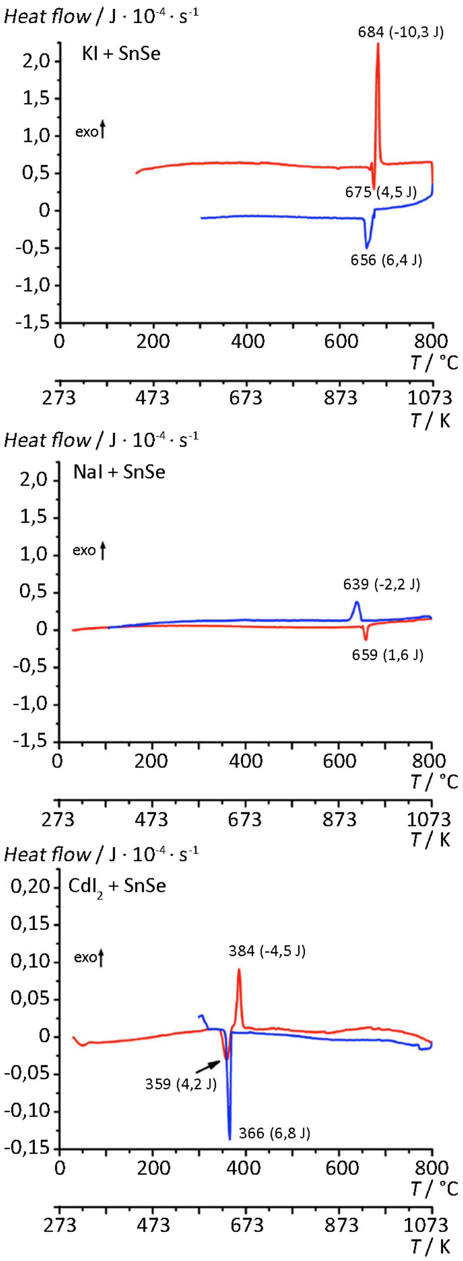

Figure 3.8 DTA curves of the flux-SnSe mixtures of 125,0 mg flux and 40,8 mg SnSe (heating at 5 ℃ min^{-1} in red; cooling at 10 ℃ min^{-1} in blue)

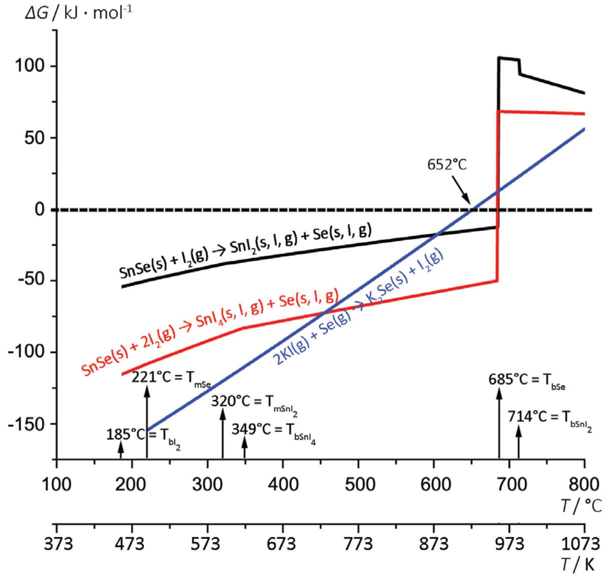

Figure 3.9. Results of (software HSC6 Chemistry Ver. 6.0.) calculations for the considered reactions (3.12-3.14)

No new phases were found in the sample that was quenched at 710 °C (983 K). The mixture of KI-SnSe (Figure 3.8) melts at 675 °C (948 K), giving an endothermic signal of 4,5 ± 0,5 J for KI melting, which is partly obscured by 18,1 J -4,5 J = 13,6 ± 1,4 J because of the next exothermic effect. The next exothermic peak with the heat effect value of -10,3 ± 1,0 J compensates for the melting heat of KI and is -10,3 J -13,6 J = -23,9 ± 2,4 J in total. The phenomenon for how the melting temperature of KI can be decreased was discussed in **Paper II**. The depression of the melting temperature is caused by dissolved SnSe, which increases the entropy of the system but does not change the enthalpy, when *ΔG* = 0,0 kJ mol^{-1} during the melting process. Since the formation of anions, such as such as $[SnI_4]^-$, is not known and because K_2Se was not found experimentally as discussed in the section on the KI-ZnSe mixture, it is more believable that the following exothermic process at 684 °C (957 K) with a thermal effect of -23,9 ± 2,4 J can be attributed to the difference in solvation energy to break the bonds into ions (K^+, I^-, Sn^{2+} and Se^{2-}) *via* a physical dissolution process. According to calculations described in Section 3.4, $20{,}0 \cdot 10^{-5}$ mol of SnSe dissolves in $75{,}3 \cdot 10^{-5}$ mol of KI. If we take into account the solubility of SnSe in KI (in 125,0 mg) and the heat effect from the current DTA experiment, the calculated value of dissolution enthalpy is -31,0 ± 3,1 kJ mol^{-1}. Upon cooling, a reversible process to dissolution was detected at 656 °C (929 K). This endothermic peak of 6,4 ± 0,6 J at 656 °C (929 K) is obscured by KI solidification at 18,1 ± 1,8 J, and its total value is 24,5 ± 2,5 J. Considering experimental errors, this value is close to the one detected in the heating curve.

The **NaI-SnSe** system was studied and discussed in **Paper III**. In the heating curve of NaI-SnSe (Figure 3.8), the endothermic peak for melting at 659 °C or 932 K (with signal of 1,6 ± 0,1 J) is partially obscured by some invisible exothermic process occurring during the melting of the mixture, since the melting of NaI of an equal amount gave a signal at 19,8 ± 2,0 J. The exothermic effect for physical dissolution in the NaI-SnSe mixture can be calculated as 1,6 J -19,8 J = -18,2 ± 1,8 J, according to the DTA heating curve. The exothermic peak in the cooling curve of NaI-SnSe in the vicinity of the melting and solidification points of NaI at 639 °C (912 K) exhibited a signal at -2,2 ± 0,2 J. The thermal effects of the reversible process were calculated to be -2,2 J +19,8 J = 17,6 ± 1,8 J. The enthalpy values of the forward and reversible processes are rather similar. After annealing at 660 °C (933 K), the sample did not show any additional formed phases. Thus, the complex formation likely occurs only in the liquid phase, and it is a reversible process. The dissolution process is believed to be physical. The solubility of SnSe in NaI was not determined and therefore cannot be expressed in kJ mol^{-1}. Additionally, this performed sample test is evidence that KSn_2I_5 and Se were formed during sample preparation for XRD according to reaction (3.13), as mentioned in the section above.

The results for the **CdI_2-SnSe** system are provided in **Paper IV**. The DTA curve of the CdI_2-SnSe mixture shows an endothermic effect of 4,2 ± 0,4 J in the heating curve (red) at 359 °C or 632 K (Figure 3.8). This value of 4,2 J is lower than the value of CdI_2 melting shown in Figure 3.3 (7,1 J), which indicates that the following thermal effect with an exothermic peak at 384 °C (657 K) compensates for the melting heat of CdI_2 by 4,2 J -7,1 J = -2,9 J. This exothermic process yields a value of -2,9 J -4,5 J = -7,4 ± 0,7 J. The XRD analysis of the opened DTA sample, shown in Figure 3.5 (c), showed the following compounds: CdIOH, CdSe, Se_2O_5 and SnI_2. The appearance of CdIOH and Se_2O_5 in the XRD pattern can be attributed to the oxide groups detected on the surface of the SnSe powder precursor, as shown in **Paper IV**. The $Sn(OH)_2$ structure is not known and cannot be detected by XRD. Most likely, it was formed from SnO_2. A detailed study of how SnO_2 was formed from $Sn(OH)_2$ was not the focus of this study; however, there could be an expected reduction reaction from Sn^{4+} to the Sn^{2+} state. According to Spandau and Kohlmeyer (as cited in Perrone, 2012), it is possible that surface reactions at room temperature to 227 °C (500 K) *via* the set of reactions of (3.16-3.20) may have occurred. However, these have not been found in the database (software HSC6 Chemistry Ver. 6.0.). These processes could be induced by reaction (3.3), see Section 3.2., with a ΔG for reaction 3.20 -11,6 kJ mol^{-1}.

$$2\ SnO_2\ (s) + Sn\ (s) \rightarrow Sn_3O_4\ (s) \tag{3.16}$$

$$Sn_3O_4\ (s) + Sn\ (s) \rightarrow 4\ SnO\ (s) \tag{3.17}$$

or

$$3\ SnO_2\ (s) + Sn\ (s) \rightarrow 2\ Sn_2O_3\ (s) \tag{3.18}$$

$$Sn_2O_3\ (s) + Sn\ (s) \rightarrow 3\ SnO\ (s) \tag{3.19}$$

then

$$SnO\ (s) + H_2O\ (g) \rightarrow Sn(OH)_2\ (s) \tag{3.20}$$

Therefore, the following reaction (3.21) is proposed, which is similar to that described in (Chikanov, 2006), where the formation of the CdIOH solid solution was found to be possible from CdI_2 and $Cd(OH)_2$ at 25 °C (298 K) with an enthalpy of formation of $\Delta H_{f298,15}$ = -375,7 kJ mol^{-1}.

$$2\ CdI_2\ (s) + Sn(OH)_2\ (s) \rightarrow 2\ CdIOH\ (s) + SnI_2\ (s, l, g) \qquad (3.21)$$

Next, the processes occurring during the melting of CdI_2 were considered. The melting of CdI_2 is emphasized in Figure 3.10 (a) by a vertical arrow. These reactions occur more intensely in liquid CdI_2, and the gaseous products leave the mixture and can no longer interfere. According to the calculations performed using the database (software HSC6 Chemistry Ver. 6.0.), as shown in Figure 3.10 (a), SnSe can react with CdI_2 at temperatures above 348 °C (621 K) *via* reaction (3.22), forming liquid SnI_2 and solid CdSe (these phases were also found during the XRD analysis; see Figure 3.8 (c)). The formation of SnI_2 explains why the CdI_2 melting temperature was lowered to 359 °C (632 K) (compare Figures 3.8 and 3.3). The gaseous phase of CdI_2 is hereafter excluded because the solid phase can only directly interact with other solid or liquid phases. $SnSe_2$ was also detected *via* Raman spectroscopy in the SnSe precursor. However, the calculations for this study yielded positive ΔG values for the reaction between $SnSe_2$ and CdI_2 for the formation of SnI_2, CdSe and Se in the experimentally applied temperature range. The formation of solid CdSe and gaseous SnI_4 in reaction (3.23) is possible at temperatures above 368 °C or 641 K (see Figure 3.10 (a)). Figure 3.10 (b) shows that SnI_4 does not decompose to SnI_2 and I_2 due to the positive ΔG values for this process in the temperature range between room temperature and 800 °C (1073 K).

$$SnSe\ (s) + CdI_2\ (s, l) \leftrightarrow SnI_2\ (l, g) + CdSe\ (s) \qquad (3.22)$$

$$SnSe_2\ (s) + 2\ CdI_2\ (s, l) \leftrightarrow SnI_4\ (g) + 2CdSe\ (s) \qquad (3.23)$$

As shown in **Paper IV**, the negative ΔG values of reaction (3.24) exclude the decomposition of $SnSe_2$ to SnSe and Se up to the melting point of $SnSe_2$. Se, released from molten $SnSe_2$ at 675 °C (948 K), can react with SnO_2 according to reaction (3.25) with a ΔG = -313,8 kJ mol^{-1}. However, the release of Se was not observed in the DTA (Figure 3.8), despite the confirmation of the presence of the $SnSe_2$ phase during the analysis of the SnSe precursor when larger amounts were analyzed. Since T_{bSe} = 685 °C (958 K), Se_2O_5 can thus form *via* the gas phase reaction (3.26) at temperatures above 685 °C (958 K), and illustrative curves are provided in Figure 3.10 (b).

$$SnSe\ (s) + Se\ (s, l) \rightarrow SnSe_2\ (s) \qquad (3.24)$$

$$SnO_2\ (s) + Se\ (l) \leftrightarrow SnSe\ (s) + O_2\ (g) \qquad (3.25)$$

$$4\ Se\ (g) + 5\ O_2\ (g) \rightarrow 2\ Se_2O_5\ (s) \qquad (3.26)$$

To investigate the exothermic process observed in the DTA heating curve at 384 °C (657 K) in Figure 3.8 in more detail, a single-crystal sample of SnSe was heated in CdI_2 at 740 °C (1013 K) for 168 h. It was found that the initial mass of the SnSe sample increased from 229,0 mg to 897,1 mg, as determined after separating it from soluble phases by washing it with water. Detailed EDX investigations revealed that its composition varied in different places. For one studied location, it comprised 28,4 at.% Cd, 11,1 at.% Sn and 60,5 at.% I, suggesting a $Sn_{1-x}Cd_{2x}I_4$ phase. In another location, its composition of 30,0 at.% Cd and 57,9 at.% I could be attributed to a CdI_2 phase. The evaporated and dried residue of the washing water contained 94,8 at.% Sn and 5,2 at.% Cd. Iodine may have evaporated during the drying process. However, as described in Allen and Howe (1991) for a system of cadmium and tin iodides, eutectic forms are generated that contain less than 5,0 mol% of both components. The CdI_2-SnI_2 system has also been described as a system with limited solid solubility, *e.g.*, the solubility of SnI_2 is smaller than 20,0 mol%. This is consistent with the findings in this study. The $Sn_{1-x}Cd_xI_2$ phase was observed to grow into a single SnSe crystal, leading to an increase in the mass of the initial SnSe crystal. The following reactions are proposed:

$$(1\text{-}x)\ SnI_2\ (s,\ l) + x\ CdI_2\ (s,\ l) \rightarrow Sn_{1-x}Cd_xI_2\ (s) \tag{3.27}$$

$$(1\text{-}x)\ SnI_4\ (s,\ l) + 2x\ CdI_2\ (s) \rightarrow Sn_{1-x}Cd_{2x}I_4\ (s) \tag{3.28}$$

The reversible process shown in the DTA curve at 366 °C (639 K) is similar to that observed for the CdI_2-ZnSe mixture. The crystallization of the CdI_2-SnSe mixture was not detected because the experiment was terminated at 300 °C (573 K). SnI_4 may not have been detected in the sample of the opened DTA ampoule *via* XRD analysis because it evaporates at 348 °C (621 K). Condensation of the SnI_4 phase was visually observed as orange deposits on the wall of the ampoule.

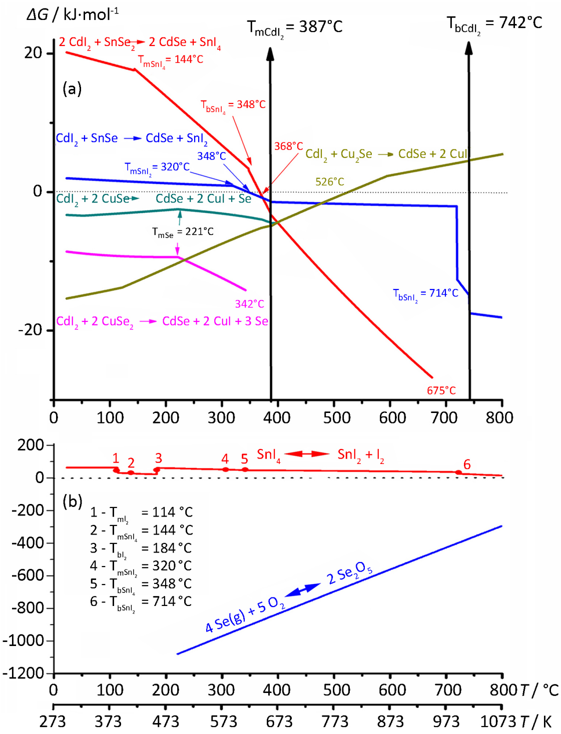

Figure 3.10. Results of (software HSC6 Chemistry Ver. 6.0.) calculations for the considered reactions in mixtures of CdI_2-SnSe and CdI_2-CuSe

3.5.3 Flux-CuSe

The DTA curves of the **flux-CuSe** mixtures (Figure 3.11) are more complicated because of the multiple phase changes in the binary Cu-Se system. As shown in **Papers I and II**, the endothermic peak for the **KI-CuSe** mixture at 379 °C (652 K) of 3,1 ± 0,3 J is less intense than that in the CuSe precursor. This might be caused by deviations in the Cu-Se precursor composition and exothermic dissolution of the flux in liquid Se. It corresponds to the phase transformation of CuSe to $Cu_{2-x}Se$ (reaction (3.4) in the Section 3.2). The determined enthalpy of 8,0 ± 0,8 kJ mol^{-1} for CuSe could be attributed to the enthalpy of transformation of CuSe to $Cu_{1.8}Se$ and Cu_3Se_2. These phases were detected by XRD in the sample quenched at 420 °C (693 K) (not presented). The heat of the peritectic CuSe decomposition at 377 °C (650 K) determined by Bernardini (as cited in Glazov *et al.*, 2000) was 11,8 ± 0,0 kJ mol^{-1}, which agrees with the experimental value for this mixture.

The effect shown in the heating curves of the enthalpy of 4,0 ± 0,4 J expressed as 11,0 ± 1,1 kJ mol^{-1} for the CuSe amount in the sample at 517-534 °C or 790-807 K (also in Section 3.2) can be correlated with the temperature-dependent change in composition of the liquid phase, which corresponds to the increase in the liquidus line from 52,5 at.% Se (monotectic composition at 523 °C or 796 K) to 50,0 % Se (in CuSe). This is in agreement with the Cu-Se phase diagrams given in Glazov *et al.* (2000) and Chakrabarti and Laughlin (1981). Additionally, CuI was found in the Raman spectra at 122 cm^{-1} for the washed sample that was quenched at 540 °C (813 K), which is below the melting point of the flux. Since phases, such as $CuSe_2$, CuSe and Cu_2Se, are possible during fast quenching, then in the opened ampoule, reactions (3.29-3.31) at room temperature can occur. The ΔG for these reactions are: -57,3 kJ mol^{-1}, -62,0 kJ mol^{-1}, and -74,1 kJ mol^{-1} in the case of solid I_2. However, in the case of sublimated gas-phase I_2, they are -76,9 kJ mol^{-1}, -81,7 kJ mol^{-1}, and -93,7 kJ mol^{-1}. This means that Cu_2Se most likely reacts with free I_2; however, solid KI keeps the phases separate, whereas liquid Se increases the interactions. CuSe or $CuSe_2$ can also react with I_2, if they are formed during fast quenching. In this case, CuSe, $Cu_{1.5}Se$ and $Cu_{1.8}Se$ were found by XRD. The CuI formation does not affect the enthalpy determined for the Cu-Se phase transformation since it formed after opening the ampoule and upon Raman and XRD analysis.

$$2\ CuSe_2\ (s) + I_2\ (s, g) \rightarrow 2\ CuI\ (s) + 4\ Se\ (s) \qquad (3.29)$$

$$2\ CuSe\ (s) + I_2\ (s, g) \rightarrow 2\ CuI\ (s) + 2\ Se\ (s) \qquad (3.30)$$

$$Cu_2Se\ (s) + I_2\ (s, g) \rightarrow 2\ CuI\ (s) + Se\ (s) \qquad (3.31)$$

At 669 °C (942 K), the endothermic effect of KI melting (7,1 ± 0,7 J) is partially masked by the following exothermic effect of -18,8 ± 1,9 J. The KI-CuSe mixture starts to melt at a lower temperature than pure KI since the entropy of the system is larger than in pure KI (**Paper II**). According to the XRD pattern of the sample quenched at 680 °C (953 K) (Figure 3.12), $CuSe_2$ was observed. The presence of this low-temperature phase at this temperature could be explained by the crystallization from liquid upon fast cooling (quenching). Additionally, K_2Se_3 formed during the melting process. Its formation could be described by means of Se formation in reaction (3.4) from the

CuSe precursor (this also explains the absence of Se) and K_2Se formation reactions (3.12). Then, the proposed reactions of (3.32) or (3.33) could directly proceed.

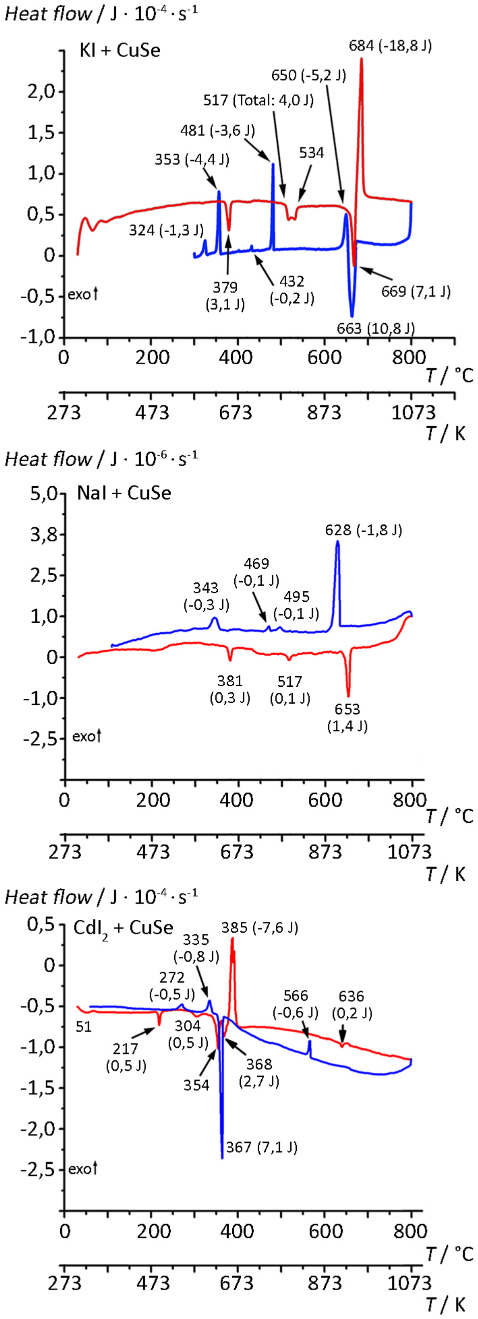

Figure 3.11 DTA curves of flux-CuSe mixtures of 125,0 mg flux and 54,4 mg CuSe (heating at 5 °C min^{-1} in red; cooling at 10 °C min^{-1} in blue)

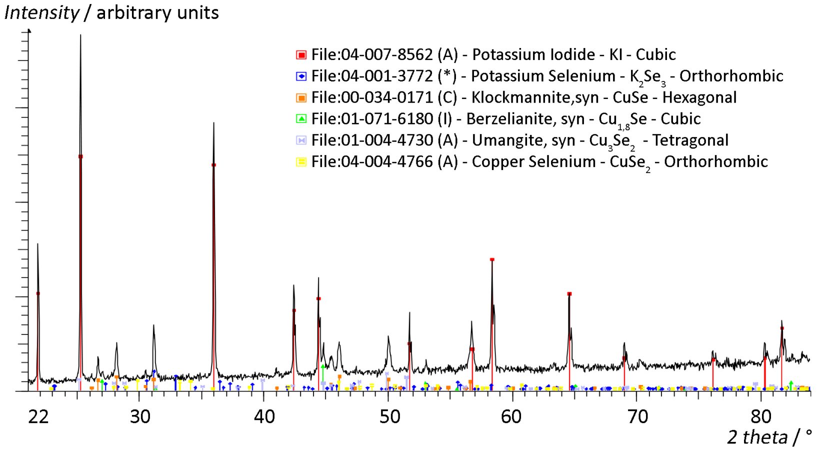

Figure 3.12 XRD pattern of the KI-CuSe mixture heated to 680 ℃ or 953 K (4 h) and quenched; the files from database ICDD-PDF-4+2016 were used

K_2Se (s) + 2 Se (s, l, g) $\rightarrow$ K_2Se_3 (s, l) (3.32)

It was assumed that increasing the vapor pressure of KI above molten KI makes reaction (3.33) more likely; however, in the study of the flux-SnSe systems, this possibility was questioned. Gaseous Se formed after any Se melting in the ampoule, as described above:

2 KI (g) + 3 Se (g) $\rightarrow$ K_2Se_3 (s, l) + I_2 (g) (3.33)

The other possible mechanism of CuI and K_2Se_3 formation is explained below. The melting of KI is compensated by 18,1 J -7,1 J = 11,0 $\pm$ 1,1 J; then, the exothermic effect is -11,0 J -18,8 J = -29,8 J at 684 °C (957 K). In this study the solubility of CuSe in KI was experimentally determined (Section 3.4), and it was 3,6 ± 0,4 mol% of CuSe ($75,3 \cdot 10^{-5}$ mol KI is possible to dissolve $2,8 \cdot 10^{-5}$ mol of CuSe); however, in DTA was used $38,2 \cdot 10^{-5}$ mol of CuSe (see Table 2.2). According to reaction (3.4), 2 mol of CuSe produces 1 mol of Cu_2Se; then, $14,1 \cdot 10^{-5}$ mol of Cu_2Se can dissolve according to reactions (3.34-3.38). Upon cooling, the solidification effect of KI of -5,2 J at 650 °C (923 K) is masked by the endothermic effect of 18,1 J -5,2 J = 12,9 $\pm$ 1,3 J. Then, the reversible process (endothermic) has a total effect of 12,9 J + 10,8 J = 23,7 $\pm$ 2,4 J. The process was detected upon cooling and was used understand the reversible part of the chemical dissolution at 663 °C (936 K) as expressed as 30,0 ± 3,0 kJ mol^{-1} for reaction (3.38) since 1 mol of KI ($75,3 \cdot 10^{-5}$ mol used) produces 1 mol of CuI ($75,3 \cdot 10^{-5}$ mol) and $0,7 \cdot 10^{-5}$ mol of Cu_2Se is required to form 1 mol of CuI. There was no complex formation, but CuI formed in this system, and this (30,0 ± 3,0 kJ mol^{-1}) is attributed to the reversible process and enthalpy of CuI formation in reaction (3.38). According to the reaction, the exothermic enthalpy values for all KI-precursor mixtures are similar to each other since the solubility values are not large. Additionally, a CuI phase was found *via* XRD analysis in the quenched sample at 710 °C (983 K), and it most likely formed during the dissolution process.

However, it was not possible to define by the XRD or Raman data, wether CuI forms during the sample preparation process (Cu-selenides are reacting with I_2) or CuI is formed because of $Cu_{2-x}Se$ chemical dissolution in KI. The dissolved part (determined in Section 3.4) could be explained from the dissolution process as for other flux-binary mixtures since the ΔG at 684 °C (957 K) for the reaction of Cu_2Se with I_2 or KI is positive. The dissolution process is then proposed as follows:

Melting of KI: $2\ KI\ (l) \rightarrow 2\ I^-\ (l) + 2\ K^+\ (l)$ (3.34)

Cu_2Se dissolution in KI: $Cu_2Se\ (s) \rightarrow 2\ Cu^+\ (l) + Se^{2-}\ (l)$ (3.35)

$2\ Cu^+\ (l) + 2\ I^-\ (l) \leftrightarrow 2\ CuI\ (l)$ (3.36)

$2\ K^+\ (l) + Se^{2-}\ (l) \leftrightarrow K_2Se\ (l)$ (3.37)

$2\ KI\ (l) + Cu_2Se\ (s) \leftrightarrow 2\ CuI\ (l) + K_2Se\ (l)$ (3.38)

The disappearance of K_2Se_3 in the XRD pattern after the formation of the CuI phase can be explained by the reversible process since there is a strongly negative ΔG value (-256,1 kJ mol^{-1}) at 684 °C (957 K) for the reversible reaction (3.38). The analogous reversible reaction (3.39) for K_2Se_3 could be written as follows:

$K_2Se_3\ (l) + 2\ CuI\ (l) \rightarrow 2\ KI\ (l) + Cu_2Se\ (s) + 2\ Se\ (l, g)$ (3.39)

Upon cooling, the equilibrium between $Cu_{2-x}Se$ and the Se-rich liquid is reached at a monotectic point (Glazov *et al.*, 2000) and (Chakrabarti & Laughlin, 1981) at 481 °C (754 K) as an endothermic effect of -3,6 ± 0,4 J (see also in Section 3.2). The temperature is shifted due to the cooling process. The weak thermal effect of -0,2 ± 0,0 J, which is observed as the peak at 432 °C (705 K) in the DTA cooling curve, could correspond to the phase transition of γ-CuI to β-CuI as reported by Carré, Pham and Rolin (as cited in Ferrate *et al.*, 1930). This confirms the fact that during melting, the formed CuI was also present in the closed ampoule. In principle, all CuSe is used in the dissolution and formation of CuI. CuSe ($381{,}7\cdot10^{-6}$ mol) is the limiting factor; then, the enthalpy of the phase transition can be expressed as approximately 0,5 ± 0,1 kJ mol^{-1} (or as provided in **Paper I** rounded to 1,0 ± 0,1 kJ mol^{-1}), and it is comparable to the data in Table 1.3. shown in Section 1.7. At 353 °C (626 K) with a thermal effect of -4,4 ± 0,4 J, $CuSe_2$ crystallizes from CuSe + Se solution (Glazov *et al.*, 2000) and (Chakrabarti & Laughlin, 1981) and is detected in the CuSe precursor more intensively. At 324 °C (597 K), the exothermic effect of -1,3 ± 0,1 J belongs to the peritectic transformation of liquid Se + solid CuSe to $CuSe_2$ (Glazov *et al.*, 2000) and (Chakrabarti & Laughlin, 1981).

Paper III reports the study of the **NaI-CuSe** mixture. The thermal effect (in Figure 3.11) at 381 °C (654 K) in the heating curve exhibited an endothermic signal of 0,3 ± 0,0 J, corresponding to the formation of $Cu_{2-x}Se$ because the peritectic decomposition of CuSe. The signal is very weak since dissolution of NaI in liquid Se also likely occurs or it is caused by deviations in the CuSe precursor. The formation of the $Cu_{2-x}Se$ phase was confirmed by its Raman peak at 263 cm^{-1}. The XRD pattern of the sample quenched at 380 °C or 653 K (Figure 3.13) also confirmed the transformation of CuSe to $Cu_{1.8}Se$ (berzelianite), and the formation of CuI was observed. In the Raman spectra, the peaks at 122 and 139 cm^{-1} were attributed to CuI (Appendix 3, Table A2.2). As discussed in **Papers I** and **III**, CuI perhaps formed from Cu-binaries interacting with free I_2 in reactions (3.29-3.31) since it was detected before the melting of the flux. However, as shown in **Paper IV**, more intense CuI formation occurred during Cu_2Se dissolution in the molten flux.

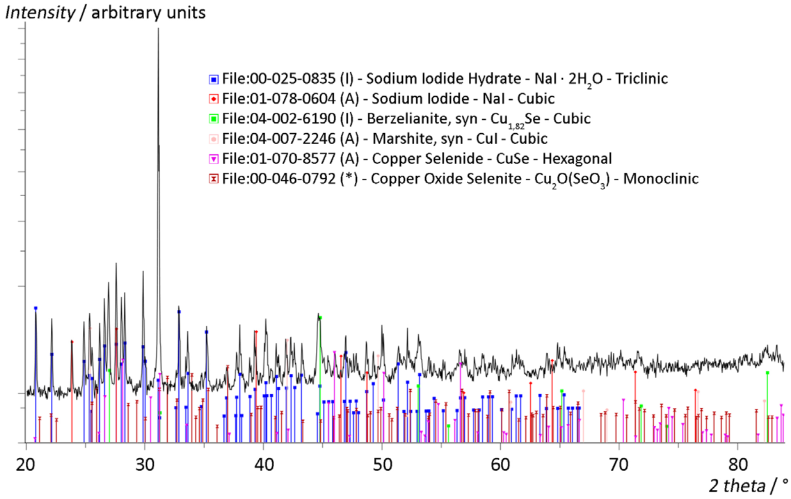

Figure 3.13 XRD pattern of the NaI-CuSe mixture heated to 380 ℃ or 653 K (114 h) and quenched; the files from database ICDD-PDF-4+2016 were used

$Cu_2O(SeO)_3$ could be present due to some impurities, such as CuO (not found in the precursor analysis) and NaI·$2H_2O$, in the flux. NaI·$2H_2O$ forms due to the hygroscopic nature of NaI; see the results of the flux analysis in Section 3.1. Cu could be oxidized with O_2 and H_2O gases in air to form $Cu(OH)_2$ at room temperature at a ΔG = -289,1 kJ mol^{-1}, as in reaction (3.40):

$$2\ Cu\ (s) + 2\ H_2O\ (g) + O_2\ (g) \rightarrow 2\ Cu(OH)_2\ (s) \qquad (3.40)$$

However, according to Cudennec and Lecerf (2003), copper hydroxide $Cu(OH)_2$ is metastable. It easily transforms into more stable compounds, such as copper oxide (CuO), either in the solid state by thermal dehydration or at room temperature in aqueous basic solutions. In the solid state, the transformation is performed at a relatively low temperature of 150 °C (423 K) *via* the following reaction (3.41); however, the database (software HSC6 Chemistry Ver. 6.0.) does not support this reaction due to its positive ΔG:

$$Cu(OH)_2\ (s) \rightarrow CuO\ (s) + H_2O\ (l, g) \qquad (3.41)$$

Since the Se oxidation in O_2 is possible at room temperature *via* reaction (3.42), the ΔG = -171,9 kJ mol^{-1}, according to the database (software HSC6 Chemistry Ver. 6.0.) for:

$$Se\ (s) + O_2\ (g) \rightarrow SeO_2\ (s) \qquad (3.42)$$

The synthesis in Panella, Trump, Marcus, and McQueen (2017) reported, that it is possible to form $Cu_2O(SeO)_3$ from CuO and SeO_2.

The thermal effect at 517 °C (790 K) in the heating curve with a less intense signal at 0,1 ± 0,0 J is similar to that in the mixed KI-CuSe precursor. Additionally, in this mixture, the melting temperature of NaI is drastically reduced to 653 °C (926 K) by a depression effect. The endothermic melting signal of 1,4 ± 0,1 J for NaI is masked by the thermal effect of another exothermic process with a signal of 19,8 J -1,4 J = -18,4 ± 1,8 J, corresponding to some dissolution in the formed liquid phase due to the solvation of Cu_2Se in NaI similar to reactions (3.34-3.38). The thermal effect at 628 °C (901 K) in the cooling curve that has a signal of -1,8 ± 0,2 J can be attributed to the solidification of NaI-CuSe. This signal is covered by another signal for some endotherm with a value of 19,8 J -1,8 J = 18,0 ± 1,8 J. This could be the reversible endothermic precipitation of CuSe from NaI.

The thermal effects at 495 °C or 768 K and 469 °C or 742 K (-0,07 ± 0,0 J or in Figure 3.11 seen as rounded 0,1 J) (in sum of -0,14 ± 0,0 J) in the cooling curve belong to the liquidus line (precipitation of $Cu_{2-x}Se$) and represents the temperature of the monotectic point (formation of liquid L_4), corresponding to the reversible process detected in the heating curve with the peak at 517 °C or 790 K (0,1 ± 0,0 J). See phase diagram in Figure 1.8.

The thermal effect at 343 °C or 616 K (-0,3 ± 0,0 J) in the cooling curve corresponds to the peritectic process detected in the heating curve at 381 °C or 654 K (see the text above). The temperatures could be shifted to the lower side due to impurities or a delay in cooling, also as in the KI-CuSe system.

Additionally, a study of the **CdI_2-CuSe** mixture was performed and published in **Paper IV**. In the DTA curve of this mixture (Figure 3.11), the read-out at 51 °C (324 K) was also observed in the DTA curve of the precursor CuSe. An endothermic peak at 217 °C or 490 K (0,5 ± 0,1 J) corresponded to the melting of Se, according to the database (software HSC6 Chemistry Ver. 6.0.). However, it was not observed in the CuSe precursor; see **Paper IV**. The CuSe precursor was tested *via* XRD and Raman analysis, and no free Se was found. These data suggest that the appearance of free Se is caused by the addition of CdI_2. If Se is released in the system, $CuSe_2$ could be formed by reaction (3.43). The analysis (software HSC6 Chemistry Ver. 6.0.) yielded negative ΔG values for reaction (3.43) up to 168 °C (441 K); however, the phase diagram (shown in Figure 1.8) shows $CuSe_2$ stability up to 322 °C or 595 K (Glazov *et al.*, 2000) and (Chakrabarti & Laughlin, 1981).

$$CuSe\ (s) + Se\ (s, l) \leftrightarrow CuSe_2\ (s) \tag{3.43}$$

The analysis of the XRD pattern (Figure 3.14) of the CdI_2-CuSe sample, which was quenched at 400 °C (673 K), revealed that the following new compounds were formed: Se, $CdCu_2$ and CuI in small concentrations and $Cu_{2-x}Se$ ($Cu_{1.75}Se$, $Cu_{1.5}Se$) and CdSe in relatively high concentrations. The presence of CuI and Se could be explained partially by reactions (3.29-3.31), as described for the KI-CuSe mixture. Unreacted $Cu_{1.75}Se$ and $Cu_{1.5}Se$ were found because the molar ratio for CuSe : CdI_2 in the mixture was 1,85 : 1,65. Raman spectroscopy (Figure 3.15) confirmed the presence of peaks at 122 cm^{-1}, which corresponded to CuI, broad peaks at 168, 198, and 205 cm^{-1}, which corresponded to CdSe; and peaks at 93, 141 and 241 cm^{-1}, which corresponded to Se-Se stretching. These were compared to the references in Appendix 3 (Table A2.2) and in Burns, Rollo, Sarfati and Morgan (1991). The ΔG calculations revealed that CuSe and Cu_2Se can react with CdI_2 at room temperature, reactions (3.44) and (3.45), whereas $CuSe_2$ begins to react *via* reaction (3.46) at 73 °C (346 K) and continues until it is transformed to CuSe and further transformed to Cu_2Se (see graphical data in Figure 3.10 (a)). However, it is not possible to determine if CuI is formed due to reactions with I_2 or exchange reactions. Reaction (3.45) is only possible between Cu_2Se and liquid CdI_2 (and it is reversible) at 526 °C (799 K), according to the ΔG calculations. No reversible process was detected in the DTA curve at 526 °C (799 K), and CuI was only found at low concentrations at 400 °C (673 K), whereas CdSe occurs in high concentrations. This indicates that the formed CuI should be consumed by another process. Other researchers (Ghanbari, Sabet & Salavati-Niasari, 2016) reported the formation of a Cu_2CdI_4 phase at 200 °C (473 K) in the CuI-CdI_2 system with a molar ratio of CuI : CdI_2 = 2 : 1 *via* reaction (3.47). This Cu_2CdI_4 phase presented as irregular nanostructures and aggregates in the SEM images. In Noorussaba (2017), Cu_2CdI_4 was synthesized by the solid-state reaction (3.47) at 300 °C (573 K) in 48 h. The XRD in Ghanbari *et al.* (2016) and the Raman peaks in Noorussaba (2017) for Cu_2CdI_4 have been reported to be similar to those of CuI and CdI_2; therefore, the Raman and XRD analyses could not lead to the determination of the Cu_2CdI_4 phase. The CuI-CdI_2 system exhibits three broad regions of solid solutions based on α-, β- and γ-CuI modifications. CuI and CdI_2 form a complete series of solid solutions with a minimum at the liquidus for 90,0 wt% CdI_2 at 350 °C or 623 K (Blachink & Stöter, 1989). An endothermic peak occurs in the DTA heating curve at 354 °C (627 K); see Figure 3.11. The phase transition of α-CuI (cubic) to β-CuI (hexagonal) occurs at 368 °C (641 K) during the melting of the mixture. The total signal value of 2,7 ± 0,3 J corresponds to these processes. As found in Blachink and Stöter (1989), these phase transitions can vary from 414 °C to 260 °C (687 K to 533 K), depending on the CdI_2 content. The other phase transition of β-CuI (hexagonal) to γ-CuI (cubic) at 407 °C or 680 K (Blachink & Stöter, 1989) seems to be hidden by the dissolution effect at 385 °C or 658 K (-7,6 ± 0,7 J), and only a weak peak splitting is observed. The solubility of CuI in CdI_2 is limited (6,0 mol%), whereas all modifications of CuI are dissolvable in CdI_2. The α-CuI phase has a maximum solubility of 25,0 mol% CdI_2 at 281 °C (554 K) and transforms to a solid solution with the β-phase at 382 °C (655 K). The melting point of CdI_2 shown in Figure 3.3 and the heat of CuSe transformation to Cu_2Se shown in **Paper IV** gave the endothermic effects of 7,1 J and 8,2 J. The exothermic peak at 385 °C (658 K) then leads to the total effect with a value of 2,7-7,1-8,2-7,6 = -20,2 ± 2,0 J. Most likely, dissolution also occurs to produce CuI, as these processes cannot be separated.

$$2\ CuSe\ (s) + CdI_2\ (s) \rightarrow 2\ CuI\ (s) + CdSe\ (s) + Se\ (s,\ l) \qquad (3.44)$$

$$Cu_2Se\ (s) + CdI_2\ (s,\ l) \leftrightarrow 2\ CuI\ (s,\ l) + CdSe\ (s) \qquad (3.45)$$

$$2\ CuSe_2\ (s) + CdI_2\ (s) \rightarrow 2\ CuI\ (s) + CdSe\ (s) + 3\ Se\ (s,\ l) \qquad (3.46)$$

$$2\ CuI\ (s,\ l) + CdI_2\ (s,\ l) \leftrightarrow Cu_2CdI_4\ (s,\ l) \qquad (3.47)$$

As the XRD analyses revealed the formation of Cu_2Cd in the sample quenched at 400 °C (673 K) and because in this study was not find elemental Cu and Cd in the binary precursor (CuSe) or in the CdI_2 flux, it was assumed that ε-Cu_3Cd_{10} formed first *via* reaction (3.48) but that the formed I_2 and SnI_4 quickly evaporated and did not react with any of compounds. In theory, liquid SnI_4 can react with Cu_2Se (ΔG = -33,48 kJ mol^{-1}) at 217 °C (490 K) *via* reaction (3.49); however, at 400 °C (673 K), the ΔG of reaction (3.23) (in the previous item for the CdI_2-SnSe mixture) is also negative, and $SnSe_2$ can react with CdI_2; see Figure 3.10 (a). This chain of reactions will then result in gaseous SnI_4 and CdSe as products. SnI_4 was not detected in the sample because it had probably condensed at the top of the ampoule (*i.e.*, in the lowest-temperature region).

$$Cu_3Sn\ (s) + 10\ CdI_2\ (s) \rightarrow \varepsilon\text{-}Cu_3Cd_{10}\ (s) + SnI_4\ (g) + 8\ I_2\ (g) \qquad (3.48)$$

$$SnI_4\ (l) + 2\ Cu_2Se\ (s) \rightarrow SnSe_2\ (s) + 4\ CuI\ (s) \qquad (3.49)$$

As it was not possible to find process that could be attributed the signal of 0,5 ± 0,1 J in the DTA heating curve at 304 °C (577 K) (Figure 3.11), this signal was attributed to the eutectic melting of Cd (according to reaction (3.50)). In Okamoto and Okamoto (2013), it was reported to occur at 317 °C (590 K). The melting effect of Cu_3Cd_{10} in accordance with reaction (3.51) at 397 °C or (670 K) (Okamoto & Okamoto, 2013) was not detected in the DTA heating curve, and we assume that it is masked by the exothermic effect at 385 °C (658 K).

$$L \leftrightarrow \varepsilon\text{-}Cu_3Cd_{10}\ (s) + Cd\ (l) \qquad (3.50)$$

$$2\ \varepsilon\text{-}Cu_3Cd_{10}\ (s) \rightarrow 3\ Cu_2Cd\ (l) + 17\ Cd\ (l) \qquad (3.51)$$

Perhaps, Cd formed *via* reactions (3.50-3.51) and did not react with Cu-selenides because no elemental Cu was found and because reaction (3.52) has a negative ΔG. In this system, Se, which was mostly released from CuSe to transform to $Cu_{2-x}Se$ (reaction (3.4)) and to react with Cd, can result in the formation of CdSe (3.52) at 304 °C or 577 K (ΔG = -139,3 kJ mol^{-1}).

$$Cd\ (s, l) + Se\ (l) \rightarrow CdSe\ (s) \qquad (3.52)$$

To investigate the next endothermic peak at 636 °C or 909 K (0,2 J), a sample of the CdI_2-CuSe mixture was prepared and heated to 740 °C (1013 K) for 4 h. The phases found *via* XRD (Figure 3.14) were as follows: Se (at low concentrations), CdI_2, $Cu_{1.5}Se$ and CdSe (at relatively high concentrations). The Raman spectrum (Figure 3.15) confirmed the phases. Broad signals at 168 and 198 cm^{-1} can be attributed to CdSe; the signals at 93, 141 and 241 cm^{-1} correspond to Se-Se stretching; and a signal at 110 cm^{-1} corresponds to CdI_2, as shown in Appendix 3, Table A2.2. The most obvious change is that the CuI phase disappeared; however, the concentrations of CdI_2 and $Cu_{2-x}Se$ increased. This can be explained by the reversible reaction of (3.45). Cu_2Cd was no longer present, probably due to reaction (3.53) at 639 °C (912 K) to form $Cu_{2-x}Se$ and CdSe. Similar reactions have been reported in Schurr *et al.* (2009) for Cu-Zn and Cu-Sn alloys. Additionally, the undissolved β-$Cu_{2-x}Se$ melts at 636 °C or 909 K (in which the total signal of these processes is 0,2 J), according to the Cu-Se phase diagram (Figure 1.8). It was not possible to make significant conclusions from the EDX analyses of the composition of the CuSe single-crystalline sample, which was heated to 740 °C (1013 K) in CdI_2, quenched and then washed.

$CdCu_{2-x}$ (l) + 2 Se (l) $\leftrightarrow$ $Cu_{2-x}Se$ (s) + CdSe (s) (3.53)

In the cooling curve, the thermal effect at 566 °C (839 K) corresponds to cross between the $L_3 = L_3 + L_2$ mixtures of liquids in the Cu-Se phase diagram in Figure 1.8, according to Glazov *et al.* (2000) and Chakrabarti and Laughlin (1981). This occurs as a signal of -0,6 ± 0,1 J, which is less intense than that in the CuSe DTA curve, as some of the Cu_2Se reacted with CdI_2 to form CuI. The endothermic peak at 367 °C (640 K) corresponds to a number of reversible processes, which were detected as a DTA signal of 7,1 ± 0,7 J. Of note, the thermal effect of CdI_2 solidification was masked. Its value could not be determined because some of the CdI_2 participated in the reactions. Free Se appears to be available in the system, and the peak at 335 °C or 608 K (-0,8 ± 0,1 J) in the cooling curve corresponds to the precipitation of $CuSe_2$ from the melt according to reaction (3.43), as also reported in Glazov *et al.* (2000) and Chakrabarti and Laughlin (1981) at 332 °C (605 K). The peak at 272 °C or 545 K (-0,5 J) can be attributed to the cross between the $L_3 = L_3 + L_2$ mixtures of liquids in the Cu-Se phase diagram Figure 1.8 (Glazov *et al.*, 2000) and (Chakrabarti & Laughlin, 1981) or the formation of the solid solution of β-CuI with CdI_2 upon cooling, as reported in Blachink and Stöter (1989) at 271 °C (544 K). In this system, since free Se was observed after cooling, it indicated that reaction (3.54) did not occur and that gaseous CdI_2 practically did not form in the closed ampoules.

CdI_2 (g) + Se (g) $\rightarrow$ CdSe (s) + I_2 (g) (3.54)

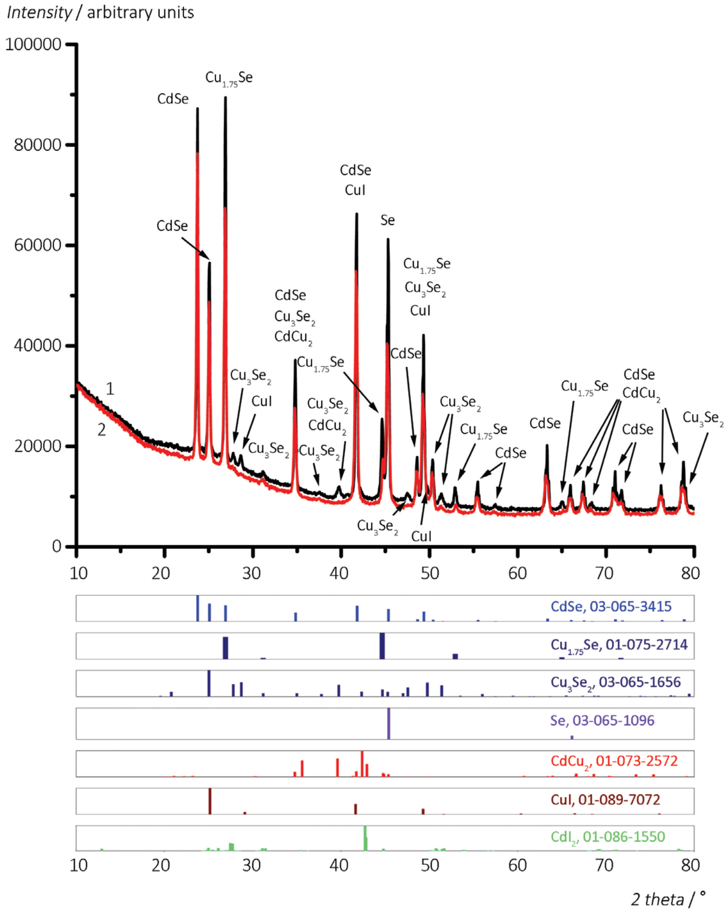

Figure 3.14 XRD patterns of the CdI_2-CuSe sample quenched at 400 ℃ or 673 K (black line 1) and at 740 ℃ or 1013 K (red line 2). For phase detection, the files from database JCDPS-2009 were used

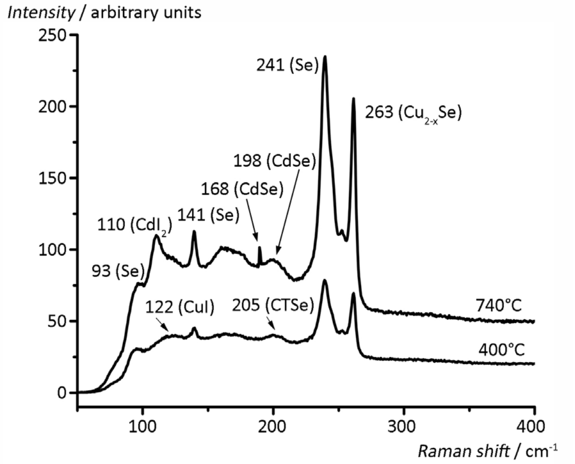

Figure 3.15 Raman spectra of CdI_2-CuSe quenched at 400 ℃ (673 K) and 740 ℃ (1013 K)

3.5.4 Flux-SnSe-CuSe

The **KI-CuSe-SnSe** mixture was described in **Papers I** and **II**. In the DTA heating curve for this mixture (Figure 3.16), there was weak endothermic effect of 0,3 ± 0,0 J at 379 °C or 652 K (similar to the analysis for CuSe in Section 3.2 and **Paper IV**), which corresponds to the CuSe transformation to Cu_2Se with the release of Se, reaction (3.4). The endothermic effect is not as large as could be expected for CuSe transformation to $Cu_{2-x}Se$, since some exothermic formation reactions simultaneously occur. According to the XRD results, the following phases were found in the sample quenched at 400 °C (673 K): $Cu_{0,714}Sn_{0,214}Se_{1,072}$, $Cu_{1,8}Se$, Cu_2SnSe_3, $Cu_{7,16}Se_4$, KI, CuI (probably formed during sample delivery to XRD), and $SnSe_2$. In this study, this effect was mostly masked by $SnSe_2$ formation, and the compensated value did not matter on its own if Se (l) or Se (g) formed since the ΔH is this same at -6,0 kJ mol^{-1} at 377 °C (650 K). $SnSe_2$ forms *via* two mechanisms: reaction (3.55) or the sequential reactions of (3.4) + (3.24). Reaction (3.55) can occur at temperatures below flux melting if the particles interact; however, it proceeds in very small amounts, since the task of the flux is to keep particles separate up to flux melting and then perform the desired reaction. For reaction (3.55), the ΔG values in the entire experimental temperature range are negative; see Figure 3.17. At room temperature, ΔG is -10,4 kJ mol^{-1}. The $SnSe_2$ formation in bulk occurs at 377-383 °C (650-656 K) when reaction (3.4) releases Se from the CuSe precursor. Additionally, there is another Se source from CuI formation due to Cu-selenide reactions with I_2. Then, reaction (3.24) can proceed, as described in Item 3.5.2, at 377 °C (650 K) with ΔG = -12,9 kJ mol^{-1}.

$$2\ CuSe\ (s) + SnSe\ (s) \rightarrow Cu_2Se\ (s) + SnSe_2\ (s) \qquad (3.55)$$

Nevertheless, in **Paper III,** the possibility of solid-state reaction (3.55) was recognized, and in **Paper V,** the ΔG dependency of temperature was plotted (see Figure 3.17). CuI was formed before the melting of the flux, similar as described for the KI-CuSe system. The formation of the abovementioned compounds was confirmed by Raman analysis. The intensive peaks at 226 and 246 cm^{-1} were attributed to the copper tin selenide phase with a defect structure of $Cu_{3,34}SnSe_5$, as found by XRD (Figure 3.18 (a) and (b)). According to the data gathered in Appendix 3 (Table A2.2), the peaks at 95 and 122 cm^{-1} belong to KI and CuI; however, 178 and 204 cm^{-1} belong to Cu_2SnSe_3; 212 cm^{-1} belongs to SnSe, 233 and 237 cm^{-1} belong to Se; and 258 cm^{-1} belongs to $Cu_{2-x}Se$. Before the melting of KI, the formation of the CTSe ternary compound formation is possible in several ways (but again in small amounts). However, of note, the interactions of impurities are excluded because their effect on the formation pathway is negligible. The CTSe formation processes below flux melting can be described as follows:

1) CTSe can be formed from CuSe and SnSe *via* a reduction-oxidation reaction, if those particles interact; however, it is not epitaxially supported from low-temperature SnSe; high-temperature SnSe forms only at 520,2 °C (793,2 K) (see Figure 1.9), and CuSe is not present at that temperature due to its phase transition at 377 °C (650 K), (see Figure 1.8);

2) If Cu_2Se and $SnSe_2$ formed according to reaction (3.55) or if (3.4) + (3.24) proceeded CTSe can be formed via an epitaxial reaction (1.13) as described in Item 1.4.2; this is more likely;

3) From Cu_2Se, Se and SnSe as in reaction (1.11) described in Item 1.4.2, CTSe can be formed; however, this is not epitaxially supported.

The free Se in the system also causes the formation of $Cu_{3,34}SnSe_5$, as suggested by reaction (3.56):

$$Cu_2SnSe_3\ (s) + CuSe_2\ (l) \rightarrow Cu_3SnSe_5\ (s) \tag{3.56}$$

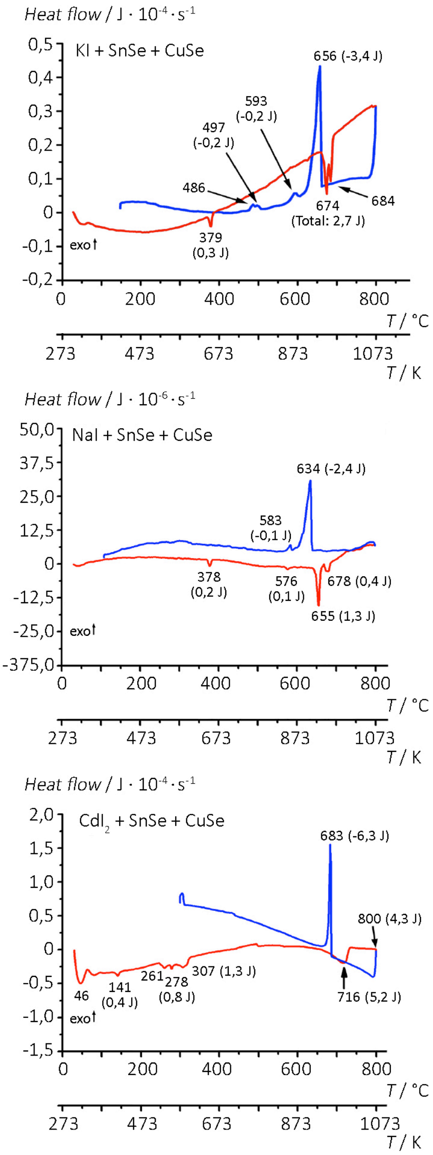

Figure 3.16 DTA curves of the flux-SnSe-CuSe mixtures with 125,0 mg flux, 40,8 mg SnSe and 54,4 mg CuSe (heating at 5 °C min^{-1} in red; cooling at 10 °C min^{-1} in blue)

The largest differences in the KI-SnSe-CuSe mixture compared with the DTA of the CuSe precursor are that there was no monotectic point (at 523 °C or 796 K) and no melting of CuSe (at 533 °C or 806 K) observed in the DTA heating curve. This effect at

517-534 °C or 790-807 K was detected in the KI-CuSe and NaI-CuSe mixtures and was correlated with the temperature-dependent change in composition of the liquid phase, which corresponds to the increase in the liquidus line from 52,5 at.% Se (monotectic composition at 523 °C or 796 K) to 50,0 at.% Se (in CuSe). This corresponds with the Cu-Se phase diagrams given in Glazov *et al.* (2000) and Chakrabarti and Laughlin (1981). The absence of this effect in the KI-SnSe-CuSe mixture means that all Se produced from 1,85 mol CuSe with 0,925 mol of SnSe formed Cu_2Se and $SnSe_2$ in the bulk. Additionally, the elemental analyses of Se in Section 3.3 showed that Se moves free in the closed ampoule because of the existence of a liquid or gaseous phase and can react with SnSe to form $SnSe_2$ in the bulk. More pronounced endothermic peaks compared with those presented in **Paper II** were found and reported in **Paper I** (at 574 °C or 847 K and 626 °C or 899 K). The effect at 574 °C (847 K) could be connected to the Cu-Se phase diagram shown in Figure 1.8 (Glazov *et al.*, 2000) and (Chakrabarti & Laughlin, 1981); this was also observed for the CdI_2-CuSe mixture. The endothermic peak at 626 °C (899 K) can be attributed to the melting of the eutectic mixture of SnSe-$SnSe_2$ (Bletskan, 2005). The difference in the shape of the DTA curves can be explained by differences in the two DTA samples used for the experiments reported in **Paper I** *vs* **Paper II**, where the size of precursor particles and, therefore, the solid contact area between particles was different. Furthermore, the solid flux between precursor particles impeded the reactions. $SnSe_2$ and $Cu_{2-x}Se$ are not consumed practically in the bulk for Cu_2SnSe_3 formation in solid-state reactions; however, the CTSe mostly forms in the molten flux, producing a more pronounced shape for the DTA curve (in **Paper I**). However, in the DTA sample used for **Paper II,** for some reason, there had been an interaction between the $SnSe_2$ and $Cu_{2-x}Se$ phases before melting of the flux. The melting of the KI-CuSe-SnSe mixture was detected as the typical endothermic effect at 675 °C (948 K) followed by an exothermic effect at 683 °C (956 K), as described in **Paper I**, whereas in the results of **Paper II,** two split peaks at 674-684 °C (947-957 K) were observed. This could be explained due to some delay in the exothermic dissolution and heat compensation immediately after melting of KI; however, the summary heat values in those experimental results are the same within experimental error. The thermal effect of the KI melting process (2,7 ± 0,3 J) is masked by the exothermic effect of intense Cu_2SnSe_3 formation of 18,1 J -2,7 J = 15,4 ± 1,5 J at 684 °C (957 K). From this value, the enthalpy of reaction (1.13), as described in Item 1.4.2 from Cu_2Se and $SnSe_2$ at 684 °C or 957 K (-26,0 ± 2,6 kJ mol^{-1}), was calculated per reacting amount of the binaries; see Table 2.2 in Section 2.7. Thus, the intense Cu_2SnSe_3 formation occurs during the melting process of KI, while in small amounts, it could be formed below flux melting. During the cooling cycle, the KI solidification at 656 °C (929 K) is covered with the endothermic thermal effect of 18,1 J -3,4 J = 14,7 ± 1,5 J, and it corresponds to the reformation process of CTSe from the melt with an enthalpy of 25,0 ± 2,5 kJ mol^{-1}. At 593 °C or 866 K (-0,2 ± 0,0 J), there was solidification of γ-CuI that was formed during dissolution since the DTA ampoule was closed; see Item 3.5.3. This could be possible due to the CTSe melting and decomposition into Cu_2Se and $SnSe_2$; see the phase diagram in Figure 1.11. The amount of CuI participating in this transformation is approximately 10^{-4} mole. Upon cooling, the equilibrium between $Cu_{2-x}Se$ and Se-rich liquid is reached at 497 °C (770 K) and 486 °C or 759 K (-0,2 ± 0,0 J), as also described previously (Glazov *et al.*, 2000) and (Chakrabarti & Laughlin, 1981); see Figure 1.8. Cooling causes a shift in temperature because of the delay in the processes.

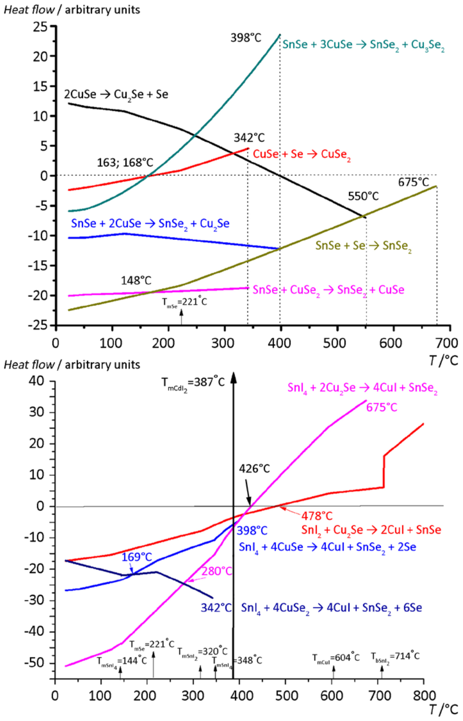

Figure 3.17 Results of (software HSC6 Chemistry Ver. 6.0.) calculations for the considered reaction

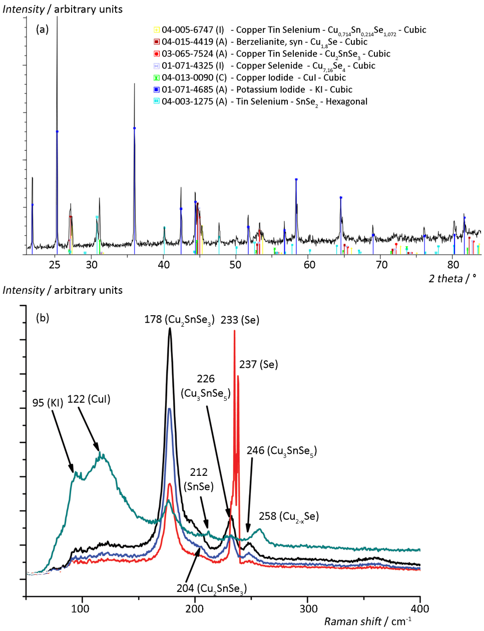

Figure 3.18 Measurements of the KI-SnSe-CuSe mixture that was heated to 400 ℃ or 673 K (4 h) and quenched: (a) XRD pattern, the files from database ICDD-PDF-4+2016 were used; (b) Raman spectra

For **NaI-CuSe-SnSe**, the endothermic peak at approximately 378 °C (651 K) was present in te heating curves of both mixtures (NaI-CuSe-SnSe and KI-CuSe-SnSe) with thermal effects producing similar values of 0,2 ± 0,0 J. CuSe decomposition was compensated for by $SnSe_2$ formation. This effect at this temperature was also observed in all the DTA heating curves in which CuSe was one of the precursors. Most intensively, it was observed for the CuSe precursor; see **Paper IV**. This effect is described as the CuSe phase transformation to $Cu_{2-x}Se$ + Se. In the sample quenched at 380 °C (653 K), $Cu_{1.8}Se$ (berzelianite) was confirmed by XRD analysis, and the $Cu_{2-x}Se$ phase was detected by a Raman peak at 263 cm^{-1}; this is the same as that reported in Ishii *et al.* (1993); see Appendix 3, Table A2.2. At a temperature below flux melting, CuI is formed as described above in the flux-CuSe system. CuI was confirmed by XRD and by the Raman shift at 122 cm^{-1} (Appendix 3, Table A2.2). The presence of $SnSe_2$ in the XRD pattern can be explained as in the KI-SnSe-CuSe system. Also SnSe peaks at 130 and 150 cm^{-1}, $SnSe_2$ at 109 and 180 cm^{-1} and Se at 240 cm^{-1} were found in the Raman spectra of the sample heated and quenched at 580 °C or 853 K. Free Se may have resulted from CuI formation at room temperature because of reaction with I_2 in the opened ampoule. However, the Se formed from CuSe phase transformation is usually consumed *via* $SnSe_2$ formation. Some unreacted SnSe could be found due to the applied ratio of 1,85 mole of CuSe and 1 mole SnSe. Cu_2SnSe_3 formation in the sample that was quenched at 380 °C (653 K) was confirmed by Raman measurements with Raman peaks at 179, 235, and 250 cm^{-1}. Possibilities for CTSe formation were described in detail for the KI-SnSe-CuSe mixture. Additionally, here, no monotectic point (at 523 °C or 796 K) and no melting of CuSe (at 533 °C or 806 K) were observed in the DTA heating curve. This means that Cu_2Se and $SnSe_2$ formed in the bulk, as described for the KI-SnSe-CuSe mixture.

The other thermal effects in the DTA curves of NaI-SnSe-CuSe can be described as follows:

- The endothermic peak at 576 °C or 849 K (0,05 ± 0,0 J) in the heating curve and at 583 °C or 856 K (-0,08 ± 0,0 J) in the cooling curve (in Figure 3.16 effects of 0,1 J and -0,1 J) can be attributed to the eutectic point of Cu_2SnSe_3-$SnSe_2$ (Dudchak & Piskach, 2003);
- Endothermic melting of NaI (19,8 ± 2,0 J, see Fig. 3.3) was observed at 655 °C (928 K) as a summary thermal effect with a value of 1,3 ± 0,1 J because it was partially masked by the following exothermic effect value of 1,3 J -19,8 J = -18,5 ± 1,9 J. The exothermic process can be attributed to the Cu_2SnSe_3 formation as reaction (1.13) described in Section 1.4.2 with an enthalpy of -32,0 ± 3,2 kJ mol^{-1} at the NaI melting temperature (661 °C or 934 K). However, the formation of ternary compound CTSe in the bulk from Cu_2Se and $SnSe_2$ more likely occurs in the liquid flux. The reversible process (30,0 ± 3,0 kJ mol^{-1}) can be calculated from the NaI solidification effect of the detected signal value of -2,4 ± 0,2 at 634 °C (907 K), where it is covered by the endothermic process of 19,8 J -2,4 J = 17,7 ± 1,8 J.
- The melting enthalpy of CTSe of 1,0 ± 0,1 kJ mol^{-1} was determined only for the first heating curve at 678 °C or 951 K (0,4 ± 0,0 J). The experimental heat of fusion for CTSe has not been previously reported. However, it was not detected during the cooling cycle, possibly because of the multiple overlapping thermal effects.

The CdI2-CuSe-SnSe system is more complicated, and the investigations occurred inseveral stages (**Paper V**). The reactions occurring in the two separate systems of CdI_2-CuSe and CdI_2-SnSe were discussed in **Paper IV** and are very likely to occur in the CdI_2-CuSe-SnSe system.

The additional reactions can be basically divided into three groups: 1) reactions between Cu-Se and Sn-Se compounds; 2) reactions with CdSe, causing the formation of $Cu_2CdSnSe_4$; and 3) reactions with iodide compounds. In the DTA curve of the CdI_2-CuSe-SnSe mixture, the first peak at 141 °C or 414 K (Figure 3.16) could be attributed to the melting of SnI_4 as in the database (software HSC6 Chemistry Ver. 6.0.) since the formation of SnI_4 in the CdI_2-SnSe mixture was found, as discussed in **Paper IV**. If the heat of fusion of SnI_4 is 4,5 kJ mol^{-1} according to the database, then from the heat effect expressed as (0,4 ± 0,0 J), the corresponding amount of melted SnI_4 would be $18{,}4 \cdot 10^{-6}$ mol. In the Raman spectra of the CdI_2-CuSe-SnSe sample heated to 250 °C (523 K) and held at that temperature for 48 h, the peaks at 94 and 122 cm^{-1} may correspond to CuI. CuSe also has a Raman peak at 94 cm^{-1}; however, CuSe must be excluded from consideration since no peak was observed at 263 cm^{-1}. The CTSe forms at considerably low temperatures of 250 °C (523 K) or even at room temperature from solid-state reactions, as described for the KI-SnSe-CuSe mixture. First, Cu_2Se and $SnSe_2$ formed. CTSe could then form *via* an epitaxy-supported reaction from particles in locations where interactions occur. The Raman peak at 178 cm^{-1} can be attributed to Cu_2SnSe_3, and the peak at 186 cm^{-1} can be attributed to $SnSe_2$. The peak at 231 cm^{-1} could correspond to Se-Se stretching or to the less intense Cu_2SnSe_3 peak in the spectra, which was interpreted according to data in Appendix 3, Table A2.2. The mixture of CuSe-SnSe should produce the Cu_2Se and $SnSe_2$ phases according to reaction (3.55), as the value of ΔG at 23 °C (296 K) is -10,4 kJ mol^{-1} (Figure 3.17). Raman analysis revealed that no CuSe or Cu_2Se phases were detected. The absence of CuSe and/or Cu_2Se suggests that reaction (3.57) occurs and forms Cu_3Se_2, probably due to the presence of liquid-phase SnI_4, which increases the contact area between solid particles. Reactions (3.55) and (3.57) will proceed up to 377 °C or 650 K (based on the Cu-Se phase diagram in Figure 1.8). At higher temperatures, CuSe will not exist due to the transformation reaction of CuSe to $Cu_{2-x}Se$ and Se (Glazov *et al.*, 2000) and (Chakrabarti & Laughlin, 1981). As the CuSe : SnSe molar ratio of 1,85 was used, it is clear from reaction (3.55) that some SnSe will remain unreacted due to a deficiency of CuSe. No negative ΔG was found for the reaction of $SnSe_2$ with CuSe, which could form $CuSe_2$. The $Cu_{2-x}Se$ formed in reactions (3.4) and (3.55) may be transformed into compounds, such as CuSe until 377 °C (650 K) or such as $CuSe_2$ until 322 °C (595 K) according to the database (software HSC6 Chemistry Ver. 6.0.), if Cu_2Se interactions take place with Se, as was found and described in **Paper IV**, in the CdI_2-CuSe system. The comparison of data in Figure 3.17 suggests that Se is more likely to be consumed in the formation of $SnSe_2$. However, after the melting of CdI_2 (at T > 381 °C or 654 K), due to the increased contact in the molten flux between reagents, only $Cu_{2-x}Se$ and $SnSe_2$ can form.

$$SnSe\ (s) + 3\ CuSe\ (s) \rightarrow Cu_3Se_2\ (s) + SnSe_2\ (s) \qquad (3.57)$$

Additionally, in **Paper IV**, it was reported that SnI_4 had already formed at room temperature in the reactions of SnSe or $SnSe_2$ with I_2. After melting of the CdI_2-SnSe mixture, SnI_4 was undetectable in the solid quenched mixture because SnI_4 has a low boiling point (348 °C or 621 K), according to the database (software HSC6 Chemistry Ver. 6.0.), and could evaporate into the gas phase and condense on the walls of the ampoule. SnI_4 can react with copper selenides *via* reactions (3.58) and (3.59). A comparison of these data with those in Figure 3.17 revealed that reaction (3.58) is reversible at 426 °C (699 K), whereas reactions (3.59) and (3.60) can proceed until 398 °C (671 K) and 342 °C (615 K), respectively (see Figure 3.17).

SnI_4 (s, l, g) + 2 Cu_2Se (s) $\leftrightarrow$ $SnSe_2$ (s) + 4 CuI (s, l) (3.58)

SnI_4 (s, l, g) + 4 CuSe (s) $\leftrightarrow$ $SnSe_2$ (s) + 4 CuI (s, l) + 2 Se (s, l, g) (3.59)

SnI_4 (s, l, g) + 4 $CuSe_2$ (s) $\leftrightarrow$ $SnSe_2$ (s) + 4 CuI (s, l) + 6 Se (s, l, g) (3.60)

The DTA curve of the CdI_2-CuSe-SnSe mixture revealed additional peaks at 261 °C (534 K) and 278 °C or 551 K (0,8 ± 0,1 J). CuI was no longer present in the corresponding quenched sample (270 °C or 543 K), and an additional formed compound (Cu_2SnSe_4) was detectable *via* the Raman shifts at 190 and 225 cm^{-1} (a reference sample of Cu_2SnSe_4 was synthesized, and Raman measurements were performed). At these temperatures, several processes are possible: 1) free molten Se (T_m = 221 °C or 494 K) (according to software HSC6 Chemistry Ver. 6.0.) could be formed *via* reactions (3.59) and (3.60); 2) Cu_2SnSe_4 could form from Cu_2SnSe_3 and Se according to reaction (3.61), as suggested in Tomashik, Lebrun, and Perrot (2006), thus causing a shift in the Raman peak at 178 cm^{-1} from the characteristic Cu_2SnSe_3 compound to 190 cm^{-1}, indicating the formation of the Cu_2SnSe_4 phase; or 3) the formation of an eutectic solid solution of CdI_2 with β-CuI at 271 °C (544 K) and with γ-CuI could occur because the maximum solubility is 25,0 mol% CdI_2 at 281 °C or 554 K (Blachink & Stöter, 1989). The formation of solid solutions explains the absence of analytical signs of pure CuI. The next DTA peak at 307 °C or 580 K (1,3 ± 0,1 J) can be explained by the processes described in **Paper IV** for the CdI_2-CuSe system, where the DTA peak at 304 °C (577 K) was attributed to the eutectic melting of ε-Cu_3Cd_{10}. On the DTA curve of the CdI_2-CuSe-SnSe mixture, the peritectic transformation of CuSe to $Cu_{2-x}Se$ with the release of Se at 383 °C (656 K) was not observed, as was observed in the DTA curve of CuSe shown in **Paper IV**. Additionally, no effect due to CdI_2 melting was observed. This result suggests that these compounds were completely consumed during the formation of the CuI-CdI_2 solid solution (Blachink & Stöter, 1989).

Cu_2SnSe_3 (s) + Se (l) $\leftrightarrow$ Cu_2SnSe_4 (s) (3.61)

Raman studies of the quenched sample at 390 °C (663 K), which is just slightly above the expected CdI_2 melting point, showed peaks at 140 and 241 cm^{-1} (corresponding to Se) and a peak at 163 cm^{-1} (unknown or $Cu_2CdSnSe_4$); data shown in Appendix 3, Table A2.2. Additionally, the Raman peak at 196 cm^{-1} (A_1 mode of CZTSe) was found to shift to 188 cm^{-1}, which represents the formation of the $Cu_2CdSnSe_4$ phase (Altosaar *et al.*, 2008; Grossberg *et al.*, 2011). CdSe could form *via* unreacted SnSe and CdI_2; this reaction begins at 348 °C (621 K), as shown in **Paper IV,** and reaction (3.62) can proceed as follows:

Cu_2SnSe_3 (s) + CdSe (s) $\leftrightarrow$ $Cu_2CdSnSe_4$ (s) (3.62)

Since no CdSe or CuI phases were found in the quenched sample at 390 °C (663 K), the exchange reaction of Cu_2Se with CdI_2 was excluded. No change in the phase composition was found in the sample quenched at 750 °C (1023 K) compared with the previous one quenched at 390 °C (663 K). The DTA peak was 716 °C or 989 K (5,2 ± 0,5 J); therefore, it could be attributed to a eutectic reaction (3.63), similar to that in

Tomashik *et al.* (2006). The peaks at 771 °C and 793 °C (1044 K and 1066 K) is attributable to the melting of $Cu_2CdSnSe_4$ (4,3 ± 0,4 J), as reported by Matsushita *et al.* at 780 °C (1053 K) (Adachi, 2015). However, solidification of $Cu_2CdSnSe_4$ was not observed in the DTA cooling curve, which was likely caused by the solid phase CdSe separation in the liquid phases during $Cu_2CdSnSe_4$ melting. The $Cu_2CdSnSe_4$ formation reaction between solid CdSe and the liquid probably requires more time. The CdSe phase was not observed in the Raman spectra, as reaction (3.64), (see **Paper IV**) is possible at temperatures above 526 °C (799 K). The $Cu_{2-x}Se$ Raman peak at 263 cm^{-1} was also detected.

$$L \leftrightarrow Cu_2SnSe_3\ (s) + SnSe_2\ (l) \tag{3.63}$$

$$2\ CuI\ (l) + CdSe\ (s) \leftrightarrow Cu_2Se\ (s) + CdI_2\ (l,\ g) \tag{3.64}$$

No changes in the phase composition were detected during the cooling of another sample to 620 °C (893 K). The exothermic effect at 683 °C or 956 K (-6,3 ± 0,6 J) was attributed to the solidification of Cu_2SnSe_4, which occurs at a lower temperature than that of Cu_2SnSe_3 (697 °C or 970 K) (Tomashik *et al.*, 2006). According to XRD analysis (Figure 3.19), $Cu_2CdSnSe_4$, $Cu_{1.8}Se$, $Cu_{1.78}Se$, CdI_2, CuI, and CdSe phases were present in the sample of the opened DTA ampoule, and their formation can be explained by reactions (3.62-3.64). SnI_4 and $Cu_3(CO_3)_2(OH)_2$ (as 2 $CuCO_3$-$Cu(OH)_2$) were also found. The presence of SnI_4 is explained by its condensation from the gaseous phase in the closed ampoule. The formation of $Cu_3(CO_3)_2(OH)_2$ was probably caused by the 1,0 % impurities in the CdI_2 flux (see **Paper IV**) and upon handling CdI_2 in air. $Cu(OH)_2$ formation was described for the NaI-CuSe mixture; see reaction (3.40). However, a more detailed description of these impurities will not be provided since it is not the focus of this thesis.

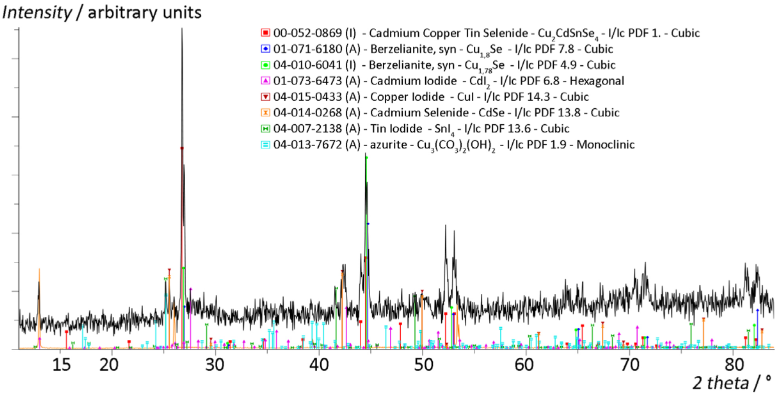

Figure 3.19 XRD pattern for the opened DTA ampoule of the CdI_2-SnSe-CuSe mixture after cooling; the files from database ICDD-PDF-4+2016 were used

3.5.5 Flux-ZnSe-SnSe-CuSe

Here, will be describe the possible ways in which CZTSe can be formed from crystallographically preferred a) Cu_2Se, $SnSe_2$, and ZnSe; b) CTSe and ZnSe or c) thermodynamically preferred CuSe, SnSe, and ZnSe. The results are compared to CZTSe formation described in the literature.

Overall, the **KI-CuSe-SnSe-ZnSe** mixture was discussed in **Paper I**, **Paper II** and Leinemann *et al.* (2011). XRD and Raman analyses of the sample quenched at 250 °C (523 K) and 270 °C (543 K) showed that only the binaries and the flux (KI at 95 cm^{-1}) were present. The phases determined by Raman included $Cu_{2-x}Se$ (at 263 cm^{-1}), ZnSe (at 204 and 250 cm^{-1}), and SnSe (at 109 cm^{-1} and 147 cm^{-1}), which are the derived precursors. The appearance of CuI in the XRD spectra and the Raman signal at 122 cm^{-1} for the sample heated to 250 °C (523 K) confirmed reactions (3.29-3.31) with I_2 at room temperature in the opened ampoule since CuI was detected before the melting of the flux. Moreover, in the Raman analyses of the samples quenched at 250 °C (523 K) and 270 °C (543 K), Se was detected (Raman peaks at 139 cm^{-1} and 240 cm^{-1}), which confirms the interaction with free I_2 at room temperature during sample preparation, whereas Se was not found *via* XRD, probably due to its amorphous nature. Se cannot be released from CuSe at this temperature, and the presence of $SnSe_2$ (185 cm^{-1} and 187 cm^{-1}) and $Cu_{2-x}Se$ (Cu_3Se_2 in XRD) could be explained by room temperature reaction (3.55). However, these reactions do not proceed in the bulk. The appearance of iodides was found to be random. This could be due to the random presence of I_2 during the sample preparation for XRD and Raman. This occasional presence of I_2 was confirmed by the fact that, primarily in the *in situ* processes simulated by DTA, no melting of the iodide compounds or elemental Se was observed. However, in a washed sample heated and quenched at 250 °C (523 K), only CZTSe was found because of its characteristic Raman peaks. This confirms CZTSe formation at room temperature below flux melting in small amounts because no effect was observed in the DTA curves (Figure 3.20) up to 379 °C (652 K). Since it is known from a prior study (Hergert & Hock, 2007) that low-temperature SnSe (until 520,2 °C or 793,2 K; see the phase diagram in Figure 1.9) cannot participate in the epitaxy. First, *via* exchange reaction (3.55), Cu_2Se and $SnSe_2$ were formed. If Cu_2Se, $SnSe_2$ and ZnSe were in contact, an epitaxial supportive reaction would proceed to form CZTSe. No CTSe was found at this temperature, probably because CZTSe formation has a more negative ΔG and is also thermodynamically supportive.

The heating curve in Figure 3.20 shows an overall endothermic effect of 1,3 J at 379 °C (652 K), which corresponds to the CuSe transformation to Cu_2Se and Se, as was analogously described above for the CuSe-containing binary and ternary mixtures in which $SnSe_2$ was formed. Calculations could not be performed to express this in kJ mol^{-1} because multiple processes occur simultaneously. Based on Raman analyses of the sample heated to 400 °C (673 K), the formation of Cu_2SnSe_3 (*via* its characteristic Raman peak at 180 cm^{-1}) and CZTSe (by Raman peaks at 171, 195, 234 cm^{-1}) were found and were reported in **Paper I**; however, these were not detected by XRD. XRD showed only a new compound, such as KCu_2Se_2 (Figure 3.21). The reason could be KI dissolution in liquid Se (at 400 °C or 673 K), as described by proposed reaction (3.65):

$$2\ Cu_2Se\ (s) + 4\ KI\ (s) + 3\ Se\ (l) \rightarrow 2\ KCu_2Se_2\ (s) + K_2Se\ (s) + 2\ I_2\ (g) \qquad (3.65)$$

The presence of liquid Se from CuSe phase transformation at 377 °C or 650 K (in DTA 379 °C or 652 K) increases the amount of CTSe formed; however, this formation is not in the bulk, as described for the KI-SnSe-CuSe mixture. No effects of the monotectic point (at 523 °C or 796 K) and no melting of CuSe (at 533 °C or 806 K) were observed in the DTA heating curve. Cu_2Se and $SnSe_2$ formed in the bulk, as described for the KI-SnSe-CuSe and NaI-SnSe-CuSe mixtures.

There were some differences in the DTA curves, as shown in **Papers I** and **II**. In **Paper I** compared with **Paper II**, an additional endothermic effect at 587 °C (860 K) in the DTA heating curve was found. This effect can be attributed to the eutectic point of Cu_2SnSe_3-$SnSe_2$ (Dudchak & Piskach, 2003). Its occurrence depends on the situation, how the solid particles are in contact with each other in the DTA samples, and the formation or not of $SnSe_2$ and Cu_2SnSe_3 before the melting of the flux in the solid-state reaction. Upon investigating the next effect, the sample quenched at 680 °C (953 K) shown in Figure 3.22 presented new compounds, including $Cu_2ZnSnSe_4$ and $Cu_{5,32}Sn_{2,68}Se_8$, in the XRD spectra compared with the previous sample. However, there were found no new compounds according to Raman (**Paper I**) since CZTSe was detected in it at lower temperatures. The appearance of CuSe at that high temperature could be explained by the fast cooling during quenching. The appearance of CZTSe in the XRD patterns is a sign that in closed vacuum ampoules in the presence of a large amount of solid KI, the CZTSe formation process is inhibited and proceeds intensively after the formation of liquid phase KI. After flux melting, CZTSe forms in the bulk.

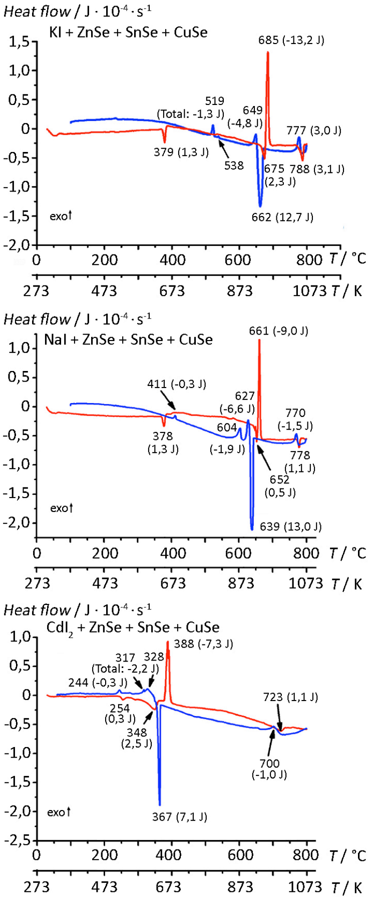

Figure 3.20 DTA curves of the flux-ZnSe-SnSe-CuSe of 125,0 mg flux, 29,8 mg ZnSe, 40,8 mg SnSe and 54,4 mg CuSe (heating at 5 ℃ min^{-1} in red; cooling at 10 ℃ min^{-1} in blue)

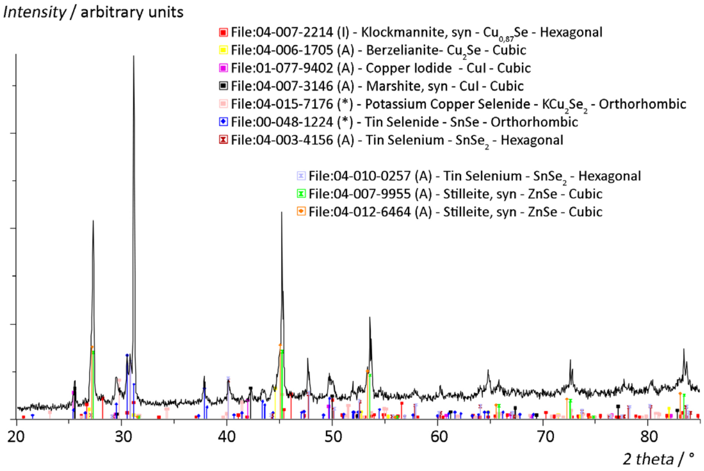

Figure 3.21 XRD pattern of the KI-ZnSe-SnSe-CuSe mixture heated to 400 ℃ or 673 K (1 h); the files from database ICDD-PDF-4+2016 were used

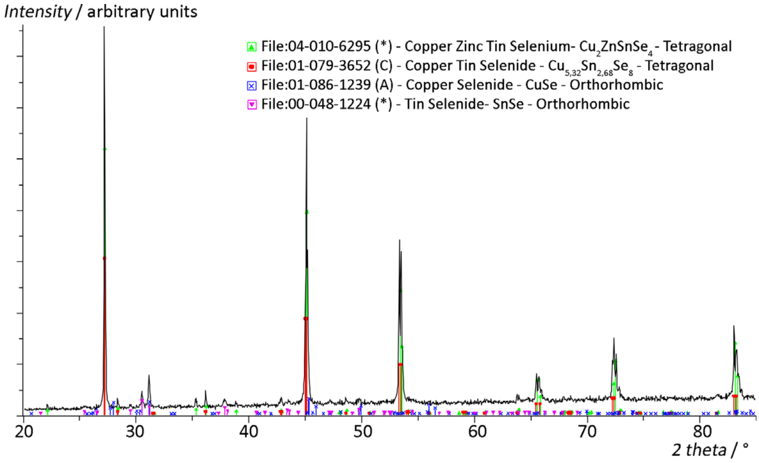

Figure 3.22 XRD pattern of the KI-ZnSe-SnSe-CuSe mixture heated to 680 ℃ or 953 K (1 h) and quenched; the files from database ICDD-PDF-4+2016 were used

The endothermic effect of KI melting (normally at 18,1 J) was observed as the thermal effect at 2,3 J for 675 °C (948 K). The thermal effect of KI melting is partially compensated by the next exothermic effect (Figure 3.20). The compensated part can be calculated as 2,3 J -18,1 J = -15,8 ± 1,6 J. The total value of this exothermic effect is -13,2 J -15,8 J = -29,0 ± 2,9 J, which is due to the intense CZTSe formation process in the molten KI at 685 °C (958 K) from binaries Cu_2Se, $SnSe_2$ and ZnSe in reaction (3.66).

$$Cu_2Se\ (s) + SnSe_2\ (s, l) + ZnSe\ (s) \leftrightarrow Cu_2ZnSnSe_4\ (s, l) \qquad (3.66)$$

From this heat value, the enthalpy of reaction (3.66) was experimentally determined to be -36,0 ± 3,6 kJ mol^{-1} as calculated per the reagents according to Table 2.2 in Section 2.7. When KI melts, it brings the precursor particles together, and upon melting, the reaction is induced. According to Nakamura *et al.* (2011), the CZTSe formation enthalpy was calculated to be -84,1 kJ mol^{-1} at -273 °C (0 K) from Cu_2Se, $SnSe_2$, and ZnSe. However, researchers Xiancong *et al.* (2013) have stated that any calculations should be taken as predictions, and they presented a value of $\Delta G \approx \Delta H$ of -3000 kJ mol^{-1} from Cu_2Se, $SnSe_2$, and ZnSe. Upon eventual heating, the melting of CZTSe at 788 °C or 1061 K (3,1 ± 0,3 J) was achieved, and the experimentally determined heat of fusion was determined to be 4,0 ± 0,4 kJ mol^{-1}. During the cooling cycle, the solidification of CZTSe was observed at 777 °C or 1050 K (-3,0 ± 0,3 J) with an enthalpy of -4,0 ± 0,4 kJ mol^{-1}. The endothermic effect of the process corresponds to the reverse process of the CZTSe reformation at 662 °C (935 K) and is 12,7 ± 1,3 J, which includes the following KI solidification at 649 °C (922 K) of 18,1 J -4,8 J = 13,3 ± 1,3 J. The total endothermic effect of 12,7 J +13,3 J = 26,0 ± 2,6 J can be expressed as 35,0 ± 3,5 kJ mol^{-1} for the reaction of CZTSe reformation. The lower thermal effect of the reverse process during cooling could be due to a difference between the melting and solidification processes. The melting of CZTSe is incongruent, and CZTSe forms a liquid phase that has a composition close to that of Cu_2SnSe_3 and solid ZnSe (Dudchak & Piskach, 2003). The reformation of CZTSe from solid ZnSe and the liquid phase could be inhibited *via* kinetics and occurs with some time delay. This also explains the low heat of fusion for CZTSe melting that was detected. The liquid phase formed upon cooling can split into different solid phases. This was affirmed by the following results. In the DTA cooling curve, thermal effects at 538 °C (811 K) and at 519 °C (792 K) were visible. Similar effects were observed in other CuSe-containing systems. Upon cooling, the equilibrium between $Cu_{2-x}Se$ and Se-rich liquid is reached as described in Glazov *et al.* (2000) and Chakrabarti and Laughlin (1981) at 519 °C (792 K) and 538 °C or 811 K (-1,3 ± 0,1 J) and as described above for the CuSe-containing systems and precursor analysis. In a sample heated to 800 °C (1073 K) and cooled to 520 °C (793 K), the presence of Cu_2Se and Se could be due to CZTSe melting, which forms CTSe and ZnSe. CTSe decomposes to $SnSe_2$ and Cu_2Se, while $SnSe_2$ decomposes to SnSe and Se. Additionally, unreacted CuSe is possible.

The **NaI-ZnSe-SnSe-CuSe** mixture was discussed in **Paper III** and in Leinemann *et al.* (2011). In Figure 3.20, the endothermic peak is less intense (1,3 J) at 378 °C (651 K) during heating as also observed for other CuSe-containing DTA samples, which was attributed to the peritectic process in the Cu-Se binary system, the CuSe phase transformation and decomposition to $Cu_{2-x}Se$ + Se, according to Glazov *et al.* (2000) and Chakrabarti and Laughlin (1981). The quenched sample at 380 °C (653 K) in the XRD analyses (Figure 3.23) showed the formed compounds, including Cu_3Se_2, $SnSe_2$, CuI, Na_2SeO_4, and $Na_2Cu(OH)_4$, in addition to the initial flux and precursors of ZnSe, SnSe, CuSe, NaI, and $NaI\cdot 2H_2O$. However, the washed sample (Figure 3.24) showed only the nonsoluble part ($Cu_{1.8}Se$, CuSe, SnSe, $SnSe_2$, and ZnSe). Raman analyses (see Appendix 3, Table A2.2) showed the peaks at 81, 170, 191, and 231 cm^{-1} for CZTSe, 95, 107, and 122 cm^{-1} for $NaI\cdot 2H_2O$, and 139 and 240 cm^{-1} for Se. There were also Raman signals at 145 cm^{-1} for SnSe, 181 cm^{-1} for Cu_2SnSe_3, and 263 cm^{-1} for $Cu_{2-x}Se$, whereas the washed sample showed only CZTSe at 173, 196, and 236 cm^{-1} and ZnSe at 252 cm^{-1} (see Figure 3.25). Compensation of CuSe phase transformation by $SnSe_2$ formation was described for the KI-SnSe-CuSe mixture. For the sample quenched at 380 °C (653 K), CTSe formation was confirmed by XRD and Raman; however, the XRD analysis did not confirm the formation of CZTSe at 380 °C (653 K). This was detected by Raman spectroscopy.

The formation of these compounds formed at temperatures below the flux melting could be explained similarly as for the KI-SnSe-CuSe and KI-ZnSe-SnSe-CuSe mixtures. They can form due to the release of Se in the system. The reactions for CZTSe and CTSe formation that begin after the liberation of Se from CuSe consume the available Se; then, the reactions are inhibited after Se over-pressurizes in the closed ampoules. Se evaporates after melting in a closed system. The resulting amounts of formed CZTSe and CTSe are lower than the sensitivity of XRD, even in the washed samples. Additionally, the large amount of solid NaI between solid precursor particles inhibits the rate of the CZTSe formation reaction. Therefore, the characteristic Raman peaks and the reflections of the unreacted binary compound are present in the XRD patterns for samples heated to temperatures below the melting point of NaI. Because the main CZTSe formation process occurs with melting of NaI, and only a small amount of it forms at 380 °C (653 K). The formed liquid phase between solid particles allows fast diffusion of the reaction components; this occurs because of the much higher diffusion rates between reaction components in the molten media (**Paper III**). Otherwise, in the presence of a large amount of solid NaI, only solid-state reactions could be expected at this temperature. The Na-containing byproducts, $Na_2[Cu(OH)]_4$ and Na_2SeO_4, could be a sign of the presence of $NaI{\cdot}2H_2O$ in NaI; however, in the Raman spectra of the studied mixtures, these compounds were not found by their characteristic Raman peaks**.** CuI presence at temperatures below flux melting was explained for the KI-CuSe mixture since copper selenides reacted with some free I_2 after opening the ampoule. All sodium-containing compounds are easily soluble in water and can be removed *via* washing. Only CuI is poorly soluble in water ($4{,}2{\cdot}10^{-4}$ g per liter at 25 °C or 298 K); however, it dissolves in the presence of NaI or KI by forming the linear anion, $[CuI_2]^-$. Dilution of such solutions with water leads to the reprecipitation of CuI, as described by Kauffman, Fang, Viswanathan and Townsend (as cited in Smith, 2007). The appearance of $Na_2[Cu(OH)]_4$ could be due to the sample opening process. It is quite different in the presence of hydroxide ions (OH^-), as described by Cudennec and Lecerf (2003). The kinetics of the transformation is very fast because divalent copper ions are dissolved under the form of tetrahydroxocuprate(II) anions ($Cu(OH)^{2-}$) (Brauer, 1963). NaOH and $Cu(OH)_2$ formation were described by reactions (1.26) and (3.40); then, reaction (3.67) can proceed as follows:

$$Cu(OH)_2\ (s) + 2\ NaOH\ (aq) \rightarrow Na_2Cu(OH)_4\ (s) \qquad (3.67)$$

NaOH releases water at 280-450 °C (553-723 K) and forms Na_2O as Sofronov *et al.* (2005) described *via* equation (1.27). Since Se oxidation in O_2 is possible at room temperature *via* reaction (3.42), the ΔG = -171,9 kJ mol^{-1} according to the database (software HSC6 Chemistry Ver. 6.0.).

Then, Volf (as cited in Jitwatcharakomol, 2005) suggested that at temperatures below 715 °C (988 K), reaction (3.68) is possible, and the database (software HSC6 Chemistry Ver. 6.0.) shows that ΔG = -801,5 kJ mol^{-1} at room temperature.

$$Na_2O\ (s) + SeO_2\ (s) + 0{,}5\ O_2(g) \rightarrow Na_2SeO_4\ (s) \qquad (3.68)$$

Additionally, the following set of reactions (3.69-3.78) at room temperature should be considered as reported by Volf (as cited in Jitwatcharakomol, 2005) and presented with their ΔG values in the database (software HSC6 Chemistry Ver. 6.0.):

Na_2SeO_3 (s) + 0,5 O_2 (g) $\rightarrow$ Na_2SeO_4 (s) (ΔG = -79,9 kJ mol^{-1}) (3.69)

3 Se (s) + 3 Na_2O (s) $\rightarrow$ 2 Na_2Se (s)+ Na_2SeO_3 (s) (ΔG = -393,6 kJ mol^{-1}) (3.70)

1,5 O_2 (g) + Na_2Se (s) $\rightarrow$ SeO_2 (s) + Na_2O (s) (ΔG = -221,5 kJ mol^{-1}) (3.71)

Se (s) + O_2 (g) + Na_2O (s) $\rightarrow$ Na_2SeO_3 (s) (ΔG = -492,8 kJ mol^{-1}) (3.72)

2,5 O_2 (g) + Na_2Se_2 (s) $\rightarrow$ Na_2SeO_3 (s) + SeO_2 (s) (ΔG = -671,4 kJ mol^{-1}) (3.73)

Na_2Se (s) + 1,5 O_2 (g) $\rightarrow$ Na_2O (s) + SeO_2 (s) (ΔG = -350,5 kJ mol^{-1}) (3.74)

Na_2Se (s) + 1,5 O_2 (g) $\rightarrow$ Na_2SeO_3 (s) (ΔG = -542,4 kJ mol^{-1}) (3.75)

Na_2Se_2 (s) + 3 O_2 (g) $\rightarrow$ SeO_2 (s) + Na_2SeO_4 (s) (ΔG = -751,2 kJ mol^{-1}) (3.76)

Na_2Se (s) + 0,5 O_2 (g) $\rightarrow$ Na_2O (s) + Se (s) (ΔG = -49,6 kJ mol^{-1}) (3.77)

Na_2Se_2 (s) + O_2 (g) $\rightarrow$ Na_2Se (s) + SeO_2 (s) (ΔG = -129,0 kJ mol^{-1}) (3.78)

Na_2Se formation can be described similarly to K_2Se formation in reaction (3.38) because of NaI dissolution in liquid Se. As described by Babko and Lisetskaya and Hseu and Rechnitz (as cited in Perrone, 2012), SnS_2 also dissolves in Na_2S. Na_2SnSe_3 formation is explained by reaction (3.79):

$SnSe_2$ (s) + Se^{2-} (l) $\leftrightarrow$ $SnSe_3^{2-}$ (s) (3.79)

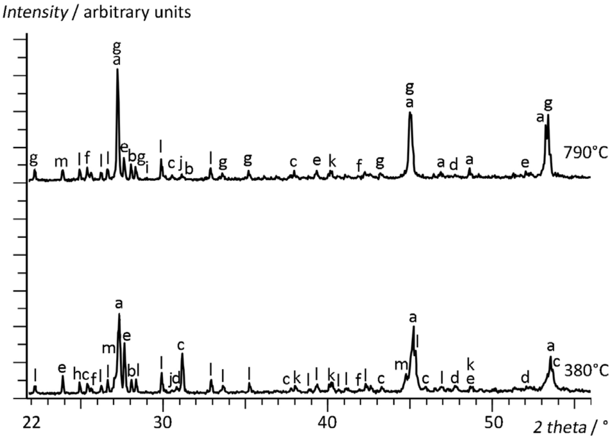

a - File: 04-006-3174 - Stilleite, syn - ZnSe - Cubic
b - File: 00-049-1456 - Copper Selenium - CuSe - Monoclinic
c - File: 04-003-1277 - Tin Selenium - SnSe - Orthorhombic
d - File: 04-010-0257 - Tin Selenium - $SnSe_2$ - Hexagonal
e - File: 01-078-0604 - Sodium Iodide - NaI - Cubic
f - File: 04-007-2246 - Marshite - CuI - Cubic
g - File: 04-010-6295 - Copper Zinc Tin Selenium - $Cu_2ZnSnSe_4$ - Tetragonal
h - File: 01-004-4730 - Umangite - Cu_3Se_2 - Tetragonal
i - File: 04-009-3578 - Sodium Tin Selenium - Na_2SnSe_3 - Orthorhombic
j - File: 00-024-1113 - Sodium Selenate - Na_2SeO_4 - Orthorhombic
k - File: 04-011-3248 - Sodium Copper Hydroxide - $Na_2Cu(OH)_4$ - Orthorhombic
l - File: 00-025-0835 - Sodium Iodide Hydrate - NaI · $2H_2O$ - Triclinic
m - File: 01-071-6180 - Berzelianite - $Cu_{1,8}Se$ - Cubic

Figure 3.23 XRD patterns of the NaI-ZnSe-SnSe-CuSe mixture heated to 380 °C (653 K) and 790 °C (1063 K) (4 h) and quenched; the files from database ICDD-PDF-4+2016 were used

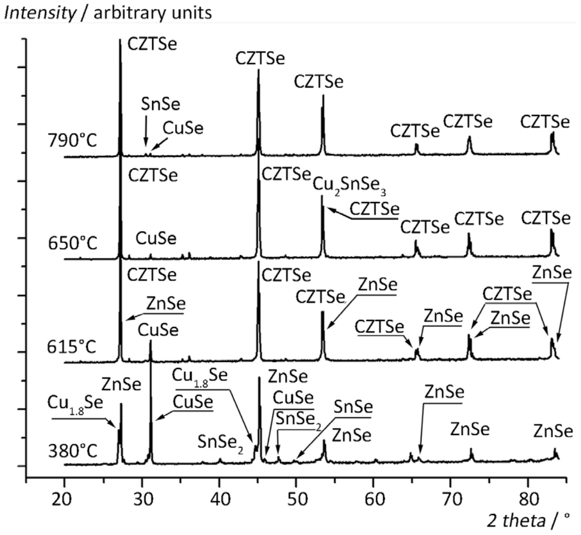

Figure 3.24 XRD patterns of the NaI-ZnSe-SnSe-CuSe samples (heated to 380 °C or 653 K for 90 h, 615 °C or 888 K for 11 h, 650 °C or 923 K for 15 h, and 790 °C or 1063 K for 4 h and washed). For phase detection, the files from database ICDD-PDF-4+2016 were used

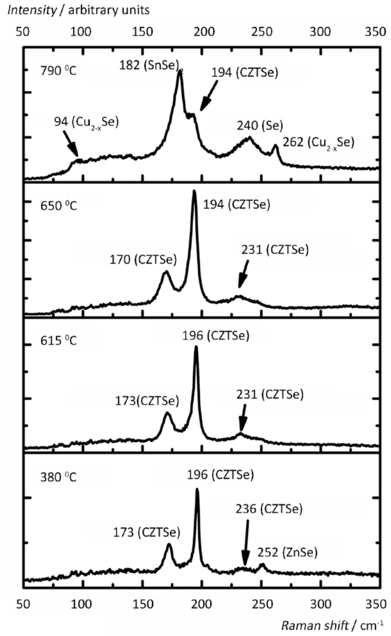

Figure 3.25 Raman analyses of the NaI-ZnSe-SnSe-CuSe samples (heated to 380 ℃ (653 K) for 90 h, 615 ℃ (888 K) for 11 h, 650 ℃ (923 K) for 15 h, and 790 ℃ (1063 K) for 4 h and washed)

Additionally, no monotectic point (at 523 °C or 796 K) and no melting of CuSe (at 533 °C 806 K) were observed in the DTA heating curve. This suggests that Cu_2Se and $SnSe_2$ were formed in the bulk, as described in the section above. For the washed samples quenched at 615 °C (888 K) and 650 °C (923 K), below the melting of the NaI-ZnSe-SnSe-CuSe mixture (peak at 652 °C or 925 K in the DTA curve in Figure 3.20), unreacted binaries and CTSe were detected in the XRD analysis (Figure 3.24). However, the Raman spectra showed a single CZTSe phase with peaks at 170, 173, 194, 196, and 231 cm^{-1} (Figure 3.25), attributed as shown in Appendix 3, Table A2.2 (Altosaar *et al.*, 2008) and (Grossberg, Krustok, Timmo & Altosaar, 2009). The nonwashed samples quenched at 615 °C (888 K) and 650 °C (923 K) are not presented due to their similar results as for those that were washed. The nonwashed samples contained more binary compounds and soluble phases compared to the washed samples. The main Raman peaks for CZTSe synthesized in NaI shifted from 196 to 194 and 191 and from 173 to 170 cm^{-1}. These shifts to lower peak values are similar as for solid solutions, for example $Cu_2ZnSn(S_{1-x}Se_x)_4$ (Grossberg *et al.*, 2011), and for solid solutions of CZTS with Cu_2CdSnS_4 (Nkwusi *et al.*, 2012).

At 652 °C (925 K), near the melting temperature of pure NaI (660 °C or 933 K) in Figure 3.3, an endothermic effect (melting process of 0,5 ± 0,1 J) is observable in the heating curve of the NaI-ZnSe-SnSe-CuSe mixture in Figure 3.20. This suggests that the thermal effect of NaI melting (19,8 ± 2,0 J) is covered by an exothermic effect of 19,3 J ± 2,0 J. The following intense exothermic interaction between the compounds at 661 °C or 934 K (-9,0 J) ends with CZTSe formation. The total exothermic effect for CZTSe formation in NaI is -28,3 ± 2,8 J for the reaction from the binaries Cu_2Se, $SnSe_2$ and ZnSe for the reagents shown in Table 2.2 in Section 2.7. Thus, the specific enthalpy of CZTSe formation (at 661 °C or 934 K) is -36,0 ± 3,6 kJ mol^{-1}. This value was experimentally determined for the first time. It is a reversible process during the cooling cycle at 639 °C or 912 K (13,0 ± 1,3 J), where the thermal effect of NaI solidification (seen at 627 °C or 900 K (-6,6 ± 0,7 J) requires -13,2 ± 1,3 J. The total reversible process of 26,2 ± 2,6 J results in an enthalpy value of 33,0 ± 3,3 kJ mol^{-1}. This value differs by few kJ mol^{-1}, probably because the formation enthalpy depends on the temperature and upon cooling, the detected effect is shifted from 661 °C (934 K) to 639 °C (912 K). In addition, of note, it is complicated to predict the influence of the CZTSe formation pathway starting from the ternary compound of Na_2SnSe_3, which was also found by XRD for low concentrations at 790 °C (1063 K) (Figure 3.23).

It was established in Dudchak and Piskach (2003) that $Cu_2ZnSnSe_4$ melts incongruently at 788 °C (1061 K), leaving ZnSe : Cu : Sn in the solid phase. Therefore, the peaks of 1,1 ± 0,1 J (1,0 ± 0,1 kJ mol^{-1}) at 778 °C (1051 K) in the heating curve and of -1,5 ± 0,2 J (2,0 ± 0,2 kJ mol^{-1}) at 770 °C (1043 K) in the cooling curve can be attributed to the melting/solidification of CZTSe. The shift of these peaks from 788 °C (1061 K) to lower temperatures can be attributed to the formation of a sodium-containing pentanary compound (solid solution of $Cu_2ZnSnSe_4$ and $Na_2ZnSnSe_4$) similar to $Cu_2Zn_{1-x}Cd_xSnSe_4$. The samples quenched at 790 °C (1063 K) again show a peak for the ternary compound of Cu_2SnSe_3 at 178 cm^{-1} (or according to XRD Na_2SnSe_3) in the Raman spectra, as shown in Figures 3.24 and 3.25. The samples quenched at 790 °C (1063 K), over the highest incongruent melting point of CZTSe (Dudchak & Piskach, 2003) again show a more binary compound. In Figure 3.23, besides the quaternary compound of CZTSe in the XRD pattern, SnSe, $SnSe_2$, NaI, NaI·$2H_2O$, CuI, Cu_3Se_2, $Cu_{1.8}Se$, Na_2SnSe_3, Na_2SeO_4, and $Na_2Cu(OH)_4$ were found, whereas in addition to CZTSe, the washed sample showed some SnSe and CuSe (Figure 3.24). In the Raman spectra of the nonwashed samples, the peaks could be attributed as follows: 95 cm^{-1} to NaI·$2H_2O$, 139 and 240 cm^{-1} to Se, 171 and 195 cm^{-1} to CZTSe, 178 cm^{-1} to Cu_2SnSe_3, 251 cm^{-1} to ZnSe, 263 cm^{-1} to $Cu_{2-x}Se$. However, in the Raman spectra of the washed samples (in Figure 3.25), peaks at 94 and 263 cm^{-1} were attributed to $Cu_{2-x}Se$, that at 182 cm^{-1} was attributed to $SnSe_2$, that at 194 cm^{-1} was attributed to CZTSe, and that at 240 cm^{-1} was attributed to Se. Due to the fast cooling, the reformation of CZTSe from the melt may not be completed during the cooling process.

The peaks in the DTA cooling curve at 604 °C (877 K) (-1,9 ± 0,2 J) should belong to the melting point of CuI (T_m = 606 °C or 879 K (software HSC6 Chemistry Ver. 6.0.)), as found by the XRD studies of the sample quenched at 790 °C or 1063 K and shown in Figure 3.23; the exothermic peak at 411 °C or 684 K (-0,3 ± 0,0 J) can be attributed to the phase change of γ-CuI to β-CuI, as reported in Rapaport and Pistorius (1968) at 408,5 ± 1,5 °C (681,5 ± 1,5 K).

The DTA curves of the **CdI_2-ZnSe-SnSe-CuSe** mixture are presented in Figure 3.20. The peaks at 254 °C or 527 K (0,3 ± 0,0 J) and 290 °C (563 K) in the DTA heating curve (corresponding to the DTA peaks of the CdI_2-SnSe-CuSe mixture at 261 °C or 534 K and 278 °C or 551 K) can be attributed to a similar mechanism, which is the formation of a CuI solid solution with CdI_2 (Blachink & Stöter, 1989).

To investigate the processes causing the next endothermic peak at 348 °C (621 K) during the melting of the mixture, a corresponding sample was quenched at 370 °C (643 K). Only nonwashed samples were investigated. In (see Figure 3.26 (a) and (b)) CdI_2, $SnSe_2$, ZnSe and $Cu_2CdSnSe_4$ were found according to their XRD and Raman characteristic peaks.

Raman peaks for the CdI_2 (at 110 cm^{-1}), SnSe (at 147 cm^{-1}), ZnSe (at 250 cm^{-1}) and $Cu_2Zn_{1-x}Cd_xSnSe_4$ (at 171 cm^{-1} and 188 cm^{-1}) phases were present. For comparison, pure substances were measured. An endothermic melting effect at 348 °C or 621 K (2,5 ± 0,3 J) was observed that is much lower than that requires to melt 125,0 mg of CdI_2 (7,1 ± 0,7 J). Therefore, the endothermic effect of CdI_2 melting is likely covered by the following exothermic thermal effect of 2,5 J -7,1 J = -4,6 J. The visible part of the exothermic effect was observed as -7,3 J at 388 °C (661 K). Then, the full exothermic effect at 388 °C (661 K) represents the sum of (-7,3 J) + (-4,6 J) = -11,9 ± 1,2 J. Based on phase analyses, the compensating exothermic effect at 388 °C (661 K) can be attributed to the formation of $Cu_2CdSnSe_4$ *via* the following route. CTSe forms from transformed CuSe and SnSe to Cu_2Se and $SnSe_2$, which is followed by reaction (3.62) between Cu_2SnSe_3 and CdSe. No Cu-Se compounds were found. Unreacted $SnSe_2$ could be present due to the initial molar ratio of 1,85(CuSe) : 1(ZnSe) : 1(SnSe) : 1,65(CdI_2), which is similar to that described for other ternary and quaternary mixtures.

In the next sample quenched at 400 °C (673 K), the presence of the (compared with the previous sample) CdI_2, $Cu_{1.8}Se$, Cu_2SnSe_3 and SnSe were determined by XRD. Raman analysis confirmed the XRD results regarding the presence of the CdI_2, SnSe, Cu_2SnSe_4 and Se phases based on their characteristic Raman peaks at 110 cm^{-1}, 147 cm^{-1}, 190 cm^{-1} and 238 cm^{-1}, respectively. The peak at 238 cm^{-1} may also be due to $Zn_xCd_{1-x}Se$; see Appendix 3, Table A2.2. In this case, the Cu_2SnSe_4 compound can also be formed *via* reaction (3.61). Most likely, during the exothermic process, the dissolution of $Cu_2CdSnSe_4$ in CdI_2 occurs *via* the reversible reaction (3.62) because Cu_2SnSe_3, $Cu_{2-x}Se$ and SnSe are now present. The released CdSe with ZnSe is used for the formation reaction of the solid solution *via* equation (3.80).

$$x\ CdSe\ (s) + (1-x)\ ZnSe\ (s) \leftrightarrow Zn_{1-x}Cd_xSe\ (s) \qquad (3.80)$$

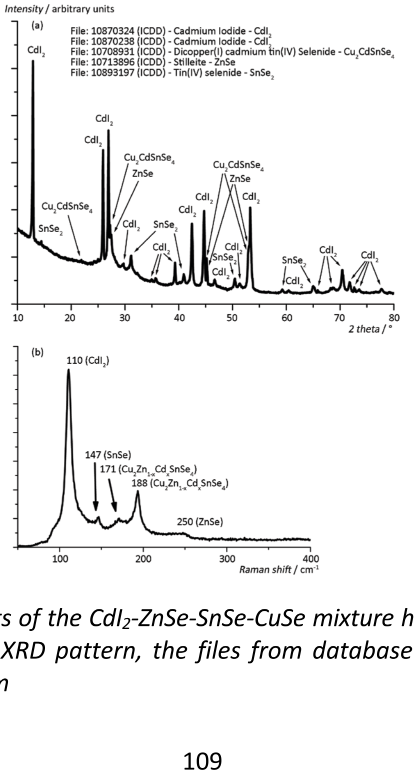

Figure 3.26 Measurements of the CdI_2-ZnSe-SnSe-CuSe mixture heated to 370 ℃ or 643 K (1 h) and quenched: (a) XRD pattern, the files from database ICDD-PDF-4+2016 were used; (b) Raman spectrum

In the sample quenched at 590 °C (863 K), the newly formed (compared with the previous sample quenched at 400 °C (673 K)) CuI, $Cd_{0.22}Zn_{0.78}Se$ and $Cu_2ZnSnSe_4$ phases were detected by XRD. In the washed sample, CZTSe and ZnSe were observed *via* XRD (Figure 3.27). The Raman spectrum of the nonwashed sample was not readable due to strong noise; the washed sample showed a strong peak at 193 cm^{-1}, which could be attributed to $Cu_2Zn_{1-x}Cd_xSnSe_4$ solid solution. The peaks at 93 cm^{-1} and 240 cm^{-1} were attributed to Se (or $Zn_xCd_{1-x}Se$), a weak signal at 122 cm^{-1} may be due to CuI, and 263 cm^{-1} was attributed to $Cu_{2-x}Se$. Due to the incorporation of Cd into the CZTSe lattice, the main characteristic peak of CZTSe at 196 cm^{-1} shifted to a lower wavelength (Altosaar *et al.*, 2008; Grossberg *et al.*, 2011); see Appendix 3, Table A2.2. 3,0 at.% of Cd incorporates in CZTSe at 740 °C (1013 K) (Klavina *et al.*, 2010). The presence of $Cu_{2-x}Se$ can be explained by the reversible reactions of (3.63) and (3.64). $Cu_2Zn_{1-x}Cd_xSnSe_4$ forms *via* the following proposed reaction (3.81):

$$Cu_2SnSe_3\ (s) + Zn_{1-x}Cd_xSe\ (s) \leftrightarrow Cu_2Zn_{1-x}Cd_xSnSe_4\ (s) \qquad (3.81)$$

In all of the studied CdI_2-containing mixtures where unreacted ZnSe, SnSe or $SnSe_2$ were found, there were two reasons for the presence of these compounds: first, the initial molar ratio was off-stoichiometric for $Cu_2ZnSnSe_4$ – Cu : Zn : Sn : Se = 1,85 : 1 : 1 : 3,85; second, the chemical activity of CdI_2; part of Cu was consumed in the formation of CuI in the copper selenide reactions with CdI_2 (see the CdI_2-CuSe mixture), leading to the formation of off-stoichiometric CZTSe and unreacted ZnSe and SnSe. The experimentally measured and expressed value of -11,9 ± 1,2 J for the formation of $Cu_2Zn_{1-x}Cd_xSnSe_4$ in reaction (3.81) at 388 °C (661 K) is smaller (-15,0 ± 1,5 kJ mol^{-1}) than that found for the formation of CZTSe in KI and NaI. $Cu_2Zn_{1-x}Cd_xSnSe_4$ forms according to reaction (3.81), if $Zn_{1-x}Cd_xSe$ is formed in reaction (3.11) from ZnSe and CdI_2. For reaction (3.11), the determined enthalpy was -18,8 ± 1,9 kJ mol^{-1}. Then, according to reaction (3.82), the formation enthalpy from ZnSe, CdI_2 and Cu_2SnSe_3 is -18,8 J -15,0 J = -33,8 ± 3,4 kJ mol^{-1}.

$$ZnSe\ (s) + CdI_2\ (l) + Cu_2SnSe_3\ (s) \rightarrow Cu_2Zn_{1-x}Cd_xSnSe_4\ (s) + Zn_xCd_{1-x}I_2\ (s, l) \qquad (3.82)$$

To investigate the processes behind the endothermic peak at 723 °C (996 K) in the DTA heating curve, a sample quenched at 740 °C (1013 K) was analyzed *via* XRD and Raman before and after being washed with water. In addition to $Cu_2ZnSnSe_4$ or $Cu_2Zn_{1-x}Cd_xSnSe_4$ (they are difficult to separate in XRD), the CuSe and Cu_4Se_3 phases were also found *via* XRD. After washing, only the $Cu_2ZnSnSe_4$, $Zn_{0.69}Cd_{0.31}Se$ and $Zn_{0.78}Cd_{0.22}Se$ phases were detected by XRD (Figure 3.27). The Raman spectrum of the nonwashed sample was not possible to analyze because of strong noise, and the washed sample shows peaks as in the quenched sample at 590 °C or 863 K (Figure 3.28). Therefore, the endothermic peak near 723 °C (996 K) 1,1 ± 0,1 J in the DTA heating curve and the exothermic peak at 700 °C (973 K) in the cooling curve can be attributed to the eutectic reaction (3.81) because Cu_2SnSe_3 solidifies at 693 °C or 966 K (Tomashik *et al.*, 2006) and $Cu_2Zn_{1-x}Cd_xSnSe_4$ appears to decompose. In the cooling curve of the studied system, the endothermic peak of 7,1 J at 367 °C (640 K) near the melting point of CdI_2 (included in 7,1 J, with a total endothermic effect of 7,1 J +7,1 J = 14,2 J) can be attributed to the dissolution process of the formed compounds in the molten phase of the flux. The values for the thermal effects in the DTA curves were reproducible in two runs.

The exothermic peaks at 328 °C (601 K), 317 °C (590 K) and 244 °C (517 K) in the cooling curve (with a total value of -2,5 ± 0,3 J) correspond to the solidification of $CuSe_2$, the formation of CuI-CdI_2 solid solution and the precipitation of CuI, respectively, as described in the analyses of the CdI_2-CuSe system and in Blachink and Stöter (1989). However, the enthalpy determined in this system should be determined with care since reactions to form iodides occur; however, it is not clear how much material actually reacts.

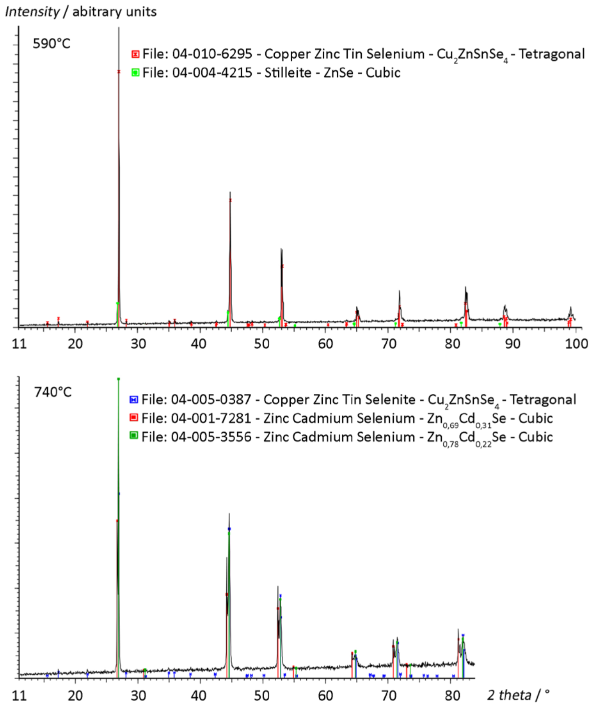

Figure 3.27 XRD patterns of the washed CdI_2-CuSe-ZnSe-SnSe mixture heated to 590 °C (863 K) and 740 °C (1013 K) and annealed for 1 h; the files from database ICDD-PDF-4 +2016 were used

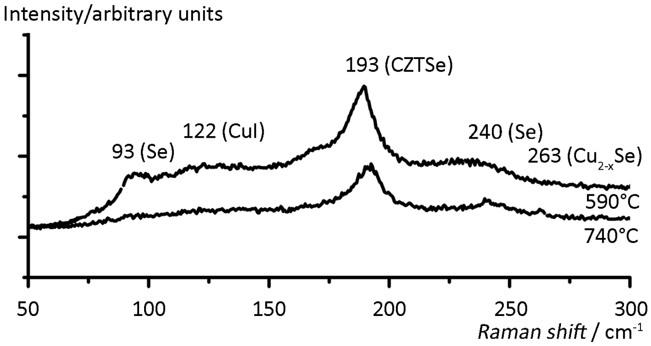

Figure 3.28 Raman measurements of the washed CdI_2-CuSe-ZnSe-SnSe mixture heated to 590 °C (863 K) and 740 °C (1013 K) and annealed for 1 h

Summary. Low-temperature SnSe cannot participate in the formation of CZTSe or CTSe; however, at temperatures above 520,2 °C (793,2 K) where high-temperature SnSe forms, no more CuSe exists. CuSe undergoes phase transformation to form $Cu_{2-x}Se$ and liquid Se at temperatures above 377 °C (650 K), as reported in the literature, or at 383 °C (656 K), as found in this study experimentally. Cu_2Se is not suitable for reaction with SnSe. The actual pressure of S or Se during annealing, as described in the literature, holds the CZTS(e) equilibrium and Cu(II) oxidation state at impossible temperatures on the reactant side, according to reaction (3.83). Only with an extra load of Se can the pressure of Se increase in the system; thus, the CZTSe formation could be performed from the thermodynamically more negative reaction (3.83) from binaries such as CuSe, SnSe and ZnSe. However, this investigation was not the focus of this study.

$$2\ CuS(e)\ (s, l) + SnS(e)\ (s, l) + ZnS(e)\ (s) \leftrightarrow Cu_2ZnSnS(e)_4\ (s) \qquad (3.83)$$

Sn loss can likely occur from SnS(e) gas formation in the environment of gas flow and if some SnS(e) gas is removed during the flow. In this study, no decomposition before CZTSe melting was observed, and SnS or SnSe loss may have occur only during annealing in the performed syntheses. Additionally, in this study, synthesis at 266-455 °C (539-728 K) of CZTS was reported to be at risk since SnS_2 decomposes to Sn_2S_3 and liquid S (**Paper IV**), and if this reaction exceeds the negative CZTS formation of (Cu_2S, SnS_2 and ZnS), then in this temperature range, CZTS will decompose into Cu_2S, Sn_2S_3, S and ZnS. This decomposition is thermodynamically impossible for CZTSe. However, Sn loss investigations were also not the focus of this study, and it is discussed in the context of possible decomposition of CZTS or CZTSe. Importantly, during CZTS or CZTSe formation SnS or SnSe participate instead of SnS_2 and $SnSe_2$, and Sn loss can occur during synthesis, whereas the decomposition of CZTS or CZTSe is not very likely below the melting of the quaternary compound. However, this case does not rely on the monograin growth process from the ready binaries.

The experimentally obtained results are shown in Figure 3.29. At 377 °C (650 K), the mixture 2 mol of CuSe and 1 mol of SnSe becomes equivalent at 1 mol of Cu_2Se, 1 mol of liquid Se and 1 mol of SnSe or a mixture of Cu_2Se and $SnSe_2$. $Cu_2Zn_{1-x}Cd_xSnSe_4$ in the CdI_2 flux forms (due to $Cu_2CdSnSe_4$ decomposition) from Cu_2SnSe_3 and $Zn_{1-x}Cd_xSe$ at 388 °C (661 K) with a formation enthalpy of $-15{,}0 \pm 1{,}5$ kJ mol^{-1}. Additionally, two sequential reactions can be proposed in which ZnSe dissolves in CdI_2 and forms $Zn_{1-x}Cd_xSe$ and $Zn_xCd_{1-x}I_2$ with a reaction enthalpy of $-18{,}8 \pm 1{,}9$ kJ mol^{-1}. Then, the sum of these two reactions is $-33{,}8 \pm 3{,}4$ kJ mol^{-1}.

In general, there are two factors that affected the investigations of the mechanisms (see Table 3.1). First, if the ampoule is opened, the binaries can react with free I_2 that was released from the flux. Only reactions of tin and copper selenides were found experimentally with iodine; however, their appearance was random. Second, impurities of binary precursors and oxygen compounds in the flux produced other compounds, although their concentrations should be too low to influence the overall pathway. Additionally, their appearance was random.

The contact locations are shown in Figure 3.30. Below the flux melting point, there are 3 options: 1) CuSe, SnSe, and ZnSe are completely separated by the flux, and this occurs mostly in the bulk; 2) 2 mol of CuSe interact with 1 mol of SnSe, producing an exchange reaction of 1 mol of Cu_2Se and 1 mol of $SnSe_2$ and then immediately CTSe;

3) all binaries interact with each other somewhere (1 mol of Cu_2Se, 1 mol of $SnSe_2$, 1 mol of ZnSe) and immediately form CZTSe in a small amount. At CuSe phase transformation temperatures of 377-383 °C (650-656 K), "*Option I*" occurs because of the mixture of Cu_2Se, $SnSe_2$ and ZnSe in the bulk since gaseous Se moves in the ampoule; however, the binaries are still separated by the flux. At flux melting in the bulk, CZTSe forms *via* "*Option I*" and *via* "*Option II*" in small amounts; it is also formed from CTSe and ZnSe, whereas *via* "*Option III*" recrystallization forms a small amount of CZTSe.

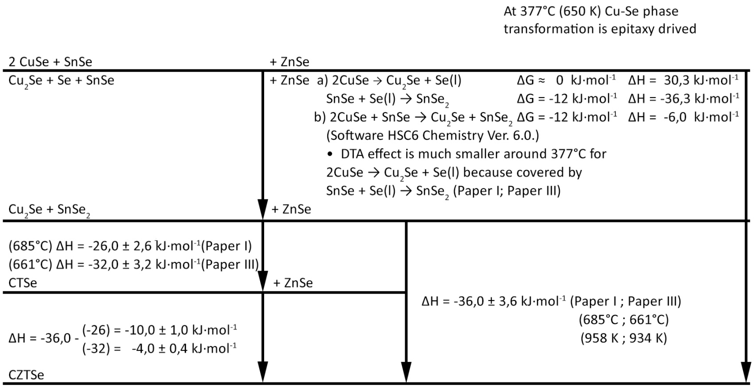
At 377°C (650 K) Cu-Se phase
transformation is epitaxy drived
2 CuSe + SnSe
+ ZnSe
Cu$_2$Se + Se + SnSe
+ ZnSe a) 2CuSe → Cu$_2$Se + Se(l) ΔG ≈ 0 kJ·mol^{-1} ΔH = 30,3 kJ·mol^{-1}
SnSe + Se(l) → SnSe$_2$ ΔG = -12 kJ·mol^{-1} ΔH = -36,3 kJ·mol^{-1}
b) 2CuSe + SnSe → Cu$_2$Se + SnSe$_2$ ΔG = -12 kJ·mol^{-1} ΔH = -6,0 kJ·mol^{-1}
(Software HSC6 Chemistry Ver. 6.0.)
• DTA effect is much smaller around 377°C for
2CuSe → Cu$_2$Se + Se(l) because covered by
SnSe + Se(l) → SnSe$_2$ (Paper I; Paper III)
Cu$_2$Se + SnSe$_2$
+ ZnSe
(685°C) ΔH = -26,0 ± 2,6 kJ·mol^{-1}(Paper I)
(661°C) ΔH = -32,0 ± 3,2 kJ·mol^{-1}(Paper III)
CTSe
+ ZnSe
ΔH = -36,0 ± 3,6 kJ·mol^{-1} (Paper I ; Paper III)
(685°C ; 661°C)
(958 K ; 934 K)
ΔH = -36,0 - (-26) = -10,0 ± 1,0 kJ·mol^{-1}
(-32) = -4,0 ± 0,4 kJ·mol^{-1}
CZTSe

Figure 3.29 llustrative summary of the obtained ΔH values for CZTSe formation

Table 3.1 Summary of disturbing factors

Room *T* reactions from flux instability after opening the ampoule		Other impurities in the precursors and fluxes in the closed ampoules
$ZnSe (s) + I_2 (s, g) \rightarrow ZnI_2 (s) + Se (s)$ $\Delta G_{I2(s)} = -41{,}9$ kJ mol^{-1}; $\Delta G_{I2(g)} = -61{,}5$ kJ mol^{-1}	X	Se in ZnSe
$SnSe (s) + I_2 (s, g) \rightarrow SnI_2 (s) + Se (s)$ $\Delta G_{I2(s)} = -56{,}7$ kJ mol^{-1}; $\Delta G_{I2(g)} = -76{,}4$ kJ mol^{-1}	√	$SnSe_2$ and SnO_2 in SnSe; it also produces Se_2O_5 and CdIOH
$SnSe (s) + 2 I_2 (s, g) \rightarrow SnI_4 (s) + Se (s)$ $\Delta G_{I2(s)} = -119{,}8$ kJ mol^{-1}; $\Delta G_{I2(g)} = -159{,}0$ kJ mol^{-1}	X	CuO, Cu_3Se_2, Cu_3Sn in CuSe; Cu_3Sn produces Cu_2Cd; CuO and $NaI{\cdot}2H_2O$ produces $Cu_2O(SeO)_3$
$SnSe_2 (s) + I_2 (s, g) \rightarrow SnI_2 (s) + 2 Se (s)$ $\Delta G_{I2(s)} = -34{,}3$ kJ mol^{-1}; $\Delta G_{I2(g)} = -53{,}9$ kJ mol^{-1}	X	$CuCO_3$ impurity from CdI_2
$SnSe_2 (s) + 2 I_2 (s, g) \rightarrow SnI_4 (s) + 2 Se (s)$ $\Delta G_{I2(s)} = -97{,}3$ kJ mol^{-1}; $\Delta G_{I2(g)} = -136{,}6$ kJ mol^{-1}	√	Na_2SeO_4 produced by $NaI{\cdot}2H_2O$
$2 CuSe_2 (s) + I_2 (s, g) \rightarrow 2 CuI (s) + 4 Se (s)$ $\Delta G_{I2(s)} = -62{,}0$ kJ mol^{-1}; $\Delta G_{I2(g)} = -76{,}9$ kJ mol^{-1}	√	KI and NaI dissolution in liquid Se produces Na_2SnSe_3 and KCu_2Se_2
$2 CuSe (s) + I_2 (s, g) \rightarrow 2 CuI (s) + 2 Se (s)$ $\Delta G_{I2(s)} = -41{,}9$ kJ mol^{-1}; $\Delta G_{I2(g)} = -81{,}7$ kJ mol^{-1}	√	
$Cu_2Se (s) + I_2 (s, g) \rightarrow 2 CuI (s) + Se (s)$ $\Delta G_{I2(s)} = -74{,}1$ kJ mol^{-1}; $\Delta G_{I2(g)} = -93{,}7$ kJ mol^{-1}	√	

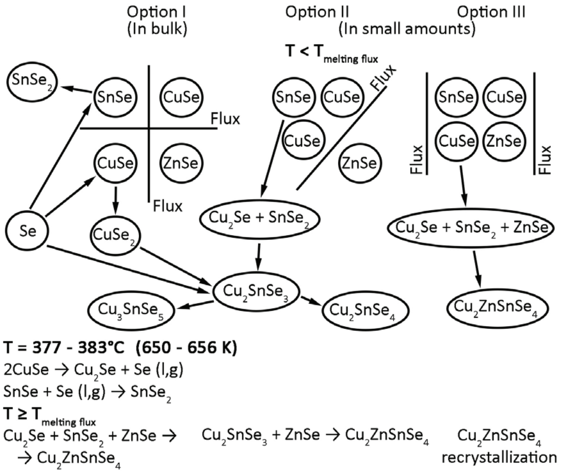
Option I
(In bulk)
Option II
(In small amounts)
Option III
T < T melting flux
SnSe2
SnSe
CuSe
Flux
CuSe
ZnSe
Flux
Se
CuSe2
SnSe
CuSe
CuSe
ZnSe
Flux
Cu2Se + SnSe2
SnSe
CuSe
CuSe
ZnSe
Flux
Flux
Cu2Se + SnSe2 + ZnSe
Cu2SnSe3
Cu3SnSe5
Cu2SnSe4
Cu2ZnSnSe4
T = 377 - 383°C (650 - 656 K)
2CuSe → Cu2Se + Se (l,g)
SnSe + Se (l,g) → SnSe2
T ≥ T melting flux
Cu2Se + SnSe2 + ZnSe →
→ Cu2ZnSnSe4
Cu2SnSe3 + ZnSe → Cu2ZnSnSe4
Cu2ZnSnSe4
recrystallization

Figure 3.30 Possible mechanisms of CZTSe formation in the fluxes

3.6 Determination of Doping

The concentrations of K and Na in the CZTSe monograins grown in KI and NaI at 740 °C (1013 K) were determined by ICP-MS to be 100-215 µg g^{-1} and 70-110 µg g^{-1}, respectively. According to equation (2.3), the number of moles of potassium and sodium were $2{,}6\text{-}5{,}5 \cdot 10^{-6}$ and $3{,}0\text{-}4{,}8 \cdot 10^{-6}$. Then, according to equation (3.84), the atoms of potassium and sodium can be calculated to be $15{,}6\text{-}33{,}0 \cdot 10^{17}$ and $18{,}0\text{-}28{,}8 \cdot 10^{17}$, respectively.

$$n = \frac{N}{N_A} \tag{3.84}$$

where n – moles of potassium or sodium, mol,
N – number of atoms of potassium or sodium,
N_A – Avogardo's constant, $6{,}0 \cdot 10^{23}$, mol^{-1}.

If the density of CZTSe (Ito, 2015) is 5,7 g cm^{-3}, then from equations (2.4) and (3.85), the doping level is calculated to be $\sim 10^{19}$ at. cm^{-3}.

$$r_{doping} = \frac{N}{V} \tag{3.85}$$

where r_{doping} – doping level,
N – number of atoms of potassium or sodium
V – the volume of CZTSe, g cm^{-3}.

Unfortunately, iodine evaporation during the analysis did not allow determination of its concentration in the powder using the ICP-MS method.

3.7 CZTSe and SnS Recrystallization

In this chapter, the recrystallization process of CZTSe in CdI_2 and SnS in $SnCl_2$, KI and CdI_2 based on the results of **Papers V** and **VI** will be described. The possible byproducts will also be discussed.

3.7.1 CZTSe Recrystallization in CdI_2

Efforts to dissolve the binary precursors in CdI_2 led to chemical reactions, indicating their importance in the CZTSe synthesis and recrystallization. Therefore, the recrystallization of CZTSe in CdI_2 was studied and discussed in **Paper V**.

The DSC heating and cooling curves of pure CZTSe and the CdI_2-CZTSe mixture are presented in Figure 3.31 (a) and (b). The first effect is observable at 217 °C or 490 K, which may be related to Se melting, according to the database (software HSC6 Chemistry Ver. 6.0.). The amount of Se, as determined from the melting effect of 0,02 J, can be expressed as $3 \cdot 10^{-4}$ g. This effect is present in both DSC curves (Figure 3.31 (a) and (b)). When not mixed with CdI_2, CZTSe melts at 795 °C or 1068 K (788 °C or 1061 K) (Dudchak & Piskach, 2003) with an enthalpy effect of 2,3 ± 0,2 J (expressed as 44,6 ± 4,5 kJ mol^{-1}) and solidification at 796 °C (1069 K) upon cooling (1,5 ± 0,2 J) by 29,1 kJ mol^{-1}. The CdI_2 sample mixed with CZTSe shows an endothermic effect at 378 ° C (651 K) due to the melting of CdI_2. Since the expected intensity of the melting of the added amount of CdI_2 was 1,3 ± 0,1 J and that according to DSC is 2,9 ± 0,3 J, a series of other endothermic processes with a total effect of 1,6 ± 0,2 J must have occurred. The absence of the melting and solidification effects of pure CZTSe that was revealed upon the comparison of Figure 3.31 (a) and (b) indicated that another compensating process occurred simultaneously. This could be the mixing of two liquids, *i.e.*, liquid CdI_2 and the formed liquid CZTSe (or the dissolution of liquid CZTSe in liquid CdI_2). The CdI_2-CZTSe mixed sample was annealed at 650 °C (923 K) for 168 h, quenched to room temperature and washed with water. In Figure 3.32, the XRD pattern shows that $Cu_2CdSnSe_4$ and $ZnCdSe_2$ were formed. Raman analysis (Figure 3.33) showed peaks at 93 cm^{-1} and 122 cm^{-1}, which were attributed to CuI (Appendix 3, Table A2.2), and peaks at 188 cm^{-1} and 231 cm^{-1}, which could be attributed to $Cu_2Zn_{1-x}Cd_xSnSe_4$ solid solution (Altosaar *et al.*, 2008; Grossberg *et al.*, 2011). In addition, the washing water was collected, dried and investigated. XRD analysis showed the presence of $Zn_{0.69}Cd_{0.31}Se$, $Zn_{0.7}Cd_{0.3}Se$, $Cu_2CdSnSe_4$, CdSe, Cu_2Se, and SnSe phases. It is well known that molten salts dissolve some of the used precursor compounds, as discussed in Section 3.4. Since the used flux salt is removed upon leaching with water, the compounds dissolved at high temperatures are precipitated into the leaching solvent as an amorphous or fine crystalline powder. In the Raman studies, it was difficult to observe any distinct Raman spectrum.

In the cooling curve, the peak at 845 °C or 1118 K (860 °C or 1133 K) (software HSC6 Chemistry Ver. 6.0.) may correspond to SnSe solidification, and that at 634 °C (907 K) may correspond to the eutectic point of ZnSe-$SnSe_2$ (642 °C or 915 K) (Dudchak & Piskach, 2003); if some $Cu_2Zn_{1-x}Cd_xSnSe_4$ or $Cu_2CdSnSe_4$ were detected, these peaks may correspond to their solidification and phase transformation, as was reported for $Cu_2CdSnSe_4$ (Adachi, 2015). The effects observed at 350 °C (623 K), 331 °C (604 K) and 317 °C or 590 K (total -2,4 ± 0,2 J) in the cooling curve corresponded to the solidification and formation of the CuI-CdI_2 solid solution described above and in Blachink and Stöter (1989).

Some of the SnSe or $SnSe_2$ may have reacted to generate SnI_4 (evaporated) and CdSe because at 634 °C (907 K) Cu_2Se does not form CuI and CdSe (see mixture CdI_2-CuSe in Item 3.5.3); however, CdSe and ZnSe form a solid solution of $Zn_{1-x}Cd_xSe$. The appearance of the CuI-CdI_2 solid solution at 317-350 °C (590-623 K) could also be explained by the fact that during quenching to room temperature, exchange reactions of copper selenides with CdI_2 are possible (see mixture CdI_2-CuSe in Item 3.5.3).

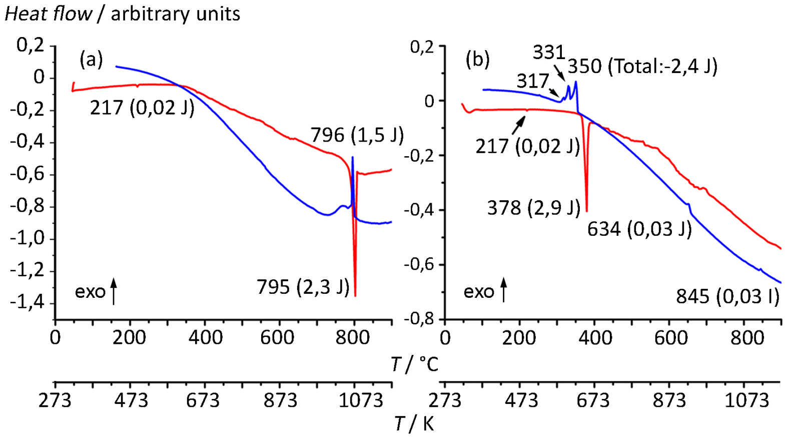

Figure 3.31. DSC of 30,0 mg CZTSe and 64,0 mg CdI_2 with 27,0 mg CZTSe (heating corresponds to red; cooling corresponds to blue)

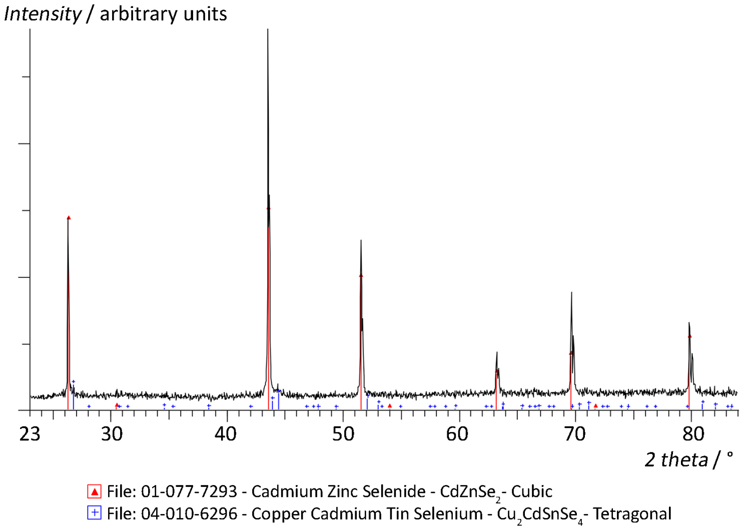

Figure 3.32. XRD of washed CdI_2-CZTSe (annealed for 168 h at 650 °C or 923 K); the files from database ICDD-PDF-4+2016 were used

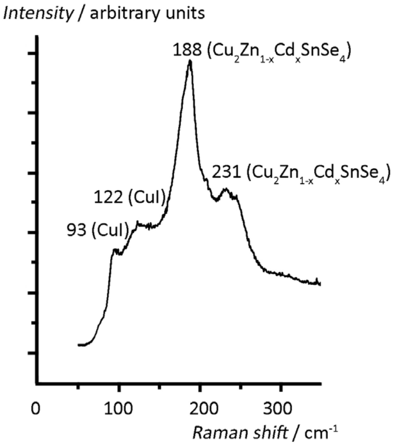

Figure 3.33. Raman spectrum of washed CdI_2-CZTSe (annealed for 168 h at 650 °C or 923 K)

3.7.2 SnS Recrystallization in CdI_2, $SnCl_2$, and KI

The findings for the flux-SnS mixtures are published in **Paper VI**. Additionally, the stability of SnS itself as a precursor was discussed in **Paper IV**.

The heating curves (in Figure 3.34) for CdI_2-SnS showed three endothermic processes at 331 °C (604 K), 371 °C (644 K) and 383 °C (656 K). In the cooling curve, four exothermic processes were revealed at 326 °C (599 K), 354 °C (627 K), 595 °C (868 K) and 672 °C (945 K). The thermal effect at 383 °C (656 K) could be attributed to the melting point of pure CdI_2, according to the database (software HSC6 Chemistry Ver. 6.0.). The thermal effect at 331 °C (604 K) is much lower than the melting temperature of CdI_2. Perhaps some new compound with a low melting temperature formed in the mixture. The ΔG for the exchange reaction between CdI_2 and SnS is positive upon the formation of CdS and SnI_2. Most probably, it is SnI_2 (melting point at 320 °C or 593 K from software HSC6 Chemistry Ver. 6.0.). From software HSC6 Chemistry Ver. 6.0., SnI_2 and CdS could be formed in the CdI_2-SnS mixture *via* reactions (3.86-3.87); room temperature $\Delta G = -58{,}0\ \mathrm{kJ\ mol^{-1}}$ and $\Delta G = -162{,}0\ \mathrm{kJ\ mol^{-1}}$. Free gaseous iodine could be released from CdI_2 as described in Item 1.4.1. and in **Papers IV** and **VI**.

$$\mathrm{SnS\ (s) + I_2\ (g) \rightarrow SnI_2\ (s, l, g) + S\ (l)} \tag{3.86}$$

$$\mathrm{CdI_2\ (s, l) + S\ (g) \rightarrow CdS\ (s) + I_2\ (g)} \tag{3.87}$$

SnI_2 melting or crystallization is observable at 326-327 °C (599-600 K) in the cooling curve and during the second heating run. During the cooling process, the mixture of formed products crystallized at 354 °C (627 K), and upon repeated heating it melted at 371 °C (644 K), followed by melting of pure CdI_2 at 383 °C (656 K) to produce an overlapping peak. The endothermic effects at 595 °C (868 K) can be ascribed to the phase transition of α-SnS to β-SnS. The thermal effect at 672-674 °C (945-947 K) in the cooling curve corresponds to the phase transition of α-Sn_2S_3 to β-Sn_2S_3 as described in Sharma and Chang (1986). CdS and Sn_2S_3 were also found in the XRD and Raman studies (see the spectra in **Paper VI**). Sn_2S_3 could be formed from SnS and S, released as shown in reaction (3.86). Additionally, SnS dissolves in molten CdI_2 to form CdS and SnI_2.

The mixture of $SnCl_2$-SnS melted endothermically at 246 °C (519 K) and froze at 235 °C or 508 K (Figure 3.34). The melting of pure $SnCl_2$ was also detected at 246 °C (519 K), and the experimentally determined heat of fusion of 14,6 kJ mol^{-1} is in good agreement with the database value (software HSC6 Chemistry Ver. 6.0.), where the melting of $SnCl_2$ was reported at 247 °C (520 K) with a heat of fusion of 14,5 kJ mol^{-1}. The next thermal effect at 596 °C (869 K) corresponds to the phase transition of low-temperature α-SnS to the high-temperature β-SnS form. The experimentally determined (in this study) enthalpy value of the phase transition of α-SnS to β-SnS is 0,1 ± 0,0 kJ mol^{-1}. No new compounds were found in the XRD and Raman studies (see **Paper VI**) in the sample annealed at 500 °C (773 K).

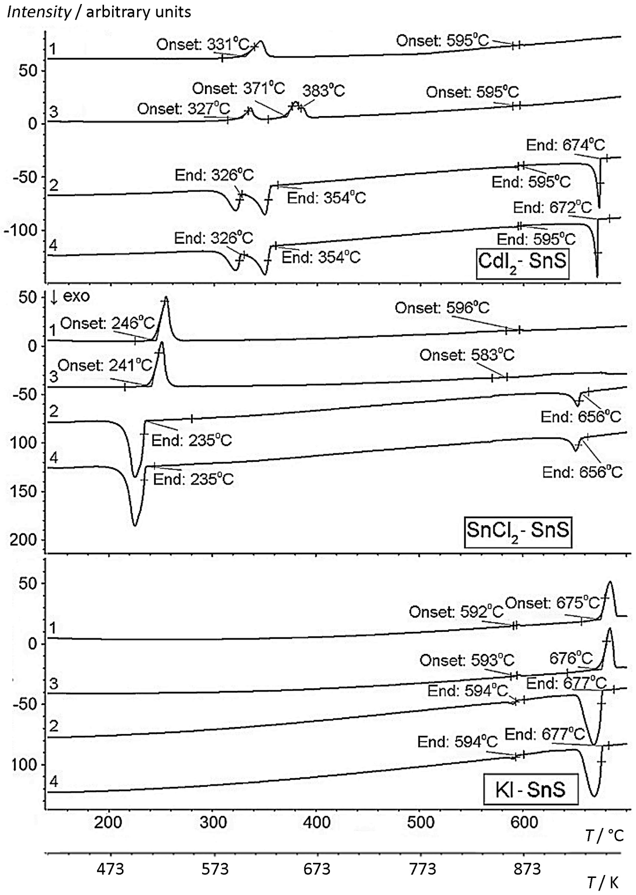

Figure 3.34 DTA curves of: 125,0 mg CdI_2 and 125,0 mg SnS; 123,0 mg $SnCl_2$ and 123,0 mg SnS; and 125,0 mg KI and 125,0 mg SnS mixtures

In the mixture of KI-SnS (Figure 3.34), the phase transition of α-SnS to β-SnS occurs during heating and cooling cycles in the range of 592 to 594 °C (865 to 867 K). The mixture melts endothermally at 675-676 °C (948-949 K) at much lower temperatures than pure KI (685 °C or 958 K, as determined in Section 3.1) and freezes at 677 °C (950 K). The lowering of the melting temperature of the mixture compared with pure KI provides a hint of the solubility of SnS in KI. The α- to β-phase transition was found at ~602 °C (875 K). As discussed previously (Sharma & Chang, 1986), low-temperature α-SnS is essentially stoichiometric, whereas β-SnS can dissolve in some excess of S. β-SnS has a maximum S content of 50,5 at.% on the border of the single phase area at approximately 700 °C (973 K) when in equilibrium with the 2-phase area of β-SnS and β-Sn_2S_3. Therefore, it was concluded that stoichiometric SnS compound can be synthesized at temperatures below 596 °C (869 K). In the KI-SnS system, it is important to use slow cooling after recrystallization for complete phase transition from β- to α-SnS to provide a stoichiometric absorber material for solar cells (Reddy, Gedi, Park, Miles & Reddy, 2015; Steinmann *et al.*, 2014). However, no new compounds were found in the XRD and Raman studies (see **Paper VI**), and monograin single phase SnS was obtained in the annealed sample even at 740 °C (1013 K).

Conclusions

To reach the aims, different analysis methods were applied, including DTA, DSC, TG, MS, Raman, XRD, SEM, EDX, and ICP-MS. In addition, thermodynamic calculations (using the database from HSC6 Chemistry Ver. 6.0.) for the probable reactions were performed. The step-by-step investigations involved the analysis of the flux materials and binary precursors; the analysis of the more complicated mixtures; and solubility determination. The investigations led to the description of the chemical pathway of CZTSe synthesis and SnS recrystallization in the molten salt medium.

The main conclusions from the studies are as follows:

1) CZTSe formation in molten KI and NaI from the polycrystalline binary compounds (ZnSe, SnSe and CuSe) used as the starting materials is now understood. Before melting of the flux salt, the formation of CZTSe is inhibited by the solid phase flux material surrounding the solid particles of the precursor compounds. However, the formation of CTSe and CZTSe is possible to a small extent through solid-state reactions before the melting of the flux. CuSe phase transformation to $Cu_{2-x}Se$ with deliberation of liquid Se at 377-383 °C (650-656 K) activates the reaction of Se with SnSe to form $SnSe_2$ because of the Se evaporation and fast spreading in the ampoule. The intense formation of CZTSe (or CTSe) proceeds that of the binary compounds of Cu_2Se, $SnSe_2$ and ZnSe in the melting of the flux (melting temperature of the flux is always decreased and accompanied by an intense exothermic formation process). The formation enthalpy of CZTSe from Cu_2Se, $SnSe_2$ and ZnSe was determined experimentally for the first time and is $-36{,}0 \pm 3{,}6$ kJ mol^{-1} for both: in KI at 685 °C (958 K) and in NaI at 661 °C (934 K). CZTSe melts at 795 °C (1068 K) and the heat of fusion was experimentally determined to be $44{,}6 \pm 4{,}5$ kJ mol^{-1}. The CTSe formation enthalpy from Cu_2Se and $SnSe_2$ in KI at 684 °C (957 K) is $-26{,}0 \pm 2{,}6$ kJ mol^{-1} and in NaI at 661 °C (934 K), it is $-32{,}0 \pm 3{,}2$ kJ mol^{-1}. The determined doping level of CZTSe (grown in KI and NaI at 740 °C (1013 K)) is $\sim 10^{19}$ at. K or Na cm^{-3}. The single phase CZTSe can be obtained in KI and NaI fluxes.
2) CdI_2 as a flux material is chemically active. Solid CdI_2 interacts with the solid precursor compounds of ZnSe, SnSe and CuSe to a small extent, forming CdSe (CdSe interacts with Cu_2SnSe_3 to form $Cu_2CdSnSe_4$), and in molten CdI_2, the solid precursor compounds show chemical dissolution that results in the formation of CdSe and iodides. In molten CdI_2, CdSe with ZnSe forms $Zn_{1-x}Cd_xSe$. $Zn_{1-x}Cd_xSe$ interacts with Cu_2SnSe_3 to form $Cu_2Zn_{1-x}Cd_xSnSe_4$. The formation enthalpy (starting from $Zn_{1-x}Cd_xSe$ and Cu_2SnSe_3) of $Cu_2Zn_{1-x}Cd_xSnSe_4$ at 388 °C (661 K) was determined to be $-15{,}0 \pm 1{,}5$ kJ mol^{-1}. The recrystallization of presynthesized CZTSe in CdI_2 leads to the formation of $Cu_2Zn_{1-x}Cd_xSnSe_4$.
3) Upon recrystallizing polycrystalline SnS in the different molten salts of CdI_2, $SnCl_2$ and KI as the flux materials, a single phase SnS monograin powder was obtained at 740 °C (1013 K) in KI and at 500 °C (773 K) in $SnCl_2$. Recrystallization of SnS in molten CdI_2 resulted in a multiphase mixture of SnS, Sn_2S_3 and CdS crystals due to the chemical interactions between the SnS, CdI_2, I_2, and released S.

4) Low melting phases that can interfere with the size and shape formation due to the sintering of solid precursor particles were found as follows: SnI_2 (T_m = 320 °C or 593 K) and SnI_4 (T_m = 144 °C or 417 K) form during the reactions of CdI_2 with SnSe at 348 °C (621 K) or with $SnSe_2$ at 368 °C (641 K). Se (T_m = 221 °C or 494 K) is formed at 377-383 °C (650-656 K) in the CuSe phase transformation to $Cu_{2-x}Se$. Impurities brought along into the CZTSe molten salt synthesis-growth process with precursors or with flux materials can have a considerable influence on the process: a) free I_2, formed due to the instability of KI, NaI and CdI_2 under atmospheric conditions, reacts with binary precursor compounds and resulted in the formation of CuI, SnI_2, SnI_4, and ZnI_2; thus, a dried flux is recommended; b) oxygen brought along with SnSe in the form of SnO_2, causes the formation of oxygen-containing compounds; c) Se (unreacted elemental Se in ZnSe and overstoichiometric Se in SnSe) melts below the melting point of the flux and can induce the primary sintering of precursor particles that disturb the monograin growth of CZTSe.

The aims of the research work of this thesis were achieved. In addition, for the DTA studies performed in the closed quartz vacuum ampoules that specially designed for the DTA set-up, a new calibration method was developed in which the same inorganic salts (KI, NaI, and CdI_2) were used as references because the classical calibration materials reacted with quartz.

References

Adachi, S. (2015). *Earth-abundant materials for solar cells: Cu_2-II-IV-VI_4 Semiconductors*. Chichester, United Kingdom: John Wiley & Sons Ltd. doi: 10.1002/9781119052814

Aguiar, J. A., Patel, M., Aoki, T., Wozny, S., & Al-Jassim M. (2016). Contrasting the Material Chemistry of $Cu_2ZnSnSe_4$ and $Cu_2ZnSnS_{4-x}Se_x$. *Adv Sci (Weinh), 3*(6), Retrieved from https://doi.org/10.1002/advs.201500320

Ahmed, M. I., Habib, A., & Javaid, S. S. (2015). Perovskite Solar Cells: Potentials, Challenges, and Opportunities. *International Journal of Photoenergy, 2015*, Retrieved from http://dx.doi.org/10.1155/2015/592308

Allen, D. A., & Howe, R.A. (1991). Tetrahedral Coordination of Zn Ions in Molten Zinc Halides. *J Chem Phys., 94*(7). Retrieved from https://doi.org/10.1063/1.460544

Altosaar, M., Raudoja, J., Timmo, K., Danilson, M., Grossberg ,M., Krustok J., & Mellikov E. (2008). $Cu_2Zn_{1-x}Cd_xSn(Se_{1-y}S_y)_4$ Solid Solutions as Absorber Materials for Solar Cells. *Phys. Stat. sol. (a), 205*(1), 167-170. doi: 10.1002/pssa.200776839

Askari, M. B., Mirzaei, M. A. V., & Mirhabibi, M. (2015). Types of Solar Cells and Applications. *American Journal of Optics and Photonics, 3*(5), 94-113. doi: 10.11648/j.ajop.20150305.17

Atkins, P., Paula, J., & Keeler, J. (2018). *Atkins' Physical Chemistry, Eleventh Edition.* Oxford, United Kingdom: Oxford University Press.

Bashkirov, S. A., Gremenok, V. F., & Ivanov, V. A. (2011). Physical properties of SnS Thin Films Fabricated by Hot Wall Deposition. *Semiconductors, 45*(6), 749. doi: 10.1134/S106378261106003.

Benaicha, M., Hamla, M., & Derbal, S. (2016). Electrochemical Formation and Selenization of Ternary CuZnSn Alloy for Growing $Cu_2ZnSnSe_4$ Photoactive Thin Films. *Int. J. Electrochem. Sci., 11*, 4909-4921. doi: 10.20964/2016.06.76

Blachink, R., & Stöter, U. (1989). The Phase Diagrams of Mixtures of CuI with ZnI_2, CdI_2, and HgI_2. *Thermochim Acta, 143*, 115-222. doi: 10.1016/0040-6031(89)85048-8

Bletskan, D. I. (2005). Phase equilibrium in binary systems $A^{IV}B^{VI}$. *Journal of Ovonic Research, 1*(5), 61-69. Retrieved from http://www.chalcogen.ro/Bletskan2.pdf

Blomgren, G. E., & Artsdalen, E. R. (1960). *Annu. Rev. Phys. Chem. 11*, 273-306. doi: 10.1146/annurev.pc.11.100160.001421

Brauer, G. (Ed.). (1963). *Sodium Tetrahydroxocuprate (II) in Handbook of Preparative Inorganic Chemistry, 2nd Ed. Vol.1*. New Yourk, USA: Academic Press. Retrieved from https://library.sciencemadness.org/library/books/brauer_ocr.pdf

Burns, G. R., Rollo, J. R., Sarfati, D. J., & Morgan, K. (1991). Phases of Tetraphosphorus Triselenide Analysed by Magic Angle Spinning 31P NMR and Raman Spectroscopy, and the Raman Spectrum of Tetraphosphorus Tetraselenide. *Spectrochimica Acta Part A: Molecular Spectroscopy, 47*(6), 811-818. doi: 10.1016/0584-8539(91)80153-A

Burton, L. A., Colombra, D., Abellon, D. R., Grozema, F. C., Peter, L. M., Savenije, T. J., … Walsh, A. (2013). Synthesis, Characterization, and Electronic Structure of Single-Crystal SnS, Sn_2S_3, and SnS_2. *Chem. Mater., 25*, 4908-4916. doi: 10.1021/cm403046m

Burton, L. A., & Walsh, A. (2012). Phase Stability of the Tin Sulfides SnS, SnS_2, and Sn_2S_3. *J. Phys. Chem. C 116*, 24262-24267. doi: 10.1021/jp309154s

Chakrabarti, D. J., & Laughlin, D. E. (1981). The Cu-Se System. *Bull. Alloy Phase Diagram, 2*(3), 305-315. doi: 10.1007/BF02868284

Chandrasekhar, H. R., Humphreys, R. G., Zwick, U., & Cardona, M. (1997). Infrared and Raman spectra of the IV-VI Compounds SnS and SnSe. *Phys. Rev. B: covering condensed matter and materials physics, 15*(4), 2177-2183. doi: 10.1103/PhysRevB.15.2177

Chikanov, V. N. (2006). Reactions in Binary Iodide Systems. *Russ. J. Inorg. Chem., 51*(7), 1132-1138. doi: 10.1134/S0036023606070187

Chiu, P. T., Law, D. C., Woo, R. L., Singer, S. B., Bhusari, D., Hong, W. D., … Karam, N. H. (2015). Direct Semiconductor Bonded 5J Cell For Space And Terrestrial Applications. Retrieved from https://www.spectrolab.com/pv/support/Direct_Semiconductor_Bonded_5J_Cells_for_Space_Terrestrial_Applications.pdf

Chuan-Pei, L., Chun-Ting, L., & Kuo-Chuan H. (2017). Use of Organic Materials in Dye-Sensitized Solar Cells. *Materials Today, 20*(5), 267-283. doi: 10.1016/j.mattod.2017.01.012

Cudennec, Y., & Lecerf, A. (2003). The Transformation of $Cu(OH)_2$ into CuO, revisited. *Solid State Sciences, 5*(11-12), 1471-1474. doi: 10.1016/j.solidstatessciences.2003.09.009

Danilson, M. (2016). *Temperature Dependent Electrical Properties of Kesterite Monograin Layer Solar Cells* (Doctoral dissertation, Tallin University of Technology). Retrieved from https://digi.lib.ttu.ee/i/file.php?DLID=5113&t=1

Donald, K. J., Hargittai, M., & Hoffmann, R. (2008). Group 12 Dihalides: Structural Predilections from Gases to Solids. *Chem A Eur J, 15*(1), 158-177. doi: 10.1002/chem.200801035

Dudchak I. D., & Piskach L. V. (2003). Phase Equilibria in the Cu_2SnSe_3-$SnSe_2$-ZnSe System. *Journal of Alloys and Compounds, 351*(1-2), 145-150. doi: 10.1016/S0925-8388(02)01024-1

Eperon, G. E. (2015). *Active Layer Control for High Efficiency Perovskite Solar Cells* (Doctoral dissertation, University of Oxford). Retrieved from https://ora.ox.ac.uk/objects/uuid:1fa78aab-7479-4fe2-8192-e1be1d12c171/download_file?file_format=pdf&safe_filename=GE%2BThesis%2Bv3.0.pdf&type_of_work=Thesis

Fairbrother, A., Fontané, X., Izquierdo-Roca, V., Placidi, M., Sylla, D., Espondola-Rodriguez, M., … Saucedo, E. (2014). Secondary Phase Formation in Zn-rich $Cu_2ZnSnSe_4$-Based Solar Cells Annealed in Low Pressure and Temperature Conditions. *Prog. Photovolt: Res. Appl., 22,* 479-487. doi: 10.1002/pip.2473

Fella, C. M., Uhl, A. R., Hammond, C., Hermans, I., Romanyuk ,Y., & Tiwari A. N. (2013). Formation Mechanisms of $Cu_2ZnSnSe_4$ Absorber Layers during Selenization of Solution Deposited Metal Precursors. *Journal of Alloys and Compounds, 567,* 102-106. doi: 10.1016/j.jallcom.2013.03.056

Feng, F. (2013). *Sonochemistry Synthesis and Characterization* (Master thesis, The University of Delaware) Retrieved from http://udspace.udel.edu/handle/19716/13018

Ferrate, M. J., Mrazek, R. V., & Brown R. R. (1930). High-Temperature Relative Enthalpies and Related Thermodynamic Properties of CuI. *Report of Investigations 9074. United States. Bureau of Mines.* Retrieved from *https://stacks.cdc.gov/view/cdc/10520/cdc_10520_DS1.pdf*

Fraas, L. M. (Ed.). (2014). *Low-Cost Solar Electric Power.* Switzerland: Springer International Publishing. doi: 10.1007/978-3-319-07530-3

Freunek, M., Freunek, M., & Reindl, M. L. (2013). Maximum Efficiencies of Indoor Photovoltaic devices. *IEEE Journal of Photovoltaics, 3*(1), 59-64. doi: 10.1109/JPHOTOV.2012.2225023

Gaune-Escard, M. (Ed.). (2002). *Molten Salts: From Fundamentals to Applications*. Amsterdam, Netherlands: Kluwer Academic Publishers. https://doi.org/10.1007/978-94-010-0458-9.

Ghanbari, M., Sabet, M., & Salavati-Niasari M. (2016). Synthesis of Different Morphologies of Cu_2CdI_4/CuI Nanocomposite *via* Simple Hydrothermal Method. *J Mater Sci: Mater Electron, 27*(19), 11092-11101. doi: 10.1007/s10854-016-5226-6.

Gibbs, A. H. (2015). *Combinatorial Investigation of the Effects of Sodium on $Cu_2ZnSnSe_4$ Polycrystalline Thin Films* (Master thesis, The University of Utah). Retrieved from https://search.proquest.com/docview/1844105756

Glazov, V. M., Pashinkin, A. S., & Fedorov, V. A. (2000). Phase Equilibria in the Cu-Se System. *Inorganic materials, 36*(7). doi: 10.1007/BF02758413

Goldstein, J. I., Newbury, D. E., Michael, J. R., Ritchie, N. W. M., Scott, J. H. J., & Joy, D. C. (2018). *Scanning Electron Microscopy and X-Ray Microanalysis. Fourth Edition*. New Your, USA: Springer. doi: 10.1007/978-1-4939-6676-9

Greve, D. W., & Mahi, F. T. (2016). *Reference Module in Materials Science and Materials Engineering: Chemical Vapor Deposition of Group IV Alloys on Silicon*. Elsevier Inc. Retrieved from https://www.sciencedirect.com/science/article/pii/B9780128035818037000

Grinyov, B. V., Gerasimov, V. G., Voloshko, A. J., Smirnov, N. N., Sofronov, D. S., Shishkin, O. V., & Kisil, E. M. (2004). Specific Features of Sodium Iodide ($NaI{\cdot}2H_2O$) Dehydration in Vacuum. *Functional materials, 11*(3), 575-578. Retrieved from https://www.researchgate.net/publication/256077501_Specific_Features_of_Sodium_iodide_NaJ2H2O_dehydration_in_vacuum

Gross, J. H. (2017). *Mass Spectrometry. A Textbook, Third Edition.* Switzerland: Springer. doi: 10.1007/978-3-319-54398-7

Grossberg, M., Krustok, J., Raudoja, J., Timmo, K., Altosaar, M., & Raadik, T. (2011). Photoluminescence and Raman Study of $Cu_2ZnSn(Se_xS_{1-x})_4$ Monograins for Photovoltaic Applications. *Thin Solid Films, 519*(21), 7403-7406. doi: 10.1016/j.tsf.2010.12.099

Grossberg, M., Krustok, J., Timmo, K., & Altosaar M. (2009). Radiative Recombination in $Cu_2ZnSnSe_4$ Monograins Studied by Photoluminescence Spectroscopy. *Thin Solid Films, 517*, 2489–2492. doi:10.1016/j.tsf.2008.11.024

Guo, L., Zhu, Y., Gunawan, O., Gokmen, T., Deline, V. R., Ahmed, S., … Deligianni, H. (2014). Electrodeposited $Cu_2ZnSnSe_4$ thin film solar cell with 7 % power conversion efficiency. *Prog. Photovoltaics, 22*, 58-68. doi: 10.1002/pip.2332

Hergert, F., & Hock R. (2007). Predicted formation reactions for the solid-state syntheses of the semiconductor materials Cu_2SnX_3 and Cu_2ZnSnX_4 (X = S, Se) starting from binary chalcogenides. *Thin Solid Films, 515*, 5953-5956. doi: 10.1016/j.tsf.2006.12.096

Hernandez-Martinez, A., Placidi, M., Arques, L., Giraldo, S., Sanchez, Y., … Saucedo, E. (2018). Insights into the Formation Pathways of $Cu_2ZnSnSe_4$ Using Rapid Thermal Processes. *ACS Appl. Energy Mater., 1*, 1981-1989. doi: 10.1021/acsaem.8b00089

Ishii, M., Shibata, K., & Nozaki, H. (1993). Anion Distributions and Phase Transitions in $CuS_{1-x}Se_x$(x = 0-1) Studied by Raman Spectroscopy. *J Solid State Chem. 105*(2), 504-511. doi: 10.1006/jssc.1993.1242

Ito, K. (Ed.). (2015). *Copper Zinc Tin Sulfide – Based Thin Film Solar Cells.* Chichester, United Kingdom: John Wiley & Sons Ltd.

Jackson, A. J., & Walsh, A. (2014). *Ab initio* Thermodynamic Model of Cu_2ZnSnS_4. *J. Mater. Chem. A, 2*(21), 7829-7836. doi: 10.1039/C4TA00892H

Jitwatcharakomol, T. (2005). *Optimization and Control of Selenium Chemistry and Color in Flint Glass Melts* (Doctoral dissertation, RWTH Aachen University). Retrieved from https://d-nb.info/975188291/34

Kaarna, K. (2014). *Growth of $Cu_2ZnSnSe_4$ Monograin Powders in Molten Potassium Iodide* (Master Thesis, Tallinn University of Technology). Retrieved from https://digi.lib.ttu.ee/i/?1774

Kaiho, T. (Ed.). (2014). *Iodine Chemistry and Applications.* New Jersey, Canada: Wiley & Sons.

Kasatani, K., Mori, K., Kawasaki, M., & Hiroyasu, S. (1987). Photodissociation of Cadmium Diiodide. *Laser Chem., 7*(2-4), 95-107. doi: 10.1155/LC.7.95

Kaune, G., Hartnauer, S., Syrowatka, F., & Scheer, R. (2014). Phase Formation in $Cu_2ZnSnSe_4$ Thin Films Deposited with Multi-Stage Co-Evaporation processes. *Solar Energy Materials & Solar Cells, 120*, 596-602. doi: 10.1016/j.solmat.2013.09.043

Kawasaki, M., Lee, S. J., & Bersohn, R. (1979). The photodissociation of cadmium iodide. *J. Chem. Phys., 71*(3), 1235-1240. doi: 10.1063/1.438478

Kevin, P., Malik, N. S., Malik, M. A., & O'Brien. (2015). Growth of $Cu_2ZnSnSe_4$ and $Cu_2FeSnSe_4$ Thin Films by AACVD from Molecular Precursors. *Materials Letters 152*, 60-64. doi: 10.1016/j.matlet.2015.03.087

Klavina, I., Raudoja, J., Altosaar, M., Mellikov, E., Meissner, D., & Kaljuvee, T. (2010). CZTS ($Cu_2ZnSnSe_4$) crystal growth for use in monograin membrane solar cells, *CYSENI 2010 International Conference of Young Scientists on Energy Issues* (pp. VII-345-VII-353). Kaunas, Lithuania: Lithuanian Energy Institute. Retrieved from https://www.researchgate.net/publication/284715065_CZTS_Cu_2_ZnSnSe_4_CRYSTAL_GROWTH_FOR_USE_IN_MONOGRAIN_MEMBRANE_SOLAR_CELLS

Kolay, S., Mishra, R., Das, D., & Dharwadkar. S. R. (2011). Determination of Standard Enthalpy of Vaporization and Thermal Decomposition Reactions from Derivative Thermogravimetric (DTG) Curves. *Thermochimica Acta, 512(*1-2), 110–117. doi: 10.1016/j.tac.201009.010

Krishnamurthu, N., & Krishnan, R. S. (1965). Raman Spectra of Alkali Halides. *R. S. Z. Physik, 183*(2), 130-139. doi: 10.1007/BF01380789

Kuncewicz-Kupczyk, W., Kapała, J., Roszak, S., & Miller, M. (1998). The thermodynamic properties of the gaseous dimer of CdI_2. *J. Chem. Phys., 108*(18), 7743-7746. doi: 10.1063/1.476209

Larkin, P. J. (2018). *Infrared and Raman Spectroscopy: Principles and Spectral Interpretation. Second Edition*. Cambrige, USA: Elsevier.

Lee, M. (2016). *X-Ray Diffraction for Materials Research: From Fundamentals to Applications*. Oakville, Canada: Apple Academic Press Inc.

Lee, Y. S., Gershon, T., Gunawan, O., Todorov, T. K., Gokmen, T., Virgus, Y., & Guha, S. (2015). $Cu_2ZnSnSe_4$ Thin-Film Solar Cells by Thermal Co-evaporation with 11,6% Efficiency and Improved Minority Carrier Diffusion Length. *Adv. Energy Mater.*, 5(7), Retrieved from https://doi.org/10.1002/aenm.201401372

Leinemann, I., Raudoja, J., Grossberg, M., Altosaar, M., Meissner, D., Traksmaa, R. & Kaljuvee, T. (2011). Comparison of copper zinc tin selenide formation in molten potassium iodide and sodium iodide as flux materials, *CYSENI 2011 International Conference of Young Scientists on Energy Issues* (pp. 8-15). Kaunas, Lithuania: Lithuanian Energy Institute. Retrieved from https://www.researchgate.net/publication/284715158_COMPARISON_OF_COPPER_ZINC_TIN_SELENIDE_FORMATION_IN_MOLTEN_POTASSIUM_IODIDE_AND_SODIUM_IODIDE_AS_FLUX_MATERIALS

Li, D. (2013). Fast and mass synthesis of ZnS nanosheet via ultra-strong surface interaction. *Cryst. Eng. Comm., 48*(15), 10631-10637. doi: 10.1039/C3CE41529E

Li, Q., Meng, H., Zhou, P., Zheng, Y., Wang, J., Yu, J., & Gong, J. (2013). $Zn_{1-x}Cd_xS$ Solid Solutions with Controlled Bandgap and Enhanced Visible-Light Photocatalytic H_2-Production Activity. *ACS Catal. 3*(5), 882-889. doi: 10.1021/cs400975

Lin, Y., & Chen, X. (Ed.). (2016). *Advanced Nano Deposition Methods.* Weinheim, Germany: Wiley-VCH Verlag GmbH & Co.

Lin, Y.-C., Lai, C.-M., & Hsu, H. R. (2017). Impact of Sodium on the Secondary Phases and Current Pathway in $Cu_2ZnSnSe_4$. *Thin Film Solar Cells. Materials Chemistry and Physics, 192*, 131-137. doi: 10.1016/j.matchemphys.2017.01.070

Linde, R. D. (Ed.). (2004). *Handbook of Chemistry and Physics. A Ready-Reference Book of Chemical and Physical Data. 84th edition 2003-2004*. Stanford, United States of America: CRC Press.

Liu, D., Han, D., Huang, M., Zhang, X., Zhang, T., Dai, C., & Chen, S. (2018). Theoretical Study of the Kesterite Solar Cell Based on $Cu_2ZnSn(S,Se)_4$ and Related Photovoltaic Semiconductors. *Chin. Phys. B, 27*(1), Retrieved from http://dx.doi.org/10.1088/1674-1056/27/1/018806

Liu, F., Huang, J., Sun, K., Yan, C., Shen, Y., Park, J., … Hao, X. (2017). Beyond 8 % Ultrathin Kesterite $Cu_2ZnSnSe_4$ Solar Cells by Interface Reaction Route Controlling and Self-Organized Nanopattern at the Back Contact. *NPG Asia Materials, 9*, Retrieved from http://dx.doi.org/10.1038/am.2017.103

Lucovsky, G., Mikkelsen J. C., Liang, W. Y., White, R. M., & Martin, R. M. (1976). Optical Phonon Anisotropies in The Layer Crystals SnS_2 and $SnSe_2$. *Phys. Rev. B, 14*(4), 1663-1669. doi:10.1103/PhysRevB.14.1663

Maeda, T., Nakamura, S., & Wada, T. (2011). First Principles Calculations of Defect Formation in In-Free Photovoltaic Semiconductors Cu_2ZnSnS_4 and $Cu_2ZnSnSe_4$. *Jpn. J. Appl. Phys., 50*(2011), Retrieved from https://www.researchgate.net/publication/252577909_First_Principles_Calculations_of_Defect_Formation_in_In-Free_Photovoltaic_Semiconductors_Cu2ZnSnS4_and_Cu2ZnSnSe4

Mamedov, S., Bolotov, A., Kisliuk, A., Brinker, L., Soltwisch, M., Vlček, M., & Sklenar, A. (1999). Structure of Chalcogenide Glasses in the As_2-Se_3-CuI System. *Solid State Communications, 112*(10), 545-548. doi: 10.1016/S0038-1098(99)00401-9

Mao, J., Zhang, S., Peng, X., Zhang, J., Zhang, H., Gu, L., & Xiang Y. (2015). Formation of $Cu_2ZnSnSe_4$ through Direct Selenization of Metal Oxides. *Vacuum, 118*, 137-141. doi: 10.1016/j.vacuum.2015.01.015

Marcano, G., Rincon, C., Lopez, S. A., Perez, G. S., Herrera-Perez, J. L., Mendoza-Alvarez, J. G., & Rodriguez, P. (2011). Raman Spectrum of Monoclinic Semiconductor Cu_2SnSe_3. *Solid State Commun. 151*(1), 84-86.

Massalski, T. B., & Okamoto, H. (1990). *Binary Alloy Phase Diagrams, 2nd ed.* Materials Park, Ohio: ASM International.

Matsushita, H., & Katsuni, A. (2005). Materials Design for Cu-Based Quaternary Compounds Derived from Chalcopyrite-Rule. *Journal of Physics and Chemistry of Solids, 66*, 1933-1936. doi: 10.1016/j.jpcs.2005.09.028

Mcguire, K., Pan, Z. W., Wang, Z., L., Milkie, D., Menéndez, J., & Rao, A. M. (2002). Raman Studies of Semiconducting Oxide Nanobelts. *J. Nanosci. Nanotech., 2*(5), 1-4. doi: 10.1166/jnn.2002.129

Minaev, V. S., Timoshenkov, S. P., & Kalugin, V. V. (2005). Structural and Phase Transformation in Condensed Selenium. *J Optoelectron Adv Mater., 7*(4), 1717-1741. Retrieved from https://joam.inoe.ro/arhiva/pdf7_4/Minaev.pdf

Mishra, R., Bharadwaj, S. R., Kerkar, A. S., & Dharwadkar, S. R. (1997). Standard Gibbs Energy of Formation of Cs_2CdI_4. *J. Nucl. Mater, 240*(3), 236-240. doi: 10.1016/S0022-3115(96)00674

Montero, S., & Kiefer, W. (1973). The Raman Spectra of Cadmium Iodide. *Journal of Raman Spectroscopy, 1*(6), 565-572. doi: 10.1002/jrs.1250010606

Morales-Acevedo, A. (2013). *Solar Cells. Research and Application Persprctives.* IntechOpen. doi: 10.5772/3418

Murray, R. T., & Heyding, R. D. (1975). The Copper-Selenium System at Temperatures to 850 K and Pressures to 50 kbar. *Can. J. Chem., 53*(6), 878-887. Retrieved from http://www.nrcresearchpress.com/doi/pdf/10.1139/v75-122

Nakamura, S., Maeda, T., & Wada, T. (2011). Phase Stability and Electronic Structure of In-Free Photovoltaic Materials $Cu_2IISnSe_4$ (II: Zn, Cd, Hg). *Jpn. J. Appl. Phys., 50*(2011), Retrieved from http://dx.doi.org/10.1143/JJAP.50.05FF01

Nateprov, A., Kravtsov, V. C., Gurieva G., & Schorr S. (2013). Single Crystal X-ray Structure Investigation of $Cu_2ZnSnSe_4$. *Surf. Engin. Appl. Electrochem., 49*(5), 423-426. doi: 10.3103/S1068375513050098

Nkwusi, G. C. (2017). *Formation and Growth of Cu_2ZnSnS_4 Monograin Powder on Molten CdI_2* (Doctoral dissertation, Tallinn University of Technology). Retrieved from https://digi.lib.ttu.ee/i/?7690

Nkwusi, G., Leinemann, I., & Altosaar, M. (2016). The Processes and Enthalpies in Synthesis of Cu_2ZnSnS_4 in Molten CdI_2. *International Advanced Research Journal in Science, Engineering and Technology, 3*(5), 1-9. doi: 10.17148/IARJSET.2016.3524

Nkwusi, G., Leinemann, I., Raudoja, J., Mikli, V., Kärber, E., & Altosaar, M. (2016). Impact of Growth-Synthesis Conditions on $Cu_2Zn_{1-x}Cd_xSnS_4$ Monograin Material Properties. *Superlattices and Microstructures, 98*, 400-405. doi: 10.1016/j.spmi.2016.09.006

Nkwusi, G., Leinemann, I., Raudoja, J., Mikli, V., Kauk-Kuusik, M., Altosaar, M., & Mellikov, E. (2014). Synthesis of $Cu_2(ZnCd)SnS_4$ Absorber Material for Monograin Membrane Applications, *2013 MRS Fall Meeting:* ScholarOne Manuscripts, 1638 (pp. 1-6) Boston, USA: Massachusetts. doi: 10.1557/opl.2014.245

Noorussaba, A. A. (2017). Investigations of Nanostructure of a New Fast Ionic Conductor [Cu_2CdI_4 : 0.xRbI] where (x = 0,1, 0,2 and 0,3 mol wt%). *Int J Recent Eng Res Dev (IJRERD), 2*(1), 31–41. Retrieved from http://www.ijrerd.com/papers/v2-i1/4.IJRERD-B001.pdf

Okada, Y., Ekins-Daukes, N. J., Kita, T., Tamaki, R., Yoshida, M., Pusch, A., … Guillemoles, J.-F. (2015). Intermediate Band Solar Cells: Recent Progress and Future Directions. *Applied Physics Reviews, 2*(021302) 1-49. doi: 10.1063/1.4916561

Okamoto, H. (2013). Cl-Sn (Chlorine-Tin). *JPEDAV, 34*(2), 145. doi: 10.1007/s11669-012-0149-2

Okamoto, H., & Okamoto, H. (2013). Cd-Cu (Cadmium-Copper). *J. Phase Equilib. Diffus., 34*(1) 65-65. doi. 10. 1007/s11669-012-0131-z,1547-7037.

Olekseyuk, I. D., Dudchak, I. V., & Piskach, L. V. (2001). Fazovi rivnovagi v kvazipotrijnij sistemi Cu_2Se-ZnSe-Cu_2SnSe_3. Phase Equilibrium in Quasibynary System Cu_2Se-ZnSe-Cu_2SnSe_3. *Physics and Chemistry of Solid State, 1*(1), 195-200. Retrieved from http://old.pu.if.ua/inst/phys_che/start/pcss/vol2/number2/0202-03.pdf

Ostraverkhova, O. (Ed.). (2013). *Handbook of Organic Materials for Optical and (Opto)Electronic Devices: Properties and Applications.* Philadelphia, USA: Woodhead Publishing. Retrieved from https://books.google.ee/books?id=IINwAgAAQBAJ&printsec=frontcover&source=gbs_ge_summary_r&cad=0#v=onepage&q&f=false

Özen, A. S., Akdeniz, Z., Ruberto, R., Pastore, G., & Tosi M. P. (2014). The Origins of Tetrahedral Coordination in Molten and Glassy $ZnCl_2$ and Other Group-2B Metal Dihalides. *Phys Lett. A, 378*(4), 431-433. doi: 10.1016/j.physleta.2013.11.040

Paluch, M. (Ed.). (2016). *Dielectric Properties of Ionic Liquids.* Swithzerland: Springer Nature. doi: 10.1007/978-3-31932487-6

Panella, J. R., Trump, B. A., Marcus, G. G., & McQueen, T. M. (2017). Seeded Chemical Vapor Transport Growth of Cu_2OSeO_3. *Cryst. Growth Des. 17*(9), 4944-4948. doi: 10.1021/acs.cgd.7b00879

Parasyuk, O. V., Olekseyuk, I. D., & Marchuk, O. V. (1999). The Cu_2Se–HgSe–$SnSe_2$ System. *Journal of Alloys and Compounds, 287*, 197-205. doi: 10.1016/S0925-8388(99)00047-X

Park, J., Lee, W. Y., Hwang, C. H., Kim, H., Kim, Y., & Shim, Il-W. (2014). Synthases of Cu_2SnSe_3 and Their Transformation into $Cu_2ZnSnSe_4$ Nanoparticles with Tunable Band Gap under Multibubble Sonoluminescence Conditions. *Bull. Korean Chem. Soc., 35*(8), 2331-2334. doi: 10.5012/bkcs.2014.35.8.2331

Perna, G., Capozzi, L., Plantamura, M. C., Minafra, A., Orlando, S., & Marotta, V. (2002). ZnSe Films Deposited on Crystalline GaAs and Amorphous Quartz Substrates by Means of Pulsed Laser Ablation Technique. *Eur. Phys. J. B 29*, 541-545. doi: 10.1140/epjb/e2002-00337-0

Perrone, J. (2012). *Chemical Thermodynamics: Chemical Thermodynamics of Tin* (Vol. 12). Paris, France: OECD Publicatiuons. Retrieved from https://www.oecd-nea.org/dbtdb/pubs/tin.pdf

Poborchii, V. V., Kolobov, A. V., & Tanaka, K. (1998). An *in Situ* Raman Study of Polarization-Dependent Photocrystallization in Amorphous Selenium Films. *Appl Phys Lett. 72*(10), 1167-1169. doi: 10.1063/1.121002

Raadik, T. (2015). *Aplication of Modulation Spectroscopy Methods in Photovoltaic Materials Research* (Doctoral dissertation, Tallin University of Technology). Retrieved from https://digi.lib.ttu.ee/i/file.php?DLID=2521&t=1

Rapaport, E., & Pistorius, C. W. F. T. (1968). Phase Diagrams of the Cuprous Halides to High pressures. *Phys. Rev., 172*(3), 838-847. doi: 10.1103/PhysRev.172.838

Reddy, V. R. M., Gedi, S., Park, C., Miles, R. W., & Reddy K. T. R. (2015). Development of Sulphurized SnS Thin Film Solar Cells. *Current Applied Physics, 15*, 588-598. doi: 10.1016/j.cap.2015.01.022

Revathi, N., Bereznev, S., Lehner, J., Traksmaa, R., Safonova, M., Mellikov, E., & Volobujeva, O. (2015). Thin Tin Monosulfide Films Deposited with the HVE Method for Photovoltaic Applications. *Materials and technology, 49*(1), 149−152. Retrieved from http://mit.imt.si/Revija/izvodi/mit151/revathi.pdf

Rühle, S. (2016). Tabulated Values of the Shockley-Queisser Limit for Single Junction Solar Cells. *Solar Energy, 130*, 139–147. doi: 10.1016/j.solener.2016.02.015

Russell, T.D. (1986). Vapor-Phase Composition above the CdI_2-NaI and the ThI_4-NaI Systems. *J. Phys. Chem., 90*(24*)*, 6590-6594. doi: 10.1002/chin.198708023

Safonova, M. (2016). *SnS Thin Films Deposited by Chemical Solution Method and Characterization* (Doctoral dissertation, Tallin University of Technology). Retrieved from https://digi.lib.ttu.ee/i/?3964

Safonova, M., Mellikov, E., Mikli, V., Kerm, K., Revathi, N., & Volobujeva, O. (2014). Chemical Bath Deposition of SnS Thin Films from the Solutions with Different Concentrations of Tin and Sulphur. *Advanced Materials Research, 1117*, 183-186. doi: 10.4028/www.scientific.net/AMR.1117.183

Safonova, M., Nair, P. P. K., Mellikov, E., Aragon, R., Kerm, K., Revathi, N., … Volobujeva, O. (2015). Thermal Annealing of Sequentially Deposited SnS Thin Films. *Proceedings of the Estonian Academy of Sciences, 64*(4), 488-494. doi: 10.3176/proc.2015.4.04

Sahayaraj, S., Brammertz, G., Buffiere, M., Meuris, M., Vleugels, J., & Poortmans, J. (2016). Effect of Cu Content and Temperature on the Properties of $Cu_2ZnSnSe_4$ solar cells. *EPJ Photovoltaics 7*, Retrieved from https://doi.org/10.1051/epjpv/2016004

Samieipour, A., Kouhiisfahani, E., Galajev, S., & Meissner, D. (2015). CZTS Monograin Membranes for Photoelectrochemical Fuel Production Preparation and characterization. In *5th International Conference on Clean Electrical Power: Renewable Energy Resources Impact* (pp. 212-215). Taormina: Italy. Retrieved from http://dx.doi.org/101109/ICCEP.2015.7177625

Sangster, J., & Pelton, A. D. (1997). Phase Diagram Evalutions: Section II. *Journal of Phase Equilibria, 18*(2), 177-189. doi: 10.1007/BF02665702 and doi: 10.1007/BF02665704

Sardela, M. (Ed.). (2014). *Practical Materials Characterization*. New York, USA: Springer. doi: 10.1007/978-1-4614-9281-8

Schurr, R., Hölzing, A., Jost, S., Hock, R., Voβ, T., Schulze, J., … Schock, H. W. (2009). The Ceystallisation of Cu_2ZnSnS_4 Thin Film Solar Cell Absorbers from Co-Electroplated Cu-Zn-Sn precursors. *Thin Solid Films, 517*, 2465-2468. doi: 101016/j.tsf.2008.11.019

Scragg, J. J. (2010). *Studies of Cu_2ZnSnS_4 Films Prepared by Sulphurization of Electrodeposited Precursors* (Doctoral dissertation, University of Bath). Retrieved from https://purehost.bath.ac.uk/ws/portalfiles/portal/297317/UnivBath_PhD_2010_J_Scragg.pdf

Scragg, J. J., Dale, P. J., Colombara, D., & Peter, L. M. (2012). Thermodynamic Aspects of the Synthesis of Thin-Film Materials for Solar Cells. *ChemPhysChem, 13*, 3035-3046. doi: 10.1002/cphc.201200067

Scragg, J. J., Ericson, T., Kubart, T., Edoff, M., & Platzer-Björkman, C. (2011). Chemical Insights Into the Instability of Cu_2ZnSnS_4 Films during Annealing. *Chemistry of Materials, 23*, 4625-4633. doi: 10.1021/cm202379s

Sharma, R. C., & Chang Y. A. (1996). The Cd-Se (Cadmium-Selenium) System. *Journal of Phase Equilibria, 17*(2), 140-145. doi: 10.1007/BF02665791

Sharma, R. C., & Chang Y. A. (1986). The Se-Sn (Selenium-Tin) system. *Bulletin of Alloy Phase Diagrams, 7*(1), 68-72. doi: 10.1007/BF02874984

Sharma, R. C., & Chang Y. A. (1986). The S-Sn (Sulfur-Tin) System. *Bulletin of Alloy Phase Diagrams, 7*(3), 269-273. doi: 10.1007/BF02869004

Sinsermsuksakul, P., Hartman, K., Kim, S. B., Heo, J., & Sun, L. (2013). Enhancing the Efficiency of SnS Solar Vells *via* Band-Offset Engineering with a Zinc Oxysulfide Buffer Layer. *Appl. Phys. Lett., 102*(5), Retrieved from http://dx.doi.org/10.1063/1.4789855

Sinsermsuksakul, P., Sun, L., Lee, S. W., Park, H. H., Kim, S. B., Yang, C., & Gordon, R. G. (2014). Overcoming Efficiency Limitations of SnS-Based Solar Cells. *Adv. Energy Mater., 2014*, Retrieved from https://pdfs.semanticscholar.org/8fb5/74d68cfc8b744b36f12f33af8d0e93fe141b.pdf

Skudlarski, K., Dudek, J., & Kapała, J. (1987). Thermodynamics of Sublimation of Cadmium Halides Investigated by the Mass-Spectrometric Method. *J. Chem. Thermodyn, 19*, 857-862. Retrieved from https://sd-cart.elsevier.com

Smith, A. J., Meek, P. E., & Liang, W. Y. (1977). Raman Scattering Studies of SnS_2 and $SnSe_2$. *J Phys C Solid State Phys. 10*(8), 1321-1333. doi: 10.1088/0022-3719/10/8/035

Smith, L. H. J. (Ed.). (2007). *Purification of Copper (i) Iodide*. Chichester, United Kingdom: John Wiley & Sons Ltd. doi: 10.1002/9780470132531.ch20

Sofronov, D. S., Grinyov, B. V., Voloshko, A. Y., Gerasimov, V. G., Kisil, E. M., Smirnov, N. N., & Shishkin, O. V. (2005). Dehydration of Alkali Metal Iodides in Vacuum. *Functional materials, 12*(3), 559-562. doi: 10.1109/CRMICO.2005.1565148

Sofronov, D. S., Kudin, K. A., Voloshko, A. Y., Kudin, A. M., & Shishkin, O. V. (2009). Origin of the Thermal Desorption Peaks of Gases in NaI above 180 °C. *Inorganic Materials, 45*(11), 1314-1318. doi: 10.1134/S0020168509110235

Son, D.-H., Kim, D.-H., Yang, K.-J., Nam, D., Gansukh, M., Cheong, H., & Kang, J.-K. (2014). Influence of Precursor Sulfur Content on Film Formation and the Properties of Sulfurized Cu_2ZnSnS_4 Thin Films for Solar Cells. *Phys. Status Solidi A, 211*(4), 946–951. doi: 10.1002/pssa.201330425

Son, D.-H., Kim, D.-H., Park, S.-N., Yang, K.-J., Nam, D., Cheong, H., & Kang, J.-K. (2015). Growth and Device Characteristics of CZTSSe Thin-Film Solar Cells with 8,03 % Efficiency. *Chem. Mater., 27*(15), 5180-5188. doi: 10.1021/acs.chemmater.5b01181

Sreedevi, G., & Reddy, K. T. R. (2013). Properties of Tin Monosulphide Films Grown by Chemical Bath Deposition. *Conference Papers in Energy, 2013*, Retrieved from https://www.hindawi.com/journals/cpis/2013/528724/

Stammreich, H., Forneris, R., & Tavares Y. (1956). Raman Spectra and Force Constant of GeI_4 and SnI_4. *J Chem Phys., 25*(6), 1278-1279. doi: 10.1063/1.1743195

Steinmann, V., Jaramillo, R., Hartman, K., Chakraborty, R., Brandt, R. E., Poindexter, J. R., … Buonassisi T. (2014). 3,88 % Efficient Tin Sulfide Solar Cells Using Congruent Thermal Evaporation. *Adv Mater. 26*(44), 7488-7492. doi: 10.1002/adma.201402219

Sun, Y., Lin, S., Li, W., Cheng, S., Zhang, Y., Liu, Y., & Liu, W. (2017). Review on Alkali Element Doping in Cu(In,Ga)Se_2 Thin Films. *Engineering, 3*(2017), 452-459. doi: 10.1016/J.ENG.2017.04.020

Supreeth, A., & Shreya, Y. S. (2016). Perovskite Solar Cells: a Review. *IJEDR, 4*(2), 1974-1977. Retrieved from https://www.ijedr.org/papers/IJEDR1602347.pdf

Teredesai, P. V., Leonard D. F., Govindarja, A., Sood A. K., & Rao, C. N. R. (2002). A Raman Study of CdSe and ZnSe Nanostructures. *J Nanosci Nanotechnol. 2*(5), 495-498. Retrieved from https://www.ncbi.nlm.nih.gov/pubmed/12908286

Thomas, R. (2013). *Practical Guide to ICP-MS: a Tutorial for Beginners*. Third Edition. Boca Raton, USA: CRC Press.

Timmo, K., Altosaar, M., Raudoja, J., Mellikov, E., Varema, T., Danilson, M., & Grossberg, M. (2007). The Effect of Sodium Doping to $CuInSe_2$ Monograin Powder Properties. *Thin Solid Films, 515*(15), 5887-5890. doi: 10.1016/j.tsf.2006.12.087

Tomashik, V. N., Lebrun, N., & Perrot P. (2006). *Copper-Selenium-Tin.* Non-Ferrous Metal Ternary Systems. Semiconductor Systems: Phase Diagrams, crystallographic and thermodynamic data. Landolt-Bornstein new series IV/11C1, 361-373.

Tosi, P. M. (2015). Metal-Halide Systems: from Molecular Clusters to Liquid-State Structure. *Atti Accad. Pelorit. Cl. Sci. Fis. Mat. Nat., 93*(1), R1-1-R1-10. doi: 10.1478/AAPP.931R1

Triolo, R., & Narten, A. H. (1981). X-ray Diffraction Study of Molten Zinc Chloride at 323 °C. *J Chem Phys., 74*(1), 703-704. doi: 10. 1063/1.440829.

Voloshko, A. Y., Grinyov, B. V., Goriletsky, V. I., Smirnov, N. N., Sofronov, D. S., Shishkin, O. V., & Kisil, E. M. (2004). Effect of Microwave Energy on Dehydration Process of Sodium Iodide Used in Single Crystal Growing. *Functional Materials, 11*(3), 571-574. Retrieved from https://www.researchgate.net/publication/256077630_Effect_of_microwave_on_dehydration_process_of_sodium_iodide_used_in_single_crystal_growing

Wagner, M. (2017). *Thermal Analysis in Practise: Fundamental Aspects.* Munich, Germany: Carl Hanser Verlag GmbH & Company KG

Wakita, H., Johansson, G., Sandström, M., Goggin, P. L., & Ohtaki, H. J. (1991). Structure Determination of Zinc Iodide Complexes Formed in Aqueous Solution. *Solution Chem., 20*(7), 643-668. Retrieved from https://slideheaven.com/structure-determination-of-zinc-iodide-complexes-formed-in-aqueous-solution.html

Wallace S. K., Mitzi D. B., & Walsh A. (2017). The Steady Rise of Kesterite Solar Cells. *ACS Energy Lett., 2*(4), 776-779. doi: 10.1021/acsenergylett.7b00131

Wang, W., Winkler, M. T., Gunawan, O., Gokmen, T., Todorov, T. K., Zhu, Y., & Mitzi, D. B. (2013). Device Characteristics of CZTSSe Thin-Film Solar Cells with 12,6 % Efficiency. *Adv. Energy Mater., 4*(7), Retrieved from https://doi.org/10.1002/aenm.201301465

Wibowo, R. A., Jung, W. H., Al-Faruqi, M. H., Amal, I., & Kim, K. H. (2010). Crystallization of $Cu_2ZnSnSe_4$ Compound by Solid State Reaction Using Elemental Powders. *Materials Chemistry and Physics, 124,* 1006-1010. doi: 10.1016/j.matchemphys.2010.08.020

Wojakowska, A. (1989). Phase Equilibrium Diagram for the Tin (II) Iodide-Copper (I) Iodide System. *J. Thermal Anal., 35*(7), 2433-2439. doi: 10.1007/BF01911907

Woods, A., & Chavez, L. (2018). *Differential Scanning Calorimetry: Basics and Applications.* New Yourk, USA: Nova Science Publishers, Incorporated.

Xiancong, H. E., Jinhong, P. I., Yuming D. A. I., & Xiaoquan L. I. (2013). Elastic and Thermo-Physical Properties of Stannite-Type Cu_2ZnSnS_4 and $Cu_2ZnSnSe_4$ from First-Principles Calculations. *Acta Metall. Sin. (Engl. Lett.), 26*(3), 285-292. doi: 10.1007/s40195-012-0248-4

Yang, Y., Wang, G., Zhao, W., Tian, Q., Huang, L., & Pan, D. (2014). Solution-Processed Highly Efficient $Cu_2ZnSnSe_4$ Thin Film Solar Cells by Dissolution of Elemental Cu, Zn, Sn, and Se Powders. *ACS Appl. Mater. Interfaces, 7*(1), 460-464. doi: 10.1021/am5064926

Yannopoulos, S. N., & Andrikopoulos, K. S. (2004). Raman Scattering Study on Structural and Dynamical Features of Noncrystalline Selenium. *J Chem Phys. 121*(10), 4747-4758. doi: 10.1063/1.1780151

Yin, X. S., Tang, C. H., Sun, L. F., Shen, Z. X., & Gong, H. (2014). Study on Phase Formation Mechanism of Non- and Near-Stoichiometric $Cu_2ZnSn(S,Se)_4$ Film Prepared by Selenization of Cu-Sn-Zn-S Precursors. *Chem. Mater., 26*(6), 2005-2014. doi: 10.1021/cm403423e

Yoo, H., Wibowo, R. A., Hölzing, A., Lechner, R., Palm, J., Jost, S., … Hock, R. (2013). Investigation of the Solid State Reactions by Time-Resolved X-ray Diffraction while Crystallizing Kesterite $Cu_2ZnSnSe_4$ Thin Films. *Thin Solid Films, 535*, 73-77. doi: 10.1016/j.tsf.2013.01.054

Yu-Shan, S. (2013). Competing in the Global Solar Photovoltaic Industry: The Case of Taiwan. *International Journal of Photoenergy, 2013*, 1-11. doi: 10.1155/2013/794367

Zhang, W. (2013). *Study of Chemical Pathway of $Cu_2ZnSnSe_4$ Formation in NaI as Flux Material.* Tallinn, Estonia: Tallinn University of Technology.

Zheng, P., Rougieux, F. E., Samundsett, C., Yang, X., Wan, Y., Degoulange, J., … Macdonald, D. (2016). Simulation of 20,96 % Efficiency *n*-type Czochralski UMG Silicon Solar Cell. *Energy Procedia, 92*(2016), 434-442. doi: 10.1016/j.egypro.2016.07.124

Acknowledgments

I am deeply grateful to my supervisor, senior research scientist Dr. Mare Altosaar, for her support, motivation, guidance and sharing of knowledge over the years. This thesis would not be possible without her help.

I cannot express enough thanks to the Heads of the Departments and Deans (Institute of Materials Science, Department of Materials and Environmental Technology, Faculty of Chemical and Materials Technology, School of Engineering), Dr. Marit Kauk-Kuusik, Prof. Malle Krunks, Prof. Andres Öpik, and Dr. Arvo Oorn, for giving me the opportunity to join and work on this research. I would like to especially thank Prof. Enn Mellikov, who, although no longer with us, continues to inspire by his example and dedication to the students he served over the course of his career.

My thanks go to opponents for finding the time to review this thesis.

I sincerely appreciate the learning opportunities and experimental support and apparatus provided by Dr. Rein Kuusik, who is head of the Laboratory of Inorganic Materials and Prof. Urve Kallavus, who was head of the Centre for Materials Research.

I would like to thank all my colleagues who took part in this study for sharing their time and ideas and for assisting me with the experiments. I have learned much through our conversations. In particular, I thank Prof. Dieter Meissner, Prof. Maarja Grossberg Prof. Jüri Krustok and Prof. Arvo Mere; senior researchers Tiit Kaljuvee, Kaia Tõnsuaadu, Jaan Raudoja, Kristi Timmo, Olga Volobujeva, Valdek Mikli, Ilona Oja Acik; Dr. Sergei Bereznev, Dr. Taavi Raadik, Dr. Karin Kerm, Dr. Maris Pilvet, Dr. Mati Danilson, Dr. Erki Kärber, and Dr. Nkwusi Godswill Chimezie; researcher Rainer Traksmaa; PhD students Mihkel Loorits and Reelika Kaupmees; and master's student Weihao Zhang.

This research was supported by the Doctoral Studies and Internationalization Program DoRa of the European Social Funds; Estonian Science Foundation grants 9425 and 8964, project TK117T, National R&D programs AR10128 and AR12128, the Estonian Ministry of Education and Research Contract No. SF0140099s08, IUT 19-28, and EAS project EU29713 and the ASTRA “TUT Institutional Development Programme for 2016-2022” Graduate School of Functional Materials and Technologies" (2014-2020.4.01.16-0032). Acknowledgements of financial support also go to the following projects: TK141 (TAR16016) "Advanced materials and high-technology devices for sustainable energetics, sensorics and nanoelectronics"; IUT19-28 "New materials and technologies for solar energetics". The thanks go to *Inga Invest OÜ* for covering the costs of language correction.

My deepest gratitude goes to my family for their unconditional support and encouragement during my studies and thesis writing.

Abstract

Chemical Processes Involved in $Cu_2ZnSnSe_4$ Synthesis and SnS Recrystallization in a Molten Salt Medium

This thesis is focused on the synthesis process of CZTSe and recrystallization of SnS in molten salts to determine the factors influencing the process to produce single-phase solar cell absorber materials in monograin powder form. CZTSe and SnS were the subjects of the studies and were chosen because of their cheap and abundant constituent elements, high absorption coefficients (> 10^4 cm^{-1}), suitable band gap energies, and a promising CZTSe solar cell record power conversion efficiency of 11,6 % that has been previously achieved. One of the cheapest technologies for solar cell absorber material production is the molten salt synthesis-growth method, which results in monograin powders. The certified efficiency of a CZTSSe monograin layer solar cell is 8,4 % (10,8 % for the active area).

The studies were performed to describe the chemical interactions between the compounds used in the CZTSe molten phase synthesis-growth process and to determine how to synthesize and produce single-phase monograin powders for monograin membrane solar cells. The studies were necessary because the production of a single-phase absorber material in the liquid media of flux salts is difficult because of the high possibility of forming secondary phases and byproducts. The chemical interactions between precursor compounds (CuSe, ZnSe, and SnSe) and molten salts (KI, NaI, and CdI_2) have not been previously studied. Additionally, the chemical processes involved in SnS recrystallization in molten $SnCl_2$, KI and CdI_2 were not previously known.

The investigations involved the analysis of the precursors, flux materials and different binary precursor-flux mixtures. The chemical pathway of CZTSe formation and the chemical reactions occurring during the SnS recrystallization in molten salt media were described. Different analysis methods were used, including DTA, DSC, TG, MS, Raman, XRD, SEM, EDX, ICP-MS and thermodynamic calculations using a database (software HSC6 Chemistry Ver. 6.0.). The purities of the precursors, flux instabilities and reactions probabilities were determined in different flux-precursor mixtures. The DTA studies were performed in vacuum-closed quartz ampoules that were specially designed for the DTA set-up. For the DTA, a new calibration method was developed in which the same inorganic salts (KI, NaI, and CdI_2) were used as references because classical calibration materials react with quartz.

In this study was found that single phase CZTSe monograins form in molten KI and NaI. CZTSe formation in molten salts occurs as follows: before melting of the flux salt, the formation of CZTSe is inhibited by the solid phase flux material surrounding the solid particles of the precursor compounds. However, the formation of CZTSe and CTSe is possible to a small extent *via* solid-state reactions. DTA analyses and Cu-Se phase diagram showed CuSe phase transformation to $Cu_{2-x}Se$ and Se at 377-383 °C (650-656 K), Se activates the reaction with SnSe to form $SnSe_2$ because of the Se evaporation and fast spreading in the ampoule. The intense formation of CZTSe (or CTSe) occurs from the binary compounds of Cu_2Se, $SnSe_2$ and ZnSe during the melting of the flux. The formation enthalpy of CZTSe from Cu_2Se, $SnSe_2$ and ZnSe was determined experimentally for the first time and is $-36{,}0 \pm 3{,}6$ kJ mol^{-1} in both KI at 685 °C (958 K) and in NaI at 661 °C (934 K). CZTSe melts at 795 °C (1068 K) and the heat

of fusion was experimentally determined to be 44,6 ± 4,5 kJ mol^{-1}. The CTSe formation enthalpy from Cu_2Se and $SnSe_2$ in KI at 684 °C (957 K) is -26,0 ± 2,6 kJ mol^{-1}, and in NaI at 661 °C (934 K) it is -32,0 ± 3,2 kJ mol^{-1}. The determined doping level of CZTSe (grown in KI and NaI at 740 °C (1013 K)) is ~10^{19} at. K or Na cm^{-3}.

It was found that CdI_2 as a flux material is chemically active – solid CdI_2 racts with the solid precursor compounds of CuSe, SnSe and ZnSe to a small extent, forming CdSe (CdSe interacts with Cu_2SnSe_3 to form $Cu_2CdSnSe_4$), and in molten CdI_2, the solid precursor compounds show chemical dissolution that results in the formation of CdSe and iodides. In molten CdI_2, CdSe with ZnSe forms $Zn_{1-x}Cd_xSe$, and $Zn_{1-x}Cd_xSe$ interacts with CTSe to form $Cu_2Zn_{1-x}Cd_xSnSe_4$. The formation enthalpy of $Cu_2Zn_{1-x}Cd_xSnSe_4$ at 388 °C (661 K) was determined to be -15,0 ± 1,5 kJ mol^{-1}. The recrystallization of presynthesized CZTSe in CdI_2 leads to the formation of $Cu_2Zn_{1-x}Cd_xSnSe_4$.

Upon recrystallizing polycrystalline SnS in the different molten salts of CdI_2, $SnCl_2$ and KI as the flux materials, a single phase SnS monograin powder was obtained at 740 °C (1013 K) in KI and at 500 °C (773 K) in $SnCl_2$. Recrystallization of SnS in molten CdI_2 resulted in a multiphase mixture of SnS, Sn_2S_3 and CdS crystals. SnS chemically dissolves in CdI_2. The released I_2 due to the CdI_2 instability reacts with SnS. The formed S leads also to the formation of CdS and Sn_2S_3.

Low melting phases that can interfere with the size and shape formation because of the sintering of solid precursor particles were found as follows: SnI_2 (T_m = 320 °C or 593 K) and SnI_4 (T_m = 144 °C or 417 K) form during the reactions of CdI_2 with SnSe at 348 °C (621 K) or with $SnSe_2$ at 368 °C (641 K). Se (T_m = 221 °C or 494 K) formed at 377-383 °C (650-656 K) in the CuSe phase transformation to $Cu_{2-x}Se$. Impurities involved in the CZTSe molten salt synthesis-growth process with precursors or with flux materials can have a considerable influence on the process: a) free I_2, formed due to the instability of KI, NaI and CdI_2 under atmospheric conditions and reacts with binary precursor compounds, resulting in the formation of CuI, SnI_2, SnI_4, and ZnI_2; thus, a dried flux is recommended; b) oxygen brought along with SnSe in the form of SnO_2, causes the formation of oxygen-containing compounds; c) Se (unreacted elemental Se in ZnSe and overstoichiometric Se in SnSe) melts below the melting point of the flux, and can induce the primary sintering of precursor particles that disturb the monograin growth of CZTSe.

The aims of the research work of this thesis were completed. The novelty of this work involved filling the gap in knowledge regarding the chemical formation of CZTSe and recrystallization of SnS in different flux salts. The determined thermodynamic data can also be used in inorganic databases for other research purposes. Recommendations for the CZTSe molten salt synthesis-growth technological process can be provided (for flux selection, to minimize the risks of byproduct formation and sintering). The formation enthalpies of CTSe and CZTSe were experimentally determined. The influence of impurities during the synthesis process with precursor compounds and the instabilities of the flux salts were discussed and evaluated. Several important aspects determine the synthesis pathway of CZTSe and influence the crystal growth mechanism, and the size distribution and change in the shape of the grains were found during this study.

Lühikokkuvõte

Keemilised protsessid $Cu_2ZnSnSe_4$ sünteesil ja SnS rekristallisatsioonil sulade soolade keskkonnas

Antud doktoritöö on keskendunud keemiliste protsesside uurimisele, mis toimuvad $Cu_2ZnSnSe_4$ (CZTSe) monoterapulbri süntees-kasvatusel ja SnS rekristallimisel sulade soolade keskkonnas eesmärgiga kasutada neid pulbreid absorbermaterjalina monoterakiht päikesepatareides. CZTSe ja SnS koostiselementide suhteliselt madal hind, laialdane esinemine maakoores, nende ühendite suur valguse neeldumisvõime (absorptsioonikoefitsient $> 10^4$ cm^{-1}), sobilik keelutsooni väärtus ning CZTSe päikesepatareidega saavutatud rekordefektiivsus 11,6 % teevad need ühendid (eriti CZTSe) atraktiivseteks päikesepatarei absorbermaterjalideks. Monoterapulbrite kasvatus on üheks odavaks absorbermaterjali saamismeetodiks, kus iga kristall moodustub ja kasvab kui mikromonokristall. CZTSe-tüüpi monoterakiht-päikesepatarei sertifitseeritud kasutegur on 8,4 % (10,8 % aktiivse pindala kohta).

Töö eesmärgiks oli kirjeldada keemilisi vastasmõjusid CZTSe süntees-kasvatuse protsessis osalevate ühendite vahel ja leida võimalused ühefaasiliste monoterapulbriliste absorbermaterjalide sünteesiks ja tootmiseks. Uuringud olid vajalikud, kuna ühefaasilise absorbermaterjali saamine erinevates sulades soolades on keerukas mitmete kõrvalühendite tekkevõimaluse tõttu. Keemilisi vastasmõjusid protsessis osalevate ühendite (CuSe, ZnSe, SnSe) ja sulade soolade (KI, NaI, CdI_2) vahel ei olnud senini uuritud. Samuti ei olnud teada keemilised protsessid, mis toimuvad SnS rekristallisatsioonil sulades $SnCl_2$, KI ja CdI_2 soolades.

Analüüsimisel kasutati järkjärgulist lähenemist alates üksikutest lähteühenditest ja kasutatud sooladest kuni keeruliste sünteesisegudeni. Sellisel viisil määrati antud töös CZTSe moodustumise keemiline tee ja SnS rekristalliseerimisel esinevad reaktsioonid. Doktoritöös kasutati erinevaid analüüsimeetodeid: termilist analüüsi (DTA, TG, DSC), mass-spektromeetriat (MS), Raman spektroskoopiat, röntgendifraktsiooni (XRD), skaneerivat elektronmikroskoopiat (SEM), energia-dispersiivset röntgen-spektroskoopiat (EDX), induktiiv-sidestatud plasma mass-spektromeetriat (ICP-MS) ja termodünaamilisi arvutusi andmebaasiga (*software HSC6 Chemistry Ver. 6.0.*). Määrati prekursorite puhtuse taset, sulandajate stabiilsust ja võimalikke reaktsioone sulandaja prekursorühendite segudes. DTA uuringud viidi läbi analüüsiseadmele kohandatud suletud kvartsampullides. DTA kalibratsiooniks arendati uus meetod, kus võrdlusainena kasutati samu anorgaanilisi soolasid (KI, NaI, CdI_2), mis sünteeskasvatuselgi, kuna tavaliselt termilises analüüsis kasutatavad standardained ei sobinud kalibreerimiseks kvartsampullides nende reageerimise tõttu kvartsiga.

Töö tulemusena leiti, et ühefaasilist CZTSe monoterapulbrit on võimalik kasvatada KI-s ja NaI-s. CZTSe moodustumine sulandajates toimub järgnevalt: tahke sulandaja puhul on CZTSe teke takistatud, sest tahke sulandaja osakesed ümbritsevad prekursorainete osakesi. Kuigi ka vähene CZTSe ja CTSe teke on võimalik tahke-faasilise reaktsiooni tõttu. DTA analüüsi ja Cu-Se olekudiagrammi alusel leiti, et 377-383 °C (650-656 K) juures tekib CuSe peritektilise lagunemisreaktsiooni tulemusena $Cu_{2-x}Se$ ja vaba Se, mis reageerib SnSe-ga ja tekib $SnSe_2$. Intensiivne CZTSe või (CTSe) moodustumine toimub Cu_2Se-st, $SnSe_2$-st ja ZnSe-st sulandaja sulas faasis. Esmakordselt määrati katseliselt CZTSe tekkeentalpia $-36,0 \pm 3,6$ kJ mol^{-1} nii KI-s kui ka NaI-s, vastavalt 685 °C (958 K) ja 661 °C (934 K) juures. CZTSe sulab 795 °C juures ja katseliselt

määratud sulamissoojus oli 44,6 ± 4,5 kJ mol^{-1} 795 °C (1068 K) juures. CTSe tekkeentalpia reaktsioonist Cu_2Se ja $SnSe_2$ vahel KI-s 684 °C (957 K) juures oli -26,0 ± 2,6 kJ mol^{-1} ja NaI-s 661 °C (934 K) juures -32,0 ± 3,2 kJ mol^{-1}. KI ja NaI võimaldavad süntees-kasvatada $Cu_2ZnSnSe_4$ monoterapulbreid, kus K ja Na kui lisandi sisaldus on $\sim10^{19}$ aatomid cm^{-3}.

Leiti, et CdI_2 kui sulandaja on keemiliselt aktiivne – tahke CdI_2 reageerib vähesel määral tahkete CuSe, SnSe ja ZnSe-ga moodustades CdSe (CdSe olles kontaktis Cu_2SnSe_3-ga moodustab $Cu_2CdSnSe_4$) ja sula CdI_2 lahustab endas keemiliselt binaarseid prekursorühendeid ning tulemuseks on CdSe ja iodiidide teke. CdSe ja ZnSe moodustavad sulas CdI_2-s $Zn_{1-x}Cd_xSe$-i, mis olles kontaktis Cu_2SnSe_3-ga moodustab $Cu_2Zn_{1-x}Cd_xSnSe_4$-i. $Cu_2Zn_{1-x}Cd_xSnSe_4$ moodustumise entalpiaks saadi 388 °C (661 K) juures -15,0 ± 1,5 kJ mol^{-1} . Eelsünteesitud CZTSe rekristalliseerimisel CdI_2-s moodustus samuti $Cu_2Zn_{1-x}Cd_xSnSe_4$.

Uurides SnS rekristallisatsiooni erinevates sulades soolades (CdI_2, $SnCl_2$ ja KI) näidati, et ühefaasilist SnS monoterapulbrit on võimalik kasvatada 740 °C (1013 K) juures KI-s ja 500 °C (773 K) juures $SnCl_2$-s kui sulandajas. SnS rekristallisatsioonil sulas CdI_2-s tekkis mitmefaasiline segu, mis sisaldas SnS, Sn_2S_3 ja CdS kristalle. SnS lahustab keemiliselt CdI_2-s. Samuti leiti, et CdI_2 ebastabiilsuse tõttu vabanenud I_2 reageeris SnS-ga eraldades S, mis redigeerides andis samuti CdS ja Sn_2S_3.

Analüüsides tekkinud kõrvalprodukte, leiti madalal temperatuuril sulavaid ühendeid, mis võivad mõjutada moodustuvate CZTSe kristallide kuju ja ebanormaalset osakeste suurusejaotust: SnI_2 (T_m = 320 °C või 593 K) ja SnI_4 (T_m = 144 °C või 417 K) moodustuvad CdI_2 reaktsioonil SnSe-ga 348 °C (621 K) juures ja $SnSe_2$-ga 368 °C (641 K) juures. Se (T_m = 221 °C või 494 K) vabaneb 377-383 °C (650-656 K) juures CuSe-di faasiüleminekul $Cu_{2-x}Se$-ks. Töös näidati, et lisandid, mis viiakse CZTSe sünteesiprotsessi prekursorite või sulandajaga, võivad oluliselt mõjutada protsessi käiku: a) vaba jood, mis võib sisalduda KI-s, NaI-s või CdI_2-s, reageerides prekursorühenditega, võib anda CuI-di, SnI_2-di, SnI_4-di, ZnI_2-di, seetõttu on vajalik kasutada kuivatatud sulandajat; b) hapnik, mis tuuakse süsteemi SnO_2-na SnSe pinnal, annab võimaluse tekkida hapnikku sisaldavatel ühenditel; c) Se (reageerimata elementaarne Se ZnSe-s ja üle-stöhhiomeetriline Se SnSe-s) sulades madalamal temperatuuril kui sulandaja võib põhjustada primaarset prekursorosakeste paakumist ja sellega mõjutada ka CZTSe monoterade kasvuparameetreid.

Töös püstitatud eesmärgid saavutati. Töö uuenduslik väärtus seisneb selles, et saadi informatsiooni CZTSe sünteesil ja SnS rekristallisatsioonil sulades soolades toimuvate keemiliste protsesside kohta, mille kohta teave senini puudus. Saadud termodünaamilist informatsiooni on võimalik kasutada anorgaaniliste ühendite andmebaasi täiendamisel. Lisaks saab uurimistulemusi edaspidi kasutada sulandajate valikul teistes süntees-kasvatuse protsessides, et vältida või vähendada kõrvalsaaduste teket ja esmast lähteainete osakeste paakumist. Määrati eksperimentaalselt CTSe ja CZTSe tekkeentalpiad. Samuti hinnati ka nii sulandajana kasutatud sooladega kui ka lähteainetega süsteemi viidavate lisandite mõju. Käesolevas doktoritöös leiti mitmeid erinevaid aspekte, mis mõjutavad uuritud ühendite sünteesi kulgu ja kristallide kasvu ning kuju moodustumist.

Appendix 1

Paper I

Leinemann, I., Timmo, K., Grossberg, M., Kaljuvee, T., Tõnsuaadu, K., Traksmaa, R., Altosaar, M., Meissner, D. (2015). Reaction enthalpies of $Cu_2ZnSnSe_4$ synthesis in KI. *J Therm Anal Calorim, 119*(3), 1555-1564. doi: 10.1007/s10973-014-4339-5

J Therm Anal Calorim (2015) 119:1555–1564
DOI 10.1007/s10973-014-4339-5

Reaction enthalpies of $Cu_2ZnSnSe_4$ synthesis in KI

**Inga Leinemann · Kristi Timmo · Maarja Grossberg ·
Tiit Kaljuvee · Kaia Tõnsuaadu · Rainer Traksmaa ·
Mare Altosaar · Dieter Meissner**

Received: 23 June 2014 / Accepted: 2 December 2014 / Published online: 31 January 2015
© Akadémiai Kiadó, Budapest, Hungary 2015

Abstract The phase transitions and chemical reactions in the formation process of $Cu_2ZnSnSe_4$ (CZTSe) from CuSe, SnSe, and ZnSe in the presence of KI were studied using the DTA method for the determination of thermal effects. XRD and Raman spectroscopy were performed for the phase analysis in samples after heating them for prolonged time to several degrees of temperatures higher than peak-top temperatures of DTA effects in heating and cooling curves. The chemical pathways of the CZTSe formation before and during the melting of KI were clarified. The reaction enthalpies were determined using pure KI as a substance for the calibration of enthalpy values. In the mixtures, the melting of KI is always accompanied by some dissolution of the precursor compounds and lowering of the melting temperature in comparison with pure KI. The initiator of the process of the partial CZTSe formation at around 400 °C is elemental Se. The CZTSe formation of binary precursors in liquid phase of KI takes place with the experimentally determined enthalpy of -36 ± 2 kJ mol^{-1}. The heat of fusion of formed CZTSe is 4 kJ mol^{-1} at 788 °C.

Keywords Formation enthalpy · $Cu_2ZnSnSe_4$ · KI

Introduction

CZTSe is a quaternary semiconductor compound that can be used as absorber material in solar cells [1]. It is a direct band gap semiconductor material with band gap of 1.04 eV [2] and with a high optical absorption coefficient ($>10^4$ cm^{-1}) [3]. The latest achieved efficiency for $Cu_2ZnSn(Se, S)_4$ solar cells is 12.6 % [4].

There are only few investigations of Cu_2ZnSnS_4 (CZTS) formation in thin-film process [5, 6], where it was shown that the CZTS formation involves intermediate steps with the formations of Cu_2S, SnS_2, and Cu_2SnS_3. However, other groups have not published similar investigations for CZTSe so far. The phase diagram of CZTSe is presented in [7]. In the previous papers [8, 9], we studied the chemical pathway of CZTS and CZTSe formation in molten CdI_2 as a flux material. In this paper, the formation of CZTSe in the presence of KI in evacuated, sealed quartz ampoules is described on the basis of phase analyses of samples after heating them at temperatures of thermal effects determined by the DTA heating curves and as described in the previously published work [10] and in addition, by data from DTA cooling curves. To understand fully the formation process, the enthalpy values of the thermal effects also were determined. As reported in [11], the calculated enthalpy value of CZTSe formation from elemental precursors is -312.2 kJ mol^{-1}. For the first time, the experimental CZTSe formation enthalpy was determined. The difficulties to produce homogeneous single-phase CZTS-type absorber materials have been reported in [12]; however, single-phase monograin materials can be obtained by an isothermal recrystallization process in the presence of a suitable flux material (molten KI). In the phase diagram [7], the existence of CZTSe is found in a narrow area of compositions, and therefore it is very important to start the

---

I. Leinemann (✉) · K. Timmo · M. Grossberg · M. Altosaar · D. Meissner
Department of Materials Science, Tallinn University of Technology, Ehitajate tee 5, 19086 Tallinn, Estonia
e-mail: ingaklav@inbox.lv

T. Kaljuvee · K. Tõnsuaadu
Laboratory of Inorganic Materials, Tallinn University of Technology, Ehitajate tee 5, 19086 Tallinn, Estonia

R. Traksmaa
Centre for Materials Research, Tallinn University of Technology, Ehitajate tee 5, 19086 Tallinn, Estonia

synthesis of CZTSe in molten KI with the appropriate amounts of precursor materials. The processes studied in the present work include the investigations of chemical reactions between precursor materials, taking into account off-stoichiometric amounts for the synthesis of Cu-poor composition ([Cu] = 1.85 and [Zn] + [Sn]) = 2).

Experimental

The initial binary compounds were self-synthesized from high-purity (99.999 %) elements (MERCK) in evacuated quartz ampoules. KI (MERCK, pro analysis) was dried as for NaI, as described in the previous paper [13].

In the present study, we determined experimentally the enthalpies of processes occurring in the following mixtures: CuSe + KI, ZnSe + KI, SnSe + KI, CuSe + SnSe + KI, and CuSe + ZnSe + SnSe + KI. For the last mixture, 0.125 g of binary precursors in the mole ratios of Cu:Zn:Sn:Se = 1.85:1:1:3.85 and 0.125 g KI flux material were taken. Binary-flux mixtures also were prepared according to $Cu_{1.85}ZnSnSe_{3.85}$ composition in mole ratios as described above. The preparation of the studied mixtures was described in detail in [10]. For the DTA enthalpy calibrations, pure KI was selected as standard reference material because its melting temperature is in the same temperature range where the main formation reaction and phase changes occur in the investigated samples. The molar enthalpy of fusion of KI is 24.02 kJ mol^{-1}, and it melts at 681 °C, according to references [14, 15]. In the enthalpy calibrations, the mass of KI was 0.125 g, with the same equal masses of it being used in the investigated sample mixtures. KI was considered to be the preferable substance for the DTA enthalpy calibration, because the major content of all the samples consist mostly of KI flux material. Our tested calibrations with other substances like Pb, Sn, Zn, and Al in quartz ampoules failed due to the very weak DTA signals (in µVs). From these low signal values, low correlation between melting temperatures and large errors of experimental enthalpy values could be expected. For verifying the usability of KI as the reference material, the melting temperatures of the other flux materials (NaI, KI, and CdI_2) in quartz ampoules were determined and found to be close to their melting points available in the literature. Also, their heats of fusion correlated well with the published data [15]. The sample preparation for DTA measurements is illustrated in Fig. 1. The mixture samples were sealed into vacuumized quartz ampoules. As a reference, an empty quartz ampoule of the equal mass was used. A very good contact with thermocouple was realized due to the designed cylindrical base of ampoule, which allows for the heat transition in horizontal and vertical directions from the investigated samples. The applied heating rate was 5 °C min^{-1} and that for cooling 10 °C min^{-1}. The temperatures of the peak-top positions in the DTA curves were determined. In Fig. 2a, the peak in the heating curve at 685 °C belongs to the melting point of pure KI in the closed evacuated ampoule. This is the evidence that an application of a quartz ampoule does not affect the detected temperature of the processes strongly. The peak at 660 °C in the cooling curve is attributable to the solidification process of KI. Since there were no observed remarkable deviations from the melting point of KI in closed system, the enthalpy calibration can be performed using closed evacuated quartz ampoules. The enthalpy evaluation was carried out using comparative method from two heating/cooling runs. The heat calibration was done for the closed system. The error margin (4 %) is given as the largest deviation of the individual process value from the average value. It was assumed that the transformation (reaction) was complete.

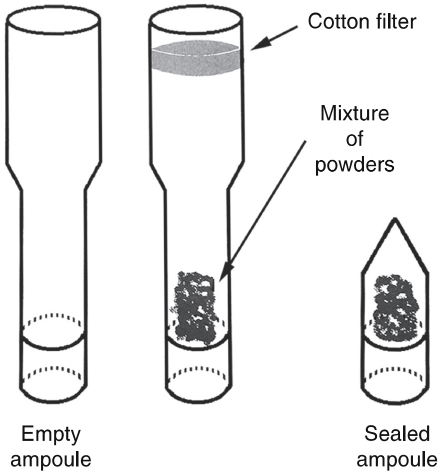

Fig. 1 Sample preparation for DTA

Raman (Horiba LabRAM HR800 spectrometer, France) and XRD (D5005Bruker AXS, Karlsruhe, Germany) analysis methods were used to determine the formed phases and in water-insoluble by-products. Mixture samples of CuSe, ZnSe, SnSe, and KI with the identical proportions of components as used in the samples for the DTA (Thermogravimetric Analyzer Labsys 1600, Setaram Instrumentation, Caluire, France) analyses but of larger amounts (1–2 g) were prepared separately as individual probes for phase analyses. They were heated and quenched at temperatures specified by the detected thermal effects in DTA curves. The number of samples prepared for Raman and XRD measurements corresponds to the number of peaks in the DTA curves. After opening the ampoules and non-washed sample analyses, the

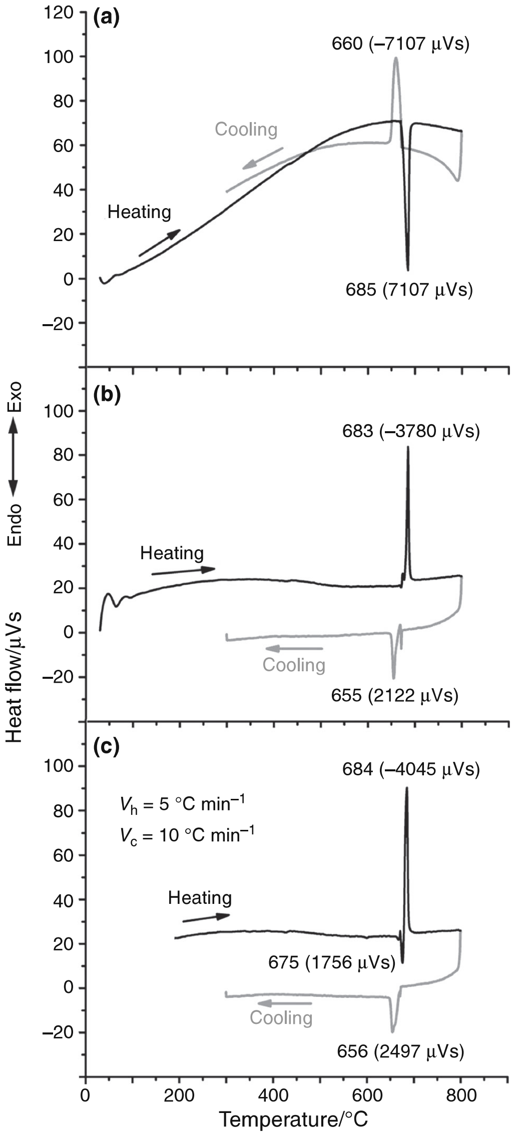

Fig. 2 DTA curves of **a** KI, **b** ZnSe + KI, **c** SnSe + KI mixtures

formed solid phases in the samples were separated from the soluble part of flux material by washing with distilled water several times (7–10) using ultrasonic bath for agitation until water used for washing became transparent. The analyses of the washed samples allow recording clearer Raman and XRD patterns and determining the by-products and the unreacted phases.

Results and discussion

Solubility of precursor compounds in KI

The solubility of precursor compounds in KI is low (see Table 1). Those determined values are used for enthalpy calculations in mixtures below. We determined the solubility of binary precursors in molten KI by the mass loss method. For the determination of mass loss, a large-sized single crystal of binary compounds was kept in molten KI at 740 °C for 1 week.

The mass loss of ZnSe was 1.67×10^{-3} g (1.16×10^{-5} mol) in 2.56 g ($1{,}542.19 \times 10^{-5}$ mol) KI. The resultant solubility of ZnSe in KI at 740 °C is therefore 0.08 mol%. It means that in DTA sample of 0.125 g (75.30×10^{-5} mol) KI, 8.15×10^{-5} g (5.63×10^{-7} mol) of ZnSe can dissolve.

The mass loss of SnSe was higher at 9.00×10^{-3} g (4.55×10^{-5} mol) in 3.25 g ($1{,}957.86 \times 10^{-5}$), and the determined solubility was 0.23 mol%. The calculated dissolved amount of SnSe in DTA sample is 34.62×10^{-5} g (17.51×10^{-7} mol).

The most soluble in KI is CuSe with 3.19 mol%. The weighed mass loss of the used CuSe single crystal was 86.67×10^{-3} g (60.82×10^{-5} mol) in 3.17 g KI ($1{,}909.66 \times 10^{-5}$ mol). Therefore, in 0.125 g (75.30×10^{-5} mol) KI, the dissolved part of CuSe is 341.76×10^{-5} g (239.82×10^{-7} mol).

Processes in KI–precursor compound mixtures

The mixture of ZnSe and KI (ZnSe + KI)

The DTA heating and cooling curves of the mixture are presented in Fig. 2b. In the heating cycle, no endothermic signal of the melting process of KI is seen. The determined value of

Table 1 Solubility of precursor compounds in KI

Compound	Mass loss/g	Mass of KI/g	Mol loss/mol	Mols of KI/mol	Solubility/mol%
ZnSe	1.67×10^{-3}	2.56	1.16×10^{-5}	$1{,}542.19 \times 10^{-5}$	0.08
SnSe	9.00×10^{-3}	3.25	4.55×10^{-5}	$1{,}957.86 \times 10^{-5}$	0.23
CuSe	86.67×10^{-3}	3.17	60.82×10^{-5}	$1{,}909.66 \times 10^{-5}$	3.19

the only exothermic signal at 683 °C is −780 μVs. If we consider that it compensates completely the endothermic signal heat of fusion of 0.125 g of KI (7,107 μVs), then the real value of the exothermic process is −3,780 μVs + (−7,107 μVs) = −10,887 μVs. There could be two possibilities to attribute this signal.

First, it is well known that usually fused salts are highly dissociated into their ionic species [16]. It is also known that the I^- ion has a strong complex forming ability with Zn to form a ${ZnI_4}^{2-}$ complex [17]. On the bases of the above given considerations, we propose that the summary exothermic signal −10,887 μVs could be attributed to the sum of the two following processes: the dissolution of ZnSe in liquid KI and the formation of K_2ZnI_4.

$$\mathrm{ZnSe\ (s) + 4KI\ (liq.) \leftrightarrow K_2ZnI_4 + K_2Se} \quad (1)$$

A similar process for ZnS dissolution and following formation of ZnS nanosheets from NaI melt by Dongsong Li in paper [18] was proposed. However, the formation of K_2ZnI_4 and K_2Se was not confirmed by the XRD patterns of samples quenched at 680 and 710 °C. It could be explained by the ${ZnI_4}^{-2}$ complex formation and existence only in the liquid phase of KI and its decomposition as a reversible process by cooling. The endothermic 4 peak at 655 °C with determined effect of 2,122 μVs in the cooling cycle completely compensates the heat of KI solidification (7,107 μVs) and it corresponds to 9,229 μVs of the reversible process of the complex formation (1). The reaction enthalpy value was calculated as 157 ± 6 kJ mol^{-1} for ZnSe + KI mixture, since the area under the DTA curve is directly proportional to the heat transferred in the reaction. The difference of the enthalpy values of the direct and reversible processes (−1,658 μVs) is probably caused by dissolved ZnSe in molten KI, which stays as a fine dispersed solid in frozen KI. The consumed energy to break the bonds of solute (ZnSe) and solvent (KI) is endothermic and it takes place during the melting. The formation of new bonds during the solvation is an exothermic process and it takes place right after the melting. The dissolution is exothermic if the released energy from bond formation is larger than the energy needed to break the bonds of solute and solvent [19]. So, the heat difference between endothermic peak in cooling and exothermic peak in heating cycle −1,658 μVs can be attributed to the enthalpy of solvation of ZnSe in KI (enthalpy of solution). Since the solvation is the process in which the solute and solvent take part therefore the effect per mixture of dissolved ZnSe and 0.125 g (75.30×10^{-5} mol) KI was calculated. In this case the enthalpy of dissolution of ZnSe in KI is −6 kJ mol^{-1}.

The other possibility is that if the reaction (1) does not take place, then exothermic peak with the value of −10,887 μVs (−37 ± 2 kJ mol^{-1}) could be attributed to the enthalpy of solution.

The mixture of SnSe and KI (SnSe + KI)

In this mixture, KSn_2I_5 and elemental Se were found to form as confirmed by XRD pattern of the sample, heated at 420 °C for 13 h and quenched. The formation reaction of KSn_2I_5 can be expected to take place between solid SnSe and gaseous I_2 used as an oxidant. We believe that the formation of KSn_2I_5 is a complex of chemical processes that need the presence of free iodine. The release of iodine from KI can be possible.

First, KI can contain adsorbed iodine as KI is produced industrially by treating KOH with iodine [20]. Iodine can be adsorbed on the surface of KI crystals [21].

Second, the reactions leading to the iodine release, necessary for KSn_2I_5 formation, could proceed also due to the instability of KI in the presence of some residual moisture and air if KI during the sample preparation had not been properly dried and degassed [22, 23]. From the literature survey, it can be found that KI is rather stable in dry air. However, the exposure to light and moisture can accelerate the decomposition of potassium iodide. The instability of KI in air is caused by the slow oxidation reaction of the salt in the presence of CO_2 between potassium carbonate and elemental iodine [14, 15, 20, 21, 24–26]:

$$\mathrm{4\,KI + 2\,CO_2(g) + O_2(g) \rightarrow 2\,K_2CO_3 + 2\,I_2(g)} \quad (2)$$

The probability for proceeding on the reaction (2) in degassed sealed vacuum ampoules should be rather low. The thermodynamical Gibbs energy calculations show negative ΔG values ($\Delta G < 0$) only in the temperature region from 0 °C (−12 kJ) to 56 °C reaching a value almost equal to 0 kJ, and the reaction can therefore take place during the storing of KI or during the sample preparation process.

Third, negative ΔG change ($\Delta G < -225$ kJ) slightly reduces close to 0 kJ at 652 °C:

$$\mathrm{2KI\ (g) + Se\ (g) \rightarrow K_2Se + I_2(g)} \quad (3)$$

The reaction (3) is very probable, and it can occur if the precursor SnSe contains some over-stoichiometric Se and if we consider that the saturated vapor pressure of Se is about 5 mm Hg at 400 °C [30], and the vapor pressure of KI is 0.31 mm Hg at 25 °C (1 mm Hg at 745 °C), while the vapor pressure of SnSe is about 3×10^{-6} mm Hg at 400 °C [14, 15, 30].

The released I_2 in turn reacts with SnSe (4–5) [15, 25, 26, 31]:

$$\begin{aligned}&SnSe + I_2(g) \rightarrow SnI_2 + Se\\&\left(\Delta G < 0 \text{ at } 0\,^\circ C \; -80 \text{ kJ mol}^{-1}\right.\\&\left.\text{and at } 900\,^\circ C \text{ almost } 0 \text{ kJ mol}^{-1}\right)\end{aligned} \tag{4}$$

$$\begin{aligned}&SnSe + 2I_2(g) \rightarrow SnI_4 + Se\\&\left(\Delta G < 0 \text{ at } 0\,^\circ C \; -166 \text{ kJ mol}^{-1}\right.\\&\left.\text{and at } 830\,^\circ C \text{ almost } 0 \text{ kJ mol}^{-1}\right)\end{aligned} \tag{5}$$

The intermediate steps of KSn_2I_5 formation should be investigated in more detail, since K_2Se, SnI_4, and SnI_2 as products are not found in the XRD patterns. It can be considered that the reaction with the released iodine occurs as follows:

$$\begin{aligned}&2SnSe + KI + 2I_2 \rightarrow KSn_2I_5\\&+ 2Se \text{ (Cannot calculate from database)}\end{aligned} \tag{6}$$

However, in the literature, there are no information and thermodynamic data available about the formation of KSn_2I_5 or any mechanism for the release of I_2 from dry and pure KI.

The mixture of SnSe + KI (Fig. 2c) melts at 675 °C, giving an endothermic signal of 1,756 μVs of KI melting, which is partly covered by that of −5,351 μVs due to next exothermic effect. It is seen that the next exothermic peak with the thermal effect value of −4,045 μVs compensates the melting heat of KI and the sum total is −4,045 − 5,351 = −9,397 μVs. The melting temperature of KI can be reduced because of any added impurities (the effect of depression of melting temperature). The added SnSe increases the entropy of the system, but does not change the enthalpy. Since $\Delta G = 0$ in the melting process, the temperature can be expressed as Eq. (7):

$$T = \Delta H\,(\Delta S)^{-1} \tag{7}$$

It is more reasonable to presume that the following exothermic process at 684 °C with the thermal effect of −9,397 μVs can be attributed to the difference between solvation energies required to break the bonds and to form a complex which exists in the liquid phase as was described above for ZnSe + KI mixture. We experimentally determined (similar to ZnSe, see above) that 0.009 g SnSe

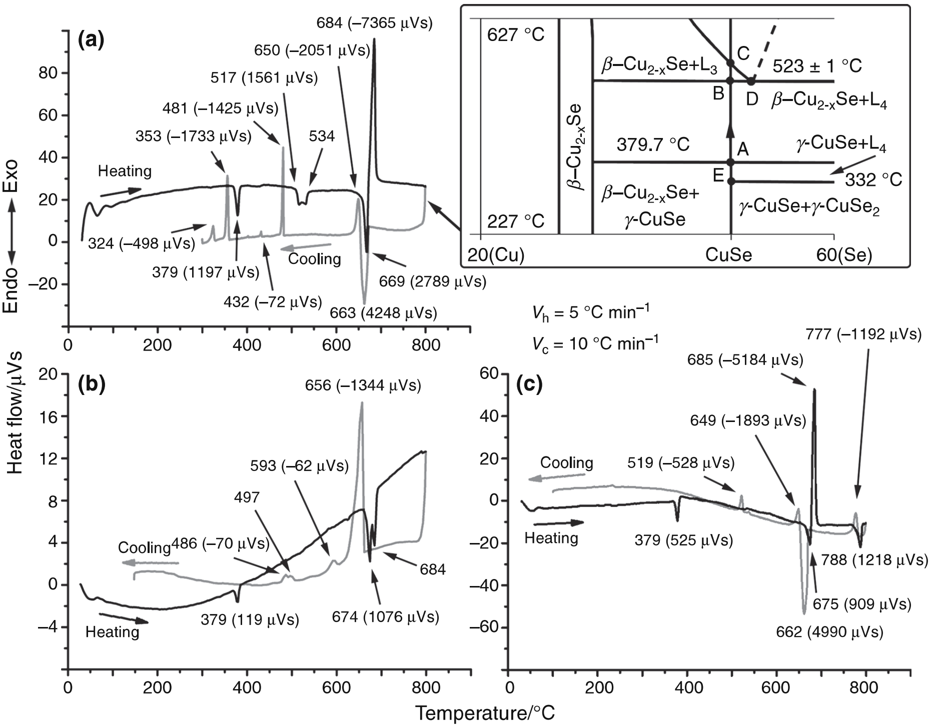

Fig. 3 DTA curves of **a** CuSe + KI with a part of phase diagram of Cu-Se system on the right side, **b** CuSe + SnSe + KI, and **c** the mixture for synthesis of quaternary CZTSe

dissolves in 3.35 g KI. If we take into account the solubility of SnSe in KI (in 0.125 g) and heat effect from the current DTA experiment, then the calculated value of dissolution enthalpy is 31 ± 1 kJ mol^{-1}. By cooling, a reversible process (endothermic 2,497 μVs are covered with KI solidification of 7,107 μVs which totals 9,604 μVs, with close values of experimental errors) is detected at 656 °C.

The mixture of CuSe and KI (CuSe + KI)

The DTA curves of this mixture (Fig. 3a) are more complicated due to the multiple phase changes in the binary Cu–Se system [10]. The endothermic peak at 379 °C of 1,197 μVs corresponds to the phase transformation of CuSe to $Cu_{2-x}Se$ (point A in Fig. 3a right-side phase diagram of Cu–Se system) [32]. The determined enthalpy value expressed as 8 kJ mol^{-1} for CuSe corresponds to the enthalpy values of transformation of CuSe to $Cu_{1.8}Se$ and Cu_3Se_2 that were detected by XRD in the sample quenched at 420 °C. The heat of the peritectic CuSe decomposition at 379 °C determined in [33] is 11.80 ± 0.03 kJ mol^{-1}, which agrees within our experimental value.

According to the XRD pattern, in the sample quenched at 540 °C, there is no newly formed compound, and therefore, the effect in the heating curves with enthalpy value of 1,561 μVs expressed as 11 kJ mol^{-1} for CuSe amount in sample at 517–534 °C can be correlated to the temperature-dependent change in composition of the liquid phase that corresponds to the lifting on the liquidus line from 52.5 at.% Se (monotectic composition at 523 °C) to 50 % Se (in CuSe), which is in correspondence with the Cu-Se phase diagram given in [32] (see points B and C in Fig. 3a right side, where liquidus line L_3 is at higher temperatures than the monotectic temperature).

At 669 °C, the endothermic effect of melting of KI (2,789 μVs) is partly covered by the following exothermic effect of −4,318 μVs. CuSe + KI mixture starts to melt at lower temperature than pure KI since the entropy of system CuSe + KI is larger than that in pure KI, according to formula (1). From the XRD pattern of the sample quenched at 680 °C, it is found that K_2Se_3 forms during the melting process. Its formation could be described by means of K_2Se formation reactions (3 and 8) or directly (9).

$$K_2Se + 2Se \rightarrow K_2Se_3 \tag{8}$$

We assume that the increasing vapor pressure of KI above that of molten KI is more likely to cause the reaction (8).

$$2KI\,(g) + 3Se\,(g) \rightarrow K_2Se_3 + I_2(g) \tag{9}$$

The melting is accompanied by strong exothermic effect of $-7365 - 4318 = -11{,}683$ μVs at 684 °C. It could be attributed to the difference between the solvation energies required to break the bonds and to form some complex which exists in the liquid phase. We determined experimentally the solubility of CuSe in KI (see Table 1). By cooling, the solidification of KI of −2,051 μVs at 650 °C is covered by the endothermic effect of 5,056 μVs, and a reversible process (endothermic) with the total effect of $4{,}248 + 5{,}056 = 9{,}304$ μVs (30 ± 1 kJ mol^{-1}) is detected by cooling at 663 °C. There is no complex formation in this system, and this value (30 ± 1 kJ mol^{-1}) is attributed to the reversible process and the enthalpy of solution, which is calculated per dissolved CuSe and KI amount. The enthalpy values are in all precursor + KI mixtures close to each other, since the solubility values are not large. In addition, CuI phase is found by XRD analysis in the quenched sample at 710 °C sample. The part of CuSe reacting to form CuI can be calculated as a difference between the total mass of CuSe and the mass of CuSe in dissolution process. According to Table 1, 34.176×10^{-3} g CuSe dissolves in 0.125 g KI. If the sample consists of 54.400×10^{-3} g CuSe and 0.125 g KI, then the mass of CuSe taking part in reaction is 54.400×10^{-3}–34.176×10^{-3} g $= 20.224 \times 10^{-3}$ g (1.419×10^{-4} mol), and it can react with 0.710×10^{-4} mol I_2 (10). From the reaction (11–12) [13, 23, 24, 27, 30, 33], the mass of Cu_2Se can be calculated as 14.620×10^{-3} g (0.710×10^{-4} mol) and from the reaction (11), the number of moles of the reacting I_2 is found to be 0.710×10^{-4} mol. The initial number of moles of reactants which are found in the area under the DTA signal 1.420×10^{-4} mol can be calculated.

$$\begin{aligned} &2CuSe + I_2(g) \rightarrow 2CuI + 2Se \\ &\big(\Delta G < 0 \text{ at } 0\,^{\circ}\mathrm{C} \ -85 \text{ kJ mol}^{-1} \\ &\quad \text{and } 800\,^{\circ}\mathrm{C} \ -17 \text{ kJ mol}^{-1}\big) \end{aligned} \tag{10}$$

$$2CuSe \rightarrow Cu_2Se + Se \tag{11}$$

$$\begin{aligned} &Cu_2Se + I_2(g) \rightarrow 2CuI + Se \\ &\big(\Delta G < 0 \text{ at } 0\,^{\circ}\mathrm{C} \ -85 \text{ kJ mol}^{-1} \\ &\quad \text{and at } 774\,^{\circ}\mathrm{C} \text{ almost } 0 \text{ kJ mol}^{-1}\big) \end{aligned} \tag{12}$$

The difference between endothermic effect in cooling and exothermic effect in heating cycles, equal to −2,379 μVs, corresponds to the formation of CuI according to the reaction (10) with enthalpy of -28 ± 1 kJ mol^{-1}. It also confirms that the CuI formation occurs as in reaction (10), $\Delta H = -51$ kJ mol^{-1} at 684 °C, but not in reaction (13), $\Delta H = -82$ kJ mol^{-1} at 684 °C. The appearance of CuI in the XRD pattern after the formation of K_2Se_3 phase (8–9) leads to the conclusion that the formation of CuI is induced by the released I_2 due to the reactions (2–3). It should be mentioned that the process is reversible, since there is a strongly negative ΔG value for reaction (13) [14, 15, 24, 27–29, 34]:

$$K_2Se + 2CuI \rightarrow 2KI + Cu_2Se$$
$$\left(\Delta G < 0 \text{ at } 0\,^{\circ}C \ -203 \text{ kJ mol}^{-1} \text{ and at } 800\,^{\circ}C \ -272 \text{ kJ mol}^{-1}\right) \qquad (13)$$

The analogous reversible reaction (14) for K_2Se_3 could be written as follows:

$$K_2Se_3 + CuI \rightarrow KI + Cu_2Se + Se \qquad (14)$$

On cooling, the equilibrium between $Cu_{2-x}Se$ and Se-rich liquid is reached at monotectic point [32] at 481 °C of −1,425 μVs (see Fig. 3a right side point D). The temperature is shifted due to the cooling process. The weak peak observed at 432 °C of −72 μVs in the DTA cooling curve could correspond to the phase transition of α-CuI to β-CuI [35]. The amount of the formed CuI, described above, can be calculated as 1 kJ mol^{-1}. At 353 °C of −1,733 μVs, $CuSe_2$ crystallizes from CuSe + Se solution [32]. The existence of $CuSe_2$ is found in XRD at 680 °C, temperature at which CuSe + KI mixture melts. This low-temperature phase present at this temperature could be explained by crystallization from liquid at fast cooling (quenching). At 324 °C, exothermic effect of −498 μVs corresponds to the peritectic transformation of liquid Se + solid CuSe to $CuSe_2$ [32] (see Fig. 3a right-side point E).

The mixture of CuSe, SnSe, and KI (CuSe + SnSe + KI)

In the DTA heating curve of this mixture (Fig. 3b) is seen a weak endothermic effect of 119 μVs at 379 °C (similar to the CuSe + KI mixture) which corresponds to the transformation of CuSe to Cu_2Se with the release of Se. The endothermic effect is not as large as could be expected for the decomposition of CuSe to $Cu_{2-x}Se$ (11), since some exothermic reactions take place at the same time. $SnSe_2$ was found in the XRD of the sample quenched at 400 °C, which forms by reaction (15) for which the thermodynamic calculations show $\Delta G = -25$ kJ mol^{-1} at 0 °C reaching almost 0 kJ mol^{-1} at 700 °C [26, 31]. The intensive peaks in Raman spectra at 226 and 246 cm^{-1} could be attributed to copper tin selenide with defect structure $Cu_{3.34}SnSe_5$, as found in XRD. After the formation of $SnSe_2$, the formation of Cu_2SnSe_3 (16) follows. CuI had been formed similarly, as in the system CuSe + KI.

$$SnSe + Se\,(l) \leftrightarrow SnSe_2 \qquad (15)$$

$$Cu_2Se + SnSe_2 \rightarrow Cu_2SnSe_3 \qquad (16)$$

The mixture CuSe + SnSe + KI melts incongruently at 674–684 °C. The thermal effect of the KI melting process (1,076 μVs) is covered by the exothermic effect of Cu_2SnSe_3 formation of 7,107–1,076 = 6,031 μVs at 684 °C. The enthalpy of reaction (16) at 684 °C is calculated to be 26 ± 1 kJ mol^{-1}. It leads to the conclusion that the intense Cu_2SnSe_3 formation takes plase during the melting process of KI.

In the cooling cycle, the KI solidification at 656 °C is covered with endothermic thermal effect of 7,101−(−1344) = 5,763 μVs, and it corresponds to the re-formation process of Cu_2SnSe_3 from the melt with enthalpy (25 ± 1 kJ mol^{-1}).

At 593 °C (−62 μVs), there is solidification of α-CuI. On cooling down, the equilibrium between $Cu_{2-x}Se$ and Se-rich liquid [32] is reached at 497 and 486 °C (−70 μVs) (see Fig. 3a right-side points B un C). Cooling causes the shift in temperature.

The mixture of CuSe, ZnSe, SnSe, and KI (CuSe + ZnSe + SnSe + KI)

The heating curve in Fig. 3c shows a summary endothermic effect −525 μVs at 379 °C, corresponding to the transformation of CuSe to Cu_2Se and Se (9), analogously as was described above in the binary and ternary mixtures. The enthalpy values of the processes differ due to fact that

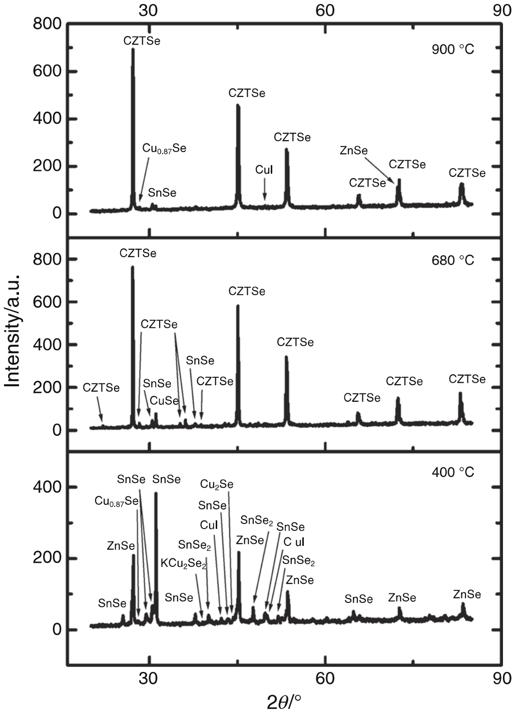

Fig. 4 XRD patterns of CuSe + ZnSe + SnSe + KI mixtures quenched at different annealing temperatures (after removing KI and soluble phases by washing with water)

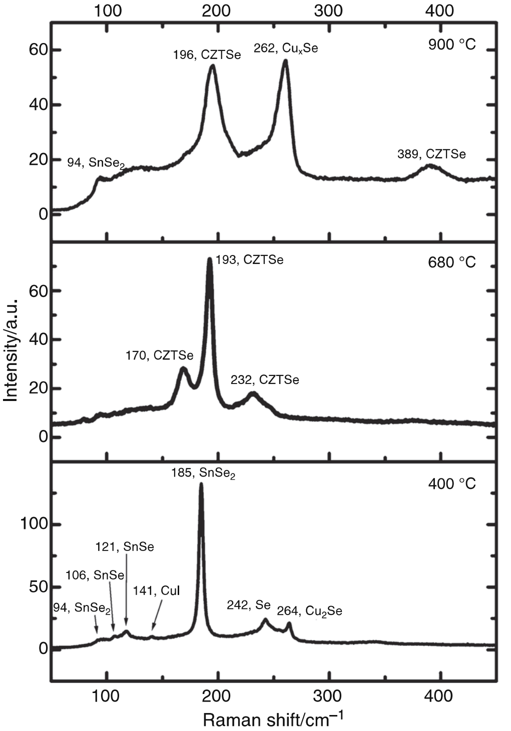

Fig. 5 Raman spectra of CuSe + ZnSe + SnSe + KI mixtures quenched at different annealing temperatures (after removing KI and soluble phases by washing with water)

multiple processes are proceeding at the same time. On the basis of Raman analyses of the sample heated at 400 °C, the formations of Cu_2SnSe_3 and CZTSe were found, although not detected by XRD. The differences in the enthalpy values of the processes of ternary and quaternary systems are probably due to the CZTSe formation process that starts (as described above in the ternary system) with the reactions (15–16), leading to the Cu_2SnSe_3 formation and continues in the reaction between ZnSe and Cu_2SnSe_3 to form CZTSe (17):

$$Cu_2SnSe_3 + ZnSe \rightarrow Cu_2ZnSnSe_4 \tag{17}$$

The endothermic effect of melting of KI (normally as 7,107 µVs) is seen as thermal effect of 909 µVs at 675 °C. The KI melting is partly compensated by the next exothermic effect. The compensated part can be calculated as $-7{,}107 + 909 = -6198$ µVs. The total value of exothermic effect is $-5184 - 6198 = -11{,}382$ µVs due to the intense CZTSe formation process in the molten KI at 685 °C. From this heat value, we get for the first time experimentally determined enthalpy of reaction (16) as -36 ± 2 kJ mol^{-1}, calculated per reagent. It is expected that this value corresponds to the CZTSe formation from Cu_2Se, $SnSe_2$, and ZnSe. When KI melts, it brings the precursor particles together, and by melting, the reaction is induced. However, in the literature, there are no similar experimental data, and this value could be compared with that obtained by extrapolation of theoretical value reported in [36] as -84.1 kJ mol^{-1} at 0 K from Cu_2Se, $SnSe_2$, and ZnSe. The changes in enthalpy values for reaction by increasing the temperature from 0 K to 958 K (685 °C) can be calculated by integral of the differences in heat capacities, using the data from [14, 31, 37] at few atmospheres and at 0 K and 298 K. Close value as determined experimentally could be calculated. Also, the authors in [37] stated that the calculations should be taken as predictions. By the eventual heating, the melting of CZTSe at 788 °C is realized, and for the first time, the experimentally determined heat of fusion 4 kJ mol^{-1} is found. The latter is close to the value determined for CZTSe in NaI, determined by our group, which will be published elsewhere. In cooling cycle, the solidification of CZTSe at 777 °C ($-1{,}192$ µVs) with enthalpy of -4 kJ mol^{-1} and an endothermic effect of a process corresponding to the reverse process of the CZTSe re-formation at 662 °C of 4,990 µVs) which occurs following KI solidification at 649 °C $7{,}107 - 4{,}990 = 2{,}117$ µVs are seen. The total endothermic effect of $4{,}990 + 5{,}913 = 10{,}903$ µVs can be expressed as 35 ± 1 kJ mol^{-1} for the reaction of CZTSe re-formation. The lower thermal effect of the reverse process in cooling could be explained as due to the difference between melting and solidification processes. The melting of CZTSe is incongruent and CZTSe forms the liquid phase with composition close to Cu_2SnSe_3 and solid ZnSe [7]. In cooling cycle, the reverse process is not complete, and a part of Cu_2SnSe_3 remains as separate phase. It is confirmed by the appearance of Cu_2SnSe_3 phase in the XRD pattern of the sample heated to 800 °C and cooled to the quenching temperature of 520 °C. On cooling, the equilibrium between $Cu_{2-x}Se$ and Se-rich liquid is reached [32] at 519 °C (-528 µVs) as described above in the ternary and binary systems.

After all these analyses, the samples for quaternary compound CZTSe syntheses were washed with the aim to remove KI and to obtain better resolution in Raman spectra and XRD patterns. In the washed samples of the mixture CuSe + ZnSe + SnSe + KI heated up to 400 °C, Raman and XRD analyses show only the existence of the initial precursor compounds (Figs. 4, 5). Also some $SnSe_2$, CuI, and KCu_2Se_2 materials were found. KCu_2Se_2 compound confirms the statement of precursor dissolution in KI. However, ternary compound Cu_2SnSe_3 formation was not found in Raman and XRD analyses for washed samples, and it is believed to be more due to the fact that most of the reaction proceeds directly from binary compounds to form CZTSe as flux material melting around 680 °C where single phase of CZTSe by Raman is detected. The appearance of CZTSe in the XRD patterns indicates that, in closed vacuum ampoules in the presence of large amounts of solid KI, the CZTSe formation process is inhibited and it proceeds intensively after the formation of liquid phase of KI. At high temperatures after CZTSe melting (900 °C), ZnSe is present in the XRD pattern, and during the melting, the quaternary compound decomposes.

Conclusions

In the investigation of the formation process of CZTSe in the presence of KI by gradually including the precursor compounds to KI + precursors mixtures, we found that melting of KI is always accompanied by some dissolution of the partner compounds and lowering of the melting temperature in comparison with pure KI. The reaction of CZTSe formation in liquid phase of KI does not involve the intermediate step of Cu_2SnSe_3 formation and takes place with the experimentally determined enthalpy of -36 ± 2 kJ mol^{-1}. The heat of fusion of CZTSe is determined for the first time, and it is 4 kJ mol^{-1} at 788 °C. The initiator of the process of the partial CZTSe formation at around 400 °C is elemental Se released from the phase-transformation process of CuSe to Cu_2Se. The subsequent $SnSe_2$ formation from Se and SnSe allows forming partly Cu_2SnSe_3 by solid-state reaction and also forming some CZTSe. It was found that, as confirmed by the appearance of CZTSe in the XRD patterns only at temperatures close to KI melting point, in closed vacuumized ampoules and in the presence of large amounts of solid KI, the CZTSe formation process is inhibited and it proceeds intensively after the formation of liquid phase of KI.

Acknowledgements The Doctoral Studies and Internationalization Program DoRa of the European Social Funds, Estonian Science Foundation grants (G8964 and G9425), the projects of Estonian Ministry of Education and Research (IUT 19-28 and TK117T), EAS (EU29713), and National R&D programs (AR10128 and AR12128) supported this research.

References

1. Barkhouse DAR, Gunawan O, Gokmen T, Todorov TK, Mitzi DB. Device characteristics of a 10.1 % hydrazine processed $Cu_2ZnSn(Se, S)_4$ solar cell. Prog Photovoltaics Res Appl. 2012;20:6–11.
2. Grossberg M, Krustok J, Timmo K, Altosaar M. Photoluminescence and Raman study of $Cu_2ZnSn(Se_x S_{1-x})_4$ monograins for photovoltaic applications. Thin Solid Films. 2009;517:2489–92.
3. Chopra KL, Paulson PD, Dutta V. Thin-film solar cells: an overview. Prog Photovoltaics Res Appl. 2004;12:69–92.
4. Wang W, Winkler MT, Gunawan O, Gokmen T, Todorov TK, Zhu Y, Mitzi DB. Device characteristics of CZTSSe thin-film solar cells with 12.6 % efficiency. Adv Energy Mater. 2013;. doi:10.1002/aenm.201301465.
5. Scragg JJ, Ericson T, Kubart T, Edoff M, Platzer-Björkman C. Chemical insights into the instability of Cu_2ZnSnS_4 films during annealing. Chem Mater. 2011;. doi:10.1021/cm202379s.
6. Weber A, Mainz R, Unold T, Schorr S, Schock HW. In-situ XRD on formation reactions of Cu_2ZnSnS_4 thin films. Phys Status Solidi C. 2009;. doi:10.1002/pssc.200881231.
7. Dudchak IV, Piskach LV. Phase equilibria in the Cu_2S–ZnS–SnS_2 system. J Alloy Compd. 2003;351:145–50.
8. Nkwusi G, Leinemann I, Grossberg M, Kaljuvee T, Traksmaa R, Altosaar M, Meissner D. CYSENI 2012. In: 9th international conference of young scientists on energy issues, Kaunas; 24–25 May 2012. p. II 38–II 46.
9. Klavina I, Raudoja J, Altosaar M, Mellikov E, Meissner D, Kaljuvee T. CYSENI 2010. Proceeding of annual conference of young scientists on energy issues. [CD]. Kaunas: Lithuanian Energy Institute; 27–28 May 2010.
10. Klavina I, Kaljuvee T, Timmo K, Raudoja J, Traksmaa R, Altosaar M, Meissner D. Study of $Cu_2ZnSnSe_4$ monograin formation in molten KI starting from binary chalcogenides. Thin Solid Films. 2011;519:7399–402.
11. Maeda T, Nakamura S, Wada T. First principles calculations of defect formation in In-free photovoltaic semiconductors Cu_2ZnSnS_4 and $Cu_2ZnSnSe_4$. Jpn J Appl Phys. 2011;. doi:10.1143/JJAP.50.04DP07.
12. Mellikov E, Hiie J, Altosaar M. Powder *materials* and *technologies* for solar cells. Int J Mater Prod Technol. 2007;28:291–311.
13. Leinemann I, Zhang W, Kaljuvee T, Tõnsuaadu K, Traksmaa R, Raudoja J, Grossberg M, Altosaar M, Meissner D. $Cu_2ZnSnSe_4$ - formation and reaction enthalpies in molten NaI starting from binary chalcogenides. J Therm Anal Calorim. 2014;118:1313–21.
14. Knacke O, Kubaschewski O, Hesselman K. Thermochemical properties of inorganic substances. 2nd ed. Berlin: Springer-Verlag; 1991.
15. Mullin JW. Crystallization. 3rd ed. Oxford: Butterworth-Heinemann, a division of Reed Educational and Professional Publishing Ltd; 1993.
16. Blomgren GE, Van Artsdalen ER. Annu Rev Phys Chem. 1960;11:273–306.
17. Wakita H, Johansson G, Sandström M, Goggin PL, Ohtaki H. Structure determination of zinc iodide complexes formed in aqueous solution. J Solut Chem. 1991;20:643–68.
18. Li D. Fast and mass synthesis of ZnS nanosheet via ultra-strong surface interaction. Cryst Eng Commun. 2013;. doi:10.1039/C3CE41529E.
19. Linde DR. Handbook of chemistry and physics. 90th ed. New York: CRC; 2010.
20. Lyday PA. Iodine and iodine compounds. Ullmann's encyclopedia of industrial chemistry. Weinheim: Wiley; 2005.
21. Whipp B. The adsorption of iodine by potassium. Proc R Soc Lond A. 1933;141:217–32.
22. Kelly FC. Study of the stability of the iodine compounds in iodized salts. Bull World Health Org. 1953;9:217–30.
23. Sofronov DS, Kudin KA, Voloshko AY, Kudin AM, Shishkin OV. Origin of the thermal desorption peeks of gases in NaI above 180 °C. Inorg Mater. 2009;45:1314–8.
24. Glushko PV. Thermocenter of the Russian Academy of Sciences. Moscow: IVTAN Association; 1994.
25. Landolt-Börnstein. Thermodynamic properties of inorganic material. scientific group thermodata europe (SGTE). Berlin: Springer-Verlag; 1999.
26. Gurvich LV, Veitz IV. Thermodynamic properties of individual substances. 4th ed. Hemisphere: Pub Co. NY, L.; 1989.

27. Mills KC. Thermodynamic data for inorganic sulfides, selenides and tellurides. London: Butterworths; 1974.
28. Binnewies M, Milke E. Thermochemical data of elements and compounds. 2nd ed. Weinheim: Wiley; 2002.
29. Yungman VS, Glushko VP, Medvedev VA, Gurvich LV. Thermal constants of substances. New York: Alden Books; 1999.
30. Gerasimov YI, Krestovnikov AN, Gorbov SI. Chimicheskaya thermodynamica v cvetnoi metallurgii. Thermodynamica selena i selenidov, tellura i telluridov. 4th ed. Moskov: Metallurgija; 1974.
31. Barin I. Thermochemical Data of Pure Substances. Weinheim: VCH Verlags Gesellschaft; 1989.
32. Glazov VM, Pashinkin S, Fedorov VA. Phase equilibria in the Cu–Se system. Inorg Mater. 2000;36:641–52.
33. Stolen S, Fjellag H, Gronvold E. Heat capacity, structural and thermodynamic properties of synthetic klockmannite CuSe at temperatures from 5 K to 652.7 K. Enthalpy of decomposition. J Chem Thermodyn. 1996;28:753–66.
34. Barin I. Thermochemical data of pure substances, Part I. Weinheim: mVCH Verlags Gesellschaft; 1993.
35. Wells AF. Structural inorganic chemistry. 5th ed. Oxford: Oxford University Press; 1984.
36. Nakamura S, Maeda T, Tabata T, Wada T. First-principles study of indium-free photovoltaic compounds $Ag_2ZnSnSe_4$ and Cu_2-$ZnSnSe_4$. In: Proceeding of the 37th IEEE photovoltaic specialist conference. Seattle: Washington State Convention Center; 2011. pp.785–786.
37. Xiancong H, Honglie S. First-principles calculation of some mechanical and thermo-physical properties of kesterite-type Cu_2-$ZnSnSe_4$. Phys Scr. 2012;. doi:10.1088/0031-8949/85/03/0353002.

Paper II

Klavina, I., Kaljuvee, T., Timmo, K., Raudoja, J., Traksmaa, R., Altosaar, M., Meissner, D. (2011). Study of $Cu_2ZnSnSe_4$ monograin formation in molten KI starting from binary chalcogenides. *Thin Solid Films, 519*(21), 7399-7402. doi: 10.1016/j.tsf.2011.01.365

Thin Solid Films 519 (2011) 7399–7402

Contents lists available at ScienceDirect

Thin Solid Films

journal homepage: www.elsevier.com/locate/tsf

Study of $Cu_2ZnSnSe_4$ monograin formation in molten KI starting from binary chalcogenides

Inga Klavina [a,*], Tiit Kaljuvee [b], Kristi Timmo [a], Jaan Raudoja [a], Rainer Traksmaa [c], Mare Altosaar [a], Dieter Meissner [a,d]

[a] Department of Materials Science, Tallinn University of Technology, Ehitajate tee 5, 19086 Tallinn, Estonia
[b] Laboratory of Inorganic Materials, Tallinn University of Technology, Ehitajate tee 5, 19086 Tallinn, Estonia
[c] Centre for Materials Research, Tallinn University of Technology, Ehitajate tee 5, 19086 Tallinn, Estonia
[d] Crytalsol OÜ, Akademia tee 15a, 12618 Tallinn, Estonia

ARTICLE INFO

Available online 3 February 2011

Keywords:
$Cu_2ZnSnSe_4$
Monograin materials
Solar cells
Solution growth

ABSTRACT

The present study deals with the possible chemical interactions of CuSe, SnSe, and ZnSe in molten KI as a flux material in vacuum ampoules. The aim is to find suitable preparation conditions for the synthesis of $Cu_2ZnSnSe_4$ monograin powders as an absorber material for solar cells. Impurities in the precursor materials and in the product powders were determined by inductively coupled plasma mass spectrometry. Differential thermal analysis was used to determine thermal effects. Phase composition in the mixtures of binary precursors and KI was determined by X-ray diffraction and Raman spectroscopy. It was found that no new compound was formed in the CuSe/KI, ZnSe/KI and SnSe/KI mixtures. The solubility of the binary chalcogenides in KI at 740 °C was determined.

© 2011 Elsevier B.V. All rights reserved.

1. Introduction

The perfect solar cell absorber should be made of a direct band gap semiconductor material with a band gap of 1–1.5 eV and a high optical absorption coefficient ($>10^4\ cm^{-1}$); provide a high quantum efficiency for excited charge carrier production, a long diffusion length (i.e. a low recombination velocity); and should be able to form a good rectifying junction [1]. For example, alloys and compounds of I–III–VI ternaries (on the base of $CuInSe_2$) and related quaternaries like $Cu_2ZnSnSe_4$ in which the resource limited and high-cost In is replaced by Zn and Sn, can form a very good photovoltaic material [2]. However, it must be emphasized that with the increasing number of components, the phase diagrams of these materials become quite complicated; [3] and, due to this, it might become difficult to produce homogeneous single phase absorber materials. As a rule, monograin growth in different molten fluxes results in homogeneous materials [4]. The isothermal heating of precursor materials in the presence of the liquid phase of a suitable solvent material (flux) leads to the formation of semiconductor materials with single-crystalline grain structures and narrow-disperse granularity, so called monograin powders. In our previous reports [5,6] we showed that monograin powders of $Cu_2ZnSnSe_4$ and also $Cu_2Zn_{1-x}Cd_xSn(Se_{1-y}S_y)_4$ solid solutions with tailored chemical composition can be prepared by isothermal recrystallization of initial binary compounds in molten KI. $Cu_2ZnSnSe_4$ powder crystals grown in molten KI have tetragonal shape with rounded grain edges [5]. Potassium iodide has a high melting temperature (685 °C) and, due to this, rather high doping of the synthesized absorber material with potassium and iodine can be predicted. However, the solubility of K and I in CZTSe had not yet been studied. In the present paper, the formation of $Cu_2ZnSnSe_4$ from binary CuSe, ZnSe and SnSe in molten KI is investigated; and the chemical interactions between the initial binary compounds and KI are investigated using DTA, XRD and Raman spectroscopy.

2. Experimental details

For the determination of phase change temperatures and of the interactions between the initial binaries and the flux material, differential thermal analysis (DTA) setups were used and different experiments performed. The following mixtures were studied: KI/CuSe, KI/ZnSe, KI/SnSe, KI, KI/CuSe/ZnSe/SnSe, and KI/CuSe/SnSe. The mass ratios of the binary compounds and the flux material were kept equal to 1:1. The compounds were mixed by grinding in a mortar and sealed into degassed quartz ampoules. As a reference, the empty quartz ampoule was used. The heating/cooling rate was 5 °C/min. The results of the DTA experiments were compared with the phase diagrams of systems Cu–Se, Zn–Se, and Sn–Se available from the literature [7].

The samples for the Raman and XRD measurements were prepared as follows: 1 g mixtures of CuSe/ZnSe/SnSe (in relation to form Cu-deficient compositions of Cu1.85ZnSnSe3.85) and KI were

---

[*] Corresponding author.
E-mail address: ingaklav@inbox.lv (I. Klavina).

0040-6090/$ – see front matter © 2011 Elsevier B.V. All rights reserved.
doi:10.1016/j.tsf.2011.01.365

heated for 1 h and annealed into degassed quartz ampoules at the temperatures: 250, 270, 400, 520, 680, and 800 °C. The ampoules were quenched in water, opened; and the powder was studied by XRD and Raman spectroscopy. For solubility investigation, single crystalline pieces of ZnSe, CuSe, and SnSe (0.5 g) were heated in KI (3 g) into degassed ampoules at 740 °C for one week and quenched to room temperature in water. After opening the ampoules, KI was removed by washing with DI water. The solid part of the binary compound that stayed undissolved in molten KI was gathered on a 30 μm filter and weighed. The dissolved part in molten KI of a binary compound formed colloidal particles in water that passed through the filter. The solubility of the used binary compounds in KI was determined by the mass loss method.

Room temperature Raman spectra were recorded using a Horiba's LabRam HR high-resolution spectrometer equipped with a multichannel CCD detection system in the backscattering configuration. In micro Raman measurements, the incident laser light with a wavelength of 532 nm can be focused on the sample within a spot of 1 μm in diameter. X-ray diffraction measurements were performed using a Bruker D5005 diffractometer (Bragg–Brentano geometry) Cu Ka1 radiation with $\lambda = 1.5406$ Å at 40 kV, 40 mA and graphite monochromator. For studies an ICDD PDF-4 + 2009 was used.

3. Results

3.1. Differential thermal analysis (DTA)

3.1.1. Quasi-binary systems

The comparison of the DTA curves presented in Fig. 1 with the corresponding phase diagrams of the semiconductor compounds gave the following results:

- DTA peaks can be attributed to phase changes of the mixture of CuSe and KI as follows: a peak at 381 °C corresponds to the formation of β-Cu$_{2-x}$Se due to the decomposition of γ-CuSe [5]: γ-CuSe → β-CuSe$_{2-x}$Se (solid) + Se (liquid); the next endothermic peak in the vicinity of 519 °C corresponds to the eutectic temperature in the pure β-Cu$_{2-x}$Se and Se quasi-binary system (523 °C). At 535 °C, the system reaches the liquidus line of the mixture of Se and β-Cu$_{2-x}$Se. The endothermic peak at 670 °C can be attributed to the melting of the CuSe/KI mixture. After this peak an exothermic peak follows at 682 °C, which is probably connected with the dissolution of CuSe in molten KI.
- In the other quasi-binary systems ZnSe/KI and SnSe/KI, only endothermic peaks followed by exothermic peaks in the vicinity

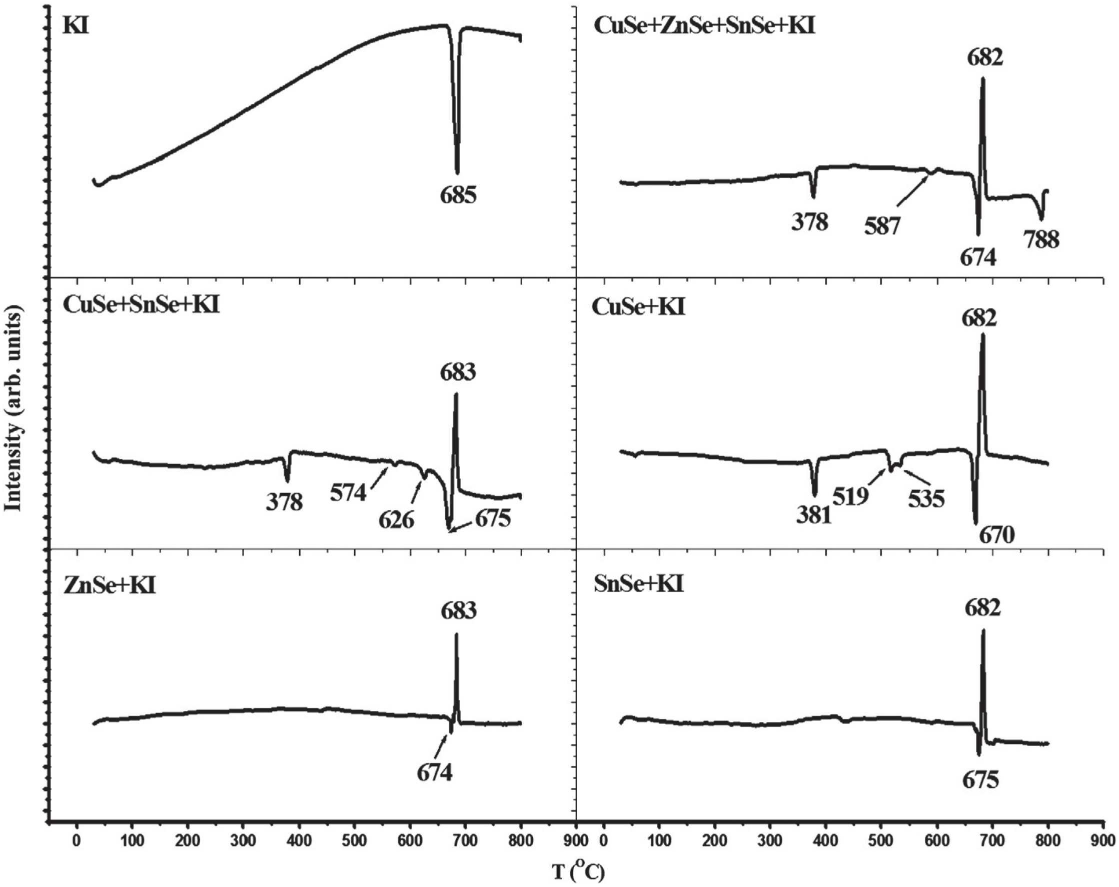

Fig. 1. DTA heating curves of KI; of quasi-binary systems: KI and CuSe, KI and ZnSe, KI and SnSe; of a KI/CuSe/SnSe sample and of the mixture for the quaternary CZTSe synthesis.

of the melting point of KI are recorded. The DTA curve of the mixture of ZnSe and KI shows an endothermic peak at 674 °C followed by an exothermic peak at 683 °C; and the DTA curve of the mixture of SnSe and KI shows an endothermic peak at 675 °C with a following exothermic peak at 682 °C.

It is remarkable that the common features for all the investigated quasi-binary systems show that the melting of the mixtures starts at considerably lower temperatures than the melting temperature of pure KI (685 °C) and that after an endothermic peak, attributable to the melting process, exothermic peaks occur.

3.1.2. Ternary and quaternary systems

The DTA heating curve of the KI/CuSe/SnSe mixture shows more pronounced endothermic peaks at 378 °C (the formation of β-$Cu_{2-x}Se$), at 574 °C (unknown) and at 626 °C followed by endothermic/exothermic peaks in the vicinity of the melting temperature of KI at 675/683 °C. The endothermic peak at 626 °C can be attributed to the melting of the eutectic mixture of $SnSe/SnSe_2$ [8] formed after the release of Se due to the formation of β-$Cu_{2-x}Se$.

The DTA heating curve of the KI/CuSe/ZnSe/SnSe mixture shows endothermic peaks at 378 and 587 °C followed by endothermic/exothermic peaks at 674/682 °C. In the cooling curve of the studied KI/CuSe/ZnSe/SnSe system, only one endothermic peak in the vicinity of the melting point of the mixture near 660 °C is detectable that can be attributed to the solidification process of the molten phase of KI with other compounds dissolved in it.

3.2. Raman analysis

In Table 1, the experimental results of Raman spectroscopy of the mixture of CuSe/ZnSe/SnSe/KI heated at several temperatures for 1 h are presented. Raman spectroscopy data reveal that the formation of $Cu_2ZnSnSe_4$ and Cu_2SnSe_3 is already detectable at 400 °C but that at a lower temperature only the binaries exist. It is common for all the used heating temperatures that some part of ZnSe (melting point at 1526 °C) and SnSe (melting point at 861 °C) remain non-reacted even at 680 °C.

3.3. Solubility, MS, and XRD analyses

3.3.1. CuSe/ZnSe/SnSe/KI

The solubility of the binary chalcogenides in KI is determined: 3.6 mole% CuSe, 0.27 mole% SnSe and 0.086 mole% ZnSe. The solubility of $Cu_2ZnSnSe_4$ in KI was 0.61 mole%. The doping concentration of K in CZTSe is determined by ICP-MS to be 215 μg/g. Unfortunately, the iodine evaporation during the analysis does not allow determining its concentration in the powder by using the ICP-MS method.

Table 1
Data for the Raman analysis of the mixture of CuSe, ZnSe, SnSe, and KI heated at several temperatures for 1 h. The characteristic Raman peaks from several spectra are gathered.

Annealing temperature, °C	Raman peaks, cm^{-1}	Component	Reference
250, 270	250	ZnSe	Experiments and [11]
	143–147	SnSe	[9]
	185	SnSe2	[9,10]
	263	CuSe	Experiments
400	250	ZnSe	Experiments and [11]
	263	CuSe	Experiments
	180	Cu_2SnSe_3	[6]
	171, 195	CZTSe	[6]
520	250	ZnSe	Experiments and [11]
	110, 145	SnSe	[9]
	171, 195, 235	CZTSe	[6]
680	250	ZnSe	[11]
	94–95, 106, 127, 149	SnSe	[9]
	182–185	$SnSe_2$	[9,10]
	81, 171, 195, 233	CZTSe	Experiments and [6]

Table 2
Data for the XRD analysis of the mixture of CuSe, ZnSe, SnSe, and KI heated at several temperatures for 1 h.

Phase/T, °C	250	270	400	520	680	800
$Cu_{0.87}Se$ (Hexagonal)	x	x				
CuSe (Hexagonal)				x		
$Cu_{1.82}Se$ (Cubic)	x		x			
$Cu_{0.67}Sn_{0.33}Se$ (Cubic)				x		
$Cu_2ZnSnSe_4$ (Tetragonal)					x	x
KI (Cubic)	x	x	x	x	x	x
SnSe (Orthorhombic)	x	x	x		x	x
$SnSe_2$ (Rhombic and Hexagonal)			x			
ZnSe (Cubic)	x	x	x		x	x

The XRD analysis (given in Table 2) shows, that the formation of CZTSe in KI involves several steps. In samples, heated at 250 °C, some $Cu_{1.85}Se$ was found; but at 400 °C, $SnSe_2$ was detected. At 520 °C, Cu_2SnSe_3 was found. At 680 °C (a little below the melting point of KI), $Cu_2ZnSnSe_4$ is formed. This provides some evidence that the formation of the liquid phase is the main mediator for the chemical synthesis reaction.

4. Discussion

On the basis of the Raman and the XRD results it can be concluded that Se, released due to the decomposition of CuSe to $Cu_{1.8}Se$, reacts with SnSe forming $SnSe_2$. The melting temperature of the eutectic mixture of the $SnSe/SnSe_2$ system is seen in the DTA curve of KI/SnSe as an endothermic peak at 626 °C (see Fig.1.). By Raman measurements, Cu_2SnSe_3 and CZTSe can be found formed already at the temperatures lower than 400 °C; however, this was not yet visible in XRD. The main formation process of CZTSe happens close to the melting point of KI. By DTA, XRD and Raman spectroscopy data, it is seen that the chemical interactions were induced by the formation of a liquid phase both in separate quasi-binary systems of the precursor compound with KI and in the mixture for the quaternary CZTSe synthesis.

5. Conclusions

Comparison of the DTA curves reveals that the common features for all the investigated quasi-binary systems (the precursor binary compounds mixed with KI) are that the melting of the mixtures started at lower temperatures than the melting of pure KI and that after an endothermic peak attributed to the melting process an exothermic peak occurs. The solubility of the binary chalcogenides in KI is low: 3.6 mole% CuSe, 0.27 mole% SnSe and 0.086 mole% ZnSe, also $Cu_2ZnSnSe_4$ in KI is only 0.61 mole%. The K impurity concentration determined by ICP-MS is 215 μg/g; the iodine impurity concentration still needs to be determined. By DTA, XRD and Raman spectroscopy data it can be concluded that all chemical interactions are induced by the formation of a liquid phase both in the separate quasi-binary systems of precursor compound and KI and in the mixture for the quaternary CZTSe synthesis.

Acknowledgements

This research was supported by the Doctoral Studies and Internationalization Program DoRa of the European Social Funds, the Estonian Ministry of Education and Research Contract No. SF0140099s08, and the EAS project EU29713. Taavi Raadik is gratefully acknowledged for Raman measurements.

References

[1] K.L. Chopra, P.D. Paulsons, V. Dutta, Prog. Photovoltaics Res. Appl. 12 (2004) 69.

[2] J.M. Raulot, C. Domain, J.F. Guillemoles, J. Phys. Chem. Solids 66 (2005) 2019.

[3] H. Matsushits, T. Maeda, A. Katsui, T. Takizava, J. Cryst. Growth 208 (2000) 416.

[4] E. Mellikov, J. Hiie, M. Altosaar, Int. J. Mater. Prod. Technol. 28 (2007) 291.

[5] M. Altosaar, J. Raudoja, K. Timmo, M. Danilson, M. Grossberg, J. Krustok, T. Varema, E. Mellikov, Proceedings of the 2006 IEEE WCPEC-4, Hawaii, May 7–12 2006.

[6] M. Altosaar, J. Raudoja, K. Timmo, M. Danilson, M. Grossberg, J. Krustok, T. Varema, E. Mellikov, Phys. Status Solidi A 205 (2008) 167.

[7] D.J. Chakrabati, D.E. Laughlin, Bull. Alloy Phase Diagrams 2 (1981) 305.

[8] D.I. Bletskan, J. Ovonic Res. I 10 (2005) 61.

[9] A.J. Smith, P.E. Meek, W.Y. Liang, J. Phys. C: Solid State Phys. 10 (1977) 1321.

[10] N.D. Boscher, J.C. Carmalt, R.G. Palgrave, I.P. Parkin, Thin Solid Films 516 (2008) 4750.

[11] A.G. Kontos, Y.S. Raptis, M. Straburg, U.W. Pohl, D. Dimberg, Thin Solid Films 428 (2003) 185.

Paper III

Leinemann, I., Zhang, W., Kaljuvee, T., Tõnsuaadu, K., Traksmaa, R., Raudoja, J., Grossberg, M., Altosaar, M., Meissner, D. (2014). $Cu_2ZnSnSe_4$ formation and reaction enthalpies in molten NaI starting from binary chalcogenides. *J Therm Anal Calorim, 118*(2), 1313-1321. doi: 10.1007/s10973-014-4102-y

J Therm Anal Calorim (2014) 118:1313–1321
DOI 10.1007/s10973-014-4102-y

$Cu_2ZnSnSe_4$ formation and reaction enthalpies in molten NaI starting from binary chalcogenides

Inga Leinemann · Weihao Zhang · Tiit Kaljuvee · Kaia Tõnsuaadu · Rainer Traksmaa · Jaan Raudoja · Maarja Grossberg · Mare Altosaar · Dieter Meissner

Received: 31 January 2014 / Accepted: 18 August 2014 / Published online: 12 September 2014
© Akadémiai Kiadó, Budapest, Hungary 2014

Abstract The present study deals with chemical reactions and enthalpies during the synthesis of $Cu_2ZnSnSe_4$ (CZTSe) from CuSe, SnSe, and ZnSe in molten NaI as flux material in closed degassed ampoules. Differential thermal analysis (DTA) at heating rates 5 °C min^{-1} and cooling rates 10 °C min^{-1} were used for the determination of temperatures of phase transitions and/or chemical reactions. XRD and Raman analyses confirmed that the formation of CZTSe starts already at 380 °C after the melting of Se that deliberates from the transformation of CuSe to $Cu_{1.8}Se$, and the CZTSe formation process impedes to a great extent due to the presence of solid NaI. After the melting of NaI, the formation of CZTSe is completed. For the determination of enthalpy values, the calibration with pure NaI was performed. The thermal effects and enthalpies were compared with the available known thermodynamical values. The specific enthalpy of exothermic $Cu_2ZnSnSe_4$ formation at 661 °C in NaI -36 ± 3 kJ mol^{-1} was determined experimentally for the first time. Ternary compound Na_2SnSe_3 was formed during the synthesis process. $NaI{\cdot}2H_2O$, if present in NaI, was found to be a critical issue in the synthesis process of CZTSe monograin powders in molten NaI—it gave rise to the formation of oxygen-containing by-products Na_2SeO_4 and $Na_2Cu(OH)_4$. The complete dehydration of $NaI{\cdot}2H_2O$ at $T \leq 70$ °C in vacuum is necessary to avoid the formation of oxygen-containing compounds.

Keywords $Cu_2ZnSnSe_4$ · Monograin material · Formation enthalpy · NaI

Introduction

The latest achieved efficiency with hydrazine slurry approach for $Cu_2ZnSn(Se, S)_4$ solar cells of 12.6 % belongs to scientific group as reported in [1], working for IBM company. However, only our group works mostly with syntheses of CZTSe, CZTS, or CZTSSe, based on flux materials. This method is preferable due to its easy preparation and up-scaling requirements. It is known that the use of suitable flux material in sufficient amounts leads to single-crystalline $Cu_2ZnSnSe_4$ powder growth. During the synthesis process, the liquid phase acts as a particle-repelling agent for precursors, preventing the sintering. The driving force in the monograin powder growth is the difference in surface energies of crystals of different sizes. Our previous reports have shown that the growth of single-crystalline powder grains takes place at temperatures above the melting point of the used flux material [2]. The liquid phase of a flux is also advantageous for the synthesis of multi-component compounds, allowing fast diffusion of constituent elements through liquid phase and providing therefore uniform composition of absorber materials for solar cells [3]. The requirement of the process is that the synthesis of $Cu_2ZnSnSe_4$ (CZTSe) monograin materials must result in the homogeneous single-phase material [4]. The flux material should have low melting temperature and high solubility in water, allowing an easy separation of the

I. Leinemann (✉) · W. Zhang · J. Raudoja · M. Grossberg · M. Altosaar · D. Meissner
Department of Materials Science, Tallinn University of Technology, Ehitajate tee 5, 19086 Tallinn, Estonia
e-mail: ingaklav@inbox.lv

T. Kaljuvee · K. Tõnsuaadu
Laboratory of Inorganic Materials, Tallinn University of Technology, Ehitajate tee 5, 19086 Tallinn, Estonia

R. Traksmaa
Centre for Materials Research, Tallinn University of Technology, Ehitajate tee 5, 19086 Tallinn, Estonia

powder particles from the flux. There are several suitable flux salts such as KI, NaI, and CdI_2 available for the synthesis, monograin growth, or re-crystallization of the absorber materials. In the previous papers [5, 6], we presented the results of studies of $Cu_2ZnSnSe_4$ formation in molten CdI_2 and KI. NaI is a compound with about 30° lower melting temperature than KI, allowing to reduce the synthesis temperature. Its chemical properties are close to KI and the non-toxicity of it is an advantage if compared with CdI_2. The present study deals with the possible chemical reactions between the binary precursor compounds-CuSe, SnSe, and ZnSe-in molten NaI and the chemical interactions of them with NaI, in order to find the critical issues and solutions for $Cu_2ZnSnSe_4$ synthesis. The aim of this study is to find suitable preparation conditions for the synthesis of $Cu_2ZnSnSe_4$, starting from binary chalcogenide compounds. The evaluation of enthalpies of syntheses allows to understand more clearly the syntheses process and chemical pathway. However, similar results of DTA curves from via syntheses of CZTSe material in literature are not available.

Experimental

The quaternary $Cu_2ZnSnSe_4$ powder materials were synthesized from binary CuSe, ZnSe, and SnSe precursor powders in molten NaI in sealed quartz vacuum ampoules. Before starting the syntheses, it is very important to have dehydrated NaI, due to its trend to form $NaI{\cdot}2H_2O$. After heating under continuous vacuum pumping for 4 h up to 370 °C there was no water emission detected by mass spectrometry (MS). For the enthalpy calculations, the DTA calibration was performed. The melting and solidification effects of pure NaI (with the molar enthalpy of fusion 23.679 kJ mol^{-1} at its melting point) were selected as standard. NaI is the preferable substance for DTA calibration, because all the studied samples consist mostly of the flux material (NaI). The melting point of NaI is at the same temperature region where the most of the thermal effects in investigated samples were detected. The maximal deviations in calibration experiments were considered as 8 % and were used for the evaluation of enthalpy deviations. The experiments and calibration were done in evacuated quartz ampoules with the aim to get a transformation constant to be able to transform the data for the open system and compare the gained results with those given in literature. The quartz ampoules were designed with cylindrical base and fitted to cylindrical thermocouple to enlarge the contact with thermocouple and be able to have precise measurements for enthalpy evaluation. Fine grinding in a mortar mixed the precursors in compliance with the stoichiometry of CZTSe. The amounts of compounds used for the mixtures were 0.00037645 mol CuSe, 0.00020637 mol ZnSe, 0.00020638 mol SnSe, and 0.00083389 mol NaI. In the mixtures, it resulted in following molar ratios: CuSe + NaI (1.85:4), ZnSe + NaI (1:4), SnSe + NaI (1:4), CuSe + SnSe +NaI (1.85:1:4), and CuSe + ZnSe + SnSe + NaI (1.85:1:1:4). DTA setups (Thermogravimetric Analyzer Labsys 1600, Setaram Instrumentation, Caluire, France) were used for the detection of the phase changes and the interactions between the initial binaries and the flux material. As a reference for the DTA, empty quartz ampoule was used. The applied heating rates were 5 °C min^{-1} and cooling rates 10 °C min^{-1}. According to the thermal effects found in DTA curves, identical larger samples (1 g) of the mixtures were prepared for Raman and XRD analyses. The samples were heated for 4 h at temperatures few degrees higher than the observed thermal changes in the DTA curves, and then quenched in water.

Room temperature Raman spectra were recorded using a Horiba's LabRam HR800 high-resolution spectrometer (France) equipped with a multichannel CCD detection system in backscattering configuration. Micro Raman measurements were performed using incident laser light of 532 nm focused on a 1-μm spot of the studied sample. In order to get true results, at least 5 Raman spectra were taken from different spots for every sample. XRD measurements were performed using a Bruker D5005 diffractometer, (Karlsruhe, Germany). For analysis of the XRD patterns, the ICDD PDF-4 + 2009 database was used.

After Raman and XRD analyses of non-washed samples, the formed solid phases in the samples were separated from the soluble part of flux material by washing with distilled water several times (7−10) using ultrasonic bath for agitation until washing water became transparent. The separation of flux material (NaI) and other soluble phases after syntheses from samples quenched at different temperatures of mixture CuSe + ZnSe + SnSe + NaI gave the possibility to record more clear spectra of Raman and XRD pattern of insoluble phases in water, by-products, and CZTSe formation.

Results and discussion

Dehydration of NaI

DTA heating/cooling curves of pure NaI are shown in Fig. 1. Only an endothermic peak at 660 °C (melting) in the heating curve and an exothermic peak at 639 °C (solidification) in the cooling curve of average signal 7,996 μVs are seen. Besides cubic NaI (Fm-3 m (225) $a = 6.47$ Å), triclinic $NaI{\cdot}2H_2O$ (P-1(2) $a = 7.146$ and $b = 7.169$, $c = 6.029$ Å) was detected in all samples by

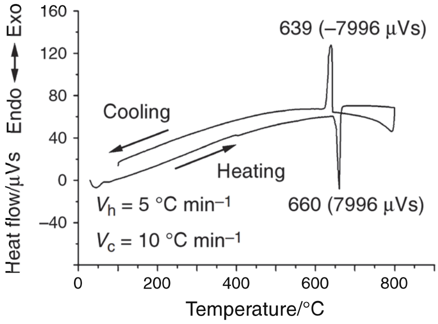

Fig. 1 DTA curves of NaI

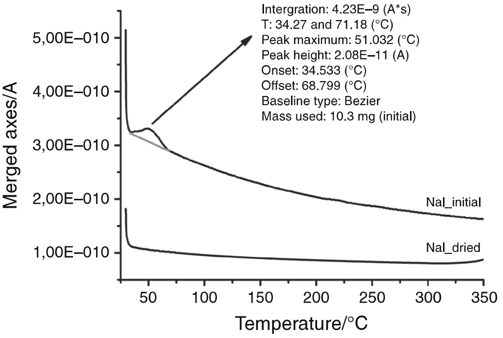

Fig. 2 TG curves of initial and dehydrated NaI

XRD. Corresponding Raman peaks of $NaI{\cdot}2H_2O$ were found experimentally at 82, 90, 95, 99, 107, 115, 122, 135, 138, 150, 187, 194, 222, 230, 244, 323, 353, and 419 cm^{-1}. It is known that NaI is very hygroscopic, and $NaI{\cdot}2H_2O$ can be easily formed when handling NaI in air. We performed thermo-gravimetrical (TG) study of NaI dehydration using mass spectrometry (MS) for the gas-phase analysis. In the TG curve of NaI (see Fig. 2) before dehydration, there is seen a mass loss starting at onset point of 35 °C with peak maximum at 51 °C and the offset point at 69 °C. MS analysis confirmed that this mass loss is caused by H_2O emission. On the basis of the paper [7], where it is reported that in the NaI-H_2O system $NaI{\cdot}2H_2O$ exists in the temperature region of -13.5 °C to 68 °C (or 68.2 and $P_{H2O} = 6.32$ kPa [8]), this peak of mass loss is attributable to the $NaI{\cdot}2H_2O$ decomposition. The authors, as described in the article [7], studied extra pure grade NaI and the crystalline hydrate of ($NaI{\cdot}2H_2O$) by differential barothermal analysis method using mass spectrometry to determine the composition of the gas phase and the partial pressures of gas-phase components. They found that the crystal hydrate $NaI{\cdot}2H_2O$ can be successfully dehydrated already at room temperature in vacuum. The vapor pressure above dehydrated NaI was low and nearly constant during heating up to 600 °C. By their study, $NaI{\cdot}2H_2O$ reacted with carbon dioxide and not with oxygen only in the gas phase during heating. They proposed that heating of $NaI{\cdot}2H_2O$ in the mixture of carbon dioxide and oxygen should lead to the formation of sodium carbonate by the reactions (1) and/or (2) [7]:

$$2NaI \cdot 2H_2O(s) + CO_2(g) \rightarrow Na_2CO_3(s) + 2HI\ (g) + 3H_2O\ (g) \tag{1}$$

$$2NaI \cdot 2H_2O(s) + CO_2(g) + 1/2O_2(g) \rightarrow Na_2CO_3(s) + I_2(g) + 4H_2O\ (g). \tag{2}$$

The reaction (2) shows the way how iodine can be released from $NaI{\cdot}2H_2O$. Sodium carbonate, in turn, can react with water vapor according to the well known scheme [7]:

$$Na_2CO_3(s) + H_2O\ (g) \rightarrow NaOH\ (s) + NaHCO_3(s). \tag{3}$$

The reaction (3) is more likely at higher temperatures, up to sodium carbonate decomposition ($T > 600$ °C). In the opinion of the authors [8], this reaction is responsible for the contamination of NaI with OH^- groups. During rehydration of NaI, the hydroxyl groups are captured by water molecules to give stable aqua complexes, which decompose only above 180 °C.

Quasi-binary systems

DTA heating/cooling curves of the mixtures CuSe + NaI (black), ZnSe + NaI (gray), and SnSe + NaI (gray) are presented in Fig. 3, and the phases found by XRD and Raman analyses are summarized in Table 1. In the heating curves of quasi-binary systems ZnSe + NaI and SnSe + NaI (Fig. 3 a gray lines), endothermic peaks of melting at 659 °C (with signals 727 μVs for ZnSe + NaI and 633 μVs for SnSe + NaI) are partly covered by some exothermic processes occurring during the melting of the mixtures since the melting of pure NaI of the equal amount gave a signal of 7,996 μVs. This exothermic effect can be calculated as 7,269 μVs (727–7,996 = −7,269 μVs) for the mixture of ZnSe + NaI. This value corresponds to the difference of solvation energy to break the bonds and to form new bonds in liquid phase. Since the solubility of ZnSe in NaI is not determined, the value of heat effect cannot be expressed in kJ mol^{-1}. The formation of a complex between liquid NaI and ZnSe (4) can be proposed similarly [9] as follows:

$$ZnSe\ (s) + 4NaI\ (l) \leftrightarrow Na_2ZnI_4(l) + Na_2Se\ (l). \tag{4}$$

The similar value of exothermic effect for the complex formation in the SnSe + NaI mixture by DTA heating curve can be calculated as 633–7,996 = −7,363 μVs.

Fig. 3 DTA curves of the: **a** ZnSe + NaI, SnSe + NaI (*gray lines*), CuSe + NaI *black line*, and a part of phase diagram of Cu-Se system on the right side of (**a**), CuSe + SnSe + NaI (**b**) and the mixture for synthesis of quaternary CZTSe (**c**)

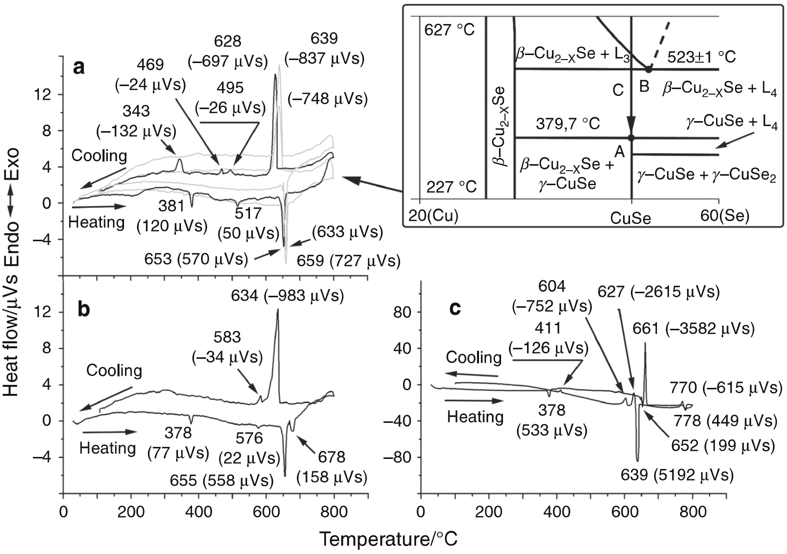

Table 1 Phases found by XRD (symmetry, space group, lattice parameters (Å)) and by Raman (Raman shift (cm^{-1})) in the studied samples, according to the detected effects in DTA curves

Phase	Raman shift/cm^{-1} and ref.	NaI +CuSe	NaI + CuSe + SnSe	NaI + CuSe + SnSe + ZnSe
CuSe, Hexagonal P63/mmc (194), $a = 3.94600$, $c = 17,17800$	–	Heating (380–660 °C)	Heating (380–680 °C)	Heating (380–790 °C)
$Cu_{1.82}Se$ (Berzelianite), Cubic F-43 m (216), $a = 5.72200$	263 [12]	Cooling (515–495 °C)	Cooling (635–550 °C)	
CuI (Marshite), Cubic F-43 m (216), $a = 6.08474$	122, 139 [exp.]			
ZnSe (Stilleite), F-43 m (216) $a = 5.66800$	204 251 [22]	–	–	
CZTSe, tetragonal I-42 m (121) $a = b = 5.73323$, $c = 11.41811$	81, 171, 191*,194*, 196, 231 [5]			
$Na_2Cu(OH)_4$, Orthorhombic, Pna2I (33) $a = 6.7500$, $b = 6.72600$, $c = 8.99300$	–			
Na_2SeO_4, Orthorhombic, Fddd (70) $a = 10.17100$, $b = 12.58700$, $c = 6.10380$	–			
SnSe, orthorhombic, $a = 11.50700$, $b = 4.15000$, $c = 4.48000$	130, 150 [23]	–	Only by heating at 580 °C	
$SnSe_2$, hexagonal, primitive P-3m1 (164), $a = b = 3.80400$, $c = 6.15100$	186 [15]	–	Only by heating at 380 °C	
Cu_2SnSe_3	178, [20] 180 236 [5]	–	Heating (380–680 °C) Cooling (635–550 °C)	Only by heating at 380 and at 790 °C
Se	240 [exp.]	–	–	
Na_2SnSe_3, Monoclinic, P21/c (14) $a = 7.24400$, $b = 16.21800$, $c = 6.17400$	–	–	–	Only by heating at 790 °C

* Shift to the lower peak values is similar to the solid solutions [27]

The exothermic peaks in the cooling curves of ZnSe + NaI and SnSe + NaI in the vicinity of the melting and solidification point of pure NaI at 639 °C are recorded as 748 and 837 µVs, respectively. The thermal effects of reversible to those processes described above can be calculated as 7,248 µVs for ZnSe + NaI mixture and 7,159 µVs for SnSe + NaI mixture. The enthalpy values of forward and reversible processes are rather close (−7,269/7,248 µVs for ZnSe + NaI and −7,363/7,159 µVs for SnSe + NaI). The samples of those mixtures investigated after annealing at 660 °C do not show any new formed phases. From this phenomenon, it can be derived that the complex formation takes place only in the liquid phase and it is a reversible process.

The detected peak positions of thermal effects in CuSe + NaI mixture are marked in Cu-Se phase diagram from the Ref. [10] (see insert in Fig. 3 a right side). The DTA peaks and enthalpies in the CuSe + NaI system can be attributed to the phase changes and reactions as follows:

The thermal effect at 381 °C in the heating curve (Fig. 3 a right side point A (379.7 °C), with detected endothermic signal of 120 µVs, corresponds to the formation of $Cu_{2-x}Se$ due to the peritectic decomposition of CuSe [10]. The formation of $Cu_{2-x}Se$ phase was confirmed by Raman peak at 263 cm^{-1} [11]. XRD pattern of the sample quenched at 380 °C confirmed also the transformation of CuSe to $Cu_{1.8}Se$ (berzelianite). At the same time, the formation of CuI was found by XRD analysis and Raman spectra with peaks at 122, and 139 cm^{-1}. The reference Raman spectra of α, β, and γ modifications of CuI with Raman shifts at 93, 122, and 139 cm^{-1} were experimentally measured by us and found to be identical with each other. The formation of CuI can be thermodynamically possible if iodine, released from NaI, see reaction (2), takes part in the formation of CuI described by the following reactions (5, 6). The thermodynamic calculations were made on the bases of data from [12–14]. The value of Gibbs energy change ΔG is negative ($\Delta G < 0$); for the reaction (5) in the region of temperatures 0–774 °C, the ΔG is −95 kJ mol^{-1} at 0 °C; −38 kJ mol^{-1} at 380 °C (the quenching temperature of the sample); and almost 0 kJ mol^{-1} at 774 °C; for the reaction (6), the ΔG is −81 kJ mol^{-1} at 0 °C; −37 kJ mol^{-1} at 380 °C; and −17 kJ mol^{-1} at 800 °C:

$$Cu_2Se\ (s) + I_2(g) \rightarrow 2CuI\ (s) + Se\ (l) \tag{5}$$

$$2CuSe\ (s) + I_2(g) \rightarrow 2CuI\ (s) + 2Se\ (l). \tag{6}$$

The thermal effect at 517 °C in the heating curve with detected signal of 50 µVs can be attributed to the formation of a liquid phase similar to the L_3 [12] (see insert in Fig. 3, right side, point B). The temperature of the liquid phase L_3 formation (517 °C) is lower than the temperature of monotectic point in Cu-Se phase diagram (523 °C) probably due to sodium and copper iodide impurities.

653 °C corresponds to the melting of NaI + CuSe mixture. The melting temperature of a substance can be reduced due to the added impurities. CuSe in NaI increases the entropy, and the melting of the mixture takes place at a much lower temperature than pure NaI. The accompanied endothermic melting signal of 570 µVs is covered by the thermal effect of another exothermic process with signal value of −7,426 µVs. It could be some complex formation in the formed liquid phase due to the solvation of CuSe in NaI. The thermal effect at 628 °C in the cooling curve with signal of −697 µVs can be attributed to the solidification of NaI + CuSe. This signal is covered by another signal of 7,299 µVs that could be accompanied by the reversible endothermic precipitation of CuSe from NaI.

The thermal effects at 495 °C (−26 µVs) and 469 °C (−24 µVs) (in sum of 24 + 26 = 50 µVs) in the cooling curve (see insert in Fig. 3, right side, where arrow C is crossing the liquidus line (precipitation of $Cu_{2-x}Se$) and temperature of monotectic point (formation of liquid L_4) and moving to point A) correspond to the reversible process detected in the heating curve at 517 °C (50 µVs).

The thermal effect at 343 °C (−132 µVs) in cooling curve corresponds to the peritectic process detected in the heating curve at 381 °C (see text above) [12]. The temperatures are shifted to lower side probably due to impurities.

Ternary and quaternary systems

The DTA heating/cooling curves of the CuSe + SnSe + NaI and CuSe + ZnSe + SnSe + NaI mixtures are presented in Fig. 3 b, c, respectively. The found phases in the heated samples of the non-washed mixtures are given in Table 1.

The endothermic peak around 378 °C occurring in heating curves of the both mixtures (with thermal effects of 77 and 533 µVs correspondingly) is seen also in the DTA heating curve of the quasi-binary system CuSe + NaI (381 °C) presented in Fig. 3 a. Therefore, we attribute this peak to the peritectic process at temperature of 379.7 °C in CuSe binary system, the CuSe phase transformation, and decomposition to $Cu_{2-x}Se$ + Se-as shown in the phase diagram of CuSe in [12]. $Cu_{1.8}Se$ (berzelianite) is confirmed by XRD analysis, and $Cu_{2-x}Se$ phase was detected by Raman peak at 263 cm^{-1} [13]. At this temperature, CuI forms in both systems as described above (see reactions 5–6), and it is confirmed by XRD data and Raman shifts at 122 and 139 cm^{-1} (see Table 1). We determined also experimentally Raman shifts of elemental Se for reference. They were found at 138, 233, and 238 cm^{-1}. The presence of $SnSe_2$ in the XRD pattern and in Raman spectra at 186 cm^{-1} [15] can be expected from reaction (7) between

SnSe and Se, released from CuSe (detected by Raman peak of elemental Se at 240 $\mathrm{cm^{-1}}$), as follows:

$$\mathrm{SnSe\ (s)} + \mathrm{Se\ (l)} \leftrightarrow \mathrm{SnSe_2(s)} \tag{7}$$

$\Delta G < 0$; at 0 °C it is -25 kJ $\mathrm{mol^{-1}}$, at 380 °C (the quenching temperature of the sample) $\Delta G = -13$ kJ $\mathrm{mol^{-1}}$ and it is almost 0 kJ $\mathrm{mol^{-1}}$ at 719 °C [16–18]. Also for the direct reaction:

$$\mathrm{2CuSe} + \mathrm{SnSe} \rightarrow \mathrm{Cu_2Se} + \mathrm{SnSe_2} \tag{8}$$

$\Delta G < 0$; at 0 °C it is -10 kJ $\mathrm{mol^{-1}}$, at 380 °C -12 and -16 kJ $\mathrm{mol^{-1}}$ at 800 °C [16–18]. Then Cu_2Se and $SnSe_2$ react with each other forming Cu_2SnSe_3:

$$\mathrm{Cu_2Se\ (s)} + \mathrm{SnSe_2(s)} \rightarrow \mathrm{Cu_2SnSe_3(s)}. \tag{9}$$

Cu_2SnSe_3 formation in the sample quenched at 380 °C was confirmed by XRD and Raman measurements (Raman peaks at 178 [19], 180, and 236 $\mathrm{cm^{-1}}$ [3]).

In the mixture of CuSe + ZnSe + SnSe + NaI, the XRD analysis does not confirm the formation of CZTSe at 380 °C; however, it was detected by Raman spectroscopy at 173, 196, and 236 $\mathrm{cm^{-1}}$ [4]. As the main CZTSe formation process occurs with melting of NaI and only a small amount of it forms at 380 °C (even not seen in the XRD pattern), then we believe that the formation of CZTSe at 380 °C is probably initiated by the release and melting of Se. Formed liquid phase between solid particles allows fast diffusion of reaction components, like in ceramics, where molten salts have been used as additives to enhance the rates of solid state reactions, due to much higher diffusion rates between reaction components in the molten media [20]. Otherwise, in the presence of a big amount of solid NaI, only the solid-state reactions could be expected at this temperature. Up to the melting of NaI (peak at 661 °C in the DTA curve) unreacted $Cu_{2-x}Se$, ZnSe, SnSe, and $SnSe_2$ are detected in Raman spectra by their characteristic peaks at 263, 254 $\mathrm{cm^{-1}}$ [11, 21] and 129, 150 $\mathrm{cm^{-1}}$ [22], and their reflections are present in the XRD pattern. Also, Na containing by-products $Na_2[Cu(OH)]_4$ and Na_2SeO_4 were detected in the sample quenched at 380 °C. The formation of these compounds could be a sign of the presence of $NaI{\cdot}2H_2O$ in NaI. $Na_2[Cu(OH)]_4$ and Na_2SeO_4 phases were found by XRD, and as we could not find the Raman data of these compounds in literature, we synthesized these compounds for reference. The $Na_2[Cu(OH)]_4$ compound was synthesized as described in [23], and Na_2SeO_4 by stoichiometric oxidation of SeO_2 with H_2O_2 and mixing with NaOH in a glove box under nitrogen atmosphere. The synthesized crystals were confirmed by XRD. The experimentally recorded Raman peaks of $Na_2[Cu(OH)]_4$ were at 219, 311, 438, and 443 $\mathrm{cm^{-1}}$ and at 120, 338, 362, 424, 454, and 477 $\mathrm{cm^{-1}}$ for Na_2SeO_4; however, in the Raman spectra of the studied mixtures, these compounds were not found by their characteristic Raman peaks. According to Table 1, the thermal effects can be described as follows:

- The endothermic peak at 576 °C (22 μVs) in the heating curve of the mixture CuSe + SnSe + NaI (see Fig. 3 b) and at 583 °C (-34 μVs) in the cooling curve can be attributed to the eutectic point of Cu_2SnSe_3-$SnSe_2$ [24].
- Endothermic melting of NaI (7,996 μVs, see Fig. 1) is seen at 655 °C as a summary thermal effect with value of 558 μVs due to its coverage by an exothermic effect of value $-7{,}438$ μVs ($-7{,}996 + 558 = -7{,}438$). The process can be attributed to the Cu_2SnSe_3 formation as reaction (9) with enthalpy of -32 ± 3 kJ $\mathrm{mol^{-1}}$ at this temperature. Since the enthalpy value is not large, it is more believable that the formation of ternary compound from Cu_2Se and $SnSe_2$ occurs in the liquid phase. Reversible process (30 ± 2 kJ $\mathrm{mol^{-1}}$) can be calculated from the NaI solidification effect of 983 μVs at 634 °C, where it is covered by an endothermic process of 7,013 μVs.
- The melting enthalpy of Cu_2SnSe_3 1 kJ $\mathrm{mol^{-1}}$ was determined only in the first heating curve at 678 °C (158 μVs). The experimental heat of fusion of Cu_2SnSe_3 has not been reported before. However, it is not detected in the cooling cycle, the reason could be the overlapping of multiple thermal effects.
- The peaks in the cooling curve of NaI + ZnSe + CuSe + SnSe at 604 °C (-752 μVs) should belong to the melting point of CuI ($T_m = 606$ °C [12, 13]) found in XRD studies (Table 1), and the exothermic peak at 411 °C (-126 μVs) can be attributed to the phase change of α-CuI to β-CuI as reported by Rapaport and Pistorius at 408.5 ± 1.5 °C [25].

In the vicinity of the melting temperature of pure NaI (660 °C) a summary endothermic effect (melting process of 199 μVs) can be seen in the heating curve of the mixture CuSe + ZnSe + SnSe + NaI at 652 °C. It means that the thermal effect of NaI melting (7,996 μVs) is covered by an exothermic effect of 7,797 μVs. The following intense exothermic interaction between compounds at 661 °C ($-3{,}582$ μVs) ends with the CZTSe formation. The total value of the exothermic effect for the CZTSe formation (from ternary compound and ZnSe by reaction (10)) can be calculated then as $-11{,}379$ μVs:

$$\mathrm{Cu_2SnSe_3} + \mathrm{ZnSe} \rightarrow \mathrm{Cu_2SnSe_4} \tag{10}$$

From these considerations the specific enthalpy of CZTSe formation (at 661 °C) is -36 ± 3 kJ $\mathrm{mol^{-1}}$. This value is experimentally determined for the first time. Reversible process in cooling cycle at 639 °C (5,192 μVs), where the thermal effect of NaI solidification (seen at 627 °C (2,615 μVs) is covered by 5,381 μVs. The total reversible process of 10,573 μVs results in enthalpy value of 33 ± 3 kJ mol^{-1}. The value differs in few kJ mol^{-1} due to the fact that the formation enthalpy depends on temperature, and by cooling, the detected effect is shifted from 661 to 639 °C. Theoretically calculated formation enthalpy of CZTSe from binary precursors Cu_2Se, $SnSe_2$, and ZnSe is −84.1 kJ mol^{-1} [26]. If to consider that for the reaction (8) $\Delta H = -7.2$ kJ mol^{-1} at 661 °C [16–18] and the determined value for the reaction (9) in the mixture CuSe + SnSe + NaI (see in Fig. 3 b at 655 °C) is −32 ± 3 kJ mol^{-1}, then the total experimental value of CZTSe formation starting from CuSe, SnSe, and ZnSe is $-7 + (-32) + (-36) = -75 \pm 6$ kJ mol^{-1} at 662 °C. This means that the determined experimental value is in good agreement with the theoretically calculated. Also, it should be taken into account that CuSe, SnSe, and ZnSe were found as unreacted in the studied samples up to high temperatures (CuSe decomposition is limited due to the forming overpressure of Se in the closed ampoule, that suppresses the decomposition of CuSe). In addition, the authors want to underline, that it is complicated to predict the influence of CZTSe formation pathway starting from ternary compound Na_2SnSe_3, which was also found by XRD in low concentrations at 790 °C.

It was established in [24] that $Cu_2ZnSnSe_4$ melts incongruently at 788 °C leaving ZnSe:Cu:Sn in the solid phase. Therefore, the peaks of 449 μVs (1 kJ mol^{-1}) at 778 °C in the heating curve and of 615 μVs (2 kJ mol^{-1}) at 770 °C in the cooling curve of CuSe + ZnSe + SnSe + NaI can be attributed to the melting/solidification of CZTSe. The shift of these peaks from 788 °C to lower temperatures can be attributed to the formation of sodium-containing quaternary compound similar to CZTSe. In the Raman spectrum of the sample quenched at 790 °C, the main Raman peaks of CZTSe are shifted from 196 to 194, 191 and from 173 to 171 cm^{-1}. Such shift to the lower peak values is similar to the solid solutions $Cu_2ZnSn(S_{1-x}Se_x)_4$ with small amounts of $Cu_2ZnSnSe_4$ [27] and also in our solid solutions of CZTS with Cu_2CdSnS_2 [to be published elsewhere]. The samples quenched at 790 °C show again ternary compound Cu_2SnSe_3 or Na_2SnSe_3 (178 cm^{-1}) in Raman spectra, while Na_2SnSe_3 as a possible precursor for the sodium-containing quaternary compound was found in the XRD pattern (Table 1). Besides the ternary and quaternary compounds in XRD pattern and Raman spectra with intensive peaks at 139, 150, 186, 240, 251, and 263 cm^{-1} belong to CuI, Se, SnSe, $SnSe_2$, ZnSe, and $Cu_{2-x}Se$ were found. Due to the fast cooling, the re-formation of CZTSe from the melt should be incomplete in the cooling process. Overpressure of Se in the ampoule obviously avoids the complete decomposition of CuSe.

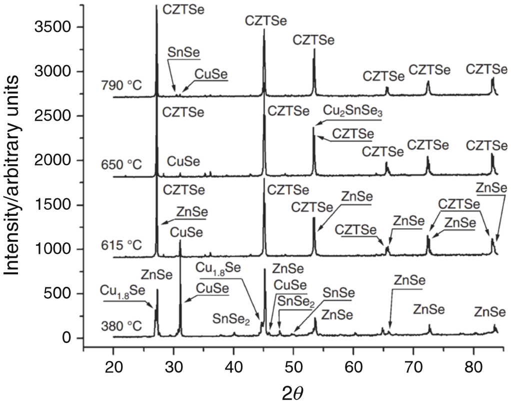

Fig. 4 XRD patterns of CuSe + ZnSe + SnSe + NaI mixtures quenched at different annealing temperatures (after washing out NaI and soluble phases with water)

All sodium-containing compounds are well soluble in water and can be removed by washing. Only CuI is poorly soluble in water (0.00042 g L^{-1} at 25 °C), but it dissolves in the presence of NaI or KI by forming the linear anion $[CuI_2]^-$. Dilution of such solutions with water leads to the re-precipitation of CuI [28].

The XRD patterns and Raman spectra of the sample mixtures of CuSe + ZnSe + SnSe + NaI quenched from different annealing temperatures and washed for separation of NaI are presented in Figs. 4 and 5. As it can be seen from the experimental data, the main CZTSe formation process occurs with melting of NaI and only a small amount of it forms at 380 °C (even not seen in the XRD pattern). We believe that the formation of CZTSe at 380 °C is initiated by the release and melting of Se due to the decomposition of CuSe. Formed liquid phase between solid particles allows fast diffusion of reaction components, like in ceramics, where molten salts have been used as additives to enhance the rates of solid state reactions, due to much higher diffusion rates between reaction components in the molten media [19]. The reactions of CZTSe and Cu_2SnSe_3 formation starting after the deliberation of Se from CuSe consume the available Se, and then the reactions are inhibited after the formation of Se overpressure in the closed ampoules. Overpressure of Se suppresses the further decomposition of CuSe, and the resultant amounts of formed CZTSe and Cu_2SnSe_3 are lower than the sensitivity of XRD, even in washed samples. Also, the big amount of solid NaI between solid precursor particles inhibits the rate of CZTSe formation reaction. Therefore, the characteristic Raman peaks and the reflections of unreacted phases of

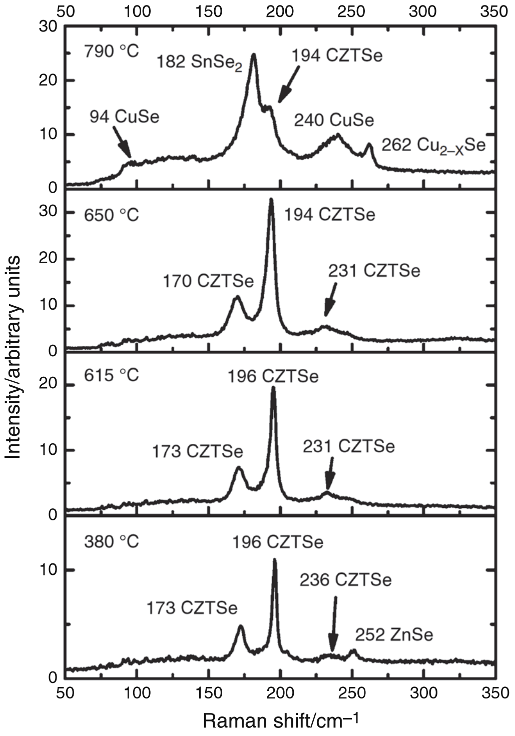

Fig. 5 Raman spectra of CuSe + ZnSe + SnSe + NaI mixtures quenched at different annealing temperatures (after washing out NaI and soluble phases with water)

ZnSe (in Raman spectra at 252 cm^{-1} [21]), Cu$_{1.8}$Se, CuSe SnSe, and SnSe$_2$ are present in XRD patterns of samples heated at temperatures below the melting of NaI. In the sample heated at 650 °C, Raman can detect only single phase of CZTSe, while the XRD reflections are shifted in 2θ scale, which could occur due to some ternary Cu$_2$SnSe$_3$ phase present. Sample, heated at 790 °C (over the highest incongruent melting point of CZTSe [24]) and quenched, shows again more binary compounds CuSe (94, 240 cm^{-1} [5]), Cu$_{2\text{-x}}$Se (262 cm^{-1} [12]), SnSe, and SnSe$_2$ (182 cm^{-1} [15]) present. Due to the fast cooling after heating, the sample over the melting temperature of CZTSe the binaries do not reach to react with each other completely.

Conclusions

It can be concluded that in the presence of solid NaI the formation of CZTSe is inhibited. Chemical reactions start with the formation of a liquid phase in all of the mixtures studied. The melting of NaI is immediately follows by the extensive formation process of CZTSe starting already a little bit below the melting point of NaI. The optimal temperature of synthesis of CZTSe in NaI is 650 °C. Dry and pure NaI allowing to reduce the synthesis temperature in comparison with KI can be successfully used as a flux material in synthesis of CZTSe in monograin powder form. On the basis of the results of Raman and the XRD analyses, it can be concluded that Se, released due to the decomposition of CuSe to Cu$_{1.8}$Se, reacts with SnSe forming SnSe$_2$. However, CuSe does not decompose completely under the formed Se overpressure in the sealed ampoules. Cu$_2$ZnSnSe$_4$ formation starts partly already at 380 °C as a result of the reaction between Cu$_2$Se, ZnSe, and SnSe$_2$. The main formation process of CZTSe is initiated by the formation of the molten phase of NaI in the precursor mixtures at temperatures a little bit lower than the melting point of pure NaI. The formation of Cu$_2$ZnSnSe$_4$ is completed in the formed molten phase of NaI. The occurrence of an intensive exothermic peak right after an endothermic peak due to the melting process in DTA curves suggests a strong chemical interaction between the precursors in the formed molten phase. The formation enthalpies of Cu$_2$SnSe$_3$ in molten NaI starting from Cu$_2$Se and SnSe$_2$ −32 ± 3 kJ mol^{-1} at 655 °C and CZTSe from CuSe, SnSe, and ZnSe −36 ± 3 kJ mol^{-1} at 661 °C are experimentally determined for the first time.

Acknowledgements The Doctoral Studies and Internationalization Program DoRa of the European Social Funds supported this research; Estonian Science Foundation grants 9425, 8964, G8964, projects TK117T, National R&D programs AR10128 and AR12128, the Estonian Ministry of Education and Research Contract No. SF0140099s08, and the EAS project EU29713. Support in the sample preparation process by Sergei Bereznev is gratefully acknowledged.

References

1. Wang W, Winkler MT, Gunawan O, Gokmen T, Todorov TK, Zhu Y, Mitzi DB. Device characteristics of CZTSSe thin-film solar cells with 12.6% efficiency. Advanced Energy Materials. 2013; doi:10.1002/aenm.201301465.
2. Mellikov E, Hiie J, Altosaar M. Powder materials and technologies for solar cells. Int J Mater Prod Technol. 2007;28:291–311.
3. Timmo K, Altosaar M, Raudoja J, Muska K, Pilvet M, Kauk M, Varema T, Danilson M, Volobujeva O, Mellikov E. Sulfur-containing Cu$_2$ZnSnSe$_4$ monograin powders for solar cells. Sol Energy Mater Sol Cells. 2010;94:1889–92.
4. Altosaar M, Raudoja J, Timmo K, Danilson M, Grossberg M, Krustok J, Mellikov E. Chemical etching of Cu2ZnSn(S, Se)4 monograin powder. Phus Stat Sol. 2008;205:167–70.
5. Klavina I, Raudoja J, Altosaar M, Mellikov E, Meissner D. CZTSe (Cu$_2$ZnSnSe$_4$) crystal growth for use in monograin membrane solar cells. CYSENI 2010. In: Proceeding of the annual conference of young scientists on energy issues. [CD VII-347-VII-353]. Kaunas: Lithuanian Energy Institute. 2010 May 27–28.
6. Klavina I, Kaljuvee T, Timmo K, Raudoja J, Traksmaa R, Altosaar M, Meissner D. Study of Cu$_2$ZnSnSe$_4$ monograin formation in molten KI starting from binary chalcogenides. Thin Solid Films. 2011;519:7399–402.

7. Sofronov DS, Grinyov BV, Voloshko AY, Gerasimow VG, Kisil EM, Smirnov NN, Shishkin OV. Origin of the thermal desorption peaks of gases in NaI above 180°C. Inorg Mater. 2009;45:1314–8.
8. Digemans P. Dehydration of the alkali metal iodides in vacuum. Rec Trav Chim. 1938;57:144.
9. Li D. Fast and mass synthesis of ZnS nanosheet via ultra-strong surface interaction. Cryst Eng Comm. 2013; doi:10.1039/C3CE41529E.
10. Glazov V, Pashinkin A, Fedorov V. Phase equilibria in the Cu-Se system. Inorg Mater. 2000;36:641–52.
11. Xue C, Papadimitriou D, Raptis YS, Richter W, Esser N, Siebentritt S, Lux-Steiner MC. Micro-Raman study of orientation effects of Cu_xSe-crystallites on Cu-rich $CuGaSe_2$ thin films. J Appl Phys 2004; doi:10.1063/1.1772885.
12. Barin I. Thermochemical data of pure substances. Part I. Weinheim: VCH Verlags Gesellschaft; 1993.
13. Barin I. Thermochemical data of pure substances. Part II. Weinheim: VCH Verlags Gesellschaft; 1993.
14. Glushko. Thermocenter of the Russian Academy of Sciences. Moscow, Russia: IVTAN Association, Izhorskaya; 1996.
15. Lucovsky G, Mikkelsen JC, Liang WY, White RM, Martin RM. Phys Rev. 1976;14:1663–9.
16. Barin I, Knacke O, Kubaschewski O. Thermochemical properties of inorganic substances. Berlin: Supplement, Springer-Verlag; 1977.
17. Barin I. Thermodynamical data of pure substances. Weinheim: VCH Verlags Gesellschaft; 1989.
18. Landolt-Börnstein. Thermodynamic properties of inorganic material. Scientific Group Thermodata Europe (SGTE). Berlin-Heidelberg: Springer-Verlag; 1999.
19. Marcano G, Rincon C, Lopez SA, Sanchez-Perez G, Herrera-Perez JL, Mendoza-Alvarez JG, Rodriguez P. Raman spectrum of monoclinic semiconductor Cu_2SnSe_3. Solid State Commun. 2011;151:84–6.
20. Arendt RH. J. Alternate fabrication process for molten carbonate fuel cell electrolyte structures. Solid State Chem. 1973;8:339.
21. Perna G, Lastella M, Ambroco M, Cappozzi V. Temperature dependence of the optical properties of ZnSe films deposited on quartz substrate. Appl Phus A. 2006;83:127–30.
22. Smith AJ, Meek PE, Liang WY, Raman J. Scattering studies of SnS_2 and $SnSe_2$. Phys C. 1977;10:1321.
23. Riou A, Cudennec Y, Gerault Y. Acta Cryst. 1989;45:374–6.
24. Dudchak I, Piskach L. Phase equilibria in the Cu_2SnSe_3-$SnSe_2$-ZnSe system. J Alloy Compd. 2003;351:145–50.
25. Rapaport E, Pistorius CWFT. Phys Rew 1968;172:838.
26. Nakamura S, Maeda T, Tabata T, Wada T. First-principles study of indium-free photovoltaic compounds $Ag_2ZnSnSe_4$ and Cu_2-$ZnSnSe_4$. In: Proceeding of the 37th IEEE photovoltaic specialist conference (Washington State Convention Center, Seattle, Washington, USA) 2011:785–786.
27. Grossberg M, Krustok J, Raudoja J, Timmo K, Altosaar M, Raadik T. Photoluminescence and Raman study of Cu_2-$ZnSn(Se_xS_{1-x})_4$ monograins for photovoltaic applications. Thin Solid Films. 2011;519:7403–6.
28. Kaufman B, Fang Y. Purification of Copper(I) Iodide. Inorg Synth. 1983;22:101–3.

Paper IV

Leinemann, I., Nkwusi, G. C., Timmo, K., Danilson, M., Raudoja, J., Kaljuvee, T., Traksmaa, R., Altosaar, M., Meissner, D. (2018). Reaction pathway to $Cu_2ZnSnSe_4$ formation in CdI_2 Part 1: Chemical reactions and enthalpies in mixtures of CdI_2-ZnSe, CdI_2-SnSe, and CdI_2-CuSe. *J Therm Anal Calorim, 134*(1), 409-421. doi: 10.1007/s10973-018-7102-5

Reprinted by permission from Springer Nature (December 02, 2018; license number 4480850324363): Journal of Thermal Analysis and Calorimetry, Reaction pathway to $Cu_2ZnSnSe_4$ formation in CdI_2. Part 1. Chemical reactions and enthalpies in mixtures of CdI_2-ZnSe, CdI_2-SnSe, and CdI_2-CuSe, Inga Leinemann, Godswill Chimezie Nkwusi, Kristi Timmo et al., [c2018], (2018), doi: 10.1007/s10973-018-7102-5

Author's personal copy

Journal of Thermal Analysis and Calorimetry
https://doi.org/10.1007/s10973-018-7102-5

Reaction pathway to $Cu_2ZnSnSe_4$ formation in CdI_2

Part 1. Chemical reactions and enthalpies in mixtures of CdI_2–ZnSe, CdI_2–SnSe, and CdI_2–CuSe

Inga Leinemann[1] · **Godswill Chimezie Nkwusi**[1] · **Kristi Timmo**[1] · **Olga Volobujeva**[1] · **Mati Danilson**[1] · **Jaan Raudoja**[1] · **Tiit Kaljuvee**[1] · **Rainer Traksmaa**[1] · **Mare Altosaar**[1] · **Dieter Meissner**[1]

Received: 14 June 2017 / Accepted: 23 February 2018
© Akadémiai Kiadó, Budapest, Hungary 2018

Abstract

We investigated various possible chemical interactions between individual precursor compounds (ZnSe, SnSe, and CuSe) and CdI_2 as a flux material used in the CZTSe monograin powder synthesis–growth process in closed vacuum ampoules. The processes occurring in these mixtures were detected by the differential thermal analysis method. The phase changes in these processes were determined using X-ray diffraction and Raman spectroscopy, scanning electron microscopy, energy-dispersive X-ray spectroscopy, thermogravimetric analysis, and mass spectrometry. The analyses showed that molten CdI_2 was chemically active, forming $Zn_{1-x}Cd_xSe$ in the CdI_2–ZnSe mixture by a chemical dissolution reaction; CdSe, SnI_2 and SnI_4 formed in the CdI_2–SnSe mixtures and CdSe; and CuI formed in the CdI_2–CuSe mixtures by exchange reactions.

Keywords CuI · Enthalpy of reaction · SnI_2 · SnI_4 · Solvent · $Zn_{1-x}Cd_xSe$

Introduction

$Cu_2ZnSnSe_4$ (CZTSe) has received substantial attention in the field of photovoltaics [1–6]. Using molten salts as flux materials is one of the cheapest methods of synthesis. Binary mixtures (ZnSe, SnSe, CuSe) in salts such as CdI_2, KI and NaI have been used for the synthesis of CZTSe [7–9]. However, the chemical processes involved in the synthesis–growth of $Cu_2ZnSnSe_4$ in molten CdI_2 have not yet been clarified. In this paper, we study and attempt to separately describe the possible chemical interactions between CdI_2 as a flux salt and use binary precursor compounds for the synthesis of CZTSe in closed vacuum ampoules. We also consider the possible influences of ambient processing conditions and impurities introduced by precursor compounds. In principle, there are two ways to predict the chemical pathway of CZTSe formation: thermodynamic [10] and epitaxial approaches [11]. The thermodynamic approach explains the formation of compounds based on differences in Gibbs free energy (ΔG), while the epitaxial model considers the crystallographic structures that are the most suitable for epitaxy. The epitaxy model has been applied to explain the formation of CZTSe in thin film growth [11]. In this study, ΔG calculations were used to evaluate reaction probabilities.

Our previous studies of the flux-precursor mixtures [7, 8] showed that the melting of flux salts (KI, NaI) was always accompanied by the intensive dissolution of precursors. Dissolution processes can be physical or chemical. Dissolution is chemical if new substances (also cations and ions) are produced [12]. In [13], it was found that Cd was incorporated from CdI_2 into Cu_2ZnSnS_4. The Cd content of the formed $Cu_2Zn_{1-x}Cd_xSnS_4$ increased with temperature and with the increase in the ratio of molar CdI_2 to its binary precursors. However, the value of x in $Cu_2Zn_{1-x}Cd_xSnS_4$ did not depend on the duration of synthesis at a constant temperature, and the mechanism of Cd incorporation was not clearly shown. In this study, the reactions of cadmium selenide formation in CdI_2-precursor mixtures will be clarified. The aim of this work was to investigate the various chemical reactions in separate mixtures of binary compounds (ZnSe, SnSe or CuSe) with CdI_2 in closed

✉ Inga Leinemann
ingaklav@inbox.lv

[1] Department of Materials and Environmental Technology, Tallinn University of Technology, Ehitajate tee 5, 19086 Tallinn, Estonia

Published online: 08 March 2018

Author's personal copy

vacuum ampoules to completely understand the final chemical synthesis process of CZTSe from these binary compounds.

Experimental

Preparation of binary precursors and analytical methods used

The CuSe and SnSe used here were self-synthesized from metal shots (purity of 99.8%) and Se shots (4 N purity from the Aldrich company) by heating in vacuum quartz ampoules at 650 and 700 °C, respectively, for 35 h. The polycrystalline ZnSe, which was grown using the chemical vapour deposition process, was purchased from the company Crystaltechno Ltd. The compounds were analysed by Raman spectroscopy, XRD and EDX-SEM. Raman spectra were recorded using a Horiba LabRam HR spectrometer equipped with a multichannel CCD detection system in a backscattering configuration. Incident laser light of 532 nm was focused on different 1-μm^2 spots in the studied sample, and the average of five readings was taken from every sample to obtain an objective phase composition of the sample. XRD measurements were taken using a Bruker D5005 AXS diffractometer (Karlsruhe, Germany), and the ICDD-PDF-4+2016 database was used for phase identification. The chemical compositions of compounds were analysed using energy-dispersive X-ray spectroscopy (EDX) on a Zeiss HR SEM ULTRA 55 with an accelerating voltage of 20 kV and a beam current of 3 nA. X-ray photoelectron spectroscopy (XPS) was performed on SnSe to investigate the oxygen bonds on its surface. It was bombarded with an Ar ion beam in the analysis chamber of the XPS system with an etching speed of 4 nm min^{-1}. XPS analyses were performed at depths of 0, 1 and 2 nm. The phase transformations of 55.18 mg CuSe (synthesized with an atomic ratio of Cu–Se equal to 1:0.9936) in a degassed sealed quartz ampoule were investigated with a DTA setup (Thermogravimetric Analyzer Labsys 1600, Setaram Instrumentation, Caluire, France). For DTA, the samples were degassed at 100 °C for 2 h in quartz ampoules and sealed. An empty quartz ampoule was used as the reference crucible. The applied heating and cooling rates were 5 and 10 °C per minute, respectively. CdI_2 was selected as the reference material for the DTA enthalpy calibrations for two reasons: first, the processes occurring during synthesis occur in the same temperature region as the melting of flux material and, second, our experimentally determined melting point of CdI_2 coincides with that published in the literature (i.e., a melting temperature of 387 °C) [14].

Preparation and analysis of expected products

We supposed that Se, ZnI_2, a ZnI_2–CdI_2 mixture, CdSe and SnI_4 could be formed in these experiments. Therefore, we studied these substances separately.

To clarify the behaviour of elemental *Se* in closed vacuum ampoules, we studied the thermal heating curve of 40 mg of commercial Se (described above) in the temperature interval from room temperature (RT) to 600 °C in differential scanning calorimetry (DSC) mode, using the NETZSCH STA 449 F3 (Germany) setup. The instrument was calibrated using available standards. The Raman analysis of Se was performed as described above.

Commercial ZnI_2 (Alfa Aesar, with a purity of 98%) was dried by vacuum heating and investigated using Raman spectroscopy (dried and non-dried) analysis to obtain the reference spectra. It is known that the molar heat of fusion of different salt eutectic mixtures depends on the melting temperature, while the heat capacity of a mixture is close to that of its pure salts in a molten state [15, 16]. To understand the formation and melting of the CdI_2–ZnI_2 mixture, we performed a DSC scan with NETZSCH STA 449 F3 for the CdI_2–ZnI_2 mixture with a molar ratio of 1:1. The mixture of 0.05 mg CdI_2 and 0.04 mg ZnI_2 was prepared in a glove box in an inert gas atmosphere and sealed within a quartz ampoule.

Commercial *CdSe* (of extra high purity from Crystaltechno Ltd, synthesized by chemical vapour deposition) and SnI_4 (self-synthesized by the iodine transport method) were analysed by Raman spectroscopy.

Procedure of CdI_2 analysis

We suppose that the stability of the used flux salt (CdI_2, in our case) can also influence the chemical pathways in flux-binary mixtures. It is known that CdI_2 does not form crystal hydrates. However, due to impurities, it may contain some crystal water. CdI_2 melts at 387 °C, and its boiling point is 742 °C; it also has a high solubility in water (847 g L^{-1} at 20 °C) [14]. The vapour pressure of liquid CdI_2, as experimentally determined by TG analysis in the temperature interval of 740 K (467 °C)–770 K (497 °C), is 2.85–5.75 10^{-3} Pa [17]. These values are lower than that theoretically calculated in [18]. Kawasaki et al. [19] found that the dissociation of CdI_2 produces Cd and 2 I atoms; the authors in [20], using a laser, determined that this direct dissociation occurs due to the linear structure of CdI_2. In [21], it was experimentally deduced that mainly CdI_2 monomers and less abundant (by approximately 3 orders of magnitude) Cd_2I_4 dimers existed in the gas phase. However, these instabilities were only found if a high-energy input was applied.

Author's personal copy

CdI_2 (Fluka) of 99.0% purity, with trace anions (Br^-, Cl^-, SO_4^{2-}) and cations (Ca^{2+}, Co^{2+}, Cu^{2+}, Fe^{2+}, K^+, Na^+), was used. CdI_2 was analysed by Raman spectroscopy, XRD, DTA, TG and MS. The melting and solidification effects of 0.125 g of vacuum-dried CdI_2 were used for the enthalpy evaluations, considering that the molar enthalpy of fusion is 20.71 kJ mol^{-1} at the melting point of 387 °C [14]. CdI_2 was selected as the standard for the SETERAM DTA calibration, and a 10% error bar was used. The MS OMNI^{Star} (produced by Pfeiffer Vacuum, Germany) setup provides the opportunity to analyse the gases emitted from the sample during heating, which are reflected as mass losses in the TG curves.

Preparation and analysis of CdI_2-binary compound mixtures

The expected reactions in the studied mixtures were simulated using the HSC6 Chemistry software [14] based on the set data of enthalpy (H), entropy (S) and heat capacity (C_p) in this software. The graphs depicting the dependency of ΔG on temperature in the interval of interest were modelled using a temperature step of 1 °C.

First, DTA was performed for every studied mixture to determine the temperatures of the occurring processes. The mixtures used for DTA in the closed quartz ampoules were prepared with the aim of imitating the conditions of the process of CZTSe synthesis. The molar ratio of CuSe–CdI_2 was equal to 1.85:1.65 and that of ZnSe (or SnSe):CdI_2 was equal to 1:1.65. The following amounts of materials were used in the separate mixtures: 0.02979 g ZnSe, 0.040796 g SnSe, and 0.0544 g CuSe; each mixture contained 0.125 g CdI_2. To determine the phase changes in the processes detected by DTA, additional samples of the CdI_2–CuSe mixture in vacuum ampoules were prepared and heated for 4 h at 400 and 740 °C and quenched after heating (using a Rigaku PDXL Ultima IV apparatus, a D/teX Ultra line detector and the JCDPS-2009 databases for phase detection). The DTA ampoules were opened, and the samples were analysed by XRD and Raman spectroscopy as described above. More information was gained by analysing extra samples of ultra-high-purity single-crystalline pieces of CuSe, SnSe, and ZnSe, which were heated at 740 °C for 1 week in CdI_2. The aim was to dissolve these binary compounds in CdI_2. The following amounts of compounds were used: 3.93×10^{-3} mol of single-crystalline ZnSe in 9.43×10^{-3} mol of CdI_2 (molar ratio of 1:2.41); 1.16×10^{-3} mol of single-crystalline SnSe in 3.76×10^{-3} mol of CdI_2 (molar ratio of 1:3.24); and 3.63×10^{-3} mol of single-crystalline CuSe in 8.51×10^{-3} mol of CdI_2 (molar ratio of 1:2.34). The formed solid phases were separated from the soluble part of the flux material by washing several times (7–10) with distilled water, using an ultrasonic bath for agitation. Separation was necessary for SEM and EDX analyses to investigate the morphology and exact compositions of the insoluble phases. The fraction dissolved in water was dried by evaporation and then analysed by SEM–EDX.

Results and discussion

Binary precursors (ZnSe, SnSe, CuSe)

The *ZnSe* Raman spectra showed characteristic peaks of single-crystalline ZnSe at 202 and 252 cm^{-1} [22] and an additional peak at 140 cm^{-1}, which was probably due to the presence of some elemental Se. The Raman spectrum of the ZnSe precursor recorded at our laboratory was published in [23]. Selenium was not found in the ZnSe precursor by XRD analysis, possibly due to an amorphous phase of Se that remained on the ZnSe crystallites after the synthesis of the gas phase.

The *SnSe* precursor contained some $SnSe_2$, as detected by its characteristic Raman peak at 182 cm^{-1}. In Ref. [24], the $SnSe_2$ Raman peak was detected at 184.5 cm^{-1}. Figure 1 shows the XPS doublet lines in the region of the Sn 3d core level spectra before and after etching by Ar^+ sputtering. Based on the etching results, SnO_2 existed on the surface of SnSe. SnO_2 was removed completely after 15 s of sputtering.

The Raman spectra of the *CuSe* precursor had a characteristic peak of $Cu_{2-x}Se$ at 263 cm^{-1} [25] and additional Raman peaks at 94, 186–194, and 307–326 cm^{-1}. The XRD pattern indicates that the $Cu_{0.87}Se$, Cu_3Se_2, and Cu_3Sn phases were also present in the CuSe precursor. The occurrence of Cu_3Sn in the XRD pattern suggests that the initial Cu used for the synthesis of CuSe contained some Sn as impurities. The DTA curves of the CuSe precursor are presented in Fig. 2a. A weak signal at 51 °C in the heating

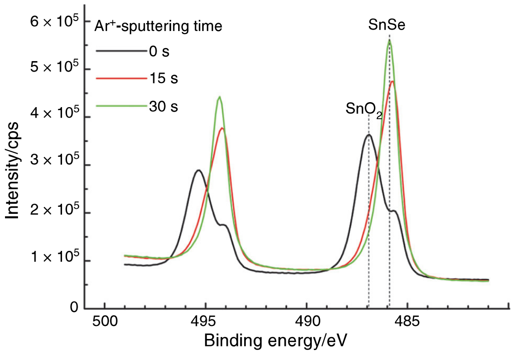

Fig. 1 XPS depth profile of SnSe

Author's personal copy

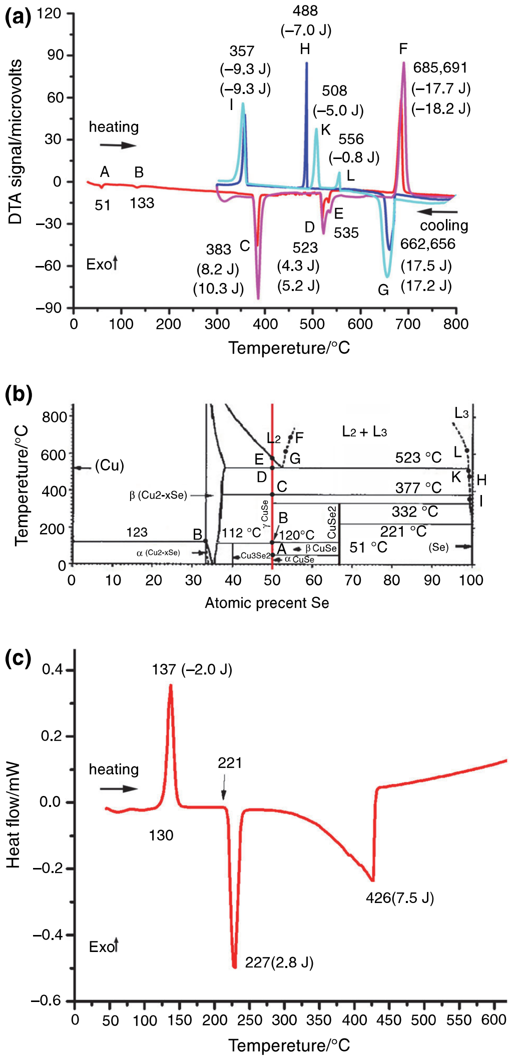

Fig. 2 **a** DTA of CuSe (heating—red/purple, cooling—blue/light blue); **b** draft of Cu–Se phase diagram (according to [26, 27]); **c** DSC of Se. (Color figure online)

curve (red) could correspond to a phase change of α-CuSe to β-CuSe, which is marked in the phase diagram as A (Fig. 2b). The change from the β- to γ-phase was found at 133 °C (point B at 120 °C in the phase diagram) [26, 27]. However, these phase transitions are too weak to be quantitatively analysed by DTA. During heating, the peritectic reaction (1) was reached at 383 °C (point C in the phase diagram). In the literature, this reaction occurs at 377 °C [26, 27]. However, the data for reaction (1) in the HSC6 software [14] are different; during the formation reaction of β-$Cu_{2-x}Se$ (if $x = 0$) from γ-CuSe, ΔG begins to be negative at 398 °C. The used amount of 55.18 mg (3.9 10^{-4} mol) of CuSe gave a signal of 8.2 ± 0.8 J, yielding an enthalpy of reaction (1) of 21.1 ± 2.1 kJ mol^{-1}. This value is higher than that reported in the literature for the process at 377 °C (11.8 kJ mol^{-1} [28]) but lower than that found by HSC6 calculations at 383 °C (30.4 kJ mol^{-1} [14]). The signal in the second heating curve (purple) of 10.3 ± 1.0 J corresponds to an enthalpy value of 26.4 ± 2.6 kJ mol^{-1}, which is very close to the value in [14].

$$(2-x)\,\gamma\text{-CuSe} \leftrightarrow \beta\text{-Cu}_{2-x}\text{Se} + (1-x)\text{Se} \tag{1}$$

At 523 °C, the monotectic point (D), where solid β-$Cu_{2-x}Se$ exists together with two liquids, was reached. The incongruent melting of γ-CuSe at 535 °C (D and E) [26, 27] exhibits thermal effects in the first (red) and second (purple) heating curves as 4.3 ± 0.4 and 5.2 ± 0.5 J, respectively, which can be expressed as enthalpy values of 1.0 ± 1.1 and 13.3 ± 1.3 kJ mol^{-1}, respectively. The exothermic effect *F* values of – 17.7 ± 1.8 J at 685 °C in the first (red) heating curve and – 18.2 ± 1.8 J at 691 °C in the second (purple) heating curve could correspond to the dissolution of two phases, such as $Cu_{2-x}Se$ and γ-CuSe (points G and F). In the cooling cycles at point G, reversible processes are seen, with similar heat values (17.5 ± 1.8 and 17.2 ± 1.7 J). Points H at 488 °C (– 7.0 ± 0.7 J) and I at 357 °C (– 9.3 ± 0.9 J) in the first (dark blue) cooling curve, as well as L at 556 °C (– 0.8 ± 0.1 J) and K at 508 °C (– 5.0 ± 0.5 J) in the second (light blue) cooling curve, are the places where the dashed lines in the phase diagram cross between the $L_3 = L_3 + L_2$ mixtures of liquids [26, 27].

Expected by-products (Se, CdSe, ZnI_2, ZnI_2–CdI_2, SnI_4)

Elemental Se revealed weak Raman peaks at 92–93, 120, and 140 cm^{-1}, which are characteristic of glassy Se, and peaks at 233 and 237 cm^{-1} belong to tetragonal Se [29, 30]. The DSC heating curve of 0.04 g Se in a degassed and sealed ampoule showed a DSC peak at 130–137 °C (Fig. 2c). In [31], this thermal effect was attributed to the phase transition of rhombohedral Se_6 rings into the trigonal spiral chains of Se_n. We determined the heat of this phase transition to be – 2.0 ± 0.2 J, corresponding to an enthalpy value of – 3.8 ± 0.4 kJ mol^{-1}. In Fig. 2c, the melting of Se was detected at 221 °C and 2.8 ± 0.3 J, corresponding to a melting enthalpy of 5.4 ± 0.5 kJ mol^{-1}. This value is slightly lower than that in the literature (6.2 kJ mol^{-1}) [14]. Evaporation at 685 °C, as given in [14], was not seen, but it seems that Se evaporated after melting. The evaporation

Author's personal copy

process continued until reaching 476 °C (7.5 ± 0.8 J or 14.5 ± 1.5 kJ mol $^{-1}$).

The *CdSe* Raman spectra had additional peaks at 198 and 207.5 cm^{-1} and characteristic peaks at 168, 201, and 320 cm^{-1} [32].

Dried ZnI_2 exhibited Raman peaks at 70, 77, 119, 127, and 188 cm^{-1}, while non-dried ZnI_2 had additional peaks at 62, 88, 141, 153, 161, and 178 cm^{-1}. The XRD analysis confirmed the presence of a $ZnCO_3$ compound in the non-dried ZnI_2.

CdI_2–ZnI_2 *mixture* (molar ratio 1:1) started to melt at 358 °C (with a peak at 367 °C). This was followed by smaller peaks at 381 and 393 °C (see Fig. 3), probably due to the melting of some CdI_2. The heat value of 1.8 ± 0.2 J (for the mixtures of 0.05 g CdI_2 and 0.04 g ZnI_2) corresponds to the melting enthalpy of the formed eutectic mixture (6.9 ± 0.7 kJ mol^{-1}).

SnI_4 showed Raman peaks at 147, 207, and 215 cm^{-1}. The positions of the most intensive Raman peaks differ only slightly from those published in [33] (149 and 216 cm^{-1}).

Flux material (CdI_2)

Because the salt (flux) was processed at room temperature (RT) in air, its reactions with the gaseous substances present in air (O_2, H_2O, NO_2, SO_2, CO_2) should be considered. Computations performed using the HSC6 software [14] revealed that the ΔG value of reaction (2) was negative: ΔG is − 56.4 kJ mol^{-1} at 23 °C (Fig. 4a). CdI_2 does not react directly with water vapour, and the direct formation of $Cd(OH)_2$ is not possible (i.e., its ΔG value is positive). However, $Cd(OH)_2$ can be produced by reaction (3) if CdO is formed in reaction (2), as at RT $\Delta G = -15.8$ kJ mol^{-1} [14] for reaction (3). CdO does not react with NO_2 (i.e., its ΔG value is positive), but it can react with SO_2 and CO_2 [14]. It should be emphasized that the concentrations of SO_2 and CO_2 in air are relatively low.

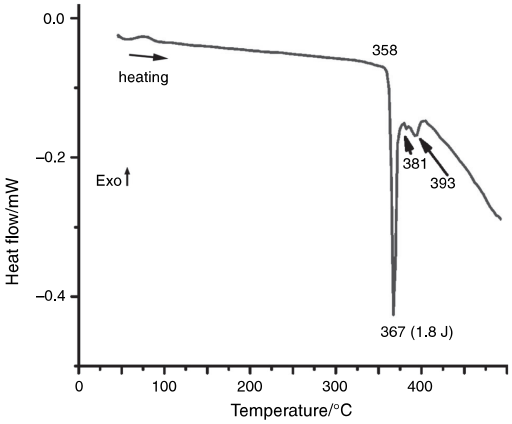

Fig. 3 DSC of CdI_2–ZnI_2 mixture

$$2CdI_2(s) + O_2(g) \rightarrow 2CdO(s) + 2I_2(s) \quad (2)$$

$$CdO(s) + H_2O(g) \leftrightarrow Cd(OH)_2(s) \quad (3)$$

The experimentally measured Raman spectra of CdI_2 showed peaks at 111 cm^{-1}; however, in [34], characteristic peaks were reported at 16, 50 and 114 cm^{-1}. We also detected a wide band at 320 cm^{-1}. The endothermic melting of CdI_2 (degassed and sealed in a closed ampoule) is seen at 385 °C in the DTA heating curve (red) in Fig. 4b. In the cooling curve (blue), exothermic solidification at 366 °C can be detected. It was experimentally determined that the melting/solidification of 0.125 g CdI_2 gave a signal with an average value of 7.1 ± 0.7 J (calculated from two heating/cooling runs). As most of the studied processes took place in the molten phase of CdI_2, this value was thus used for enthalpy evaluations in the following studies of the other CdI_2-precursor mixtures. The CdI_2 boiling point at 742 °C [14] was not seen in the DTA curves, probably due to slight overpressure in the closed ampoules. Because the room temperature XRD investigations of CdI_2 (Fig. 5a) did not show the presence of any CdO, I_2, and $Cd(OH)_2$, we can conclude that reactions (2, 3) did not occur practically. Since $Cd(OH)_2$ decomposes at 128 °C [14] (Fig. 4a) and the emission of H_2O could be detected, we took TG-MS measurements of CdI_2 (see Fig. 4c). During heating at a rate of 5 °C per minute up to 300 °C, the mass loss of 0.2% of non-dried CdI_2 was detected (shown in Fig. 4c). This loss had already started at 29 °C and continued until the end of the experiment at 308 °C. No presence of H_2O by MS was found. The low rate of mass loss at nearly room temperature leads to the hypothesis that iodine could have been released. I_2 may condense before reaching the mass spectrometer and may therefore not be detected. There are two possible explanations for the presence of I_2 in CdI_2–I_2 as a reagent is used for CdI_2 production and I_2 could form due to the photodecomposition of CdI_2 [19]. However, the melting effects of Cd and/or I_2 were not found in the DTA curves. Most likely, I_2 sublimates very quickly during sample degassing, and photodecomposition does not release elemental Cd.

CdI_2–ZnSe mixture

The melting temperature of CdI_2 in the mixture with ZnSe is four degrees lower (at 381 °C) in Fig. 6a than it is in Fig. 4b. This implies that ZnSe dissolves in molten CdI_2.

Author's personal copy

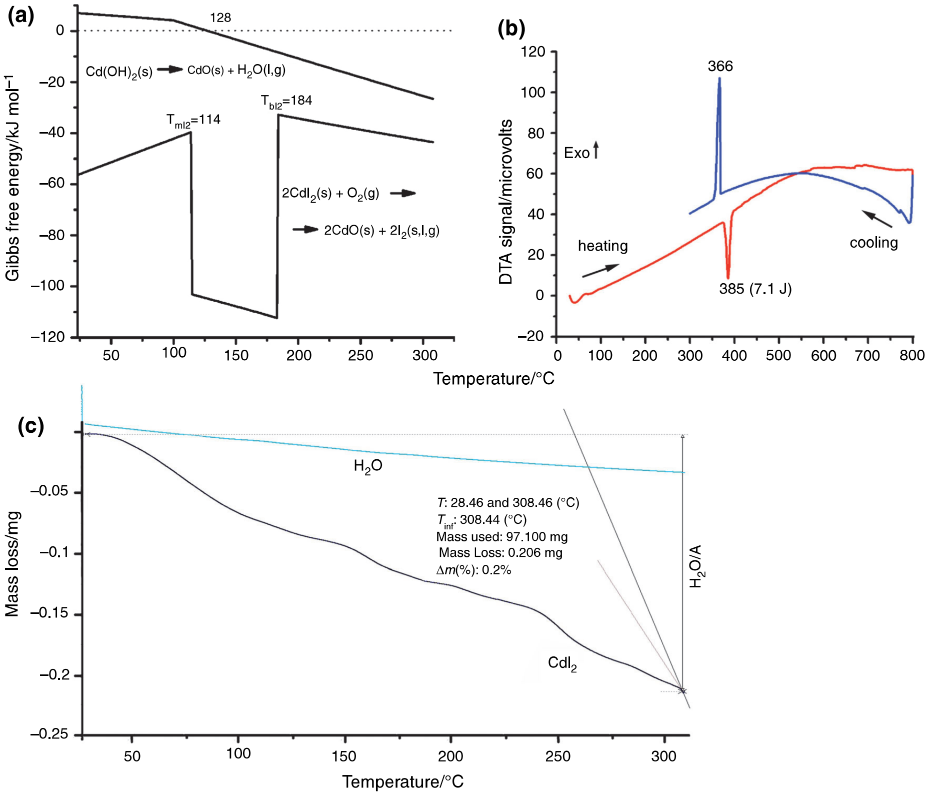

Fig. 4 **a** Reactions (2, 3) modulated according to HSC6 [14]; **b** DTA of CdI_2; **c** TG of CdI_2

The endothermic melting effect in the CdI_2–ZnSe mixture (1.9 ± 0.2 J) seems to be partly covered by an exothermic effect of some simultaneous process, as the melting of the same amount of CdI_2 was accompanied by a signal of 7.1 ± 0.7 J (Fig. 4b). As we see an endothermic effect of 1.9 J, the compensated part of the CdI_2 melting should be 7.1 J − 1.9 J = 5.2 ± 0.5 J. The exothermic effect in the heating (red) curve at 385 °C can then be calculated: (− 2.3) J + (− 5.2) J = − 7.5 ± 0.8 J. To understand this exothermic effect, the XRD pattern of the single-crystalline sample that annealed at 740 °C was analysed. XRD analysis confirmed that relatively high concentrations of $Zn_{1-x}Cd_xSe$ and a small concentration of CdSe had been formed. Visually, the colour of the external surface of this sample was inhomogeneous, exhibiting contrasts ranging from black to red and even orange. EDX analysis revealed that the orange area consisted of 31.2 at.% Zn, 48.9 at.% Se, and 17.5 at.% Cd, suggesting the presence of a $Zn_{1-x}Cd_xSe$ phase, as also determined by XRD. The black area surrounding the orange part consisted of 51.4 at.% Cd, 29.7 at.% Se, and 18.9 at.% I. However, the ΔG value of the straight exchange reaction between ZnSe and CdI_2 to form CdSe and ZnI_2 is positive. Most likely, after the formation of liquid CdI_2, some ZnSe dissolved in liquid CdI_2. $Zn_{1-x}Cd_xSe$ then formed in the molten phase. The precipitation from the molten phase is confirmed by the formation of leaf- and flower-like CdSe crystals (Fig. 7a, b). Therefore, the formed compounds should be $Zn_{1-x}Cd_xSe$ and $Zn_xCd_{1-x}I_2$. The dried precipitate of washing water was analysed; it consisted of 12.3 at.% Zn, 12.8 at.% Cd, and 74.9 at.% I, reflecting a ZnI_2–CdI_2 mixture. The formation of $Zn_{1-x}Cd_xSe$ in a mixture of liquid CdI_2 with ZnSe can now be explained after studying the properties of the liquid phase of CdI_2. It is well known that many salts in their molten phase are ionic liquids, but not CdI_2. The melt of MX_2 (M = Zn, Cd, Hg and X = Cl, Br, I) has an extremely low ionic conductivity [35]. Furthermore, MX_2 salts retain their solid phase structure even in the liquid phase, in which the small metal M^{2+} ions occupy tetrahedrally coordinated sites in a closely packed anion structure, with strong intermediate-range ordering [36, 37]. Additionally, measurements of the scattering of thermal

Author's personal copy

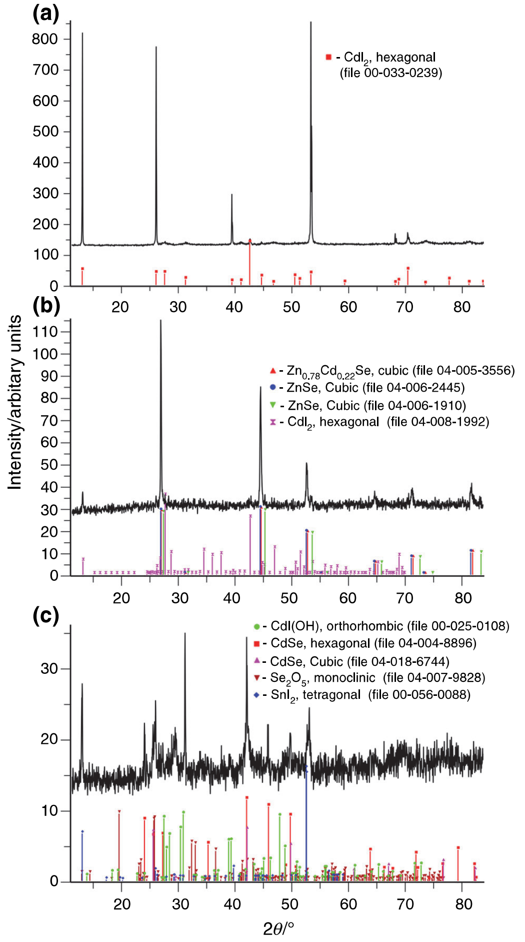

Fig. 5 Measured XRD patterns of: **a** CdI_2, **b** opened DTA sample of CdI_2-ZnSe and **c** CdI_2-SnSe. For phase detection, the files from database ICDD-PDF-4 + 2016 were used

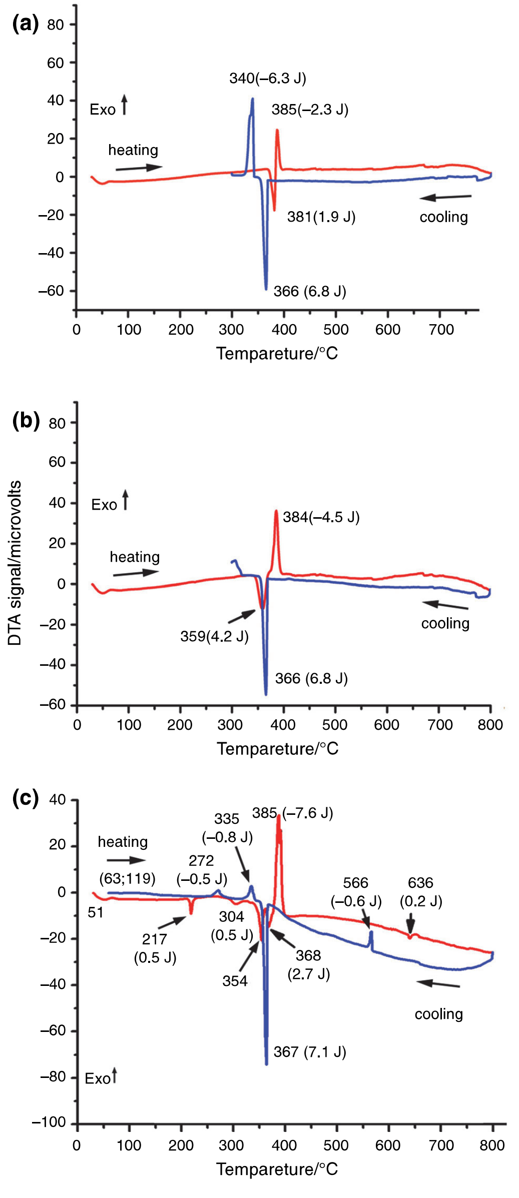

Fig. 6 DTA curves of mixtures: **a** CdI_2–ZnSe, **b** CdI_2–SnSe, **c** CdI_2–CuSe (heating—red; cooling—blue). (Color figure online)

neutrons in natural samples of molten $ZnCl_2$, $ZnBr_2$ and ZnI_2 confirmed the above given structural model of $[ZnI_4]^{2-}$ with strong intermediate-range ordering [38, 39]. According to Chikanov [40], CdI_2–ZnI_2 mixtures form a continuous row of solid solutions. Therefore, we propose that ZnSe dissolves in liquid CdI_2 and that the bonds of solid ZnSe will be broken and dissolved; Zn^{2+} can be displaced by Cd^{2+} ions in the closely packed anion structure, as indicated in reactions (4–9). We found that the enthalpy of reaction (9) is -18.8 ± 1.9 kJ mol^{-1}. In summary, we conclude that the observed exothermic effect in the DTA heating curve can be attributed to the chemical dissolution of ZnSe in molten CdI_2, resulting in the formation of $Zn_{1-x}Cd_xSe$ and $Zn_xCd_{1-x}I_2$.

As seen from the DTA curve of the CdI_2–ZnI_2 mixture (Fig. 3), the presence of ZnI_2 in CdI_2 strongly reduces the melting temperature. During cooling, the precipitation of the $Zn_{1-x}Cd_xSe$ solid solution from the melt occurs at 366 °C, and the $Zn_{1-x}Cd_xI_2$ liquid solution freezes at 340 °C. This is a much lower temperature than that of the

Author's personal copy

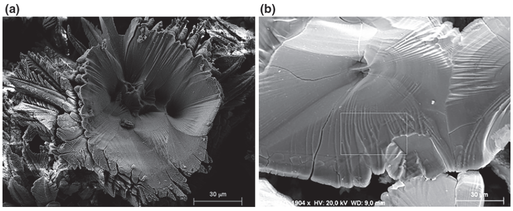

Fig. 7 SEM images of CdI_2–ZnSe sample (heated at 740 °C for 1 week and washed)

CdI_2–ZnI_2 mixture (Fig. 3). Since the CdI_2 solidification should be − 7.1 J (Fig. 4b), the effect in the cooling (blue) curve at 340 °C is covered by − 7.1 J − (− 6.3 J) = − 0.8 J, and the endothermic effect of cooling at 366 °C is 6.8 J + 0.8 J = 7.6 ± 0.8 J, which is the same as the exothermic effect of heating (− 7.5 ± 0.8 J), taking the error bars into account. An analogy in the second DTA cycle was found. Opening the ampoule used for DTA and performing XRD analysis revealed that in addition to the $Zn_{1-x}Cd_xSe$ ($Zn_{0.78}Cd_{0.22}Se$) phase, precipitated ZnSe and CdI_2 (no separate CdSe) were also found (see Fig. 5b). Those differences in comparison with the sample that annealed at 740 °C may be ascribed to different cooling regimes and different contact areas of liquid–solid phases. In the case of single-crystalline ZnSe, the solid–liquid contact area (which is equal to the surface area of the crystal) is much smaller compared to the surface of the ZnSe powder used for the DTA sample. The dissolution process can be described by the following reactions (4–9):

$$\text{Melting of CdI}_2\text{: } 2\mathrm{CdI_2(l)} \rightarrow [\mathrm{CdI_4}]^{2-}(\mathrm{l}) + \mathrm{Cd^{2+}(l)} \tag{4}$$

$$\text{ZnSe dissolution in CdI}_2\text{: } \mathrm{ZnSe(s)} \rightarrow \mathrm{Zn^{2+}(l)} + \mathrm{Se^{2-}(l)} \tag{5}$$

$$\mathrm{Zn^{2+}(l)} + [\mathrm{CdI_4}]^{2-}(\mathrm{l}) \rightarrow [\mathrm{ZnI_4}]^{2-}(\mathrm{l}) + \mathrm{Cd^{2+}(l)} \tag{6}$$

$$\text{Solidification: } \mathrm{Se^{2-}(l)} + (x)\mathrm{Cd^{2+}(l)} + (1-x)\mathrm{Zn^{2+}(l)} \rightarrow \mathrm{Zn_{1-x}Cd_xSe(s)} \tag{7}$$

$$(x)[\mathrm{ZnI_4}]^{2-}(\mathrm{l}) + (x)\mathrm{Zn^{2+}(l)} + (1-x)[\mathrm{CdI_4}]^{2-}(\mathrm{l}) + (1-x)\mathrm{Cd^{2+}(l)} \rightarrow 2\mathrm{Zn_xCd_{1-x}I_2(s)} \tag{8}$$

$$\mathrm{ZnSe(s)} + \mathrm{CdI_2(l)} \rightarrow \mathrm{Zn_{1-x}Cd_xSe(s)} + \mathrm{Zn_xCd_{1-x}I_2(s,l)} \tag{9}$$

CdI_2–SnSe mixture

The DTA curve of the CdI_2–SnSe mixture shows an endothermic effect of 4.2 ± 0.4 J in the heating curve (red) at 359 °C (Fig. 6b). This value of 4.2 J is lower than the value of CdI_2 melting in Fig. 4b (7.1 J), which indicates that the following exothermic peak at 384 °C compensates for the melting heat of CdI_2 by 4.2–7.1 = − 2.9 J. This exothermic process yields a value of − 2.9 − 4.5 = − 7.4 ± 0.7 J. The XRD analysis of the opened DTA sample (Fig. 5c) shows the following compounds: CdIOH, CdSe, Se_2O_5, and SnI_2. The appearance of CdIOH and Se_2O_5 in the XRD pattern can be attributed to the oxide groups detected on the surface of the SnSe powder precursor by XPS (Fig. 1). The $Sn(OH)_2$ structure is not known and cannot be detected by XRD; it most likely formed from SnO_2. Therefore, we propose the following reaction (10), which is similar to that described in [41], where the formation of the CdIOH solid solution was found to be possible from CdI_2 and $Cd(OH)_2$ at 298 K (25 °C), with a formation enthalpy of $\Delta H_{f298} = -375.7$ kJ mol^{-1}.

$$2\mathrm{CdI_2(s)} + \mathrm{Sn(OH)_2(s)} \rightarrow 2\mathrm{CdIOH(s)} + \mathrm{SnI_2(s,l,g)} \tag{10}$$

Next, we consider the processes occurring during the melting of CdI_2. The melting of CdI_2 is emphasized in Fig. 8a by a vertical arrow, as these reactions occur more intensely in liquid CdI_2, and the gaseous products leave the mixture and can no longer interfere. According to the calculations done using the HSC6 software [14] (Fig. 8a), SnSe can react with CdI_2 at temperatures higher than 348 °C by reaction (11), forming liquid SnI_2 and solid CdSe. (These phases were also found in the XRD analysis, see Fig. 5c.) The formation of SnI_2 explains why the CdI_2 melting temperature was lowered to 359 °C (compare Fig. 6b to 4b). The gaseous phase of CdI_2 is hereafter excluded because the solid phase can only be in direct contact with other solid or liquid phases. $SnSe_2$ was also detected by Raman spectroscopy in the SnSe precursor. However, our calculations yielded positive ΔG values for the reaction between $SnSe_2$ and CdI_2 for the formation of SnI_2, CdSe, and Se in the experimentally applied temperature region. However, the formation of solid CdSe and gaseous SnI_4 in reaction (12) is possible at temperatures higher than 368 °C (Fig. 8a) [14]. Figure 8b demonstrates that SnI_4 does not decompose to SnI_2 and I_2 due to the positive ΔG values in the temperature region between RT and 800 °C.

$$\mathrm{SnSe(s)} + \mathrm{CdI_2(s,l)} \leftrightarrow \mathrm{SnI_2(l,g)} + \mathrm{CdSe(s)} \tag{11}$$

$$\mathrm{SnSe_2(s)} + 2\mathrm{CdI_2(s,l)} \leftrightarrow \mathrm{SnI_4(g)} + 2\mathrm{CdSe(s)} \tag{12}$$

The negative ΔG values of reaction (13) exclude the decomposition of $SnSe_2$ to SnSe and Se up to the melting point of $SnSe_2$ (Fig. 8c). Unfortunately, the HSC6 software does not allow us to perform calculations with the $SnSe_2$ liquid phase. For comparison, the SnS_2 decomposition reactions are shown in Fig. 8c. It can be seen that $SnSe_2$ is

Author's personal copy

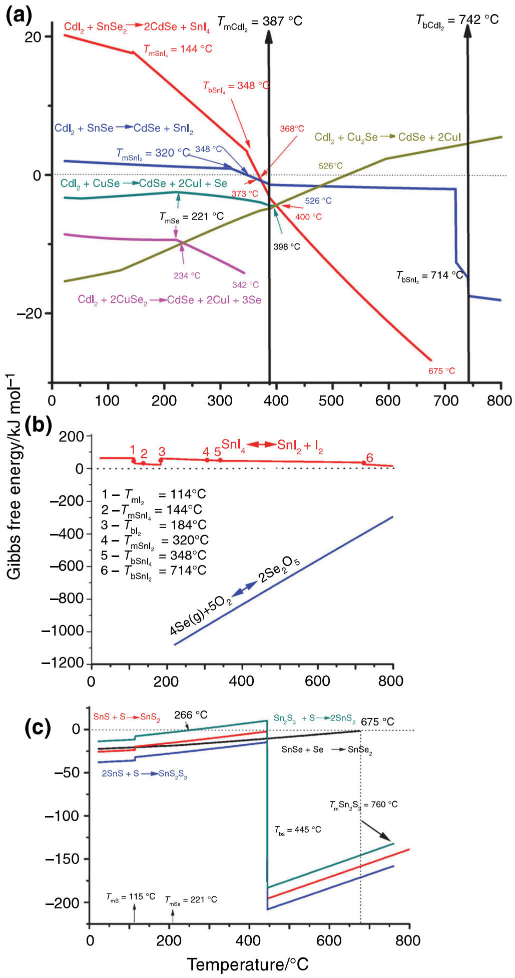

Fig. 8 Results of HSC6 calculations [14] for the considered reactions

more stable than SnS_2, which decomposes to Sn_2S_3 and liquid S in the temperature interval of 266–445 °C [14]. This explains the higher stability of CZTSe compared to that of CZTS. Se released from molten $SnSe_2$ at 675 °C [42] can react with SnO_2 according to reaction (14), with $\Delta G = -313.80$ kJ mol^{-1}. However, the release of Se is not seen in DTA (Fig. 6b), despite the fact that the presence of the $SnSe_2$ phase was confirmed during the analysis of the SnSe precursor, when larger amounts were analysed. Since the evaporation of Se in a closed ampoule is possible at temperatures lower than $T_{bSe} = 685$ °C (see the chapter of results for elemental Se), Se_2O_5 can thus form through the gas phase reaction (15) [14] at temperatures higher than 675 °C (Fig. 8b).

$$\mathrm{SnSe(s) + Se(s,l) \leftrightarrow SnSe_2(s)} \tag{13}$$

$$\mathrm{SnO_2(s) + Se(l) \leftrightarrow SnSe(s) + O_2(g)} \tag{14}$$

$$\mathrm{4Se(g) + 5O_2(g) \rightarrow 2Se_2O_5(s)} \tag{15}$$

To investigate the exothermic process seen in the DTA heating curve at 384 °C (Fig. 6b) in more detail, a single-crystalline piece of SnSe was heated in CdI_2 at 740 °C for 1 week. We found that the initial mass of the SnSe sample increased from 0.229 to 0.8971 g, as determined after separating it from soluble phases by washing it with water. Detailed EDX investigations revealed that its composition varied in different places. In one studied place, it comprised 28.4 at.% Cd, 11.1 at.% Sn, and 60.5 at.% I, suggesting a $Sn_{1-x}Cd_{2x}I_4$ phase. In another place, its composition of 30.0 at.% Cd and 57.9 at.% I could be attributed to a CdI_2 phase. The evaporated and dried residue of washing water contained 94.8 at.% Sn and 5.2 at.% Cd. Iodine may evaporate during the drying process. However, as described in [40], in a system of cadmium and tin iodides, degenerated eutectic forms contain less than 5 mol% of both components. The CdI_2–SnI_2 system has also been described as a system with limited solid solubilities, *e.g.*, the solubility of SnI_2 is smaller than 20 mol%. This is consistent with our findings. The $Sn_{1-x}Cd_xI_2$ phase was observed to grow into a single SnSe crystal, leading to an increase in the mass of the initial SnSe crystal. We thus propose the following reactions (16, 17):

$$(1-x)\mathrm{SnI_2(s,l)} + x\mathrm{CdI_2(s,l)} \rightarrow \mathrm{Sn_{1-x}Cd_xI_2(s)} \tag{16}$$

$$(1-x)\mathrm{SnI_4(s,l)} + 2x\mathrm{CdI_2(s)} \rightarrow \mathrm{Sn_{1-x}Cd_{2x}I_4(s)} \tag{17}$$

The reversible process in the DTA curve at 366 °C is similar to that observed in the CdI_2–ZnSe mixture. The crystallization of the CdI_2–SnSe mixture was not detected due to the fact that the experiment was terminated at 300 °C. SnI_4 might not be detected in the sample of the opened DTA ampoule by XRD analysis because it evaporates at 348 °C. The condensation of this phase was visually observed as orange deposits present on the wall of the ampoule.

CdI_2–CuSe mixture

In the DTA curve of this mixture (Fig. 6c), the readout at 51 °C is also seen in the DTA curve of the precursor CuSe (Fig. 2a). An endothermic peak at 217 °C (0.5 ± 0.1 J), corresponding to the melting of Se [14], is not seen in the pure CuSe precursor. The CuSe precursor was tested by XRD and Raman analysis, and no free Se was found. These data suggest that the appearance of free Se is caused by the addition of CdI_2. If Se is released in the system, $CuSe_2$ could be formed by reaction (18). The HSC6 software [14] yields negative ΔG values for reaction (18) up to 168 °C;

Author's personal copy

however, the phase diagram shows $CuSe_2$ stability up to 322 °C [26, 27].

$$CuSe(s) + Se(s,l) \leftrightarrow CuSe_2(s) \qquad (18)$$

The analysis of the XRD pattern (Fig. 9) of the CdI_2–CuSe sample, which was quenched at 400 °C, reveals that the following new compounds were formed: Se, $CdCu_2$, and CuI (in small concentrations) and $Cu_{2-x}Se$ ($Cu_{1.75}Se$, $Cu_{1.5}Se$) and CdSe (in relatively high concentrations). Unreacted $Cu_{1.75}Se$ and $Cu_{1.5}Se$ were found, because the CuSe–CdI_2 mixture was applied with a molar ratio of 1.85:1.65. Raman spectroscopy (Fig. 10) confirmed the presence of peaks at 122 cm^{-1}, corresponding to CuI; wide peaks at 168, 198, and 205 cm^{-1}, corresponding to CdSe [32]; and peaks at 93, 141 and 241 cm^{-1}, corresponding to Se–Se stretching [43].

The ΔG calculations reveal that CuSe and Cu_2Se can already react with CdI_2 at RT (reactions 19, 20), while $CuSe_2$ starts reacting in reaction (21) at 73 °C (Fig. 8) and

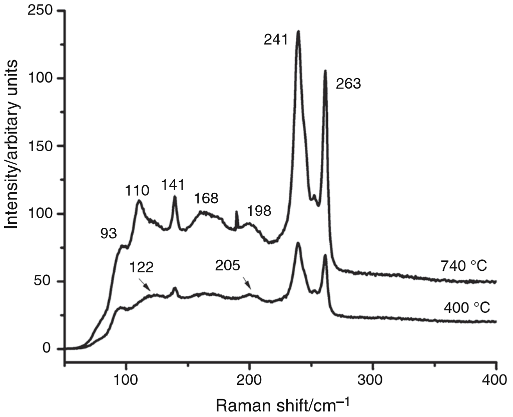

Fig. 10 Raman spectra of CdI_2–CuSe quenched at 400 °C and 740 °C

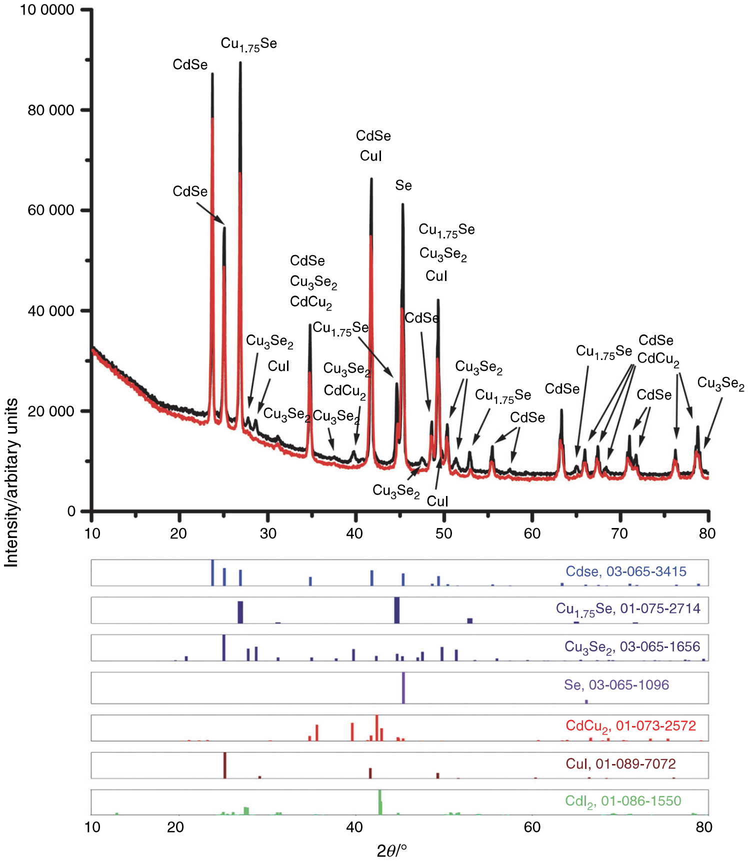

Fig. 9 XRD of CdI_2–CuSe quenched at 400 °C (black line 1) and at 740 °C (red line 2). For phase detection, the files from database JCDPS-2009 were used. (Color figure online)

Author's personal copy

continues until it is transformed to CuSe and further transformed to Cu_2Se (see graphical data from [14] in Fig. 8a). Reaction (20) is only possible between Cu_2Se and liquid CdI_2 (and it is reversible) at 526 °C, according to ΔG calculations. However, no reversible process is seen in the DTA curve at 526 °C, and CuI was only found at low concentrations at 400 °C, whereas CdSe occurs in high concentrations. This indicates that the formed CuI should be consumed by another process. Our considerations are in good agreement with the results of [44]. The authors of [44] formed the Cu_2CdI_4 phase at 200 °C in the CuI–CdI_2 system with a molar ratio of CuI–CdI_2 = 2:1 by reaction (22). This Cu_2CdI_4 phase showed irregular nanostructures and aggregates in SEM images. In [45], Cu_2CdI_4 was synthesized by the solid-state reaction (22) at 300 °C in 48 h. The XRD [44] and Raman peaks [45] of Cu_2CdI_4 are similar to those of CuI and CdI_2; therefore, the Raman and XRD analyses could not lead to the determination of the Cu_2CdI_4 phase. The CuI–CdI_2 system exhibits three broad regions of solid solutions based on the α-, β- and γ-CuI modifications. CuI and CdI_2 form a complete series of solid solutions with a minimum at the liquidus at 90 mass% CdI_2 at 350 °C [46]. An endothermic peak occurs in the DTA heating curve at 354 °C (Fig. 6c), followed by the phase transition of γ-CuI (cubic) to β-CuI (hexagonal) at 368 °C during the melting of the mixture. The total signal value of 2.7 ± 0.3 J corresponds to these processes. As found in [46], these phase transitions can vary from 414 to 260 °C, depending on the CdI_2 content. The other phase transition of β-CuI (hexagonal) to α-CuI (cubic) at 407 °C [46] seems to be hidden by the dissolution effect at 385 °C (− 7.6 ± 0.7 J), and only a weak peak splitting is seen. The solubility of CuI in CdI_2 is limited (6 mol%), while all modifications of CuI are dissolvable in CdI_2. The γ-CuI phase has a maximum solubility of 25 mol% CdI_2 at 281 °C and transforms to solid solution with the β-phase at 382 °C. The melting heat of CdI_2 (Fig. 4b) and the heat of CuSe transformation to Cu_2Se (Fig. 2a) are covered by a value of $2.7 - 7.1 - 8.2 = -12.6 \pm 1.3$ J. The exothermic peak at 385 °C then leads to the total effect having a value of $-12.6 - 7.6 = -20.2 \pm 2.0$ J. Most likely, dissolution also occurs, as these processes cannot be separated.

$$2CuSe(s) + CdI_2(s) \rightarrow 2CuI(s) + CdSe(s) + Se(s,l) \tag{19}$$

$$Cu_2Se(s) + CdI_2(s,l) \leftrightarrow 2CuI(s,l) + CdSe(s) \tag{20}$$

$$2CuSe_2(s) + CdI_2(s) \rightarrow 2CuI(s) + CdSe(s) + 3Se(s,l) \tag{21}$$

$$2CuI(s,l) + CdI_2(s,l) \leftrightarrow Cu_2CdI_4(s,l) \tag{22}$$

As the XRD analyses revealed the formation of Cu_2Cd in the sample quenched at 400 °C and we did not find elemental Cu and Cd in the binary precursor (CuSe) or in the CdI_2 flux, it was assumed that ε-Cu_3Cd_{10} formed first by reaction (23) but that the formed I_2 and SnI_4 evaporated quickly and did not react with any compounds. In principle, liquid SnI_4 can react with Cu_2Se ($\Delta G = -33.48$ kJ mol^{-1}) at 217 °C by reaction (24); however, at 400 °C, the ΔG of reaction (12) (in the previous chapter) is also negative, and $SnSe_2$ can react with CdI_2 (Fig. 8a). This chain of reactions will then result in gaseous SnI_4 and CdSe as products. SnI_4 was not detected in the sample because it had probably condensed at the top of the ampoule (i.e., in the lowest-temperature region).

$$Cu_3Sn(s) + 10CdI_2(s) \rightarrow \varepsilon - Cu_3Cd_{10}(s) + SnI_4(g) + 8I_2(g) \tag{23}$$

$$SnI_4(l) + 2Cu_2Se(s) \rightarrow SnSe_2(s) + 4CuI(s) \tag{24}$$

As we could not attribute the strong signal of 0.5 ± 0.1 J in the DTA heating curve at 304 °C (Fig. 6c) to other processes, we attribute it to the eutectic melting of Cd [according to reaction (25)], which was found for 97.9 at.% Cd at 305 °C in [47]. In [48], it was reported to occur at 317 °C. The melting effect of Cu_3Cd_{10} in accordance with reaction (26) at 397 °C [47] was not detected in the DTA heating curve, and we assume that it is covered by the exothermic effect at 385 °C.

$$L \leftrightarrow \varepsilon\text{-}Cu_3Cd_{10}(s) + Cd(l) \tag{25}$$

$$2\varepsilon\text{-}Cu_3Cd_{10}(s) \rightarrow 3Cu_2Cd(l) + 17Cd(l) \tag{26}$$

It appears that Cd formed by reactions (25, 26) does not react with Cu–selenides, as no elemental Cu was found and reaction (27) has a more negative ΔG. In this system, Se that was mostly released from reaction (1) and reactions with Cd can result in the formation of CdSe (27) at 304 °C ($\Delta G = -139.26$ kJ mol^{-1}).

$$Cd(s,l) + Se(l) \rightarrow CdSe(s) \tag{27}$$

To investigate the next endothermic peak at 636 °C (0.2 J), a sample of the CdI_2–CuSe mixture was prepared and heated at 740 °C for 4 h. The phases found by XRD (Fig. 9) were: Se (at low concentrations), CdI_2, $Cu_{1.5}Se$, and CdSe (at relatively high concentrations). The Raman spectrum (Fig. 10) confirms these phases: wide signals at 168, 198 cm^{-1} can be attributed to CdSe [32]; signals at 93, 141 and 241 cm^{-1} correspond to Se–Se stretching [29, 30, 43]; and a signal at 110 cm^{-1} corresponds to CdI_2 [34]. The most obvious change is that the CuI phase has disappeared, but the concentrations of CdI_2 and $Cu_{2-x}Se$ have increased. This trend can be explained by the reversible reaction of (20). Cu_2Cd is no longer present, probably due to reaction (29) at 639 °C forming $Cu_{2-x}Se$ and CdSe.

Author's personal copy

Similar reactions were reported in [49] for Cu–Zn and Cu–Sn alloys. Additionally, the undissolved β-$Cu_{2-x}Se$ melts at 636 °C (in which the total signal of these processes is 0.2 J) in the Cu–Se phase diagram is similar to point E (Fig. 2b). We were not able to draw significant conclusions from the EDX analyses of the composition of the CuSe single-crystalline sample, which was heated to 740 °C in CdI_2, quenched, and then washed.

$$\mathrm{CdCu}_{2-x}(\mathrm{l}) + 2Se(\mathrm{l}) \leftrightarrow \mathrm{Cu}_{2-x}\mathrm{Se(s)} + 2\mathrm{CdSe(s)} \quad (28)$$

In the cooling curve, the thermal effect at 566 °C corresponds to point L (Fig. 2b) in the phase diagram [26, 27]; this occurs as a signal of − 0.6 ± 0.1 J, which is less intense than that in the CuSe DTA curve, as some of the Cu_2Se reacted with CdI_2 to form CuI. An endothermic peak at 367 °C corresponds to a number of reversible processes, detected as a DTA signal of 7.11 ± 0.7 J. It is important to keep in mind that the thermal effect of CdI_2 solidification is covered. Its value cannot be determined because some of the CdI_2 participated in reactions. Free Se appears to be available in the system, and the peak at 335 °C (− 0.8 ± 0.1 J) in the cooling curve corresponds to the precipitation of $CuSe_2$ from the melt according to (18), as reported in [26, 27] at 332 °C. Using the enthalpy value of reaction (18), which was experimentally determined in [28] as − 12.1 kJ mol^{-1}, we can calculate the number of involved moles from the thermal effect of − 0.8 ± 0.1 J to be 4.2×10^{-5} mol. The peak at 272 °C (− 0.5 J) can be attributed to point I in the Cu–Se phase diagram [26, 27] in Fig. 2b, or the formation of the solid solution of β-CuI with CdI_2 by cooling, as reported in [46] at 271 °C. Since we observed free Se in this system after cooling, we can conclude that reaction (29) does not occur and that gaseous CdI_2 practically does not form in closed ampoules.

$$\mathrm{CdI_2(g)} + \mathrm{Se(g)} \rightarrow \mathrm{CdSe(s)} + \mathrm{I_2(g)} \quad (29)$$

Conclusions

As a first step to fully understand the chemical processes occurring during the synthesis–growth of $Cu_2ZnSnSe_4$ in molten CdI_2, we investigated separate mixtures of CdI_2 with individual precursors (ZnSe, SnSe and CuSe) used in the synthesis of $Cu_2ZnSnSe_4$ in closed vacuum ampoules. DTA, XRD, Raman, EDX, and SEM methods were applied.

The analyses showed that in the CdI_2-ZnSe mixture, some ZnSe dissolved in molten CdI_2 by a chemical dissolution reaction process, forming $Zn_{1-x}Cd_xSe$ and $Zn_xCd_{1-x}I_2$ with a process enthalpy of − 18.8 ± 1.9 kJ mol^{-1}. The melting of a CdI_2–ZnI_2 eutectic composition started at 358 °C with an enthalpy value of 6.9 ± 0.7 kJ mol^{-1}. This work also indicated that SnI_2 or SnI_4 was formed by exchange reactions in the mixture of CdI_2–SnSe. The formation of tin iodides may influence the growth process and composition of CZTSe grains, as their solubility in CdI_2 is limited. We recognized that CuSe and Cu_2Se had already begun reacting with CdI_2 at RT, while $CuSe_2$ began forming CuI and CdSe at 73 °C; this reaction is reversible at temperatures higher than 526 °C. The fact that CuI reacts with CdI_2 to form Cu_2CdI_4 was discovered. We also detected CdIOH and Se_2O_5 as secondary phases that formed due to the tin dioxide (or tin hydroxide) introduced by the precursor SnSe compound. The main conclusion of this analysis is that CdI_2 is not a neutral flux material. It reacts with precursor compounds and enables the incorporation of Cd into $Cu_2ZnSnSe_4$ crystals through the formation of CdSe during the actual process of synthesis.

Acknowledgements The authors give their sincere appreciation for the experimental support and apparatus provided for XRD and DTA measurements by the heads of the Department of Mechanical and Industrial Engineering and Laboratory of Inorganic Materials. Prof. J. Krustok, Dr. M. Grossberg and Dr. A. Mere are gratefully acknowledged for their advice and help with experimental measurements. The following projects are acknowledged for their financial support: TAR16016 "Advanced materials and high-technology devices for sustainable energetics, sensorics and nanoelectronics"; IUT19-28 "New materials and technologies for solar energetics."

References

1. Paranthaman MP, Wong-Ng W, Bhattacharya RN. Semiconductor materials for solar photovoltaic cells. Cham: Springer; 2016.
2. Adachi S. Earth-abundant materials for solar cells—Cu_2–II–IV–VI_4 semiconductors. Chichester: Wiley; 2015.
3. Ito K. Copper zinc tin sulfide-based thin-film solar cells. Chichester: Wiley; 2015.
4. Kodigala SR. Thin film solar cells from earth abundant materials—growth and characterization of $Cu_2ZnSn(SSe)_4$ thin films and their solar cells. London: Elsevier; 2013.
5. Lee YS, Gershon T, Gunawan O, Todorov TK, Gokmen T, Virgus Y, Guha S. $Cu_2ZnSnSe_4$ thin-film solar cells by thermal co-evaporation with 11.6% efficiency and improved minority carrier diffusion length. Adv Energy Mater. 2015. https://doi.org/10.1002/aenm.201401372.
6. Brammertz G, Buffière M, Oueslati S, ElAnzeery H, Messaoud KB, Sahayaraj S, Köble C, Meuris M, Poortmans J. Characterization of defects in 9.7% efficient $Cu_2ZnSnSe_4$–CdS–ZnO solar cells. Appl Phys Lett. 2013;103:163904.
7. Leinemann I, Timmo K, Grossberg M, Kaljuvee T, Tõnsuaadu K, Traksmaa R, Altosaar M, Meissner D. Reaction enthalpies of $Cu_2ZnSnSe_4$ synthesis in KI. J Therm Anal Calorim. 2015;119(3):1555–64.
8. Leinemann I, Zhang W, Kaljuvee T, Tõnsuaadu K, Traksmaa R, Raudoja J, Grossberg M, Altosaar M, Meissner D. $Cu_2ZnSnSe_4$ formation and reaction enthalpies in molten NaI starting from binary chalcogenides. J Therm Anal Calorim. 2014;118(2):1313–21.

Author's personal copy

9. Nkwusi G, Leinemann I, Altosaar M. The processes and enthalpies in synthesis of Cu_2ZnSnS_4 in molten CdI_2. IARJSET. 2016;3(5):113–9.
10. Nakamura S, Tsuyoshi M, Takahiro W. Phase stability and electronic structure of in-free photovoltaic materials $Cu_2IISnSe_4$ (II: Zn, Cd, Hg). Jpn J Appl Phys. 2011;50:05FF01.
11. Hergert F, Hock R. Predicted formation reactions for the solid-state syntheses of the semiconductor materials Cu_2SnX_3 and Cu_2ZnSnX_4 (X = S, Se) starting from binary chalcogenides. Thin Solid Films. 2007;515:5953.
12. Brantley SL, Kubicki JD. Kinetics of water-rock interaction. White, Art F. 2008. https://doi.org/10.1007/978-0-387:73563-4.
13. Nkwusi G, Leinemann I, Raudoja J, Mikli V, Kärber E, Altosaar M. Impact of growth-synthesis conditions on $Cu_2Zn_{1-x}Cd_xSnS_4$ monograin material properties. Superlattices Microstruct. 2016;98:400–5.
14. Database of HSC Chemistry Ver. 6.0. Outoukumpu Research Oy. Pori: Finland.
15. Redkin A, Korzun I, Reznitskikh O, Yaroslavtseva T, Zaikov Y, Kumkov S. Heat of fusion of halide salts and their eutectics. J Therm Anal Calorim. 2017. https://doi.org/10.1007/s10973-017-6650-4.
16. Redkin A, Korzun I, Yaroslavtseva T, Reznitskikh O, Zaikov Y. Isobaric heat capacity of molten halide eutectics. J Therm Anal Calorim. 2017;128:621. https://doi.org/10.1007/s10973-016-5869-9.
17. Mishra R, Bharadwaj SR, Kerkar AS, Dharwadkar SR. Vaporization behaviour and thermodynamic stabilities of strontium tellurites, $SrTeO_3$ and $SrTe_2O_5$. J Nucl Mater. 1997;240:236–40.
18. Skudlarski K, Dudek J, Kapala J. Separation of mass spectra of binary salt systems: calculations of mass spectra of pure system components from binary data. J Chem Thermodyn. 1987;19:857–62.
19. Kawasaki M, Lee SJ, Bersohn R. The photodissociation of cadmium iodide. J Chem Phys. 1979;71:1235–40. https://doi.org/10.1063/1.438478.
20. Kazatani K, Mori K, Kawasaki M, Sato H. Photodissociation of cadmium diiodide. Laser Chem. 1987;7:95–107.
21. Kuncewicz-Kupczyk W, Kapała J, Roszak S, Miller M. The thermodynamic properties of the gaseous dimer of CdI_2. J Chem Phys. 1998;108:7743–6. https://doi.org/10.1063/1.476209.
22. Perna G, Lastella M, Ambrico M, Capozzi V. ZnSe films deposited on crystalline GaAs and amorphous quartz substrates by means of pulsed laser ablation technique. Appl Phys. 2006;A83:127–30.
23. Klavina I, Raudoja J, Altosaar M, Mellikov E, Meissner D. CZTSe ($Cu_2ZnSnSe_4$) crystal growth for use in monograin membrane solar cells. CYSENI 2010. Proceeding of the annual conference of young scientists on energy issues. [CD VII-347-VII-353]. Lithuanian Energy Institute, Kaunas. 2010; May 27–28.
24. Smith AJ, Meek PE, Liang WY. Raman scattering studies of SnS_2 and $SnSe_2$. J Phys C Solid State Phys. 1977;10:1321–33.
25. Ishii M, Shibata K, Nozaki H. Anion distributions and phase transitions in $CuS_{1-x}Se_x(x = 0-1)$ studied by Raman spectroscopy. J Solid State Chem. 1993;105:504.
26. Glazov VM, Pashinkin S, Fedorov VA. Phase equilibria in the Cu-Se system. Inorga Mater. 2000;36:641–52.
27. Chakrabarti DJ, Laughlin DE. The Cu–Se system. Bull Alloys Phase Diagr. 1981;2(3):305–15.
28. Heyding RD. The copper/selenium system. Can J Chem. 1966;44(10):1233–6.
29. Poborchii VV, Kolobov AV, Tanaka K. An in situ Raman study of polarization-dependent photocrystallization in amorphous selenium films. Appl Phys Lett. 1998;72:1167–9.
30. Yannopoulos SN, Andrikopoulos KS. Raman scattering study on structural and dynamical features of noncrystalline selenium. J Chem Phys. 2004;121:4747.
31. Minaev VS, Timoshenkov SP, Kalugin VV. Structural and phase transformation in condensed selenium. J Optoelectron Adv Mater. 2005;7(4):17171741.
32. Teredesai PV, Leonard Deepak F, Govindarja A, Sood AK, Rao CNR. A Raman study of CdSe and ZnSe nanostructures. J Nanosci Nanotechnol. 2002;2(5):495–8.
33. Forneris HSR, Tavares Y. Raman spectra and force constant of GeI_4 and SnI_4. J Chem Phys. 1956. https://doi.org/10.1063/1.1743195.
34. Nozawa T, Nakagawa H, Matsumoto H. Memoirs of the Faculty of Engineering Fukui University. 1985;33:1.
35. Gaune-Escard M. From fundamentals to applications. Dordrecht: Kluwer; 2002. https://doi.org/10.1007/978-94-010-0458-9.
36. Donald KJ, Hargittai M, Hoffmann R. Group 12 dihalides: structural predilections from gases to solids. Chem A Eur J. 2009;15:1. https://doi.org/10.1002/chem.200801035.
37. Özen AS, Akdeniz Z, Ruberto R, Pastore G, Tosi MP. The origins of tetrahedral coordination in molten and glassy $ZnCl_2$ and other group-2B metal dihalides. Phys Lett. 2014;A:378:431–3.
38. Triolo R, Narten AH. X-ray diffraction study of molten zinc chloride at 323 °C AIP. J Chem Phys. 1981;4.https://doi.org/10.1063/1.440829.
39. Allen DA, Howe RA, Wood ND, Howells WS. Tetrahedral coordination of Zn ions in molten zinc halides. AIP J Chem Phys. 1991;94:5071. https://doi.org/10.1063/1.460544.
40. Chikanov VN. Reactions in binary iodide systems. Russ J Inorg Chem. 2006;51(7):1132–8.
41. Mohamed WM, Hisham SWB. The thermochemistry of inorganic solids. IV. Enthalpies of formation of compounds of the formula MX_aY_b. J Phys Chem Ref Data. 1987;16(3):467–70.
42. Bletskan DI. Phase equilibrium in binary systems $A^{IV}B^{VI}$. J Ovonic Res. 2005;1(5):61–9.
43. Sarfati JD, Burns GR. Spectrochimica acta part a: molecular spectroscopy. 50:12:November 1X.
44. Ghanbari M, Sabet M, Salavati-Niasari M. Synthesis of different morphologies of Cu_2CdI_4/CuI nanocomposite via simple hydrothermal method. J Mater Sci Mater Electron. 2016;27:11092–101. https://doi.org/10.1007/s10854-016-5226-6.
45. Noorussaba AA. Investigations of nanostructure of a new fast ionic conductor [Cu_2CdI_4:0.xRbI] where (x = 0.1, 0.2 and 0.3 mol wt.%). Int J Recent Eng Res Dev (IJRERD). 02:01:ISSN: 2455-8761, 31–41.
46. Blachnik R, Stöter U. The phase diagrams of mixtures of CuI with ZnI_2, CdI_2, and HgI_2. Thermochim Acta. 1989;143:115–22. https://doi.org/10.1016/0040-6031(89)85048-8.
47. Khairulaev MR, Guseinov AN. Nature of contact melting in copper-cadmium system. Izv Akad Nauk SSSR Neorg Mater. 1984;20(4):599–603.
48. Okamoto H. Cd-Cu (cadmium-copper). Supplemental literature review: section III. JPEDAV. 2013;34:65. https://doi.org/10.1007/s11669-012-0131-z,1547-7037.
49. Schurr R, Hölzing A, Jost S, Hock R, Voβ T, Schulze J, Kirbs A, Ennaoui A, Lux-Steiner M, Weber A, Kötschau I, Schock HW. The crystallization of Cu_2ZnSnS_4 thin film solar cell absorbers from co-electroplated Cu-Zn-Sn precursors. Thin Solid Films. 2009;517:2465–8.

Paper V

Leinemann, I., Pilvet, M., Kaljuvee, T., Traksmaa, R., Altosaar, M. (2018). Reaction pathway to $Cu_2ZnSnSe_4$ in CdI_2 Part 2: Chemical reactions and enthalpies in mixtures of CdI_2-CuSe-SnSe and CdI_2-CuSe-SnSe-ZnSe. *J Therm Anal Calorim, 134*(1), 433-441. doi: 10.1007/s10973-018-7415-4

Reprinted by permission from Springer Nature (December 02, 2018; license number 440841409559): Journal of Thermal Analysis and Calorimetry, Reaction pathway to CZTSe formation in CdI_2. Part 2: Chemical reactions and enthalpies in mixtures of CdI_2-CuSe-SnSe and CdI_2-CuSe-SnSe-ZnSe, Inga Leinemann, Maris Pilvet, Tiit Kaljuvee et al., [c2018], (2018), doi: 10.1007/s10973-018- 7415-4

Author's personal copy

Journal of Thermal Analysis and Calorimetry
https://doi.org/10.1007/s10973-018-7415-4

Reaction pathway to CZTSe formation in CdI_2

Part 2: Chemical reactions and enthalpies in mixtures of CdI_2–CuSe–SnSe and CdI_2–CuSe–SnSe–ZnSe

Inga Leinemann[1] · Maris Pilvet[1] · Tiit Kaljuvee[1] · Rainer Traksmaa[1] · Mare Altosaar[1]

Received: 13 September 2017 / Accepted: 25 May 2018
© Akadémiai Kiadó, Budapest, Hungary 2018

Abstract

The chemical reactions between CuSe, SnSe and ZnSe and their enthalpies in molten CdI_2 in closed vacuum ampoules were investigated. Differential thermal analysis (DTA) was used for the determination of the temperatures of processes occurring in the studied mixtures. X-ray diffraction and Raman spectroscopy were performed to discover the phase changes in the long-term annealed samples at higher than peak temperatures in DTA. The occurring chemical reactions and their enthalpies were derived. The recrystallization of CZTSe in CdI_2 was investigated. The results confirmed the formation of Cu_2SnSe_3, Cu_2SnSe_4, CdSe, $Cu_2CdSnSe_4$, $Cu_2ZnSnSe_4$, and $Zn_{1-x}Cd_xSe$ compounds and solid solutions.

Keywords CdI_2 · $Cu_2ZnSnSe_4$ · Enthalpy of reaction · Monograin powder material

Introduction

$Cu_2ZnSnSe_4$ (CZTSe) is more stable (unlikely to decompose) than Cu_2ZnSnS_4 (CZTS), and it is used as a solar cell absorber material [1–6]. The advantages and principle of the syntheses of both phases in molten salts as flux materials were described in detail in [7, 8]. The experimental results and calculations obtained with the HSC6 programme for reactions with binary precursors in mixtures of CdI_2–ZnSe, CdI_2–SnSe, and CdI_2–CuSe and their flux instabilities were discussed in Part 1 of this paper [9] and in [7, 8].

In the synthesis of $Cu_2ZnSnSe_4$ starting from elemental precursors, it was experimentally determined by Wibowo et al. [10] that the primarily formed γ-CuSe decomposes to β-Cu_2Se and Se. The following reaction of Se with SnSe leads to the formation of $SnSe_2$ and thereafter leads to the formation of the Cu_2SnSe_3 phase. It has been concluded that at temperatures of approximately 400 °C and higher, $Cu_2ZnSnSe_4$ is most likely already the dominant phase [10]. The CZTSe formation reaction has been proposed to proceed according to Eqs. (1, 2) [10]:

$$Cu_2Se\ (s) + SnSe_2(s) \leftrightarrow Cu_2SnSe_3(s) \tag{1}$$

$$Cu_2SnSe_3(s) + ZnSe(s) \leftrightarrow Cu_2ZnSnSe_4(s) \tag{2}$$

Salts such as KI, NaI and CdI_2 have been shown to be suitable flux materials for monograin growth and/or the recrystallization of solar cell absorber materials [7, 8, 11].

In a previous paper [11], we presented the results of the analyses of $Cu_2ZnSnSe_4$ formation in molten CdI_2; however, their enthalpy values were not evaluated. Therefore, the determination of enthalpy is the primary objective of this study. The formation enthalpy of CZTSe from binary compounds in molten KI and NaI was found to be 36 ± 3 kJ mol^{-1} [7, 8]. However, the formation enthalpy value for Cu_2ZnSnS_4 in CdI_2 was found to be much lower, i.e. 8 ± 2 kJ mol^{-1} [12]. The second objective of the present research was to study the recrystallization process of CZTSe powder crystals (pre-synthesized in KI) in CdI_2. The formation of any liquid phase before the melting of the used flux salt in the synthesis growth (or recrystallization) process enables the sintering of crystals and affects the shape and structure of monograins, which is technologically important in the production of monograin powder. The grain growth of the compound CZTS in CdI_2 was

---

✉ Inga Leinemann
ingaklav@inbox.lv

[1] Department of Materials and Environmental Technology, Tallinn University of Technology, Ehitajate tee 5, 19086 Tallinn, Estonia

Published online: 04 June 2018

Author's personal copy

previously investigated in [13]. The mechanism of Cd incorporation during the formation of CZTSe (or CZTS and CZTSSe) crystals in molten CdI_2 will be discussed in the present paper.

Experimental

The CuSe and SnSe precursors used in the present study were self-synthesized from metal shots (purity of 99.8%) and Se shots (4 N purity from the Aldrich company) by heating in vacuum quartz ampoules at 650 and 700 °C, respectively, for 35 h. Polycrystalline ZnSe of 99.0% purity synthesized by the chemical vapour deposition process and provided by the company Crystaltechno Ltd. CdI_2 (Fluka), with trace anions (Br^-, Cl^-, SO_4^{2-}) and cations (Ca^{2+}, Co^{2+}, Cu^{2+}, Fe^{2+}, K^+, Na^+), was used. The compounds were analysed by Raman, XRD, energy-dispersive X-ray spectroscopy (EDX) and scanning electron microscopy (SEM). Additionally, CuSe was analysed by DTA; SnSe was analysed by X-ray photoelectron spectroscopy (XPS), and CdI_2 was analysed by DTA, thermogravimetric analysis (TG) and mass spectrometry (MS). The results of the analyses of the precursor materials were reported in Part 1 of the current paper [9], where we concluded that ZnSe could contain some elemental unreacted Se; SnSe could contain some $SnSe_2$ and SnO_2 on the surfaces of particles; but CuSe was off-stoichiometric in bulk. CuSe was found to consist of $Cu_{0.87}Se$, Cu_3Se_2 and impurities such as Cu_3Sn. The release of Se from CuSe to form $Cu_{2-x}Se$ occurred at 383 °C, which was seen as an endothermic peak on the DTA heating curve.

We simulated (with sufficient accuracy) the chemical reactions and processes between binary precursors, as well as those between binary precursors and possible binary products, using the HSC6 Chemistry software [14]. The graphs (Fig. 1) depicting the temperature dependency of ΔG in the interval of interest were modelled using a temperature step of 1 °C.

We decided to use the DTA in combination with Raman and XRD analyses for the investigations of the "frozen-in" phases of quenched samples because the *in situ* XRD performance may be complicated by the fact that CdI_2 was used in a large amount of melt at a rather low temperature (387 °C) [14] and the formed liquid phase covered the other phases, thus disturbing their determination.

First, the DTA was performed for the mixtures of 0.0544 g CuSe + 0.040796 g SnSe + 0.125 g CdI_2 (with a molar ratio of 1.85:1:1.65) and 0.0544 g CuSe + 0.040796 g SnSe + 0.02979 g ZnSe + 0.125 g CdI_2 (with a molar ratio of 1.85:1:1:1.65) to determine the temperatures of the occurring processes. Fine grinding was performed using a mortar to mix the precursors using 10 times the necessary amounts in compliance with the requirement to achieve the essential accuracy. The DTA was performed on a Thermogravimetric Analyser Labsys 1600, Setaram Instrumentation, Caluire, France. The baseline for the DTA was experimentally recorded under the condition where 2 empty sealed ampoules (as the crucibles) were heated and cooled in an N_2 atmosphere by applying a heating rate of 5 °C and a cooling rate of 10 °C/min in the temperature region from room temperature (RT) to 800 °C. Analogous to Part 1 [9], the heat calibration for the enthalpy evaluation was done for a closed system, selecting the melting and solidification effects of dry CdI_2 (with the molar enthalpy of fusion of 20.71 kJ mol^{-1} at the melting point of 387 °C [14]) as a standard. DTA studies were performed on binary mixtures that were degassed at 100 °C for 2 h and sealed into quartz ampoules, which were adopted for the DTA setup (SETERAM). A 10% error bar was used. The temperatures of the peak-top positions in the DTA curves were determined.

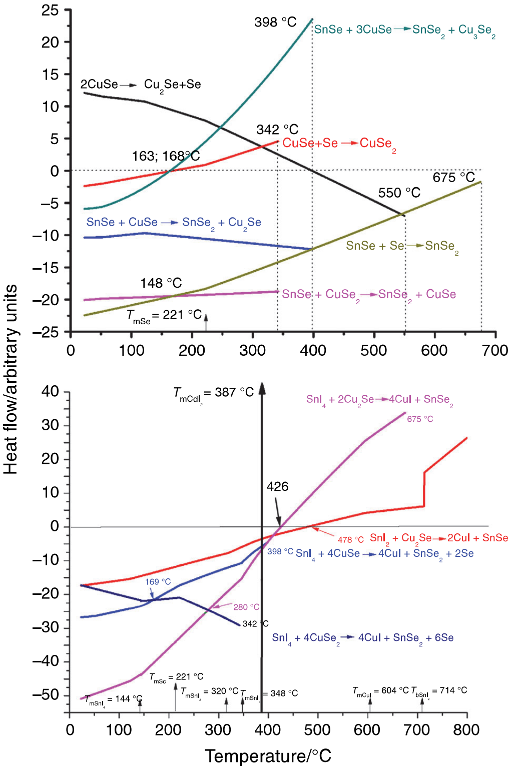

Fig. 1 Results of HSC6 [14] calculations for the considered reactions

The samples used for XRD and Raman analyses were prepared according to the detected DTA effects (separate sample for each), and the "frozen-in" quenching phase compositions were analysed. Identical 1 g samples of the

Author's personal copy

CdI_2–CuSe–SnSe and CdI_2–CuSe–SnSe–ZnSe mixtures were heated for a prolonged time at the temperatures detected by DTA curves and then quenched in water. The samples of the CdI_2–CuSe–SnSe mixture were quenched after heating at 250, 270, 390, and 750 °C; one sample was heated to 800 °C and cooled to 620 °C before being quenched. The mixtures of CdI_2–CuSe–SnSe–ZnSe were heated at 370, 400, 590 and 740 °C and then quenched. Unwashed samples were analysed by Raman and XRD; then, the solid phases that formed in the samples were separated from the soluble parts of the samples by washing with distilled water using an ultrasonic bath for agitation until the washing water became transparent (after repeating washing 7–10 times). The separation of the flux and other soluble phases in water enabled us to record the clear Raman spectra and XRD patterns of solid phases. The Cd contents in CZTSe crystals were analysed by EDX. In this article, we will describe the changes in the phase compositions of the samples during thermal treatment; the other effects of DTA will be attributed to the phase transformations based on the data available in the literature or presented in our previous research published in Part 1 [9].

The RT Raman spectra were recorded using a Horiba LabRam HR800 high-resolution spectrometer (France) equipped with a multichannel CCD detection system in a backscattering configuration. An incident laser light of 532 nm was focused on different 1-μm^2 spots in each studied sample, and the average values of five readings were taken from each sample to obtain an objective phase composition of the sample. XRD measurements were taken using a Bruker D5005 AXS diffractometer (Karlsruhe, Germany), and the ICDD-PDF-4+2016 database was used for phase identification. The chemical compositions of the compounds were analysed using energy-dispersive X-ray spectroscopy (EDX) on a Zeiss HR SEM ULTRA 55 with an accelerating voltage of 20 kV and a beam current of 3 nA.

For the recrystallization investigations, we used NETZSCH STA 449 F3 (Germany), and the calibration was done with commercially available standards. The baseline was experimentally recorded using the experimental conditions as described for DTA (SETERAM). To investigate recrystallization, differential scanning calorimetry (DSC) was performed using a probe of 0.030 g of CZTSe and a mixture of 0.027 g of CZTSe with 0.064 g CdI_2 (with a molar ratio of 1:5) in the temperature region from RT to 900 °C. The used CZTSe (synthesized in KI) had a composition of $Cu_{1.69}Zn_{1.07}SnSe_{3.62}$, as determined by EDX.

Results and discussion

CdI_2–CuSe–SnSe mixture

The reactions occurring in the two separate systems of CdI_2–CuSe and CdI_2–SnSe discussed in Part 1 of this paper [9] are also very likely to occur in the CdI_2–CuSe–SnSe system. The additional reactions can be basically divided into three parts: (1) reactions between Cu–Se and Sn–Se compounds; (2) reactions with CdSe causing the formation of $Cu_2CdSnSe_4$; (3) reactions with iodide compounds.

On the DTA curve of the CdI_2–CuSe–SnSe mixture, the first peak at 141 °C (Fig. 2a) could be attributed to the melting of SnI_4 [14] (the formation of SnI_4 in the CdI_2–SnSe mixture was found in Part 1 [9]). If the heat of fusion of SnI_4 is 4.541 kJ mol^{-1} [14], then (0.4 ± 0.1 J) corresponds to the melting of 1.84×10^{-5} mol of SnI_4. In the Raman spectra of the CdI_2–CuSe–SnSe sample heated to 250 °C and held there for 48 h, we observed peaks at 94 and 122 cm^{-1}, which may correspond to CuI. CuSe also has a Raman peak at 94 cm^{-1}, but CuSe must be excluded from consideration since no peak was observed at 263 cm^{-1} (the main Raman peak of CuSe [15]). The Raman peak at 178 cm^{-1} can be attributed to Cu_2SnSe_3 [16], and that at 186 cm^{-1} could be attributed to $SnSe_2$ [17]. The peak at 231 cm^{-1} could correspond to Se–Se stretching [18] or to the less intense Cu_2SnSe_3 peak in the spectra [16]. The mixture of CuSe + SnSe should produce the Cu_2Se and $SnSe_2$ phases according to reaction (3), as the value of ΔG at 23 °C is $-$ 10.4 kJ mol^{-1} (Fig. 1). Raman analysis revealed that no CuSe and Cu_2Se phases were detected. The absence of CuSe and/or Cu_2Se leads to the conclusion that reaction (4) occurs and forms Cu_3Se_2, probably due to the presence of the liquid phase of SnI_4, which increases the contact area between solid particles. Reactions (3, 4) will take place up to 377 °C because at higher temperatures on the Cu–Se phase diagrams, CuSe will not exist due to the transformation reaction of CuSe to $Cu_{2-x}Se$ and Se [19, 20]. As a molar ratio of CuSe to SnSe of 1.85 was used, it is clear from reaction (3) that some SnSe will remain unreacted due to the deficiency of CuSe. No negative ΔG is found for the reaction of $SnSe_2$ with CuSe, which forms $CuSe_2$. The $Cu_{2-x}Se$ formed in reactions (3, 4) may be transformed into compounds such as CuSe until 377 °C or $CuSe_2$ until 322 °C [19, 20] if Cu_2Se is in contact with Se, as was found and described in Part 1 [9] in the system of CdI_2 + CuSe. The comparison of data in Fig. 1 leads to the assumption that Se is more likely to be consumed for the formation of $SnSe_2$ from SnSe. However, after the melting of CdI_2 (at $T > 381$ °C [14]), due to the increased contact in the molten flux, only $Cu_{2-x}Se$ and $SnSe_2$ can be formed. In the quenched sample

Author's personal copy

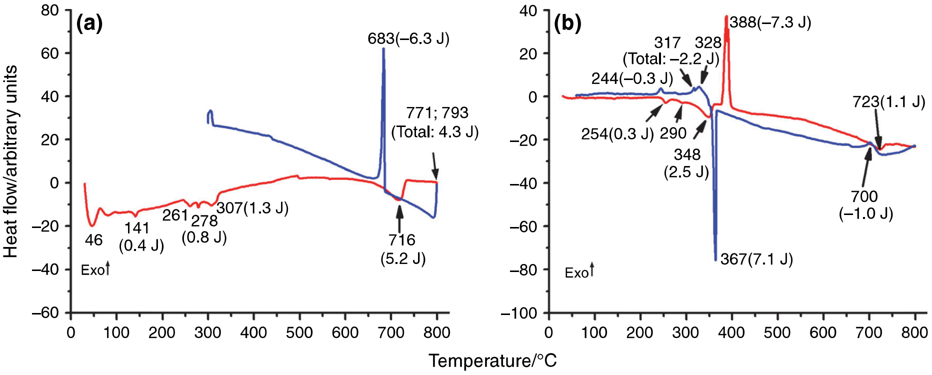

Fig. 2 DTA curves of CdI_2 + CuSe + SnSe and CdI_2 + CuSe + ZnSe+ SnSe (heating—red, cooling—blue)

at 390 °C, no CdSe and CuI phases were found; thus, the exchange reaction of Cu_2Se with CdI_2 was excluded. Cu_2SnSe_3 was present in this sample because the formation enthalpy of Cu_2SnSe_3 from Cu_2Se and $SnSe_2$ by reaction (5) has a more negative ΔG value (experimentally determined by us to be -32.3 ± 3 kJ mol^{-1} at 655 °C [8]) in comparison with the positive value for the exchange reaction (Cu_2Se with CdI_2) in the CdI_2–CuSe system, as seen in the graphs in Part 1 [9].

$$2\,\mathrm{CuSe(s)} + \mathrm{SnSe(s)} \rightarrow \mathrm{Cu_2Se(s)} + \mathrm{SnSe_2(s)} \quad (3)$$

$$\mathrm{SnSe(s)} + 3\mathrm{CuSe(s)} \rightarrow \mathrm{Cu_3Se_2(s)} + \mathrm{SnSe_2(s)} \quad (4)$$

$$\mathrm{Cu_2Se(s)} + \mathrm{SnSe_2(s)} \leftrightarrow \mathrm{Cu_2SnSe_3(s)} \quad (5)$$

Additionally, in Part 1 of this paper [9], it was found that SnI_4 had already formed at RT according to the reactions of SnSe or $SnSe_2$ with I_2. After the melting of the CdI_2–SnSe mixture, SnI_4 was undetectable in the solid quenched mixture because it has a low boiling point (348 °C) [14] and could evaporate into the gas phase and condense on the walls of the ampoule. SnI_4 can react with copper selenides following reactions (6, 7). Comparing these data to those in Fig. 1 reveals that reaction (6) is reversible at 426 °C, while (7) and (8) can proceed until reaching 398 and 342 °C, respectively (see Fig. 1).

$$\mathrm{SnI_4(s,\ l,\ g)} + 2\mathrm{Cu_2Se(s)} \leftrightarrow \mathrm{SnSe_2(s)} + 4\mathrm{CuI(s,\ l)} \quad (6)$$

$$\mathrm{SnI_4(s,\ l,\ g)} + 4\mathrm{CuSe(s)} \leftrightarrow \mathrm{SnSe_2(s)} + 4\mathrm{CuI(s,l)} + 2\mathrm{Se(s,l,g)} \quad (7)$$

$$\mathrm{SnI_4(s,l,g)} + 4\mathrm{CuSe_2(s)} \leftrightarrow \mathrm{SnSe_2(s)} + 4\mathrm{CuI(s,l)} + 6\mathrm{Se(s,l,g)} \quad (8)$$

On the DTA curve of the CdI_2–CuSe–SnSe mixture, the next peaks occur at 261 and 278 °C (0.8 ± 0.1 J). CuI is no longer present in the corresponding quenched sample (270 °C), and a new compound (Cu_2SnSe_4) is detectable by the Raman shifts at 190 and 225 cm^{-1} (a reference sample of Cu_2SnSe_4 was synthesized by us). At those temperatures, several processes are possible: (1) free molten Se (T_m = 221 °C [14]) could be formed by reactions (7, 8); (2) Cu_2SnSe_4 could form from Cu_2SnSe_3 and Se according to reaction (9) [21], thus causing the Raman peak at 178 cm^{-1} to be characteristic of the Cu_2SnSe_3 shift to 190 cm^{-1}, indicating the formation of the Cu_2SnSe_4 phase; or (3) the formation of the eutectic solid solution of CdI_2 with β-CuI at 271 °C and with γ-CuI could occur, as the maximum solubility is 25 mol% CdI_2 at 281 °C [22]. The formation of solid solutions explains the absence of analytical signs of pure CuI.

The DTA peak at 307 °C (1.3 ± 0.1 J) can be explained by the processes described in Part 1 [9] for the CdI_2–CuSe system, where the DTA peak at 304 °C was attributed to the eutectic melting of ε-Cu_3Cd_{10}.

On the DTA curve of the CdI_2–CuSe–SnSe mixture, the peritectic transformation of CuSe to $Cu_{2-x}Se$ with the release of Se at 383 °C is not seen, as it was seen on the DTA curve of CuSe in Part 1 [9]; additionally, no effect of CdI_2 melting is seen. This result means that those compounds have been completely consumed in the formation of the CuI–CdI_2 solid solution [22].

$$\mathrm{Cu_2SnSe_3(s)} + \mathrm{Se(l)} \leftrightarrow \mathrm{Cu_2SnSe_4(s)} \quad (9)$$

In the Raman spectra of the sample quenched at 390 °C, just slightly above the expected CdI_2 melting point, Raman peaks at 140 and 241 cm^{-1} (corresponding to Se), and a Raman peak at 163 cm^{-1} (unknown), were seen. Additionally, a Raman peak at 196 cm^{-1} (A_1 mode of CZTSe) was found to shift to 188 cm^{-1}, which could reflect the formation of the $Cu_2CdSnSe_4$ [23, 24] phase. CdSe could be formed by the unreacted SnSe and CdI_2; this reaction starts at 348 °C, as shown in Part 1 [9], and reaction (10) can take place as follows:

$$\mathrm{Cu_2SnSe_3(s)} + \mathrm{CdSe(s)} \leftrightarrow \mathrm{Cu_2CdSnSe_4(s)} \quad (10)$$

Author's personal copy

No change in the phase composition was found in the sample quenched at 750°C, compared to the previous one quenched at 390 °C. The peak at 716 °C (5.2 ± 0.5 J) could be attributed to eutectic reaction (11) [21]. The split of a double peak at 771 and 793 °C is attributable to the melting of $Cu_2CdSnSe_4$ (4.3 ± 0.4 J), as reported by Matsushita et al. at 780 °C in book [2]. However, the solidification of $Cu_2CdSnSe_4$ is not seen in the DTA cooling curve, which is probably because during $Cu_2CdSnSe_4$ melting, a solid CdSe phase forms in the liquid. The formation reaction between solid CdSe and the liquid probably needs more time. The CdSe phase is not seen in the Raman spectra, as reaction (12) (see Part 1 [9]) is possible at temperatures of higher than 526 °C. The $Cu_{2-x}Se$ Raman peak at 263 cm^{-1} [15] was also detected.

$$L \leftrightarrow Cu_2SnSe_3(s) + SnSe_2(l) \tag{11}$$

$$2CuI(l) + CdSe(s) \leftrightarrow Cu_2Se(s) + CdI_2(l, g) \tag{12}$$

During the cooling of one more sample to 620 °C, no changes in the phase composition were detected. The exothermic effect at 683 °C (− 6.3 ± 0.6 J) is attributed to the solidification of Cu_2SnSe_4, which occurs at a lower temperature than that of Cu_2SnSe_3 (697 °C) [21]. According to XRD analysis, phases such as $Cu_2CdSnSe_4$, $Cu_{1.8}Se$, $Cu_{1.78}Se$, CdI_2, CuI, and CdSe were present, and their formation can be explained by reactions (10, 12). SnI_4 and $Cu_3(CO_3)_2(OH)_2$ were also found. We explain the presence of SnI_4 by its condensation from the gaseous phase in the closed ampoule. The formation of $Cu_3(CO_3)_2(OH)_2$ is probably caused by 1% impurities in CdI_2 (see Part 1 [9]) and by handling CdI_2 in air.

CdI_2–CuSe–SnSe–ZnSe mixture

The DTA curves of the CdI_2–CuSe–SnSe–ZnSe mixture are presented in Fig. 2b. The peaks at 254 (0.3 ± 0.1 J) and 290 °C in the DTA heating curve (Fig. 2b) (corresponding to the DTA peaks of the CdI_2–CuSe–SnSe mixture at 261 and 278 °C) can be attributed to a similar mechanism as in chapter 3.1., i.e. to the formation of CuI solid solution with CdI_2 [22]. To investigate the processes occurring in the next endothermic peak during the melting of the mixture, the corresponding sample was quenched at 370 °C. CdI_2, $SnSe_2$, ZnSe and $Cu_2CdSnSe_4$ were found by XRD. Raman peaks characteristic of the phases CdI_2 (110 cm^{-1}), SnSe (147 cm^{-1}), and $Cu_2CdSnSe_4$ (188 and 231 cm^{-1}) were detected in the Raman spectra compared to the reference spectra made by us. In the DTA curve, an endothermic melting effect at 348 °C (2.5 ± 0.3 J) is observed that is much lower than that needed to melt 0.125 g of CdI_2 (7.1 ± 0.7 J). Therefore, it can be assumed that the endothermic effect of CdI_2 melting is covered by the following exothermic thermal effect of 2.5–7.1 = − 4.6 J. The visible part of the exothermic effect is seen as − 7.3 J at 388 °C. Then, the full exothermic effect at 388 °C represents the sum of (− 7.3) + (− 4.6) = − 11.9 ± 1.2 J. Based on phase analyses, the compensating exothermic effect at 348 °C can be attributed to the formation of $Cu_2CdSnSe_4$ by the following route: Cu_2SnSe_3 forms from CuSe and SnSe, which is followed by reaction (10) between Cu_2SnSe_3 and CdSe. No Cu–Se compounds were found. Unreacted $SnSe_2$ could be present due to the applied initial molar ratio of 1.85(CuSe):1(ZnSe):1(SnSe):1.65(CdI_2), which is similar to that described in chapter 3.1.

In the next sample quenched at 400 °C, the presence of newly formed compounds (compared to the previous sample), i.e. $Cu_{1.8}Se$, Cu_2SnSe_3 and SnSe, was determined by XRD. Raman analysis confirmed the presence of the phases of SnSe, Cu_2SnSe_4 and $Zn_{1-x}Cd_xSe$ based on their characteristic Raman peaks at 147, 190 and 240 cm^{-1}, respectively, based on the reference spectra of those compounds recorded at our laboratory. In this case, the compound Cu_2SnSe_4 can also be formed by reaction (9). Most likely, during the exothermic process, the dissolution of $Cu_2CdSnSe_4$ in CdI_2 occurs due to the reversible reaction (10, 5) because Cu_2SnSe_3, $Cu_{2-x}Se$ and SnSe are now present. The released CdSe is used for reaction (13) with ZnSe.

$$xCdSe(s) + (1 - x)ZnSe(s) \leftrightarrow Zn_{1-x}Cd_xSe(s) \tag{13}$$

In the sample quenched at 590 °C, the newly formed phases (compared to the previous sample quenched at 400 °C) of CuI and $Cu_2ZnSnSe_4$ were detected by XRD. Raman analysis showed a main peak at 193 cm^{-1}, which could be attributed to a $Cu_2Zn_{1-x}Cd_xSnSe_4$ solid solution. Due to the incorporation of Cd into the CZTSe lattice, the main characteristic peak of CZTSe at 196 cm^{-1} is shifted to lower wavelength values [23, 24]. The crystals of CZTSe grown in CdI_2 contained approximately 4 at.% Cd based on EDX analysis. For a more detailed analysis, this sample was washed with distilled water and analysed by XRD and Raman. The washed sample showed $Cu_2ZnSnSe_4$ and ZnSe peaks in the XRD pattern (Fig. 3). The Raman spectra (in Fig. 4) showed peaks at 93 and 122 cm^{-1} corresponding to CuI (see Part 1 [9]), a peak at 193 cm^{-1} attributed to $Cu_2Zn_{1-x}Cd_xSnSe_4$ solid solution, a peak at 240 cm^{-1} characteristic of $Zn_{1-x}Cd_xSe$ and a peak at 263 cm^{-1} characteristic of $Cu_{2-x}Se$ [15]. The presence of $Cu_{2-x}Se$ can be explained by the reversible reactions (12, 13). $Cu_2Zn_{1-x}Cd_xSnSe_4$ forms by the following reaction (14):

$$Cu_2SnSe_3 + Zn_{1-x}Cd_xSe \leftrightarrow Cu_2Zn_{1-x}Cd_xSnSe_4 \tag{14}$$

Author's personal copy

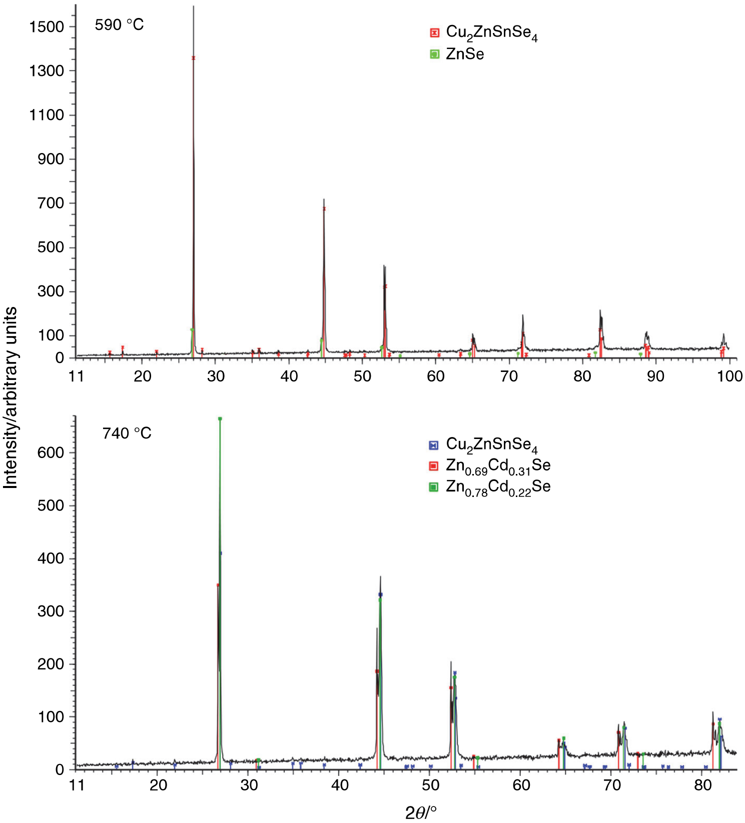

Fig. 3 XRD of washed CdI_2–CuSe–ZnSe–SnSe mixture heated to 590 and 740 °C (annealed for 1 h)

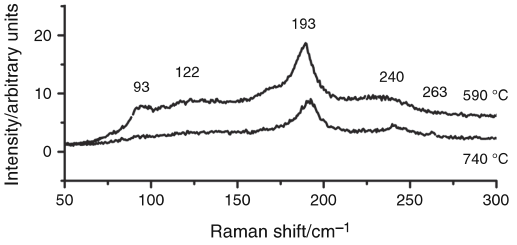

Fig. 4 Raman of washed CdI_2–CuSe–ZnSe–SnSe mixture heated to 590 and 740 °C (annealed for 1 h)

There are 2 reasons for the presence of unreacted ZnSe, SnSe or $SnSe_2$ from the initial mixture of CdI_2–CuSe–ZnSe–SnSe: first, 1.85 mol of CuSe, instead of 2, were initially used to form 1 mol of Cu_2SnSe_3 and then $Cu_2ZnSnSe_4$; second, Cu was consumed for the formation of CuI and CdSe from the reactions of copper selenides with CdI_2 (see Part 1 [9]). This process led to the formation of off-stoichiometric CZTSe. The experimentally measured value of − 7.3 ± 0.7 J for the formation of $Cu_2Zn_{1-x}Cd_xSnSe_4$ at 388 ° C is smaller than that of − 15.0 ± 1.7 kJ mol^{-1} found for the formation of CZTSe in KI and NaI in [7, 8] at higher temperatures, as it forms according to reaction (14).

To investigate the processes behind the endothermic peak at 723 °C in the DTA heating curve, a sample quenched at 740 °C was analysed by XRD and Raman before and after being washed with water. In addition to $Cu_2ZnSnSe_4$ and $Cu_2Zn_{1-x}Cd_xSnSe_4$, the phases of CuSe and Cu_4Se_3 were also found by XRD. After washing, only the $Cu_2ZnSnSe_4$, $Zn_{0.69}Cd_{0.31}Se$ and $Zn_{0.78}Cd_{0.22}Se$ phases were detected by XRD (Fig. 3). The Raman spectra of the unwashed sample show a peak at 188 cm^{-1} attributed to $Cu_2CdSnSe_4$ and a peak at 205 cm^{-1} attributed to CdSe based on comparisons to experimental references. In the washed sample, the same phases were found as those in the sample quenched at 590 °C by Raman (Fig. 4). Therefore, the endothermic peak near 723 °C 1.1 ± 0.1 J in the DTA heating curve and the exothermic peak at 700 °C in the cooling curve can be attributed to the eutectic reaction (11)

Author's personal copy

[21] because Cu_2SnSe_3 solidifies at 693 °C [21] and $Cu_2Zn_{1-x}Cd_xSnSe_4$ appears to decompose. In the cooling curve of the studied system, the endothermic peak of 7.1 J at 367 °C, near the melting point of CdI_2 (covered by 7.1 J, giving the summary value of the endothermic effect of $7.1 + 7.1 = 14.2$ J), can be attributed to the dissolution process of the formed compounds in the molten phase of flux. The values of the thermal effects in the DTA curves were reproducible in 2 runs. The exothermic peaks at 328, 317 and 244 °C in the cooling curve (with a total value of -2.2 ± 0.2 J) correspond to the solidification of $CuSe_2$, the formation of CuI–CdI_2 solid solution and the precipitation of CuI, respectively, as described in the analyses of the CdI_2–CuSe system in Part 1 [9] and [22].

CZTSe recrystallization in CdI_2

The DSC heating and cooling curves of pure CZTSe and the CZTSe+CdI_2 mixture are presented in Fig. 5a, b. The first effect is seen at 217 °C, which may be related to Se melting [14]. The amount of Se, as determined from the melting effect of 0.02 J, can be expressed as 3×10^{-4} g. This effect is present in both DSC curves (Fig. 5a, b). When not mixed with CdI_2, CZTSe exhibits melting at 795 °C (788 °C in [25]) with an enthalpy effect of 2.3 ± 0.2 J (expressed as 44.6 kJ mol^{-1}) and solidification at 796 °C in cooling (1.5 ± 0.2 J) 29.1 kJ mol^{-1}. The sample of CdI_2 mixed with CZTSe shows an endothermic effect at 378 °C due to the melting of CdI_2. Since the expected intensity of the melting of the added amount of CdI_2 is 1.3 J and that in DSC is 2.9 J, a series of other endothermic processes with a total effect of 1.6 J must have taken place. The absence of the melting and solidification effects of pure CZTSe revealed in the comparison of Fig. 5a with Fig. 5b indicates that another compensating process occurred simultaneously. This could be the mixing of two liquids, i.e. liquid CdI_2 and the formed liquid CZTSe (or the dissolution of liquid CZTSe in liquid CdI_2). The sample of the CZTSe+CdI_2 mixture was annealed at 650 °C for 168 h, quenched to RT and washed with water. In Fig. 6, the XRD pattern showed that $Cu_2CdSnSe_4$ and $ZnCdSe_2$ were formed. Raman analysis (Fig. 7) showed peaks at 93 and 122 cm^{-1} that are attributed to CuI (Paper 1 [9]) and peaks at 188 and 231 cm^{-1} that can be attributed to $Cu_2Zn_{1-x}Cd_xSnSe_4$ solid solution [23, 24]. In addition, the washing water was collected, dried and investigated. XRD analysis showed the presence of $Zn_{0.69}Cd_{0.31}Se$, $Zn_{0.7}Cd_{0.3}Se$, $Cu_2CdSnSe_4$, CdSe, Cu_2Se, and SnSe phases. It is well known that molten salts dissolve some part of their precursor compounds and form Quaternary compounds; for example, we determined the solubilities of ZnSe, SnSe, CuSe and CZTSe in KI at 740 °C to be 0.08, 0.23, 3.19 and 0.17 mol%, respectively [7]. Since the used flux salt is removed by leaching with water, the compounds dissolved at high temperatures are precipitated into the leaching solvent as amorphous or fine crystalline powder. In Raman studies, it was difficult to observe any distinct Raman spectrum.

In the cooling curve, the peak at 845 °C (860 °C in [14]) may correspond to SnSe solidification and that at 634 °C may correspond to the eutectic point of ZnSe–$SnSe_2$ (915 K = 642 °C in [25]); if some $Cu_2Zn_{1-x}Cd_xSnSe_4$ or $Cu_2CdSnSe_4$ were detected, these peaks may correspond to their solidification and phase transformation, as was reported for $Cu_2CdSnSe_4$ in [2]. The effects observed at 350, 331 and 317 °C (total 2.4 J) in cooling correspond to the solidification and formation of the CuI–CdI_2 solid solution described above and in [22]. As described in [26, 27], the molar heat of fusion of a given salt eutectic mixture depends on its melting temperature, while the heat capacity of a mixture is similar to that of its pure salt in a molten state.

It seems that some of the SnSe or $SnSe_2$ reacted to generate SnI_4 (evaporated) and CdSe because at 634 °C, Cu_2Se does not form CuI and CdSe (see Part 1 [9]), but CdSe and ZnSe form the solid solution $Zn_{1-x}Cd_xSe$. The appearance of the CuI–CdI_2 solid solution at 317–350 °C could also be explained by the fact that during quenching to

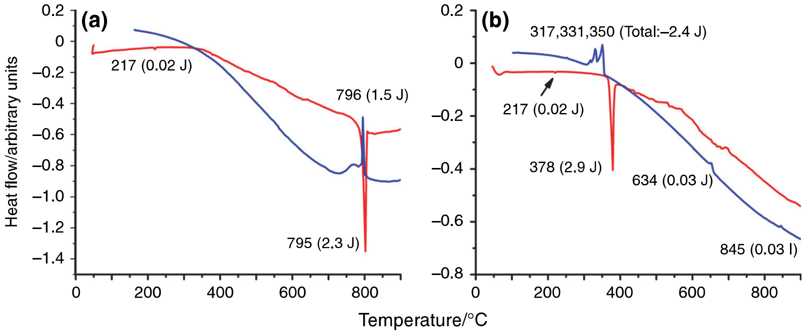

Fig. 5 DSC of CZTSe and CdI_2–CZTSe (heating—red, cooling—blue)

Author's personal copy

Fig. 6 XRD of washed CdI_2–CZTSe (annealed for 168 h at 650 °C)

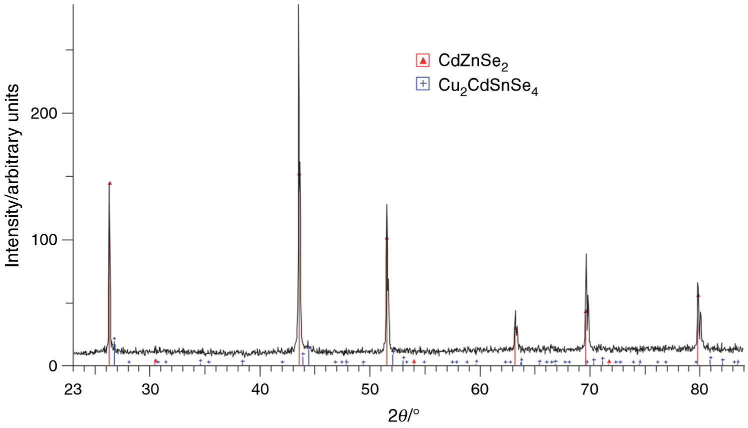

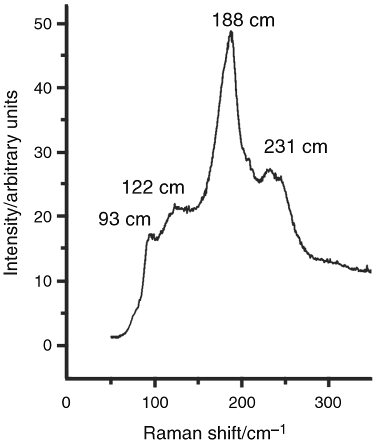

Fig. 7 Raman of washed CdI_2–CZTSe (annealed for 168 h at 650 °C)

RT, the exchange reactions of copper selenides with CdI_2 are possible (see Part 1 [9]).

Conclusions

We derived the chemical reactions from mixtures of CuSe, SnSe and CuSe, SnSe, and ZnSe in molten CdI_2 in closed vacuum ampoules using the methods of DTA, XRD and Raman spectroscopy.

At RT, Cu_2Se and $SnSe_2$ can already be formed from CuSe and SnSe. We also found that minor SnSe remains unreacted due to the poor initial copper composition of the used precursors. Therefore, the initial composition should be changed.

Cu_2SnSe_3 is formed at temperatures below 250 °C by the solid-state reaction between copper selenides and tin selenides. We discovered the presence of some free Se. Therefore, in the presence of Se and Cu_2SnSe_3, Cu_2SnSe_4 was already formed at 270 °C.

The reaction of copper selenide with CdI_2, which results in CuI and CdSe, initiates the formation of $Cu_2CdSnSe_4$ at 370 °C through the reaction between CdSe and Cu_2SnSe_3. The formation of CuI consumes some copper selenide, causes the deficiency of Cu and generates a residual unreacted amount of SnSe. At temperatures below 400 °C, CdSe also forms phases in solid solution with ZnSe, such as $Zn_{1-x}Cd_xSe$; in turn, these phases react with Cu_2SnSe_3 and form $Cu_2Zn_{1-x}Cd_xSnSe_4$ ($T \leq 590$ °C). According to the exothermic effect, the specified $Cu_2Zn_{1-x}Cd_xSnSe_4$ forms at 388 °C from Cu_2SnSe_3 and $Zn_{1-x}Cd_xSe$ with a formation enthalpy of $-\ 15.0 \pm 1.7$ kJ mol^{-1}, which is reported here for the first time. A total of 4 at.% Cd is incorporated into CZTSe at 590 °C. The recrystallization of CZTSe during CdI_2 melting resulted in the dissolution of CZTSe. CdI_2 is a material with a preferable low melting temperature flux; therefore, its use avoids the sintering effects of some other low melting by-products that can be formed in small amounts before the melting of the flux. However, its high reactivity with binary compounds is a problem during synthesis.

Acknowledgements We sincerely appreciate the experimental support with the apparatus provided for XRD and DTA measurements by the heads of the Department of Mechanical and Industrial Engineering and Laboratory of Inorganic Materials. We acknowledge the following projects for their financial support: TAR16016 "Advanced materials and high-technology devices for sustainable energetics, sensorics and nanoelectronics"; IUT19-28 "New materials and technologies for solar energetics".

Author's personal copy

References

1. Paranthaman MP, Wong-Ng W, Bhattacharya RN. Semiconductor materials for solar photovoltaic cells. Cham: Springer; 2016.
2. Adachi S. Earth-abundant materials for solar cells: Cu_2-II-IV-VI_4 Semiconductors. Chichester: Wiley; 2015.
3. Ito K. Copper zinc tin sulfide-based thin-film solar cells. Chichester: Wiley; 2015.
4. Kodigala SR. Thin film solar cells from earth abundant materials: growth and characterization of $Cu_2ZnSn(SSe)_4$ thin films and their solar cells. London: Elsevier; 2013.
5. Lee YS, Gershon T, Gunawan O, Todorov TK, Gokmen T, Virgus Y, Guha S. $Cu_2ZnSnSe_4$ thin-film solar cells by thermal co-evaporation with 11.6% efficiency and improved minority carrier diffusion length. Adv Energy Mater. 2015. https://doi.org/10.1002/aenm.201401372.
6. Brammertz G, Buffière M, Oueslati S, ElAnzeery H, Ben Messaoud K, Sahayaraj S, Köble C, Meuris M, Poortmans J. Characterization of defects in 9.7% efficient Cu2ZnSnSe4–CdS–ZnO solar cells. Appl Phys Lett. 2013;103:163904.
7. Leinemann I, Timmo K, Grossberg M, Kaljuvee T, Tõnsuaadu K, Traksmaa R, Altosaar M, Meissner D. Reaction enthalpies of $Cu_2ZnSnSe_4$ synthesis in KI. J Therm Anal Calorim. 2015;119(3):1555–64.
8. Leinemann I, Zhang W, Kaljuvee T, Tõnsuaadu K, Traksmaa R, Raudoja J, Grossberg M, Altosaar M, Meissner D. $Cu_2ZnSnSe_4$ formation and reaction enthalpies in molten NaI starting from binary chalcogenides. J Therm Anal Calorim. 2014;118(2):1313–21.
9. Leinemann I, Nkwusi GC, Timmo K, Volobujeva O, Danilson M, Raudoja J, Kaljuvee T, Traksmaa R, Altosaar M, Meissner D. Reaction pathway to $Cu_2ZnSnSe_4$ formation in CdI_2. Part 1 Chemical reactions and enthalpies in mixtures of CdI_2–ZnSe, CdI_2–SnSe, and CdI_2–CuSe. J Therm Anal Calorim. 2018. https://doi.org/10.1007/s10973-018-7102-5.
10. Wibowo RA, Jung WH, Al-Faruqi MH, Amal I, Kim KH. Crystallization of $Cu_2ZnSnSe_4$ compound by solid state reaction using elemental powders. Mater Chem Phys. 2010;124:1006–10.
11. Klavina I, Raudoja J, Altosaar M, Mellikov E, Meissner D. CZTSe ($Cu_2ZnSnSe_4$) crystal growth for use in monograin membrane solar cells. CYSENI 2010. In: Proceeding of the annual conference of young scientists on energy issues. [CD VII-347-VII-353]. Kaunas: Lithuanian Energy Institute. 2010; May 27–28.
12. Nkwusi G, Leinemann I, Altosaar M. The processes and enthalpies in synthesis of Cu_2ZnSnS_4 in molten CdI_2. IARJSET. 2016;3(5):113–9.
13. Nkwusi G, Leinemann I, Raudoja J, Mikli V, Kärber E, Altosaar M. Impact of growth-synthesis conditions on $Cu_2Zn_{1-x}Cd_xSnS_4$ monograin material properties. Superlattices Microstruct. 2016;98:400–5.
14. Software of HSC Chemistry Ver. 6.0. Outoukumpu Research Oy. Pori: Finland.
15. Ishii M, Shibata K, Nozaki HJ. Anion distributions and phase transitions in $CuS_{1-x}Se_x$ ($x = 0$–1) studied by Raman spectroscopy. Solid State Chem. 1993;105:504.
16. Marcano G, Rincon C, Lopez SA, Perez GS, Herrera-Perez JL, Mendoza-Alvarez JG, Rodriguez P. Raman spectrum of monoclinic semiconductor Cu_2SnSe_3. Solid State Commun. 2011;151:84–6.
17. Lucovsky G, Mikkelsen JC, Liang WY, White RM, Martin RM. Optical phonon anisotropies in the layer crystals SnS_2 and $SnSe_2$. Phys Rev B. 1976;14:1663–9.
18. Poborchii VV, Kolobov AV, Tanaka K. An in situ Raman study of polarization-dependent photocrystallization in amorphous selenium films. Appl Phys Lett. 1998;72:1167–9.
19. Glazov VM, Pashinkin S, Fedorov VA. Phase equilibria in the Cu–Se system. Inorg Mater. 2000;36:641–52.
20. Chakrabarti DJ, Laughlin DE. The Cu–Se system. Bull Alloy Phase Diagr. 1981;2(3):305–15.
21. Tomashik VN, Lebrun N, Perrot P. Copper-Selenium-Tin. In: Non-ferrous metal ternary systems. Semiconductor systems: phase diagrams, crystallographic and thermodynamic data. Landolt-Bornstein new series IV/11C1. 2006. p. 361–73.
22. Blachnik R, Stöter U. The phase diagrams of mixtures of CuI with ZnI_2, CdI_2, and HgI_2. Thermochim Acta. 1989;143:115–22.
23. Altosaar M, Raudoja J, Timmo K, Danilson M, Grossberg M, Krustok J, Mellikov E. $Cu_2Zn_{1-x}Cd_xSn(Se_{1-y}S_y)_4$ solid solutions as absorber materials for solar cells. Phys Stat Sol A. 2008;205:167–70.
24. Grossberg M, Krustok J, Timmo K, Altosaar M. Radiative recombination in $Cu_2ZnSnSe_4$ monograins studied by photoluminescence spectroscopy. Thin Solid Films. 2009;517:2489–92.
25. Dudchak IV, Piskach LV. Phase equilibria in the Cu_2SnSe_3–$SnSe_2$–ZnSe system. J Alloy Compd. 2003;351:145–50.
26. Redkin A, Korzun I, Reznitskikh O, Yaroslavtseva T, Zaikov Y, Kumkov S. Heat of fusion of halide salts and their eutectics. J Therm Anal Calorim. 2017. https://doi.org/10.1007/s10973-017-6650-4.
27. Redkin A, Korzun I, Yaroslavtseva T, Reznitskikh O, Zaikov Y. Isobaric heat capacity of molten halide eutectics. J Therm Anal Calorim. 2017;128:621. https://doi.org/10.1007/s10973-016-5869-9.

Paper VI

Timmo, K., Kauk-Kuusik, M., Pilvet, M., Mikli, V., Kärber, E., Raadik, T., **Leinemann, I.,** Altosaar, M., Raudoja, J. (2015). Comparative study of SnS recrystallization in molten CdI_2, $SnCl_2$ and KI. *Phys. Status Solidi C, 13*(1), 8-12.
doi: 10.1002/pssc.201510082.

Wiley Online Library Early View publication on www.wileyonlinelibrary.com
(issue and page numbers not yet assigned;
citable using Digital Object Identifier – **DOI**)

Phys. Status Solidi C, 1–5 (2015) / **DOI** 10.1002/pssc.201510082

physica status solidi c
www.pss-c.com
current topics in solid state physics

Comparative study of SnS recrystallization in molten CdI_2, $SnCl_2$ and KI

Kristi Timmo[*], Marit Kauk-Kuusik, Maris Pilvet, Valdek Mikli, Erki Kärber, Taavi Raadik, Inga Leinemann, Mare Altosaar, and Jaan Raudoja

Department of Materials Science, Tallinn University of Technology, Ehitajate tee 5, 19086 Tallinn, Estonia

Received 12 June 2015, revised 7 September 2015, accepted 19 October 2015
Published online 2 November 2015

Keywords SnS, solar cell, crystalline powder, crystal growth

---

[*] Corresponding author: e-mail kristi.timmo@ttu.ee, Phone: +372 6203362, Fax: +372 6203367

In the present study, the recrystallization of polycrystalline SnS in different molten salts CdI_2, $SnCl_2$ and KI as flux materials are presented. The recrystallization and growth of polycrystalline material in molten salts produces unique SnS monograin powders usable in monograin layer solar cells. XRD and Raman analysis revealed that single phase SnS powder can be obtained in KI at 740 °C and in $SnCl_2$ at 500 °C. Long time heating of SnS in molten CdI_2 was accompanied by chemical interaction between SnS and CdI_2 that resulted in a mixture of CdS and Sn_2S_3 crystals. SEM images showed that morphology of crystals can be controlled by the nature of the flux materials: needle-like Sn_2S_3 together with round edged crystals of CdS in CdI_2, flat crystals of SnS with smooth surfaces in $SnCl_2$ and well-formed SnS crystals with rounded edges in KI had been formed. The temperatures of phase transitions and/or the interactions of SnS and flux materials were determined by differential thermal analysis.

© 2015 WILEY-VCH Verlag GmbH & Co. KGaA, Weinheim

1 Introduction Tin monosulphide (SnS) is a promising candidate for the development of PV solar cells with absorbers containing only earth-abundant-materials. $Cu_2ZnSn(S,Se)_4$ uses also constituent elements that are abundant in nature, but its complex composition complicates its manufacture. SnS has a much simpler composition. Furthermore, the constituent elements of this compound, Sn and S are cheap, safe to handle and do not pollute the environment, whereas other thin-film absorbers require toxic elements cadmium, tellurium, selenium and/or lead. SnS occurring in nature takes the form a herzenbergite, which has an orthorhombic crystal structure. SnS also can have hexagonal (wurtzite) and cubic (sphalerite) crystal forms which are less stable than herzenbergite at room temperature. SnS has direct optical band-gap, p-type conductivity and a high absorption coefficient of 10^5 cm^{-1} [1]. The reported band gap energy for SnS varies in the range of 1.1-1.87 eV [1-4]. Large difference in the band-gap values could be caused by other phases such as SnS_2 and Sn_2S_3 in thin films. Although theoretical calculations revealed energy conversion efficiency of up to 25% for SnS photovoltaic devices, existing SnS solar cells have reached only 4.6% of power conversion efficiency [5, 6]. There could be different reasons, but one is the complexity to grow high purity and device quality SnS films. Additional studies using controlled single-phase samples and different experimental methods are needed.

Molten salt process, one of the methods of preparing semiconductor powders, involves the use of a molten salt as the medium for synthesis and growth of different compounds from their constituent elements. The growth of monocrystalline powder grains can proceed at temperatures higher than the melting point of the used flux materials and at temperatures lower than the melting point of the synthesized semiconductor compound.

In our previous reports [7-10], there is shown that, monograin powder growth in molten fluxes, results in homogeneous material with single-crystalline grain structure. In this process, the chemical nature of the liquid (molten) phase of used flux material influences the shape and size of the obtained absorber crystals, which are saturated by constituent elements of the used salt. The requirements to the flux material are chemical stability, readily available, inexpensive and easily removable (soluble in water). A low melting temperature and low vapor pressure at the heating temperature are desirable.

© 2015 WILEY-VCH Verlag GmbH & Co. KGaA, Weinheim

In this study, the results of recrystallization of polycrystalline SnS in the molten phase of CdI_2 (T_M = 387 °C [11]), $SnCl_2$ (T_M = 247 °C [12]) and KI (T_M = 685 °C [13]) salts as flux materials are used to produce unique SnS monograin powders are described and presented.

2 Experimental details SnS was self-synthesized from 3N purity Sn shots and elemental S in evacuated quartz ampoules. The precursors were slowly heated to 700 °C for 500 h, annealed for 42 h and cooled down naturally to room temperature. The batch of polycrystals was grounded in an agate mortar before use in the powder recrystallization and growth process. KI was dehydrated by heating during the dynamic vacuum-pumping process at temperatures up to 270 °C. Three different mixtures were prepared: SnS+KI, SnS+CdI_2, SnS+$SnCl_2$. The volume ratios of SnS and flux materials were equal to 1:1. After mixing and grinding the precursors, the mixtures were loaded into quartz ampoules, degassed under dynamic vacuum, sealed, and isothermally annealed at temperatures higher than melting point of salts: at 740 °C in KI flux and at 500 °C in CdI_2 and $SnCl_2$ fluxes for 336 hours. 500 °C was chosen to provide sufficient rate of crystal growth. The recrystallization processes were stopped by cooling the ampoules to room temperature. The flux materials were removed by leaching with deionized water.

The chemical composition of powder crystals were determined by energy dispersive spectroscopy (EDS). The shape and surface morphology of crystals were studied with the high resolution scanning electron microscope (SEM) Zeiss ULTRA 55. XRD patterns of the powders were recorded on a Rigaku Ultima IV diffractometer with Cu K_α radiation (λ = 1.5406 Å). PDXL 2 software was used for the derivation of crystal structure information from powder XRD data. The micro-Raman spectra were recorded by using a Horiba`s LabRam HR800 spectrometer and 532 nm laser line that was focused on the sample with spot size of about 5 µm. Temperatures of phase transitions and the interactions between the initial SnS and the flux materials were determined by DTA-DSC set-up of NETZSCH STA 449 F3 Jupiter. Mixture samples of SnS+KI, SnS+CdI_2, SnS+$SnCl_2$ with the identical proportions of components as used in monograin powder growth process, were prepared separately as individual probes for thermal analyses (TA). As a reference for TA, an identical empty quartz ampoule was used. For comparison, also the pure KI, CdI_2 and $SnCl_2$ melting and solidification effects were determined. Two heating-cooling cycles were recorded from room temperature up to 800 °C with heating rate 5 °C, then the isothermal heating segment was hold for 5 minutes at 800 °C. Cooling to 55 °C with cooling rate of 10 °C/min. was followed with an additional quasi-isothermal slow cooling with rate of 0.15 °C/min. in segment 55-45 °C. A set of standard metals (In, Sn, Bi, Zn, Al, Au) in closed ampoules was used for calibration. The onset point was used for the determination of temperature of the processes in heating since it is not depending on sample mass, but in cooling, the end of the peak as the onset of process was used.

3 Results and discussion

3.1 Morphological and compositional analysis

Different flux materials give specific morphologies of SnS crystals. According to SEM analysis the recrystallization of polycrystalline SnS in CdI_2 resulted in the powder mixture containing two types of crystals (Fig. 1): long hexagonal needle like crystals are mixed together with rounded monograins.

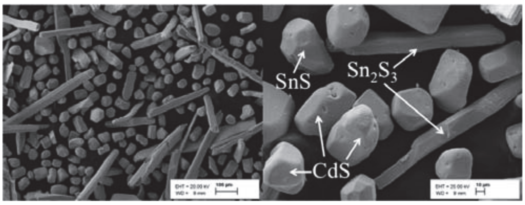

Figure 1 SEM images for powder crystals obtained by recrystallization of SnS in molten salt of CdI_2 at 500 °C.

SEM micrograph shows that in the case of using $SnCl_2$ flux, the SnS crystalline powder consists of smooth flat plates with rounded edges (Fig. 2). It can be seen from the images that the plates have layer to layer structure.

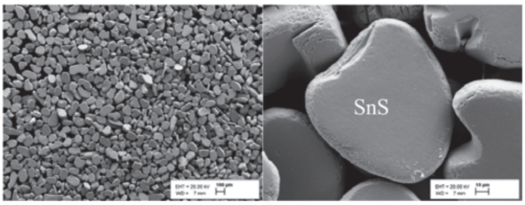

Figure 2 SEM images of SnS crystals grown in molten $SnCl_2$ at 500 °C.

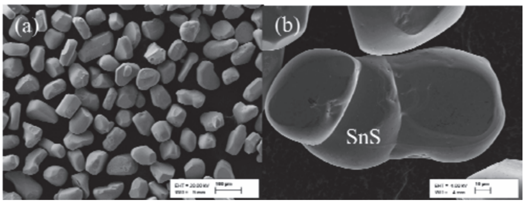

Figure 3 SEM images of SnS crystals grown in molten salt of KI at 740 °C.

Figure 3 shows SEM micrographs of SnS monograin powder crystals grown in KI. It can be seen that the SnS powder consists of non-aggregated microcrystals with rounded grain edges and also sintered crystals. The last-mentioned crystals have deep straight grooves along the perimeter of the grains (Fig. 3b). This is an indication to

© 2015 WILEY-VCH Verlag GmbH & Co. KGaA, Weinheim

the sintering process, where two or more crystals have joined and form asymmetric grains. These aggregates have very stable structure. The uniform non-aggregated crystals are indicating the growth from individual seed crystals rather than from the aggregates of crystallization nuclei. The sintering of grains is enabled when the inter-granular capillaries are partly filled with liquid phase and the particles are compressed by the capillary contracting force [14]. The results indicate that the growth of monograins through the molten phase and the sintering process are occurring simultaneously.

According to EDX analysis it could be suggested that hexagonal needles (Fig. 1) grown in CdI_2 flux are Sn_2S_3 with the elemental composition of Sn : S = 41 : 58 at.%. The compositional ratios of rounded monograins are [Cd]/[S] = 1.0, indicating to the CdS phase. The chemical composition of SnS powder crystals grown in KI and $SnCl_2$ is stoichiometric with compositional ratios of [Sn]/[S] = 1.0.

3.2 Phase analysis by XRD and Raman spectroscopy The X-ray diffraction pattern for SnS powder grown in KI, is shown in Fig. 4, and XRD patterns for powders grown in CdI_2 and $SnCl_2$ in Fig. 5. XRD patterns of SnS monograin powder recrystallized in KI correspond to the orthorhombic crystal structure with the 62:Pnma space group (ICDD PDF-2-2013, 01-073-1859) and with lattice constants a=11.18 Å, b=3.97 Å and c=4.32 Å. No other phases like SnS_2 and Sn_2S_3 were detected. XRD pattern of the monograin powder grown in $SnCl_2$ flux, showed predominantly SnS phase, with Sn_2S_3 phase present to some extent. XRD pattern of the monograin powder grown in CdI_2 flux, showed the mixture of several phases, additionally to the SnS also Sn_2S_3, CdS and CdI_2 were identified, see Fig. 5.

The X-ray diffraction patterns of multicomponent mixtures usually contain overlapping peaks. Therefore, the detection of different tin sulphide secondary phases by XRD may be complicated, as reported also by Minnam Reddy et al. [15]. The overlapping problem can be resolved by using other complementary technique to distinguish SnS, SnS_2 and Sn_2S_3 phases. Raman scattering analysis was carried out to investigate the phase composition of materials. All Raman spectra were fitted using Lorentzian functions to resolve the peaks.

Raman spectra of SnS monograin powders grown in $SnCl_2$ and KI are shown in Fig. 6. In the both cases only single phase SnS, without additional phases, was detected. The lattice vibrations at 94, 191 and 218 cm^{-1} correspond to A_g modes, and the peak at 163 cm^{-1} to the B_{3g} mode of SnS [16]. In contrast to XRD pattern, Raman measurements did not confirm the Sn_2S_3 phase in powders grown in $SnCl_2$ flux. According to literature data, the corresponding Raman frequencies of SnS_2 and Sn_2S_3 are at 312 cm^{-1} [17] and 233 cm^{-1} and 307 cm^{-1} [18], respectively.

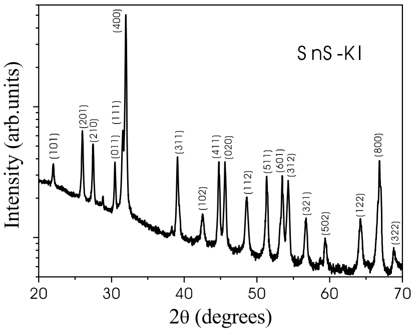

Figure 4 XRD pattern of SnS monograin powder recrystallized in KI.

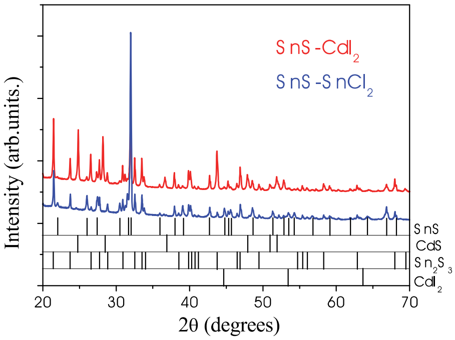

Figure 5 XRD patterns for powder crystals obtained by recrystallization of SnS in $SnCl_2$ and CdI_2.

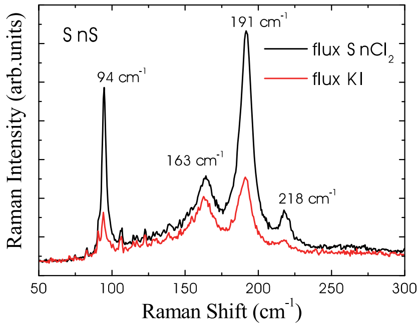

Figure 6 Room-temperature Raman spectra of SnS recrystallized in KI (red line) and in $SnCl_2$ (black line).

Raman spectra of SnS monograin powder crystals recrystallized in CdI_2 are presented in Fig. 7. The Raman spectra were taken separately from hexagonal needles and rounded crystals (Fig. 1), and the difference was remarkable. Raman measurements from hexagonal needles

© 2015 WILEY-VCH Verlag GmbH & Co. KGaA, Weinheim

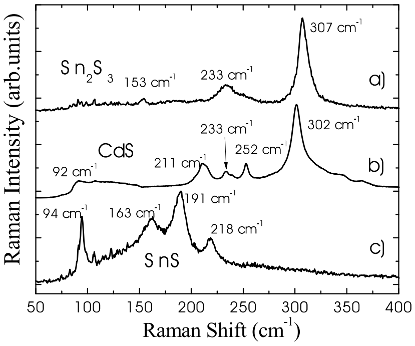

Figure 7 Room-temperature Raman spectra for powder crystals obtained by recrystallization of SnS in CdI_2, measured separately from (a) hexagonal needles and (b) and (c) from rounded crystals.

(Fig. 7a) revealed vibrational modes for Sn_2S_3 at 233 and 307 cm^{-1}. In the Raman spectra of rounded monograins (Fig. 7b and 7c), CdS and also SnS phase were observed. The Raman peaks of CdS were detected at 92 cm^{-1}, 211 cm^{-1}, 233 cm^{-1}, 252 cm^{-1} and 302 cm^{-1} [19]. The lattice vibrations at 94, 163, 191 and 218 cm^{-1} belong to the SnS phase, as it was described before.

3.3 Thermal analysis of CdI_2+SnS, $SnCl_2$+SnS and KI+SnS mixtures

Two heating-cooling cycles of the mixture of CdI_2+SnS were recorded in the temperature region RT-800 °C (Fig. 8).

The heating curves showed three exothermic processes at 331, 371 and 383 °C. In the cooling curve four endothermic processes revealed at 326, 354, 595 and 672 °C. The thermal effect at 383 °C could be attributed to the melting point of pure CdI_2 [11]. The thermal effect at 331 °C is much lower than melting temperature of CdI_2. This leads to an idea that some low temperature melting compound could be formed in the mixture. The most probably it is SnI_2 (melting point at 320 °C [11]) that was found also in [20]. SnI_2 (see reaction (1)) and also CdS (reaction (2)) could be formed from CdI_2+SnS mixture by reaction with free gaseous iodine released from CdI_2 as described in our previous work [20] by Eqs. (1) and (2) [21-24]:

$$SnS + I_2\,(g) \rightarrow SnI_2 + S\,(liq), \qquad (1)$$

$$CdI_2 + S\,(g) \rightarrow CdS + I_2\,(g). \qquad (2)$$

SnI_2 melting/crystallization is seen at 326-327 °C in cooling curves and in the second heating run. In cooling process, the mixture of formed products crystallizes at 354 °C and by repeated heating it melts at 371 °C followed by melting of pure CdI_2 at 383 °C giving an overlapping peak. The endothermic effects at 595 °C can be ascribed to the phase transition α-SnS ↔ β-SnS. The thermal effect at 672-674 °C in cooling curves corresponds to the phase transition of α-Sn_2S_3 ↔ β-Sn_2S_3 as described in [21].

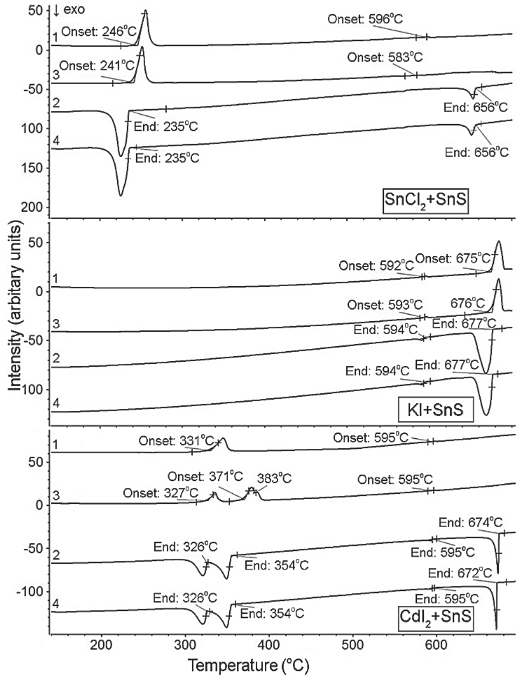

Figure 8 DTA curves of $SnCl_2$+SnS, KI-SnS and CdI_2+SnS mixtures.

The mixture of $SnCl_2$+SnS melted endothermically at 246 °C and freezes at 235 °C (Fig. 8). Melting of pure $SnCl_2$ was also detected at 246°C and the experimentally determined heat of fusion of 14.6 kJ/mol is in good agreement with literature data [12], where the melting of $SnCl_2$ is reported at 247 °C with heat of fusion of 14.52 ± 0.17 kJ/mol at this temperature. The next thermal effect at 596 °C corresponds to the process of phase transition of low temperature α-SnS to the high temperature β-SnS form shown in Eq. (3). The experimentally determined (in this study) enthalpy value of the phase transition is 0.1 kJ/mol for the reversible process:

$$\alpha\text{-SnS} \leftrightarrow \beta\text{-SnS}\,. \qquad (3)$$

In the mixture of KI+SnS (Fig. 8), the phase transition α-SnS ↔ β-SnS occurs in heating/cooling cycles in the region of 592-594 °C. The mixture melts endothermically at 675-676 °C, at much lower temperatures than pure KI (685 °C, as it was determined in our previous work [13]) and freezes at 677 °C. The lowering of melting temperature of the mixture in comparison with pure KI gives a hint to some solubility of SnS in KI. In the paper [21], the α- to β-phase transition was found at ~602 °C. As discussed in

© 2015 WILEY-VCH Verlag GmbH & Co. KGaA, Weinheim

[21], low-temperature α-SnS is essentially stoichiometric, whereas β-SnS can dissolve in it some excess of S. β-SnS has a maximum S content of 50.5 at % on the border of single phase area at around 700 °C being in equilibrium with 2-phase area of β-SnS and β-Sn_2S_3. Therefore, we can conclude that stoichiometric SnS compound can be synthesised at temperatures below 596 °C. In the system KI-SnS is important to use slow cooling after recrystallization for complete phase transition β- to α-SnS to provide stoichiometric absorber material for solar cells [25].

4 Conclusion Recrystallization of polycrystalline SnS in different molten salts CdI_2, $SnCl_2$ and KI as flux materials was studied. Compositional and structural analysis showed that single phase SnS monograin powder can be obtained at 740 °C in KI and at 500 °C in $SnCl_2$. Recrystallization of SnS in molten CdI_2 resulted in multiphase mixture of SnS, Sn_2S_3 and CdS crystals due to chemical interactions between the compounds. The morphology of crystals was controlled by the nature of the used flux materials: needle-like Sn_2S_3 together with round edged crystals of CdS were grown in CdI_2. Smooth flat crystals of SnS in $SnCl_2$ and well-formed SnS crystals with rounded edges in KI had been gained. Thermal analyses revealed that phase transition from α-SnS to β-SnS occurs in the temperature region 592-596 °C depending on the used flux.

Acknowledgements This work was supported by the Estonian Science Foundation grants ETF9346, ETF9425 and by institutional research funding IUT (IUT19-28) of the Estonian Ministry of Education and Research, Projects TK117, TK114, VFP638, AR10128 and AR12128.

References

[1] K.T. Ramakrishna Reddya, N. Koteswara Reddya, and R.W. Miles, Sol. Energy Mater. Solar Cells **90,** 3041-3046 (2006).

[2] J.Y. Kim and S.M. George, J. Phys. Chem. C **114** 17597-17603 (2010).

[3] N.K. Reddy, Y.B. Hahn, M. Devika, H.R. Sumana, and K.R. Gunasekhar, J. Appl. Phys. **101,** 093522 (2007).

[4] C. Gao, H. Shen, L. Sun, and Z. Shen, Mater. Lett. **65,** 1413-1415 (2011).

[5] R.H. Bube, Photovoltaic Materials (Imperial College Press, London, 1998).

[6] R.G. Gordon, P. Sinsermsuksakul, L. Sun, S.W. Lee, H.H. Park, S.B. Kim, and C. Yang, Adv. Energy Mater. **4,** 1400496 (2014).

[7] M. Altosaar and E. Mellikov, Jpn. J. Appl. Phys. **39**, 65-66 (2000).

[8] M. Altosaar, J. Raudoja, K. Timmo, M. Danilson, M. Grossberg, M. Krunks, T. Varema, and E. Mellikov, in: Proceedings of the 2006 IEEE WCPEC-4, Hawaii, 2006.

[9] K. Muska, M. Kauk, M. Grossberg, M. Altosaar, J. Raudoja, and O. Volobujeva, Energy Procedia **10,** 203-207 (2011).

[10] K. Muska, M. Kauk, M. Grossberg, M. Altosaar, M. Pilvet, T. Varema, K. Timmo, O. Volobujeva, and A. Mere, Thin Solid Films **535,** 35-38 (2013).

[11] D. L. Perry, Handbook of Inorganic Compounds, 2nd ed. (CRC Press, Boca Raton, 2011), ISBN 9781439814611-CAT# K10752.

[12] T.N. Sevastyanov, and N. V. Karpenko, Zh. Fiz. Khim. **45**, 1834-1835 (1971). V.R. Minnam Reddy, S. Gedi, C. Park, and R.W. Miles, and K.T. Ramakrishna Reddy, Curr. Appl. Phys. **15,** 588-598 (2015).

[13] I. Klavina, T. Kaljuvee, K. Timmo, J. Raudoja, R. Traksmaa, M. Altosaar, and D. Meissner, Thin Solid Films **519,** 7399-7420 (2011).

[14] V.N. Eremenko, Yu. V. Naidich, and I.A. Lavrinenko, Liquid Phase Sintering (Consultants Bureau, New York, 1970).

[15] V.R. Minnam Reddy, S. Gedi, C. Park, R.W. Miles, and K.T. Ramakrishna Reddy, Curr. Appl. Phys. **15,** 588-598 (2015).

[16] H.R. Chandrasekhar, R.G. Humphreys, U. Zwick, and M. Cardona, Phys. Rev. B **15**, 2177-2183 (1977).

[17] N.R. Mathews, H.B.M. Anaya, M.A.C. Jacome, C.A. Chavez, and J.A.T. Antonio, J. Electrochem. Soc. **157,** H337-H341 (2010).

[18] L.S. Price, I.P. Parkin, A.M.E. Hardy, and R.J.H. Clark, Chem. Mater. **11**, 1792-1799 (1999).

[19] M. Nippus and R. Claus, Opt. Commun. **22**, 318-322 (1977).

[20] G. Nkwusi, I. Leinemann, M. Grossberg, T. Kaljuvee, R. Traksmaa, M. Altosaar, and D. Meissner, in: Proc. 9th International Conference of Young Scientists on Energy Issues, Kaunas, Latvia, 2012, II 38-II 46.

[21] R. C. Sharma and Y.A. Chang. Bull. Alloy Phase Diagrams **7,** 269-273(1986).

[22] I. Barin, O. Knacke, and O. Kubaschewski, Thermochemical Properties of Inorganic Substances (Supplement, Springer-Verlag, Berlin, 1977), p. 861.

[23] O. Knacke, O. Kubaschewski, and K. Hesselman, Thermochemical Properties of Inorganic Substances, 2nd ed. (Springer-Verlag, Berlin, 1991), p. 91.

[24] M. Binnewies and E. Milke, Thermochemical Data of Elements and Compounds, 2nd ed. (Wiley-VCH, Weinheim, 2002).

[25] V. Steinmann, R. Jaramillo, K. Hartman, R. Chakraborty, R.E. Brandt, J.R. Poindexter, Y.S. Lee, L. Sun, A. Polizzotti, H.H. Park, R.G. Gordon, and T. Buonassisi, Adv. Mater. **26,** 7488-7492 (2014).

© 2015 WILEY-VCH Verlag GmbH & Co. KGaA, Weinheim

Appendix 2

A2.1 Calculations of Solar Cell Efficiency

$$\eta = \frac{V_{OC} I_{SC} FF}{P_{in}},$$

where V_{OC} – open-circuit voltage, V,
I_{SC} – short-circuit current, A,
FF – fill factor,
P_{in} – input power, W (Morales-Acevedo, 2013).

A2.2 Calculations of Atomic Percent

$$at.\% \ (i) \ = \frac{N_i}{N_{tot}} \times \ 100 \ \%,$$

where N_i – partial number of atoms of substance *i*,
N_{tot} – total number of atoms (Atkins *et al.*, 2013).

A2.3 Calculations of Molar Percent

$$mol\% \ (i) \ = \frac{n_i}{n_{tot}} \times \ 100 \ \%,$$

where n_i – partial number of moles of substance *i*, mol,
n_{tot} – total number of moles, mol (Atkins *et al.*, 2013).

A2.4 Calculations of Weight Percent

$$wt\% \ (i) \ = \frac{m}{m_{tot}} \times \ 100 \ \%,$$

where m_i – partial weight of substance *i*, kg,
m_{tot} – total weight, kg (Atkins *et al.*, 2013).

Appendix 3

Table A2.1 Summary of samples that were analyzed by XRD, Raman, and EDX-SEM

Mixture	Description of sample	Analysis
CdI_2-ZnSe	Heated to 740 °C (168 h) single crystal (washed)	XRD, Raman, SEM-EDX
	Opened DTA ampoule (nonwashed)	XRD
KI-SnSe	Heated to 420 °C (13 h) (nonwashed)	XRD
CdI_2-SnSe	Heated to 740 °C (168 h) single crystal (washed)	XRD, Raman, SEM-EDX
	Opened DTA ampoule (nonwashed)	XRD
KI-CuSe	Heated to 420 °C (13 h) (nonwashed)	XRD
	Heated to 540 °C (5 h) (washed)	XRD, Raman
	Heated at 680 °C (4 h) (nonwashed)	XRD
	Heated at 710 °C (12 h) (nonwashed)	XRD
NaI-CuSe	Heated to 380 °C (114 h)	XRD, Raman
CdI_2-CuSe	Heated to 400 °C (4 h) (nonwashed)	XRD, Raman
	Heated to 740 °C (4 h) (nonwashed)	XRD, Raman
KI-SnSe-CuSe	Heated to 400 °C (4 h) (nonwashed)	XRD, Raman
NaI-SnSe-CuSe	Heated to 380 °C (4 h) (nonwashed)	Raman
	Heated to 580 °C (4 h) (nonwashed)	Raman
CdI_2-SnSe-CuSe	Heated to 250 °C (48 h) (washed)	Raman
	Heated to 270 °C (4 h) (washed)	Raman
	Heated to 390 °C (4 h) (nonwashed)	Raman
	Opened DTA ampoule (nonwashed)	XRD
KI-ZnSe-SnSe-CuSe	Heated to 250 °C (97 h) (nonwashed and washed)	XRD, Raman
	Heated to 270 °C (1 h) (nonwashed)	XRD, Raman
	Heated to 400 °C (1 h) (nonwashed)	XRD, Raman

	Heated to 680 °C (1 h) (nonwashed)	XRD, Raman
	Heated to 800 °C, cooled to 520 °C (1 h) (nonwashed)	XRD
NaI-ZnSe-SnSe-CuSe	Heated to 380 °C (4 h) (nonwashed and washed)	XRD, Raman
	Heated to 615 °C (4 h) (washed)	XRD, Raman
	Heated to 650 °C (4 h), (washed)	XRD, Raman
	Heated to 790 °C (4 h) (nonwashed and washed)	XRD, Raman
CdI_2-ZnSe-SnSe-CuSe	Heated to 370 °C (1 h) (nonwashed)	XRD, Raman
	Heated to 400 °C (1 h) (nonwashed)	XRD, Raman
	Heated to 590 °C (1 h) (washed)	XRD
	Heated to 740 °C (1 h) (nonwashed and washed)	XRD

Table A2.2 Reference Raman shifts that were used in this thesis

Compound	**Raman shift / cm^{-1}**	**Reference**
CdI_2	15,8, 45,1, 111,3	(Montero & Kiefer, 1973)
	111, 320	**Paper IV**
KI	63, 89, 101, 102, 175, 210, 252	(Krishnamurthu & Krishnan, 1965)
	90, 95, 102, 106	(Leinemann *et al.*, 2011)
NaI	19, 42, 58, 88, 103, 120, 132, 200, 200-250, 310-370	(Krishnamurthu & Krishnan, 1965)
NaI (dried)	95, 107, 122, 160, 167, 189, 194, 225	(Leinemann *et al.*, 2011)
NaI + $NaI\cdot 2H_2O$	82, 90, 95, 99, 107, 115, 122, 135, 138, 150, 187, 194, 222, 230, 244, 323, 353, 419	**Paper III**
ZnSe	202, 252	(Perna *et al.*, 2002)
	140, 206, 253	(Klavina *et al.*, 2010) **Paper IV**
	250	**Paper I**
	204, 205, 249-254	(Leinemann *et al.*, 2011)
ZnSe nanorods	213, 237, 257	(Teredesai *et al.*, 2002)
SnSe	151 ± 2, 130 ± 2, 71 ± 2, 150 ± 5, 123 ± 5, 80 ± 5, 108 ± 2, 96 ± 5	(Chandrasekhar *et al.*, 1977)

$SnSe_2$	113, 186	(Lucovsky *et al.*, 1976)
	109, 184,5	(Smith *et al.*, 1977)
$Cu_{2-x}Se$	263	(Ishii *et al.*, 1993); **Paper I**
	262, 263	(Leinemann *et al.*, 2011)
Cu_2SnSe_3	180, 236, 251	(Altosaar *at al.*, 2008)
	83, 178, 204, 231, 244, 291	(Marcano *et al.*, 2011)
$Cu_2ZnSnSe_4$	173, 196, 231	(Altosaar *et al.*, 2008)
	167, 173, 196, 231, 245	(Grossberg *et al.*, 2009).
Se	233, 237 (trigonal), 250 (disordered)	(Poborchii *et al.*, 1998)
	92-93, 120, 140 amorphous	(Yannopoulos & Andrikopoulos, 2004).
	93, 141, 241 stretching	(Burns *et al.*, 1991)
	240	**Paper III**
	92-93, 120, 140, 233, 237, 253	**Paper IV**
α-, β-, γ- CuI	83, 122	(Mamedov, *et al.*, 1999)
	93, 122, 139	**Paper III**
CdSe	198; 207,5	(Teredesai *et al.*, 2002)
	209	(Klavina *et al.*, 2010)
	168,198, 201, 207,5, 320	**Paper IV**
$Zn_{1-x}Cd_xSe$	95-97, 207, 238-242, 476-477	(Klavina *et al.*, 2010)
SnO	112, 210	(Mcguire *et al.*, 2002)
$Na_2[Cu(OH)]_4$	219, 311, 438, 443	**Paper III**
Na_2SeO_4	120, 338, 362, 424, 454, 477	**Paper III**
ZnI_2 (dried)	70, 77, 119, 127, 188	**Paper IV**
ZnI_2 (nondried)	In additionally to dried peaks: 62, 88, 141, 153, 161, 178	**Paper IV**
SnI_4	147, 207, 215	**Paper IV**
	149, 216	(Stammreich *et al.*, 1956)
Cu_2SnSe_4	190	**Paper IV**

Table A2.3 The file numbers used in this thesis for XRD analysis (not presented on Figures)

Compound	**ICDD or JCDPS numbers**
$Cd_{0.37}Zn_{0.7}Se$	01-071-4160 (l)
CdI_2	330239, 10842244, 00-033-0239
CdSe	04-012-6324 (A)
$Cu_{1.8}Se$	01-071-6180 (l)
$Cu_{2+1}O$	00-005-0667 (*)
$Cu_2CdSnSe_4$	04-010-6296 (*)
Cu_2Se	04-015-3687 (A)
$Cu_2ZnSnSe_4$	10708930
Cu_3Se_2	04-007-1069 (A)

Cu_3Sn	01-081-8187
Cu_4Se_3	420925
CuI	10822112
CuO	00-048-15-48 (*)
CuSe	30653562
KI	00-004-0471
Na_2CO_3	00-055-0503 (I), 00-019-1130 (I)
Na_2SeO_4	00-024-1113 (*)
NaI	04-006-5383 (I)
SnSe	04-004-5813 (A)
$Zn_{0.78}Cd_{0.22}Se$	10714159
ZnSe	04-007-9955 (A)

Curriculum vitae

Personal data

Name: Inga Leinemann
Date of birth: 09.07.1985
Place of birth: Priekule, Latvia
Citizenship: Latvian

Contact data

E-mail: ingaklav@inbox.lv

Education

2010–2019	TalTech, School of Engineering – PhD
2007–2009	Riga Technical University, Faculty of Material Science and Applied Chemistry – M.Sc.Eng.
2003–2007	Riga Technical University, Faculty of Material Science and Applied Chemistry – BSc
2000–2003	High school Aizpute

Language competence

Latvian – Native language
English – Fluent
Estonian – Fluent
Russian – Fluent
German – Average

Professional employment

2018–	Editorial board member at PiscoMed Publishing Pte. Ltd., Singapore
2016–	Present founder and board member at *Inga Invest OÜ*
2012–2017	Junior Researcher at the Institute of Materials Science, TalTech
2009–2011	Technician at the Institute of Materials Science, TalTech
2005–2009	Assistant at Institute of Silicate, High-temperature and Nanomaterials, Faculty of Material Science and Applied Chemistry, Riga Technical University

Training courses and conferences

February 26–27, 2015	University of Tartu conference. Tartu, Estonia (oral presentation)
November 13–14, 2014	5th European Kesterite Workshop. Tallinn, Estonia (oral presentation)
August 27–30, 2013	CEEC-TAC 2, 2nd Central and Eastern European Conference on Thermal Analyses and Calorimetry. Vilnius, Lithuania (poster presentation)
July 8–12, 2013	Rietveld workshop 2013 – Combined Analysis Using X-Ray and Neutron Scattering. Caen, France
June 23–28, 2013	Summer School of Calorimetry. Calorimetry and thermal methods in catalysis. Lyon, France
November 24–25, 2011	2nd European Workshop on Kesterites. Barcelona, Spain (oral presentation)
September 7–10, 2011	CEEC-TAC 1. Craiova, Romania (poster presentation)
June 9–13, 2011	E-MRS (European Materials Research Society) Spring Meeting. Nice, France (poster presentation)
May 26–27, 2011	CYSENI (Conference of Young Scientists on Energy Issues). Kaunas, Lithuania (oral presentation)

September 18–25, 2010	International Summer School on Photovoltaics and New Concepts of Quantum Solar Energy Conversion (Quantsol Summer School). Hirschegg, Austria
June 7–11, 2010	E-MRS Spring Meeting. Strasbourg, France (poster and oral presentation)
May 27–28, 2010	CYSENI. Kaunas, Lithuania (oral presentation)

Awards

2010 EUROPEAN MATERIALS RESEARCH SOCIETY YOUNG SCIENTIST AWARD in Thin Film Chalcogenide Photovoltaic Materials at 2010 SPRING MEETING, Strasbourg 7th - 11th June, 2010

2003 Student of the year 2003 at High school in Aizpute

Supervised Defended Master Thesis

2013 God'swill C. Nkwusi, Formation of Cu_2ZnSnS_4 in Molten CdI_2 for Monograin Membrane Solar Cells, Tallinn University of Technology

2013 Weihao Zhang, Study of Chemical Pathway of $Cu_2ZnSnSe_4$ Formation in NaI as Flux Material, Tallinn University of Technology

Defended dissertation

2009 Keramikas struktūras iegūšana un īpašības ar biomimētikas un sola-gēla metodi. Riga Technical University, Master's thesis, supervisor: Dr. I. Juhņeviča

2007 Augu valsts matricas oglekli saturošas keramikas ieguvei. Riga Technical University, Bachelor's thesis, supervisor: prof. G. Mežinskis

Publications

1. **Leinemann, I.,** Pilvet, M., Kaljuvee, T., Traksmaa, R., & Altosaar, M. (2018). Reaction Pathway to $Cu_2ZnSnSe_4$ in CdI_2 Part 2: Chemical Reactions and Enthalpies in Mixtures of CdI_2-CuSe-SnSe and CdI_2-CuSe-SnSe-ZnSe. *J Therm Anal Calorim, 134*(1), 433-441. doi: 10.1007/s10973-018-7415-4
2. **Leinemann, I.,** Nkwusi, G. C., Timmo, K., Danilson, M., Raudoja, J., Kaljuvee, T., Traksmaa, R., Altosaar, M., & Meissner, D. (2018). Reaction Pathway to $Cu_2ZnSnSe_4$ Formation in CdI_2 Part 1: Chemical Reactions and Enthalpies in Mixtures of CdI_2-ZnSe, CdI_2-SnSe, and CdI_2-CuSe. *J Therm Anal Calorim, 134*(1), 409-421. doi: 10.1007/s10973-018-7102-5
3. **Leinemann, I**., Timmo, K., Grossberg, M., Kaljuvee, T., Tõnsuaadu, K., Traksmaa, R., Altosaar, M., & Meissner, D. (2015). Reaction Enthalpies of $Cu_2ZnSnSe_4$ Synthesis in KI. *J Therm Anal Calorim, 119*(3), 1555-1564. doi: 10.1007/s10973-014-4339-5
4. **Leinemann, I.,** Zhang, W., Kaljuvee, T., Tõnsuaadu, K., Traksmaa, R., Raudoja, J., Grossberg, M., Altosaar, M., & Meissner, D. (2014). $Cu_2ZnSnSe_4$ Formation and Reaction Enthalpies in Molten NaI Starting from Binary Chalcogenides. *J Therm Anal Calorim, 118*(2), 1313-1321. doi: 10.1007/ s10973-014-4102-y
5. **Leinemann, I.**, Raudoja, J., Grossberg, M., Altosaar, M., Meissner, D., Traksmaa, R., & Kaljuvee, T. (2011). Comparison of Copper Zinc Tin Selenide Formation in Molten Potassium Iodide and Sodium Iodide as Flux Materials, *CYSENI 2011 International Conference of Young Scientists on Energy Issues* (pp. 8-15). Kaunas, Lithuania: Lithuanian Energy Institute.
6. **Klavina, I.,** Kaljuvee, T., Timmo, K., Raudoja, J., Traksmaa, R., Altosaar, M., & Meissner, D. (2011). Study of $Cu_2ZnSnSe_4$ Monograin Formation in Molten KI Starting from Binary Chalcogenides. *Thin Solid Films, 519*(21), 7399-7402. doi: 10.1016/j.tsf.2011.01.365

7. **Klavina, I.**, Raudoja, J., Altosaar, M., Mellikov, E., Meissner, D., & Kaljuvee, T.(2010). CZTS ($Cu_2ZnSnSe_4$) Crystal Growth for Use in Monograin Membrane Solar Cells, *CYSENI 2010 International Conference of Young Scientists on Energy Issues* (pp. VII-345-VII-353). Kaunas, Lithuania: Lithuanian Energy Institute.
8. **Kļaviņa, I.,** & Juhņeviča, I. (2009). Keramikas struktūras iegūšana un īpašības ar biomimetikas un sola-gēla metodi. 50. RTU studentu zinātniskās un tehniskās konferences materiāli. Riga, Latvia: RTU.
9. **Kļaviņa, I**., & Juhņeviča, I. (2006). Priedes koksnes un ķērpju matricas izmantošana oglekli saturošas keramikas ieguvei. 47. RTU studentu zinātniskās un tehniskās konferences materiāli. Riga, Latvia: RTU, p. 171.
10. Nkwusi, G., **Leinemann, I.**, & Altosaar, M. (2016). The Processes and Enthalpies in Synthesis of Cu_2ZnSnS_4 in Molten CdI_2. *International Advanced Research Journal in Science, Engineering and Technology, 3*(5), 1-9. doi: 10.17148/IARJSET.2016.3524
11. Nkwusi, G., **Leinemann, I.**, Raudoja, J., Mikli, V., Kärber, E., & Altosaar, M. (2016). Impact of Growth-Synthesis Conditions on $Cu_2Zn_{1-x}Cd_xSnS_4$ Monograin Material Properties. *Superlattices and Microstructures, 98*, 400-405. doi: 10.1016/j.spmi.2016.09.006
12. Nkwusi, G., **Leinemann, I.**, Raudoja, J., Mikli, V., Kauk-Kuusik, M., Altosaar, M., & Mellikov, E. (2014). Synthesis of $Cu_2(ZnCd)SnS_4$ Absorber Material for Monograin Membrane Applications, *2013 MRS Fall Meeting:* ScholarOne Manuscripts, 1638 (pp. 1-6) Boston, USA: Massachusetts. doi: 10.1557/opl.2014.245
13. Nkwusi, G., Leinemann, I., Grossberg, M., Kaljuvee, T., Traksmaa, R., Altosaar, M., & Meissner, D. (2012). Formation of Copper Zinc Tin Sulfide in Cadmium Iodide for Monograin Membrane Solar Cells, *CYSENI 2012 International Conference of Young Scientists on Energy Issues* (pp. II 38-II 46). Kaunas, Lithuania: Lithuanian Energy Institute.
14. Timmo, K., Kauk-Kuusik, M., Pilvet, M., Mikli, V., Kärber, E., Raadik, T., **Leinemann, I.,** Altosaar, M., & Raudoja, J. (2015). Comparative Study of SnS Recrystallization in Molten CdI_2, $SnCl_2$ and KI. *Phys. Status Solidi C, 13*(1) 8-12. doi: 10.1002/pssc.201510082
15. Timmo, K., Kauk-Kuusik, M., Altosaar, M., Raudoja, J., Raadik, T., Grossberg, M., Varema, T., Pilvet, M., **Leinemann, I.**, Volobujeva, O., & Mellikov, E. (2013). Novel Cu_2CdSnS_4 and $Cu_2ZnGeSe_4$ Absorber Materials for Monograin Layer Solar Cell Aplication, *EU PVSEC 2013* (pp. 2385-2388). Paris, France: Wiley-Blackwell.
16. Mellikov, E., Meissner, D., Altosaar, M., Kauk, M., Krustok, J., Öpik, A., Volobujeva, O., Iljina, J., Timmo, K., **Klavina, I.**, Raudoja, J., Grossberg, M., Varema, T., Muska, K., Ganchev, M., Bereznev, S., & Danilson, M. (2011). CZTS Monograin Powders and Thin Films. *Adv. Mater. Res., 222*, 8-13.
17. Juhņeviča, I., Mežinskis, G., & **Kļaviņa, I**. (2009). Augu valsts materiālu un sola-gēla tehnoloģijas izmantošana keramikas ieguvei. Riga, Latvia: RTU zinātniskie raksti. 2. sēr., Materiālzinātne un lietišķā ķīmija . – 19. sēj.
18. Mezinskis, G., Juhnevica, I., & **Klavina, I**. (2007). Synthesis of Carbon, Silica and Titania Containing Ceramics by the Biotemplating Technique, *EUROMAT 2007. European Congress and Exhibition on Advanced Materials and Processes* (B12-1624). Nürnberg, Germany: Symposium – B12 Ceramic Composite Concepts.

Elulookirjeldus

Isikuandmed

Nimi: Inga Leinemann
Sünniaeg: 09.07.1985
Sünnikoht: Priekule, Läti
Kodakondsus: Läti

Kontaktandmed

E-post: ingaklav@inbox.lv

Hariduskäik

2010–2019	Tallinna Tehnikaülikool, Inseneriteaduskond – doktorantuur
2007–2009	Riia Tehnikaülikool, Materjaliteaduse ja Rakenduskeemia Teaduskond – M.Sc.Eng.
2003–2007	Riia Tehnikaülikool, Materjaliteaduse ja Rakenduskeemia Teaduskond – BSc
2000–2003	Aizpute keskkool, keskharidus

Keelteoskus

Läti keel – emakeel
Inglise keel – kõrgtase
Eesti keel – kõrgtase
Vene keel – kõrgtase
Saksa keel – kesktase

Teenistuskäik

2018–	Toimetuskolleegiumi liige, PiscoMed Publishing Pte. Ltd., Singapur
2016–	Juhatuse liige, *Inga Invest OÜ*
2012–2017	Nooremteadur, Materjaliteaduse Instituut, Tallinna Tehnikaülikool
2009–2011	Tehnik, Materjaliteaduse Instituut, Tallinna Tehnikaülikool
2005–2009	Assistent, Silikaadi, Kõrgtemperatuuri ja Nanomaterjali Instituut, Materjaliteaduse ja Rakenduskeemia Teaduskond, Riia Tehnikaülikool

Täienduskursused ja konverentsid

26.02.–27.02.2015	University of Tartu conference. Tartu, Estonia (ettekanne)
13.11.–14.11.2014	5th European Kesterite Workshop. Tallinn, Estonia (ettekanne)
27.08.–30.08.2013	CEEC-TAC 2, 2nd Central and Eastern European Conference on Thermal Analyses and Calorimetry. Vilnius, Lithuania (posteresitlus)
08.07.–12.07.2013	Rietveld workshop 2013 – Combined Analysis Using X-Ray and Neutron Scattering. Caen, France
23.06.–28.06.2013	Summer School of Calorimetry. Calorimetry and Thermal Methods in Catalysis. Lyon, France
24.11.–25.11.2011	2nd European Workshop on Kesterites. Barcelona, Spain (ettekanne)
07.09.–10.09.2011	CEEC-TAC 1. Craiova, Romania (posteresitlus)
09.06.–13.06.2011	E-MRS (European Materials Research Society) Spring Meeting. Nice, France (posteresitlus)
26.05.–27.05.2011	CYSENI (Conference of Young Scientists on Energy Issues). Kaunas, Lithuania (ettekanne)

18.09.–25.09.2010 International Summer School on Photovoltaics and New Concepts of Quantum Solar Energy Conversion (Quantsol Summer School). Hirschegg, Austria

07.06.–11.06.2010 E-MRS Spring Meeting. Strasbourg, France (posteresitlus ja ettekanne)

27.05.–28.05.2010 CYSENI. Kaunas, Lithuania (ettekanne)

Tunnustused

2010 EUROPEAN MATERIALS RESEARCH SOCIETY YOUNG SCIENTIST AWARD in Thin Film Chalcogenide Photovoltaic Materials at 2010 SPRING MEETING, Strasbourg 7th-11th June, 2010

2003 Aasta õpilane 2003, Aizpute Keskkool

Juhendatud magistritööd

2013 God'swill C. Nkwusi, Formation of Cu_2ZnSnS_4 in Molten CdI_2 for Monograin Membrane Solar Cells, Tallinn University of Technology

2013 Weihao Zhang, Study of Chemical Pathway of $Cu_2ZnSnSe_4$ Formation in NaI as Flux Material, Tallinn University of Technology

Kaitstud lõputööd

2009 Keramikas struktūras iegūšana un īpašības ar biomimētikas un sola-gēla metodi. Riga Technical University, Master's thesis, juhendaja: Dr. I. Juhņeviča

2007 Augu valsts matricas oglekli saturošas keramikas ieguvei. Riga Technical University, Bachelor's thesis, juhendaja: prof. G. Mežinskis

Publikatsioonid

1. **Leinemann, I.,** Pilvet, M., Kaljuvee, T., Traksmaa, R., & Altosaar, M. (2018). Reaction Pathway to $Cu_2ZnSnSe_4$ in CdI_2 Part 2: Chemical Reactions and Enthalpies in Mixtures of CdI_2-CuSe-SnSe and CdI_2-CuSe-SnSe-ZnSe. *J Therm Anal Calorim, 134*(1), 433-441. doi: 10.1007/s10973-018-7415-4
2. **Leinemann, I.,** Nkwusi, G. C., Timmo, K., Danilson, M., Raudoja, J., Kaljuvee, T., Traksmaa, R., Altosaar, M., & Meissner, D. (2018). Reaction Pathway to $Cu_2ZnSnSe_4$ Formation in CdI_2 Part 1: Chemical Reactions and Enthalpies in Mixtures of CdI_2-ZnSe, CdI_2-SnSe, and CdI_2-CuSe. *J Therm Anal Calorim, 134*(1), 409-421. doi: 10.1007/s10973-018-7102-5
3. **Leinemann, I**., Timmo, K., Grossberg, M., Kaljuvee, T., Tõnsuaadu, K., Traksmaa, R., Altosaar, M., & Meissner, D. (2015). Reaction Enthalpies of $Cu_2ZnSnSe_4$ Synthesis in KI. *J Therm Anal Calorim, 119*(3), 1555-1564. doi: 10.1007/s10973-014-4339-5
4. **Leinemann, I.,** Zhang, W., Kaljuvee, T., Tõnsuaadu, K., Traksmaa, R., Raudoja, J., Grossberg, M., Altosaar, M., & Meissner, D. (2014). $Cu_2ZnSnSe_4$ Formation and Reaction Enthalpies in Molten NaI Starting from Binary Chalcogenides. *J Therm Anal Calorim, 118*(2), 1313-1321. doi: 10.1007/ s10973-014-4102-y
5. **Leinemann, I.**, Raudoja, J., Grossberg, M., Altosaar, M., Meissner, D., Traksmaa, R., & Kaljuvee, T. (2011). Comparison of Copper Zinc Tin Selenide Formation in Molten Potassium Iodide and Sodium Iodide as Flux Materials, *CYSENI 2011 International Conference of Young Scientists on Energy Issues* (pp. 8-15). Kaunas, Lithuania: Lithuanian Energy Institute.
6. **Klavina, I.,** Kaljuvee, T., Timmo, K., Raudoja, J., Traksmaa, R., Altosaar, M., & Meissner, D. (2011). Study of $Cu_2ZnSnSe_4$ Monograin Formation in Molten KI Starting from Binary Chalcogenides. *Thin Solid Films, 519*(21), 7399-7402. doi: 10.1016/j.tsf.2011.01.365

7. **Klavina, I.**, Raudoja, J., Altosaar, M., Mellikov, E., Meissner, D., & Kaljuvee, T.(2010). CZTS ($Cu_2ZnSnSe_4$) Crystal Growth for Use in Monograin Membrane Solar Cells, *CYSENI 2010 International Conference of Young Scientists on Energy Issues* (pp. VII-345-VII-353). Kaunas, Lithuania: Lithuanian Energy Institute.
8. **Kļaviņa, I.,** & Juhņeviča, I. (2009). Keramikas struktūras iegūšana un īpašības ar biomimetikas un sola-gēla metodi. 50. RTU studentu zinātniskās un tehniskās konferences materiāli. Riga, Latvia: RTU.
9. **Kļaviņa, I**., & Juhņeviča, I. (2006). Priedes koksnes un ķērpju matricas izmantošana oglekli saturošas keramikas ieguvei. 47. RTU studentu zinātniskās un tehniskās konferences materiāli. Riga, Latvia: RTU, p. 171.
10. Nkwusi, G., **Leinemann, I.**, & Altosaar, M. (2016). The Processes and Enthalpies in Synthesis of Cu_2ZnSnS_4 in Molten CdI_2. *International Advanced Research Journal in Science, Engineering and Technology, 3*(5), 1-9. doi: 10.17148/IARJSET.2016.3524
11. Nkwusi, G., **Leinemann, I.**, Raudoja, J., Mikli, V., Karba, E., & Altosaar, M. (2016). Impact of Growth-Synthesis Conditions on $Cu_2Zn_{1-x}Cd_xSnS_4$ Monograin Material Properties. *Superlattices and Microstructures, 98*, 400-405. doi: 10.1016/j.spmi.2016.09.006
12. Nkwusi, G., **Leinemann, I.**, Raudoja, J., Mikli, V., Kauk-Kuusik, M., Altosaar, M., & Mellikov, E. (2014). Synthesis of $Cu_2(ZnCd)SnS_4$ Absorber Material for Monograin Membrane Applications, *2013 MRS Fall Meeting:* ScholarOne Manuscripts, 1638 (pp. 1-6) Boston, USA: Massachusetts. doi: 10.1557/opl.2014.245
13. Nkwusi, G., Leinemann, I., Grossberg, M., Kaljuvee, T., Traksmaa, R., Altosaar, M., & Meissner, D. (2012). Formation of Copper Zinc Tin Sulfide in Cadmium Iodide for Monograin Membrane Solar Cells, *CYSENI 2012 International Conference of Young Scientists on Energy Issues* (pp. II 38-II 46). Kaunas, Lithuania: Lithuanian Energy Institute.
14. Timmo, K., Kauk-Kuusik, M., Pilvet, M., Mikli, V., Kärber, E., Raadik, T., **Leinemann, I.,** Altosaar, M., & Raudoja, J. (2015). Comparative Study of SnS Recrystallization in Molten CdI_2, $SnCl_2$ and KI. *Phys. Status Solidi C, 13*(1) 8-12. doi: 10.1002/pssc.201510082
15. Timmo, K., Kauk-Kuusik, M., Altosaar, M., Raudoja, J., Raadik, T., Grossberg, M., Varema, T., Pilvet, M., **Leinemann, I.**, Volobujeva, O., & Mellikov, E. (2013). Novel Cu_2CdSnS_4 and $Cu_2ZnGeSe_4$ Absorber Materials for Monograin Layer Solar Cell Aplication, *EU PVSEC 2013* (pp. 2385-2388). Paris, France: Wiley-Blackwell.
16. Mellikov, E., Meissner, D., Altosaar, M., Kauk, M., Krustok, J., Öpik, A., Volobujeva, O., Iljina, J., Timmo, K., **Klavina, I.**, Raudoja, J., Grossberg, M., Varema, T., Muska, K., Ganchev, M., Bereznev, S., & Danilson, M. (2011). CZTS Monograin Powders and Thin Films. *Adv. Mater. Res., 222*, 8-13.
17. Juhņeviča, I., Mežinskis, G., & **Kļaviņa, I**. (2009). Augu valsts materiālu un sola-gēla tehnoloģijas izmantošana keramikas ieguvei. Riga, Latvia: RTU zinātniskie raksti. 2. sēr., Materiālzinātne un lietišķā ķīmija . – 19. sēj.
18. Mezinskis, G., Juhnevica, I., & **Klavina, I**. (2007). Synthesis of Carbon, Silica and Titania Containing Ceramics by the Biotemplating Technique, *EUROMAT 2007. European Congress and Exhibition on Advanced Materials and Processes* (B12-1624). Nürnberg, Germany: Symposium – B12 Ceramic Composite Concepts.